

INTERNATIONAL LARGE DETECTOR

IDR

ILD Detector Collaboration

2019

ILD Editors

Main Editors:

Ties Behnke, Kiyotomo Kawagoe

Detector layout, technologies and Integration:

Karsten Buesser, Claude Vallee

Physics:

Keisuke Fujii, Jenny List

Software:

Frank Gaede, Akiya Miyamoto

Performance:

Keisuke Fujii, Jenny List

Costing:

Henri Videau, Karsten Buesser

Contents

Contents	iii
1 Introduction	1
2 Science with ILC	3
3 The ILC Environment	5
3.1 The International Linear Collider Project	5
3.2 Integration of ILD into the experimental environment	8
3.3 Experimental Conditions	8
3.3.1 Beam Conditions	8
3.3.2 Machine Detector Interface	8
4 The ILD detector concept	11
4.1 The overall ILD concept	11
4.2 Optimising ILD	12
5 Detector Layout and Technologies	15
5.1 Overall structure of the detector	15
5.1.1 Global structure and parameters	15
5.1.2 Subdetector layouts	15
5.2 Subdetector technology status	26
5.2.1 Vertex detector	26
5.2.2 Silicon trackers	28
5.2.3 Time projection chamber	30
5.2.4 Electromagnetic Calorimeter	33
5.2.5 Hadronic Calorimeter	36
5.2.6 Very forward detectors	40
5.2.7 Iron instrumentation	40
6 ILD Global Integration	43
6.1 External ILD integration	43
6.1.1 Site-related Infrastructure	43
6.1.2 Detector Utilities and Cavern Ancillary Services	43
6.1.3 Access and Assembly	49
6.2 Internal ILD integration	52
6.2.1 ILD Mechanical Structure	52
6.2.2 ILD Services and Utilities	53
6.2.3 Inner Detector Integration	54
6.2.4 TPC Integration	54
6.2.5 Electromagnetic Calorimeters Integration	56
6.2.6 Hadronic Calorimeters Integration	60

6.2.7	Very Forward System Integration	61
6.3	Data acquisition	64
6.3.1	DAQ architecture	64
6.3.2	DAQ R&D	65
6.4	Mechanical structure and studies	66
6.4.1	Calorimeter structure	66
6.4.2	Other subdetectors	67
6.5	Coil and yoke studies	67
6.5.1	Magnet Engineering Studies	67
6.5.2	Field Optimisation Studies	69
6.6	Beam background studies	74
6.6.1	Beamstrahlung	74
6.6.2	Halo muons	75
6.6.3	Backscattered neutrons from beam dumps	75
6.7	Alignment/ calibration procedures	77
6.8	Earthquake Safety	77
6.8.1	Structural Design	77
6.8.2	Seismic Isolation	78
6.9	Technical Documentation	80
6.9.1	Interface Control Documents	81
7	Physics and Detector Modelling	83
7.1	Modelling of ILC Conditions and Physics Processes	83
7.2	Detector Simulation	84
7.2.1	ILD Simulation Models	84
7.2.2	Hybrid Simulation	85
7.3	Event Reconstruction	87
7.3.1	Digitization	87
7.3.2	Track reconstruction	87
7.3.3	Particle Flow	88
7.3.4	High Level Reconstruction	89
7.4	Monte Carlo Production on the Grid	89
8	Detector and Physics Performance	91
8.1	System performance	91
8.1.1	Tracking	91
8.1.2	Particle Flow performance and JER	94
8.1.3	Vertexing	94
8.1.4	Photon Reconstruction	97
8.1.5	Lepton ID	97
8.1.6	Charged Particle identification	97
8.2	High-level Reconstruction Performance	99
8.2.1	Flavour-Tag Performance	99
8.2.2	Hadronically decaying τ ID	99
8.2.3	J/ψ reconstruction	100
8.3	Physics Benchmarks	101
8.3.1	Hadronic Branching Ratios of the Higgs Boson	102
8.3.2	H iggs Mass from $ZH \rightarrow ll\bar{b}\bar{b}$	104

8.3.3	Branching Ratio of $H \rightarrow \mu^+ \mu^-$	106
8.3.4	Sensitivity to $H \rightarrow$ invisible	107
8.3.5	τ polarisation, in $e^+ e^- \rightarrow \tau^+ \tau^-$	109
8.3.6	Hadronic WW and ZZ separation in Vector Boson Scattering	110
8.3.7	Photon Energy Scale Calibration from $e^+ e^- \rightarrow \gamma Z \rightarrow \gamma \mu^+ \mu^-$	113
8.3.8	A_{FB} and A_{LR} from $e^+ e^- \rightarrow b\bar{b}$	115
8.3.9	A_{FB} and A_{LR} from $t\bar{t} \rightarrow bbqql\nu$	116
8.3.10	Discovery Reach for extra Higgs Bosons in $e^+ e^- \rightarrow Zh$	116
8.3.11	Discovery Reach for and Characterisation of low ΔM Higgsinos	119
8.3.12	WIMP Discovery Reach and Characterisation in the Mono-Photon Channel	120
9	Costing	123
9.1	Introduction	123
9.2	The method	123
9.3	The costing of the different sub-detectors	123
9.3.1	The vertex detector	124
9.3.2	The SIT	124
9.3.3	The forward tracking	124
9.3.4	The forward calorimeters	124
9.3.5	The Time Projection Chamber (TPC)	124
9.3.6	The outer silicon tracker (SET)	125
9.3.7	The electromagnetic calorimeter (ECal)	125
9.3.8	The hadron calorimeter	126
9.3.9	The magnet	127
9.4	The global cost of each of the models.	128
9.5	Comparison with the DBD cost estimate.	128
10	Future of ILD	131
11	Summary	133

1 Introduction

Ties Behnke, Kiyotomo Kawagoe
2 pages

The ILD detector is a proposed detector for the international linear collider, ILC. It has been developed over the last 10 years within a proto-collaboration with the goal to develop and eventually propose a fully integrated detector for the ILC.

The fundamental ideas and concepts behind the ILD detector have been discussed in two previous documents, the letter of intent [1] and the detailed baseline document, DBD [2]. This documents summarises the overall design of the detector, describes developments since the publishing of the DBD, and describes in more detail an effort to optimize the ILD detector.

The ILD detector concept has been designed as a multi-purpose detector. It should deliver excellent physics performance for collision energies between 90 GeV and 1 TeV, the largest possible energy reach of the ILC. The ILD detector has been optimized to perform excellently at the initial ILC energy of 250 GeV, but maintain full physics capabilities at higher energies.

The science which will be done at the ILC requires a true multi-purpose detector. A central element of the design has been the capability of the detector to reconstruct precisely complex hadronic final states as well as events with leptons or missing energy in the final state. Thus traditional precision detector elements such as vertex detectors are combined in an overall design philosophy called particle flow, which has been developed for optimal overall event reconstruction.

In this document the current state of the design of the ILD detector is summarised. The technologies which are proposed for the different parts of the detector are introduced. An extensive benchmarking has been performed, to demonstrate the performance of the ILD detector. This has been done for two different detector implementations, a large and a smaller one. Both concepts are the result of intense optimization efforts, with different goals - cost effectiveness was foremost a criterium for the smaller one, ultimate performance for the larger model.

A lot of the work presented in this report is based on intense R&D work which has taken place over the last decade to develop the necessary technologies. This work has typically happened within dedicated R&D collaborations, which are independent but maintain very close connections to ILD. All technologies selected by ILD for one of its subsystems have been proven experimentally to meet the performance goals, or to come very close.

Developing a very powerful detector concept over a long period of time requires balancing cutting edge technologies, which might become available while the concept is being developed, with safe and sound solutions. ILD in many cases is pursuing more than one technological option, to remain flexible and to be able to adopt to new developments. The concept group wants to remain open and flexible to be prepared to select the most modern and most powerful technology once it is necessary. However a distinction is made between options and alternatives: while options have undergone an extensive R&D program and have passed critical proof-of-concept tests, alternatives are potentially interesting and promising technologies which have not matured to a similar level at the time of writing this document.

The ILD group which is proposing this detector has currently some 70 member institutes from all around the world. The group has evolved into a proto-collaboration, which is positioning itself to move forward with a proposal for a detector at the ILC at the moment that ILC becomes a real project.

At the time of writing this report, no final decision on the construction of the ILC accelerator has been reached. Japan has announced that it will study in depth the ILC proposal, and will start negotiations with international partners to understand possible project schemes, including cost sharing issues. At the same time, in Europe, the discussion on the particle physics strategy for the next decade has started. A result which might include also recommendations on future colliders to be built, is expected for 2020. This document thus is a timely work to document the current state of the ILD detector, and define a possible configuration with which ILD could enter into a proposal at the ILC, should ILC move forward. At the same time, this document also serves as a reference document for the extensive R&D done over the last nearly 10 years.

The document starts with a short review of the science goals of the ILC, and how the goals can be achieved today with the detector technologies at hand. After a discussion of the ILC and the environment in which the experiment will take place the detector is described in more detail. The integration of the different sub-systems into an integrated detector is discussed, as is the interface between the detector and the collider. This is followed by a concise summary of the benchmarking which has been performed in order to find an optimal balance between performance and cost. To this end the costing methodology used by ILD is presented, and a cost estimate for the detector in 2018 costs is presented. The report closes with a summary of the proposed detector and its performance.

2 Science with ILC

ILD has been designed to operate with electron-positron collisions between 90 GeV and 1 TeV. The science goals of the ILC have been described in detail in [?], and will not be repeated here. It should be pointed out that the analyses which have been performed within the ILD concept group are based on fully simulated events, using a realistic detector model and advanced reconstruction software, and in many cases includes estimates of key systematic effects. This is particularly important when estimating the reach the ILC and ILD will have for specific measurements. Determining, for example, the branching ratios of the Higgs at the percent level depends critically on the detector performance, and thus on the quality of the event simulation and reconstruction.

In many cases the performance used in the physics analyses has been tested against prototype experiments. The key performance numbers for the vertexing, tracking and calorimeter systems are all based on results from test beam experiments. The particle flow performance, a key aspect of the ILD physics reach, could in the absence of a large scale demonstration experiment not be fully verified, but key aspects have been shown in experiments. This includes the single particle resolution for neutral and charged particles, the particle separation in jets, the linking power between tracking and calorimetry, and key aspects of detailed shower analyses important for particle flow.

While the physics case studies are based on the version of the ILD detector presented in the detector volume of the ILC DBD [?], ILD has recently initiated a systematic benchmarking effort to study the performance of the ILD concept, and to determine in particular the correlations between science objectives and detector performance. The list of benchmark analyses which are under study is given in table 2.1. Even if the ILC will start operation at a center-of-mass energy of 250 GeV, the ILD detector is being designed to meet the more challenging requirements of higher center-of-mass energies, since major parts of the detector, e.g. the coil, the yoke and the main calorimeters will not be replaced when upgrading the accelerator. Therefore, most of the detector benchmark analyses are performed at a center-of-mass energy of 500 GeV, and one benchmark even at 1 TeV. The assumed integrated luminosities and beam polarisation settings follow the canonical running scenario [3]. In addition to the well-established performance aspects of the ILD detector, the potential of new features not yet incorporated in the existing detector prototypes, e.g. time-of-flight information, is being evaluated.

The results of these studies are expected to become available in spring 2019 and will be published in the ILD Design Report [?]. They will form the basis for the definition of a new ILD baseline detector model, which will then be used for a new physics-oriented Monte-Carlo production for 250 GeV. Such a production is planned for 2019, with the most recent beam parameters of the accelerator [?] and significantly improved reconstruction algorithms, and is expected to lead to further improvements of the expected results of the precision physics program of the ILC [?].

Table 2.1. Table of benchmark reactions which are used by ILD to optimize the detector performance. The analyses are mostly conducted at 500 GeV centre-of-mass energy, to optimally study the detector sensitivity. The channel, the physics motivation, and the main detector performance parameters are given.

Measurement	Main physics question	main issue addressed
Higgs mass in $H \rightarrow b\bar{b}$	Precision Higgs mass determination	Flavour tag, jet energy resolution, lepton momentum resolution
Branching ratio $H \rightarrow \mu^+ \mu^-$	Rare decay, Higgs Yukawa coupling to muons	High-momentum p_t resolution, μ identification
Limit on $H \rightarrow$ invisible	Hidden sector / Higgs portal	Jet energy resolution, Z or recoil mass resolution, hermeticity
Coupling between Z and left-handed τ	Contact interactions, new physics related to 3rd generation	Highly boosted topologies, τ reconstruction, π^0 reconstruction
WW production, W mass	Anomalous triple gauge couplings, W -mass	Jet energy resolution, leptons in forward direction
Cross section of $e^+ e^- \rightarrow v\bar{v}q\bar{q}q\bar{q}$	Vector Bosons Scattering, test validity of SM at high energies	W/Z separation, jet energy resolution, hermeticity
Left-Right asymmetry in $e^+ e^- \rightarrow \gamma Z$	Full dim-6 EFT interpretation of Higgs measurements	Jet energy scale calibration, lepton and photon reconstruction
Hadronic branching ratios for $H \rightarrow b\bar{b}$ and $c\bar{c}$	New physics modifying the Higgs couplings	Flavour tag, jet energy resolution
A_{FB}, A_{LR} from $e^+ e^- \rightarrow b\bar{b}$ and $t\bar{t} \rightarrow b\bar{b}q\bar{q}q\bar{q}/b\bar{b}q\bar{q}\nu$	Form factors, electroweak coupling	Flavour tag, PID, (multi-)jet final states with jet and vertex charge
Discovery range for low ΔM Higgsinos	Testing SUSY in an area inaccessible for the LHC	Tracks with very low p_t , ISR photon identification, finding multiple vertices
Discovery range for WIMP's in mono-photon channel	Invisible particles, Dark sector	Photon detection at all angles, tagging power in the very forward calorimeters
Discovery range for extra Higgs bosons in $e^+ e^- \rightarrow Zh$	Additional scalars with reduced couplings to the Z	Isolated muon finding, ISR photon identification.

3 The ILC Environment

Karsten Buesser, Keisuke Fujii
3 pages

3.1 The International Linear Collider Project

The ILC is a high-luminosity linear electron-positron collider based on the 1.3 GHz superconducting RF accelerating technology. The ILC has been initially proposed for an energy range of 200-500 GeV, upgradable to 1 TeV [4]. After the discovery of the Higgs Boson at 125 GeV mass, the baseline of the ILC has been re-configured with an initial stage at 15 GeV cms energy which provides a rich harvest for a precision Standard Model and Higgs physics programme. The baseline ILC can be extended to higher energies and luminosities in well defined upgrade scenarios. The basic beam parameters for the baseline and the upgrades are given in table 3.1.

Table 3.1. Summary table of the ILC accelerator parameters in the initial 250 GeV staged configuration (with TDR parameters at 250 GeV given for comparison) and possible upgrades [5]. A 500 GeV machine could also be operated at 250 GeV with 10 Hz repetition rate, bringing the maximum luminosity to $5.4 \cdot 10^{34} \text{ cm}^{-2} \text{s}^{-1}$ [6].

Quantity	Symbol	Unit	Initial	\mathcal{L}	Upgrade	TDR	Upgrades
Centre of mass energy	\sqrt{s}	GeV	250	250	250	500	1000
Luminosity	$\mathcal{L} \cdot 10^{34} \text{ cm}^{-2} \text{s}^{-1}$		1.35	2.7	0.82	1.8/3.6	4.9
Polarisation for $e^- (e^+)$	$P_{-}(P_+)$		80 % (30 %)	80 % (30 %)	80 % (30 %)	80 % (30 %)	80 % (20 %)
Repetition frequency	f_{rep}	Hz	5	5	5	5	4
Bunches per pulse	n_{bunch}	1	1312	2625	1312	1312/2625	2450
Bunch population	N_e	10^{10}	2	2	2	2	1.74
Linac bunch interval	Δt_b	ns	554	366	554	554/366	366
Beam current in pulse	I_{pulse}	mA	5.8	5.8	8.8	5.8	7.6
Beam pulse duration	t_{pulse}	μs	727	961	727	727/961	897
Average beam power	P_{ave}	MW	5.3	10.5	10.5	10.5/21	27.2
Norm. hor. emitt. at IP	$\gamma \epsilon_x$	μm	5	5	10	10	10
Norm. vert. emitt. at IP	$\gamma \epsilon_y$	nm	35	35	35	35	30
RMS hor. beam size at IP	σ_x^*	nm	516	516	729	474	335
RMS vert. beam size at IP	σ_y^*	nm	7.7	7.7	7.7	5.9	2.7
Luminosity in top 1 %	$\mathcal{L}_{0.01}/\mathcal{L}$		73 %	73 %	87.1 %	58.3 %	44.5 %
Energy loss from beamstrahlung	δ_{BS}		2.6 %	2.6 %	0.97 %	4.5 %	10.5 %
Site AC power	P_{site}	MW	129		122	163	300
Site length	L_{site}	km	20.5	20.5	31	31	40

The layout of the baseline 250 GeV ILC facility is shown in figure 3.1. The total site length is about 20.5 km with the interaction region with an experimental area for two detectors in push-pull configuration located in the centre. The Japan Association of High Energy Physicists (JAHEP) has proposed to host the ILC as a staged project in Japan [7]. A possible site for the construction of the ILC has been identified in the Kitakami mountains in the Tohoku area in the north of Honshu main island, about 400 km north of Tokyo. Figure 3.2 shows the location that allows for a total site length of about 50 km, and therefore extension space for upgrade scenarios, in good geological conditions. Figure 3.3 shows the cross section of the ILC main linac tunnel with the cryomodules in the right and the klystrons and RF distribution in the left section. The specific location of the ILC site and the local conditions, e.g. in terms of street access and topography, has implications on the design, assembly and operations of ILD, as discussed in section 6.1.3.

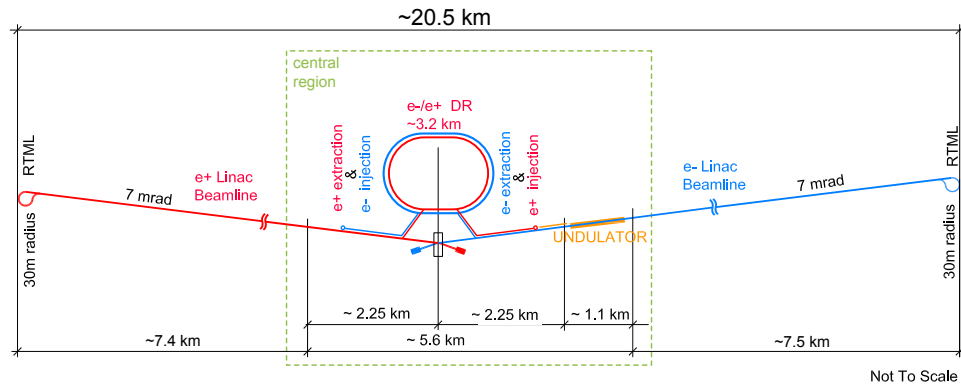


Figure 3.1. Layout of the ILC in the 250 GeV baseline configuration [5].

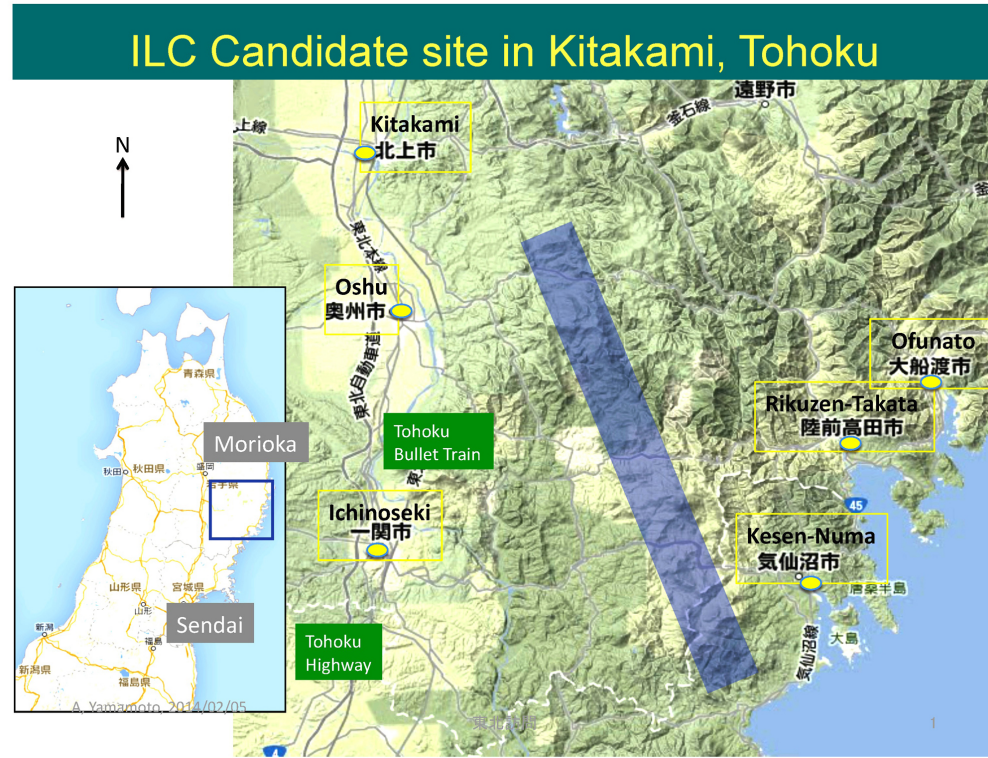


Figure 3.2. Location of the ILC candidate site in the Kitakami mountains of Tohoku, Japan [8].

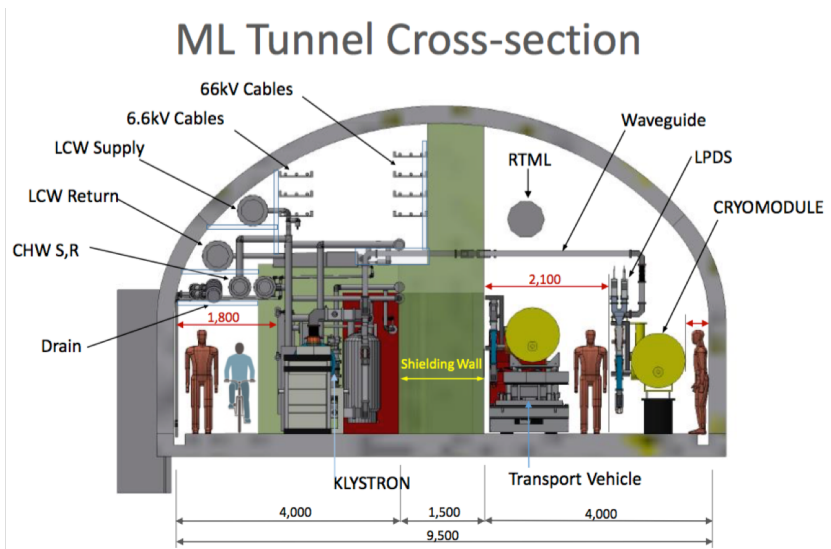


Figure 3.3. Cross section of the ILC main linac tunnel [5].

3.2 Integration of ILD into the experimental environment

ILD is designed to be able to work in a push-pull arrangement with another detector at a common ILC interaction region. In this scheme ILD sits on a movable platform in the underground experimental hall. This platform allows for a roll-in of ILD from the parking position into the beam and vice versa within a few hours. The detector can be fully opened and maintained in the parking position.

The current mechanical design of ILD assumes an initial assembly of the detector on the surface, similar to the construction of CMS at the LHC. A vertical shaft from the surface into the underground experimental cavern allows ILD to be lowered in five large segments, corresponding to the five yoke rings.

ILD is designed to fully cope with the ILD beam conditions. The expected levels of beam induced backgrounds have been simulated and are seen to be at tolerable levels, e.g. for the vertex detectors. Judiciously placed shielding keep scattered backgrounds under control. Regarding the collider, the design of the interaction region and the collimation system has been defined so as to keep the external background sources at levels below the detector requirements.

ILD is self-shielding with respect to radiation and magnetic fields to enable the operation and maintenance of equipment surrounding the detector, e.g. cryogenics. Of paramount importance is the possibility to operate and maintain the second ILC push-pull detector in the underground cavern during ILC operation.

3.3 Experimental Conditions

3.3.1 Beam Conditions

The ILC beams have specific properties that are optimised for the physics output of the colliding detectors:

- High luminosity: $1.35 \cdot 10^{34} \text{ cm}^{-2}\text{s}^{-1}$ at 250 GeV cms;
- Polarisation for the electron (80%) and positron (30%) beams;
- Moderate energy losses from beamstrahlung;
- A pulse structure with pulse lengths of less than 1 ms and low repetition rates of 5-10 Hz which enables the use of power-pulsed readout schemes in the detector.

To reach high luminosities, the ILC bunches are focused to rather small cross sections in the nanometre range in the interaction point (c.f. table 3.1). The strongly focused beams emit beamstrahlung photons in the very forward directions which leave the detector towards the main beam dumps. Secondary electron and positron pairs stemming from photon reactions are a potential source for backgrounds. The same is true for neutrons that are produced in the main beam dumps and can travel back into the detector. Both sources have been studied in detail and are under control (c.f. section 6.6).

3.3.2 Machine Detector Interface

The requirements of a linear collider also have technical implications for the ILD detector. All those aspects are summarised in the Machine-Detector Interface that has been specified and designed in close collaboration with the ILC machine groups and SiD, the other proposed detector for the ILC.

3.3.2.1 Push-Pull

The ILC is proposed to have a common Beam Delivery System that serves one interaction point. The interaction point is shared between two detectors, ILC and SiD, that operate in a push-pull scheme [4]. In such a scheme, one detector is taking data on the ILC beam, while the other one is parked close

by and waits for its turn to move in. Figure 3.4 shows a conceptual design of ILD and SiD in such a push-pull configuration where both detectors are mounted on movable concrete platforms. The system is designed for short turn-over times of one day or less. The requirements for such a push-pull

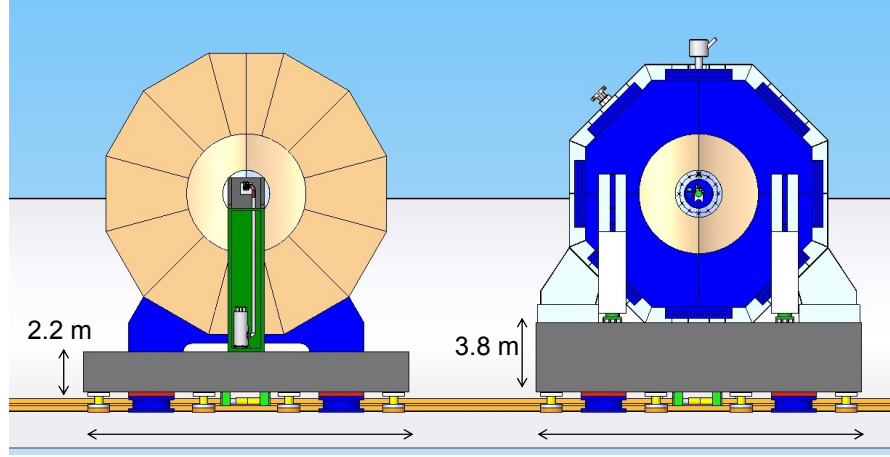


Figure 3.4. Conceptual design of the push-pull system for ILD (left) and SiD (right). Both detectors are mounted on movable concrete platforms [4].

operation scheme have been defined between both detector collaborations [9]. The impact of these requirements on the ILD design will be discussed in more detail in section 6.1.

3.3.2.2 Accelerator Elements

The final focus magnets of the ILC are at a close focal length so that they have to be accommodated by the detectors. The closest magnet to the interaction point, the QD0 quadrupole, is an integral part of ILD, as can be seen in figures 3.5 and 5.1. The QD0 magnet packages move together with the detector in case of push-pull operations, i.e. SiD and ILD both have their own set of magnets. In the

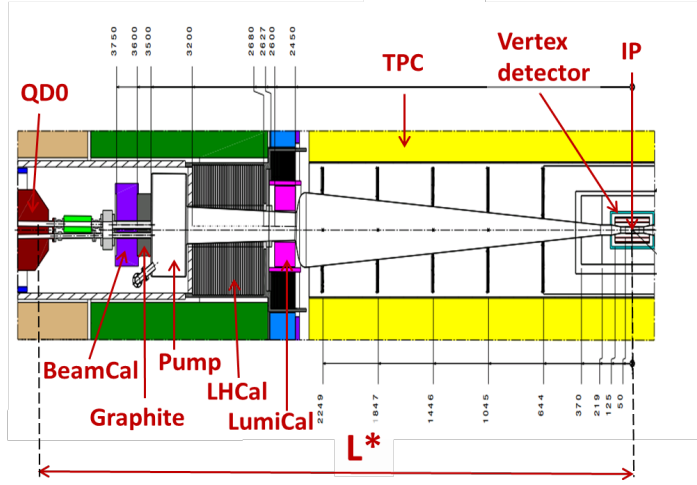


Figure 3.5. ILD forward region in the TDR version [10].

ILC TDR, two focal lengths of the QD0 magnets were foreseen, 4.4 m for ILD and 3.5 m for SiD [4]. Later, the design of the ILC has been changed and the focal lengths were harmonised at 4.1 m [11]. For ILD, this required a re-design of the forward region, as the QD0 magnet would move closer to the interaction point, while the detector dimension remained unchanged. Space that was foreseen for a vacuum pump (c.f. figure 3.5) was used in this change. The missing pump would deteriorate

the vacuum levels in the central beam pipe of ILD. However, a study on the possible impact on backgrounds from beam-gas reactions showed that the estimated levels are still negligible [12].

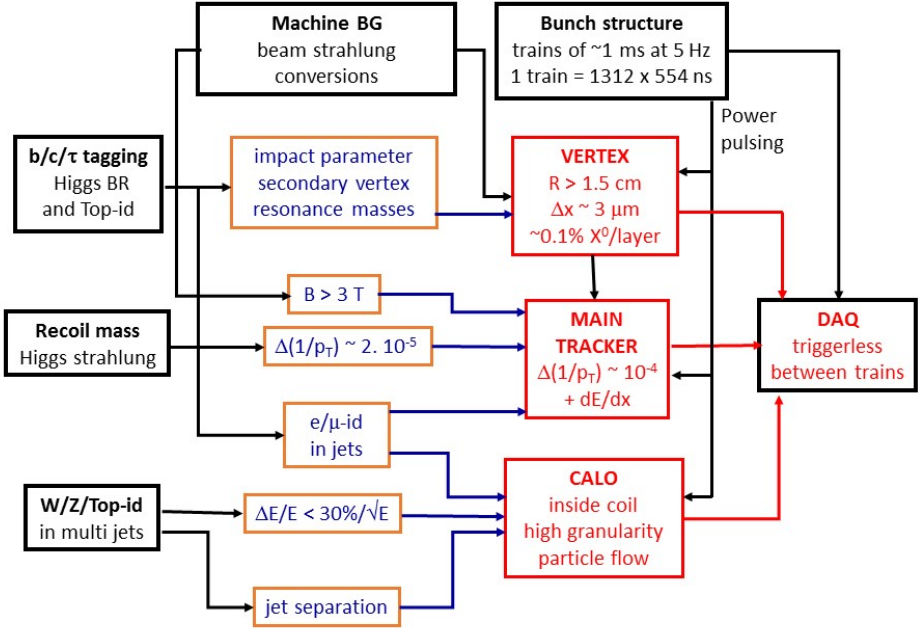


Figure 4.1. Interplay between ILC machine characteristics, physics requirements and detector specifications.

4 The ILD detector concept

Ties Behnke, Kiyotomo Kawagoe, Claude Vallee
10 pages

4.1 The overall ILD concept

The overall ILD concept has been kept unchanged since the DBD [ref]. The detector global layout and the subdetectors performances are tightly linked to the accelerator characteristics and the physics requirements, as summarized in figure 4.1.

The high beamstrahlung background at the collision point requires a magnetic field higher than 3T to maintain most of the conversion electron pairs confined within the beam pipe, and sets a minimum of ≈ 1.5 cm to the closest distance of approach of the vertex detector inner layer from the beamline. On the other hand the bunch structure into short trains separated by long idle periods sets rather relaxed conditions to the data acquisition, with the possibility to avoid a hardware trigger system. This in addition allows to power the front-end electronics only during active bunch trains (so-called "power-pulsing" mode), which minimizes the subdetector cooling requirements and associated material budgets.

The subdetector specifications are tightly linked to the physics requirements from precision Higgs and EW physics. The dominant Higgs strahlung process, which at an e^+e^- collider provides the unique opportunity to tag Higgs production independently of its decays, requires a very high-precision momentum measurement of isolated particles from Z decays, which, even taking into account the high-precision inner silicon trackers, results in a high demand on the main tracker. The efficient tagging of quark and lepton flavors to disentangle Higgs couplings requires a very high precision

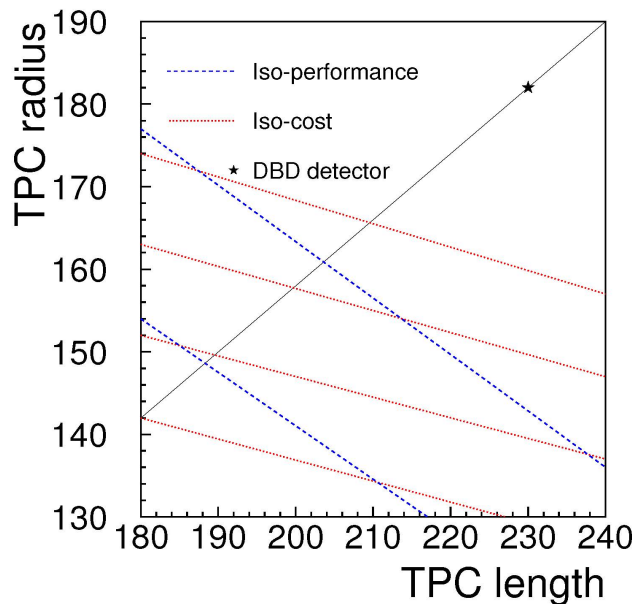


Figure 4.2. Equi-performance and equi-cost curves resulting from a parametric evaluation of the ILD detector in the tracker radius-length parameter space. The * corresponds to the large ILD version ILD-L and the diagonal to dimension changes at a constant r/z aspect ratio.

and low-material vertex detector, as well as a high calorimeter granularity to identify leptons in jets. Similarly an efficient identification of W , Z and top hadronic decays in a crowded multijet environment needs a high jet energy resolution, twice better as currently realized at LHC, as well as an efficient spatial jet separation. ILD considers that the best concept to meet all these requirements together is particle flow, where the charged and neutral particle contents of the jets are measured with the high performance trackers and the high granularity calorimeters, respectively. Within this scheme an efficient match between the trackers and the calorimeters requires to set the coil outside of the calorimeters.

Detector performance aspects to be anticipated for higher energies

4.2 Optimising ILD

The baseline ILD layout of the DBD [ref] had intentionally large dimensions in order to maximize the tracking performance and the particle flow capabilities of the calorimeters. In the past years a re-optimization process of the detector global dimensions has been launched to identify an optimal point in the cost-performance space.

In a first step, a parametric study of the dependence of the cost and performance as function of the outer radius and length of the main tracker has been performed [note Mickael]. The performance indicators were mainly based on Higgs precision observables and all subdetector costs were rescaled as function of their overall dimensions. The results of the study are summarized in figure 4.2. They show that targeting a given cost reduction maintains a higher performance when reducing the radius while keeping the overall length unchanged, instead of keeping the aspect ratio r/z unchanged.

Based on this study, detector models with different sizes were defined with the following guidelines:

- The number of detector models is limited to 2 to maintain simulations and analyses at a manageable level.
- One of the models ("ILD-L") has dimensions similar to those of the DBD model, in order to have a well understood reference in the studies. The only changes compared to DBD are

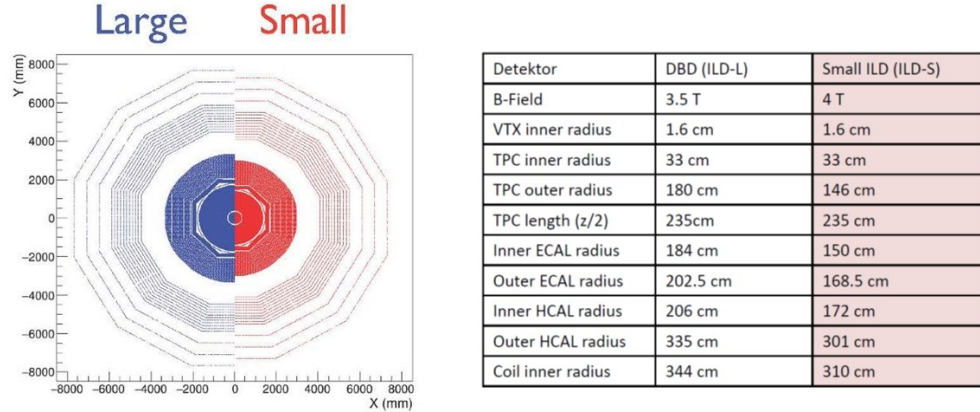


Figure 4.3. The "large" and "small" models used for the ILD optimization: R- ϕ view (left) and main subdetector dimensions (right).

associated to the collider parameters evolutions (e.g. the new L* optics, see chapter 3), and to better understanding of the subdetector technology constrains.

- The second model ("ILD-S") has a reduced outer radius of the main tracker keeping its length unchanged. The smaller radius has to be far enough from the ILD-L radius to provide a significant level-arm to the comparisons. The chosen value is equal to that of the new CLIC detector model CLICdp [ref], half way of the further smaller radius of the SiD detector [ref]. With this choice ILD-S has similar outer tracker dimensions as CLICdp for both radius and length. This offers the possibility to compare the performance of the TPC option to the all-silicon option favored by CLICdp.
- All other components of ILD-S are similar to ILD-L. The inner tracking and very forward systems are identical. The calorimeters depths and cell sizes are also kept unchanged, and the number of cells reduced as function of the calorimeters radius. All external systems such as coil, yoke and endcaps have their radial dimensions reduced accordingly.
- In order to compensate for the smaller tracking level-arm the nominal magnetic field of ILD-S is increased from 3.5T to 4T.

The resulting ILD-L and ILD-S dimensions are summarized in figure 4.3. Both models were used for detailed simulations of physics benchmark samples. The simulation framework is described in chapter 7 and the detector and physics performance of both models compared in chapter 8.

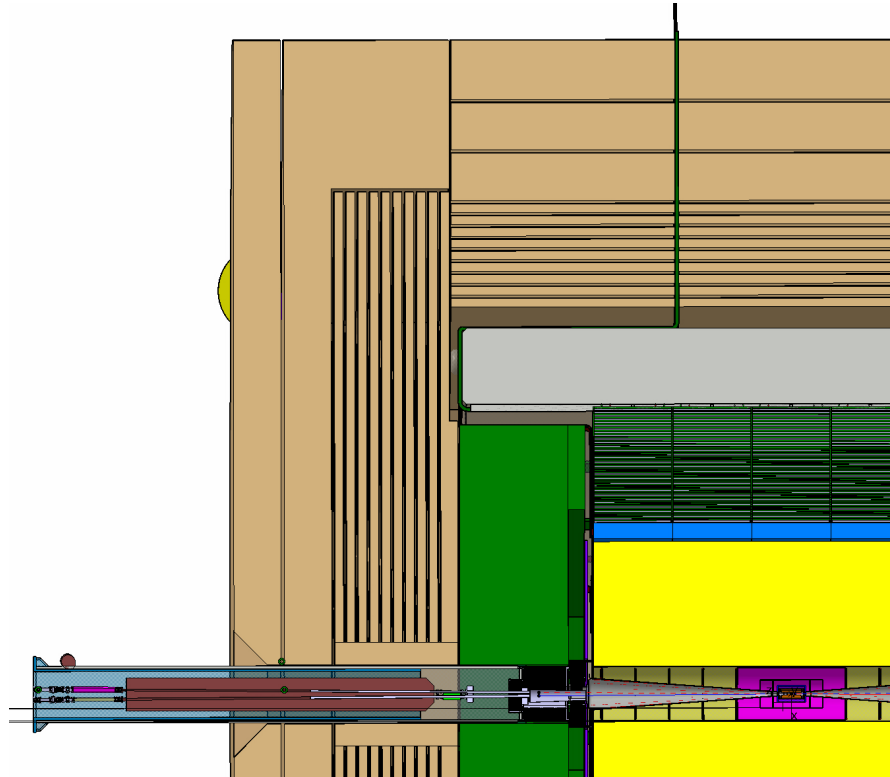


Figure 5.1. r-z structure of an ILD quadrant.

5 Detector Layout and Technologies

5.1 Overall structure of the detector

Claude Vallee, Karsten
Buesser
1 pages

The geometrical structure of the ILD detector and the individual layouts of subdetectors were described in details in the ILD LOI [ref] and DBD [ref]. This section shortly reminds the main characteristics with emphasis on the recent evolutions and open options. The main design changes implemented since the DBD take into account continuous progress in detection technologies and the new optics of the ILC interaction region (chapter 3). In the following all dimensions are given for the large version of the detector (see section 4.2 for reduction factors of the small ILD).

5.1.1 Global structure and parameters

Claude Vallee, Karsten
Buesser
1 pages

The overall ILD detector structure is shown in figure 5.1: a high precision vertex detector positioned very close to the interaction point is followed by a hybrid tracking layout, realised as a combination of

Table 5.1. List of the main parameters of the large and small ILD detector models for the barrel part. The numbers of the inner and outer radii refer to the distance from the IP at orthogonal impact of the corresponding detector plane. The reduced radii of the small model ($\delta r = 343$ mm) are labeled with superscript^s.

Barrel system						
System	r_{in}	r_{out}	z_{max}	technology	comments	
VTX	16	60	125	silicon pixel sensors	3 double layers at $\sigma_{r\phi,z} = 4.0 \mu\text{m}$ $\sigma_t = 2-4 \mu\text{s}$	$r = 17, 38, 59 \text{ mm}$ (layers 1-6)
SIT	153	303	644	silicon pixel sensors	2 double layers at $\sigma_{r\phi,z} = 5.0 \mu\text{m}$ $\sigma_t = 0.5-1 \mu\text{s}$	$r = 155, 301 \text{ mm}$ (layers 1-4)
TPC	329	1770	2350	MPGD readout	220 layers $1 \times 6 \text{ mm}^2$ pads	$\sigma_{r\phi} \approx 60-100 \mu\text{m}$
SET	1773	1776	2300	silicon strip sensors	1 double layer at $\sigma_{r\phi} = 7.0 \mu\text{m}$	$r = 1774 \text{ mm}$ $\phi_{\text{stereo}} = 7^\circ$
ECAL	1805	2028	2350	W absorber	30 layers	
	<i>1462^s</i>	<i>1685^s</i>		silicon sensor	$5 \times 5 \text{ mm}^2$ cells	SiECAL
				scintillator sensor	$5 \times 45 \text{ mm}^2$ strips	ScECAL
HCAL	2058	3345	2350	Fe absorber	48 layers	
	<i>1715^s</i>	<i>3002^s</i>		scintillator sensor, analogue	$3 \times 3 \text{ cm}^2$ cells	AHCAL
				RPC gas sensor, semi-digital	$1 \times 1 \text{ cm}^2$ cells	SDHCAL
Coil	3425	4175	3872		3.5 T field	int.lengths = 2λ
	<i>3082^s</i>	<i>3832^s</i>				
Muon	4450	7755	4047	scintillator sensor	14 layers $3 \times 3 \text{ cm}^2$ cells	
	<i>4107^s</i>	<i>7412^s</i>				

silicon tracking with a time projection chamber, and a calorimeter system. The complete system is located inside a large solenoid providing a nominal magnetic field of 3.5T (large ILD) or 4T(small ILD) . On the outside of the coil, the iron return yoke is instrumented as a muon system and as a tail catcher calorimeter. The main geometrical parameters are summarised in table 5.1 and table 5.2.

A key characteristics of the detector is the amount of material crossed by the particles: particle flow requires a thin tracker to minimise interactions before the calorimeters, and thick calorimeters to fully absorb the showers and measure neutral hadrons. Figure 5.2 shows the amount of radiation lengths of the trackers material and the total interaction lengths including the calorimeter system.

Subdetector technical conveners
4 pages

5.1.2 Subdetector layouts

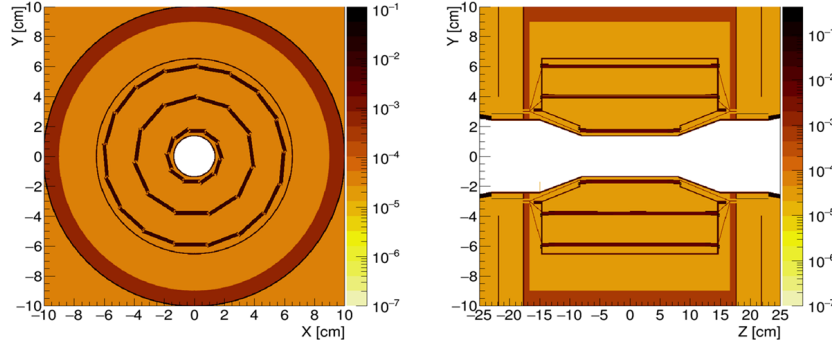
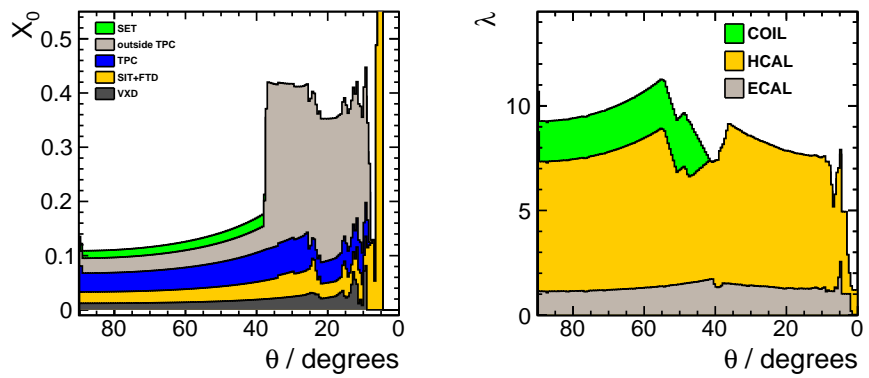
The current design of subdetectors is presented including open options and critical aspects, as well as prospects for enhanced capabilities in the future. The most recent progress and status of each detection technology will be summarized in section 5.2.

Table 5.2. List of the main parameters of the large and small ILD detector models for the end cap part. The numbers of the inner and outer radii refer to the distance from the IP at orthogonal impact of the corresponding detector plane. The reduced radii of the small model are labeled with superscript^s.

End cap system						
System	z_{\min}	z_{\max}	r_{in} [mm]	r_{out}	technology	comments
FTD	220 645	371 2212		153 300	silicon pixel sensors silicon strip sensors	2 discs 5 double discs $\sigma_{r\phi,z} = 3.0 \mu\text{m}$ $\sigma_{r\phi} = 7.0 \mu\text{m}$ $\phi_{\text{stereo}} = 7^\circ$
ECAL	2411	2635	250	2096 <i>1718^s</i>	W absorber silicon sensor scintillator sensor	30 layers $5 \times 5 \text{ mm}^2$ cells $5 \times 45 \text{ mm}^2$ strips incl. EcalPlug SiECAL ScECAL
HCAL	2650	3937	350	3226 <i>2876^s</i>	Fe absorber scintillator sensor, analogue RPC gas sensor, semi-digital	48 layers $3 \times 3 \text{ cm}^2$ cells $1 \times 1 \text{ cm}^2$ cells AHCAL SDHCAL
Muon	4072	6712	350	7716 <i>7366^s</i>	scintillator sensor	12 layers $3 \times 3 \text{ cm}^2$ cells
BeamCal	3115	3315	18	140	W absorber GaAs readout	30 layers
Lumical	2412	2541	84	194	W absorber silicon sensor	30 layers
LHCAL	2680	3160	130	315	W absorber	

Figure 5.2

Left: Average total radiation length of the trackers material as a function of polar angle.
 Right: Total interaction length seen up to the end of the electromagnetic calorimeter, the hadronic calorimeter and the solenoid coil, respectively.

**Figure 5.3.** layout of the vertex detector.

Vertex detector (Besson, Ishikawa, Vos)

The vertex detector (VTX, Figure 5.3) is realised as a multi-layer pixel detector with three double-layers. The detector has a pure barrel geometry. To minimise the occupancy from background hits, the first double-layer is only half as long as the outer two.

Critical parameters of the VTX optimisation are the point resolution for secondary vertex tagging, required to be better than 3μ , and the material thickness which should not exceed $0.1\% X_0$ per layer to minimize multiple scattering. Three main technologies are under consideration to achieve the required goals:

- **CMOS pixels:** this well-established technology offers the advantages of high granularity with fully monolithic pixel digital electronics available from industrial processes. The most critical points of focus of current R&D are the readout speed as it has single bunch tagging capacity, while keeping the power consumption low enough (with or without power pulsing) and the overall material budget of the layers.
- **DEPFET pixels:** The DEpleted Field Effect Transistor (DEPFET) concept implements a first amplification stage in a FET in the high-resistivity, depleted silicon detector [1]. Active pixel detectors with a rolling shutter read-out can meet the stringent requirements of the ILD vertex detector [13, 14]. This technology offers the advantage of high granularity with a small layer material thickness, the digital electronics being shifted at the end of the ladders: the all-silicon ladder design [15], that is fully self-supporting and requires no external support, minimizes the material in the active area to approximately $0.12\% X_0$. Critical aspects are the industrialisation of the fabrication process and the integration of large detector surfaces.

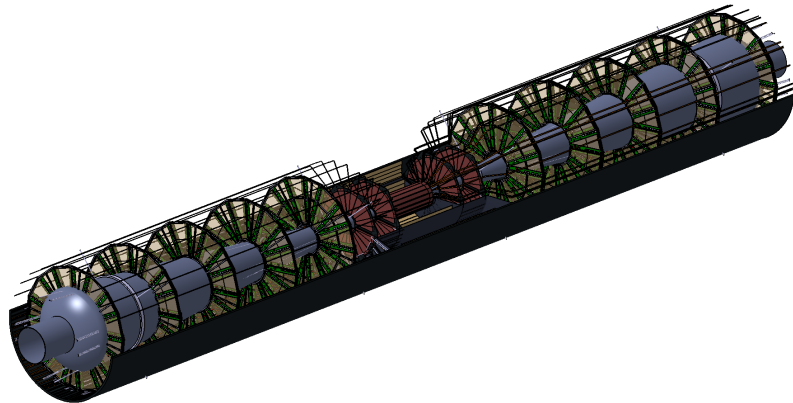


Figure 5.4. layout of the Forward Tracking Detector.

- **Fine Pixel CCD (FPCCD):** CCD's offer the prospects for the highest granularities associated with low power consumption. Another advantage is the minimal material budget of the detector layer, however counter-balanced by the need of a cryostat to ensure low-temperature operation. Critical aspects under study are the readout speed and the resistance to radiation.

The CMOS and DEPFET pixels have typical sizes of 20 microns and are readout in a continuous mode during bunch trains. The readout speed determines the capability to resolve individual bunches. The FPCCD pixels accumulate hits during one bunch train before readout and reset in-between trains. Their occupancy is kept acceptable thanks to a small pixel size of order 5 microns.

Silicon trackers (*Besson, Vos, Vila*)

A system of silicon trackers surrounds the VTX detector.

In the barrel, two layers of silicon detectors (SIT) are arranged to bridge the gap between the VTX and the TPC, and one silicon outer layer (SET) is foreseen inbetween the TPC and the ECAL. The baseline technology for the large area trackers was silicon strips but the progress made with CMOS detectors allow to equip the SIT with pixels instead of strips. The design of the SET is still open including the option to implement it as the first layer of the ECAL Calorimeter. The use of high resolution timing detectors is considered in order to provide a TOF functionality for particle identification.

The forward tracking disks (FTD) complete the coverage of the ILD experiment for charged particles emitted at shallow angles with respect to the beam (Figure 5.4). The FTD provides at least one hit for tracks with polar angles below 35 degrees ($|\cos \theta| < 0.82$) and provides nearly standalone tracking for tracks below 16 degrees ($|\cos \theta| < 0.96$).

The first two disks are installed close to the vertex detector and are equipped with highly granular pixel detectors that provide precise 3D space points with a resolution of approximately $3\text{-}5 \mu\text{m}$. The technology candidates for these disks are similar to those of the vertex detector: CMOS, DEPFET, FPCCD, SOI, and future 3D-integrated devices.

The remaining five disks extend out to the inner envelope of the TPC at $r = 30 \text{ cm}$. While the requirement on the resolution of the $r\phi$ measurement remains stringent, the cell dimension aligned with the r -coordinate is less constrained. These requirements can be met with micro-strip detectors: two single-sided detector mounted under a small stereo angle may provide the required resolution. A solution based on CMOS monolithic pixel detectors with elongated pixels is likely to be quite competitive. Also the possibility o.f a Time-Of-Flight measurement in the outermost disks merits

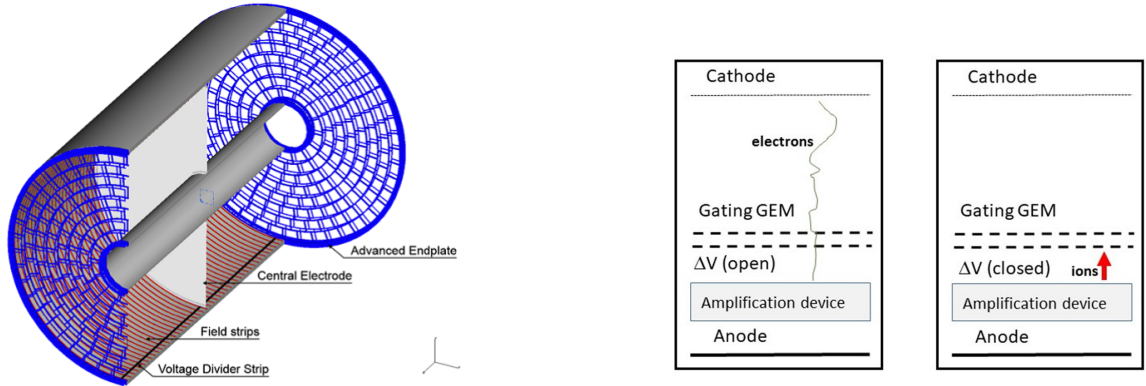


Figure 5.5. Left: Global layout of the TPC chamber. Right: Principle of the ion GEM gating scheme showing the two electric field configurations within (left) and outside (right) bunch trains.

further study.

TPC (*Colas, Sugiyama*)

A distinct feature of ILD is a large volume time projection chamber (Figure 5.5 left). The TPC allows a continuous 3-dimensional tracking, dE/dx -based particle identification and minimum material. The required performance of the TPC as a standalone tracker is a momentum resolution $\delta(1/P_T)$ better than $10^{-4} GeV^{-1}$, corresponding to a single point resolution of 100μ over about 200 points, and a dE/dx resolution better than 5%. One critical issue concerns potential field distortions due to ion accumulation within the chamber. At ILC this can be mitigated by implementing an ion gating between bunch trains: ions produced in the gas amplification region during bunch trains are confined and eliminated outside bunch trains by reverting the electric field configuration. This can be implemented with GEM foils as shown in Figure 5.5 right.

Three options are under consideration for the ionisation signal amplification and readout:

- GEM readout (Figure 5.6 left): the ionisation signal is amplified by passing through a GEM foil and is collected on pads.
- Micromegas readout (Figure 5.6 right): the ionisation signal is amplified between a mesh and the pad array where it is collected.
- GridPix: the ionisation signal is amplified as for the Micromegas case but collected on a fine silicon pixel grid providing individual pixel timing.

For the GEM and Micromegas options, the typical pad sizes are a few mm (table 5.1) and spatial resolution is improved by combining the track signals of several adjacent pads. For the GridPix option the pixel size of ≈ 50 microns matches the size of the mesh, providing pixel sensitivity to single ionisation electrons. The spatial resolution is improved and the dE/dx signal is measured by counting pixels or clusters.

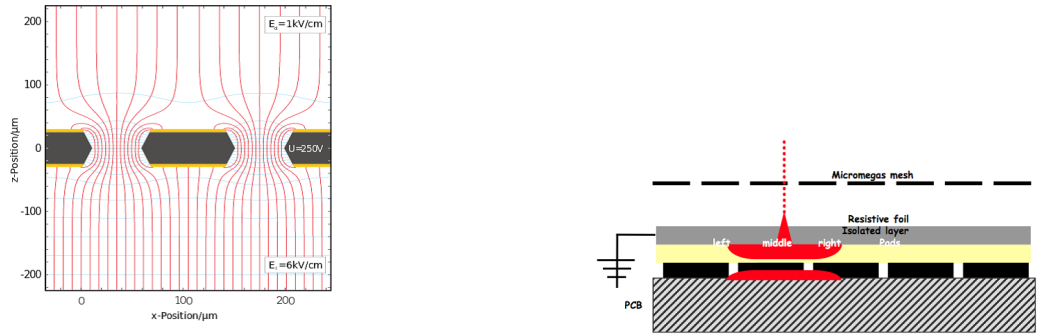


Figure 5.6. Amplification scheme of the TPC ionisation signals with GEM (left) and Micromegas (right) readout.

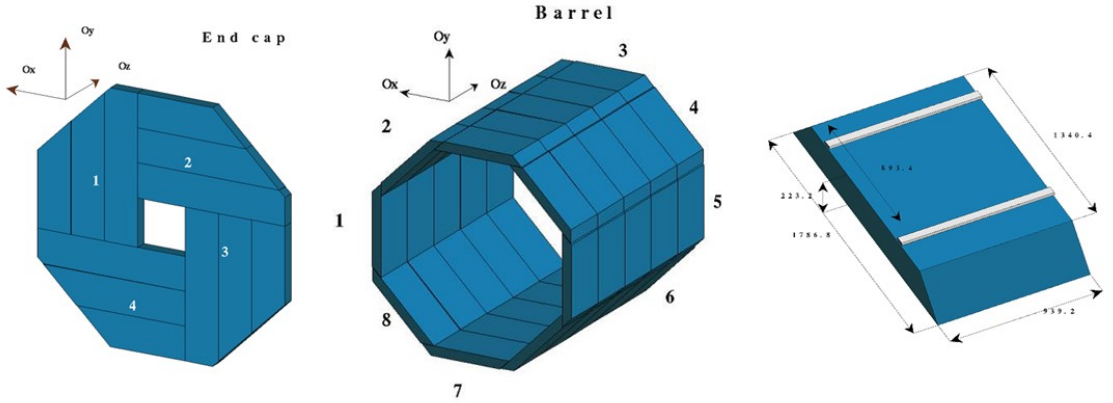


Figure 5.7. Mechanical structure of the electromagnetic calorimeter: left: end-cap; centre: barrel; right: individual barrel module.

ECAL (*Brient, Ootani*)

Electromagnetic showers are measured with a compact highly-segmented calorimeter (Figure 5.7) which absorber planes are made of tungsten. The ECAL barrel shape is octagonal with individual stacks laid such as to avoid projective dead zones in azimuth. The baseline number of layers is 30, with options to reduce the number to 26 or even 22, keeping the amount of radiation lengths identical and increasing the thickness of the sensitive medium to maintain a similar energy resolution.

The sensitive medium consists in silicon sensors with about $5 \times 5 \text{ mm}^2$ pads bonded on a PCB equipped with front-end readout ASICs (Figure 5.8 left). In order to reduce the costs it is considered to equip part of the sensitive layers with scintillator sensors readout through SiPMs (Figure 5.8 right). In that case the scintillator strips would have a larger dimension of $45 \times 5 \text{ mm}^2$ with alternate orthogonal orientation. The option to equip the first layer with high-resolution timing sensors is also

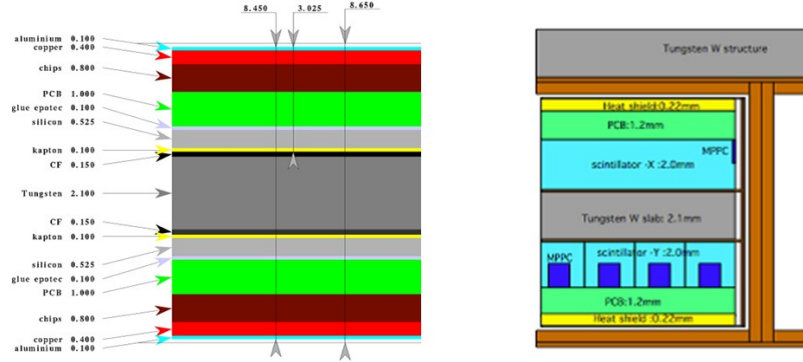


Figure 5.8. ECAL sensitive layer: left: silicium option; right: scintillator option.

under consideration to provide a TOF functionality.

HCAL (*Laktineh, Sefkow*)

The hadronic calorimeter consists in 48 longitudinal samples with steel absorber plates. Two options are currently considered for the mechanical structure, differing mainly in the barrel region (Figure 5.9): the "TESLA" barrel made of 2 wheels with signals extracted longitudinally in the gaps between the barrel and endcaps, and the "VIDEAU" barrel made of 3 to 5 wheels with signals extracted at the periphery between the HCAL and coil cryostat. The latter presents no projective dead zone in azimuth nor at 90° polar angle, and offers a better mechanical stiffness, at the cost of a reduced accessibility of the interfaces for data concentration and power supply.

The HCAL layers are instrumented with high granularity for an efficient separation of charged and neutral hadronic showers, necessary for particle flow, as well as for a good muon identification for flavor jet tagging. Two sensor options are under consideration (Figure 5.10): scintillator tiles of $3 \times 3 \text{ cm}^2$ with analog readout through SiPMs, and RPC's with pads of 1 cm^2 readout with a semi-digital resolution of 2 bits. A timing functionality is implemented in the scintillator option and under consideration for RPCs: a resolution of $O(1\text{ns})$ already achieved with the scintillator option allows to tag late neutral components of the showers for particle flow, whereas a resolution of a few 10 ps, also achievable with multigap RPCs, would provide TOF measurements.

VFS (*Benhammou, Schuwalow*)

The ILD very forward region is equipped with dedicated detectors to perform:

- a precise determination of the luminosity from Bhabha scattering electron pairs (LumiCAL);
- an extension of the hadronic calorimetry coverage in the forward region (LHCAL);
- calorimetric hermeticity down to the beam pipe and fast monitoring of beam conditions (BeamCAL).

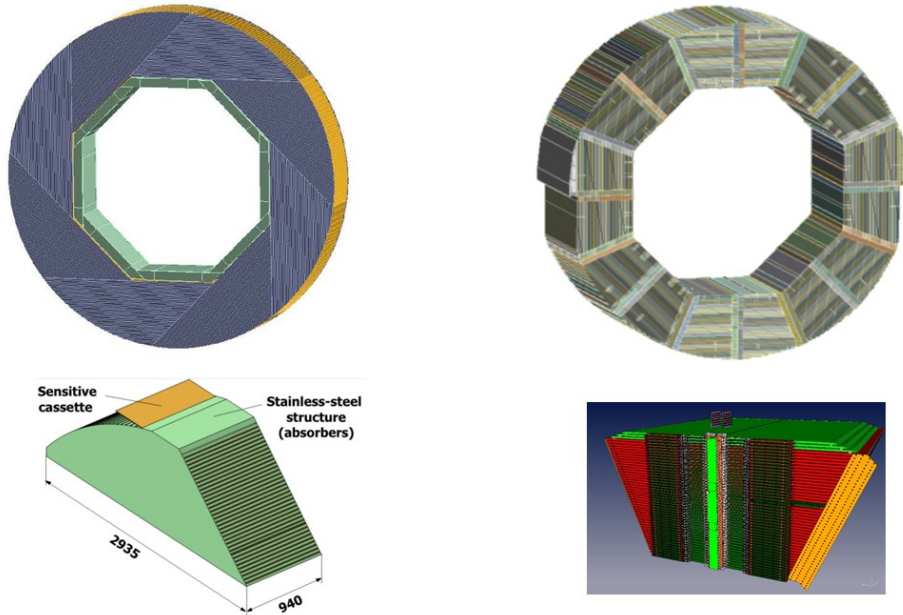


Figure 5.9. HCAL barrel mechanical structure: full wheel (top) and individual stack (bottom) for the two configurations under consideration: the "Videau" option (left) and the "TESLA" option (right).

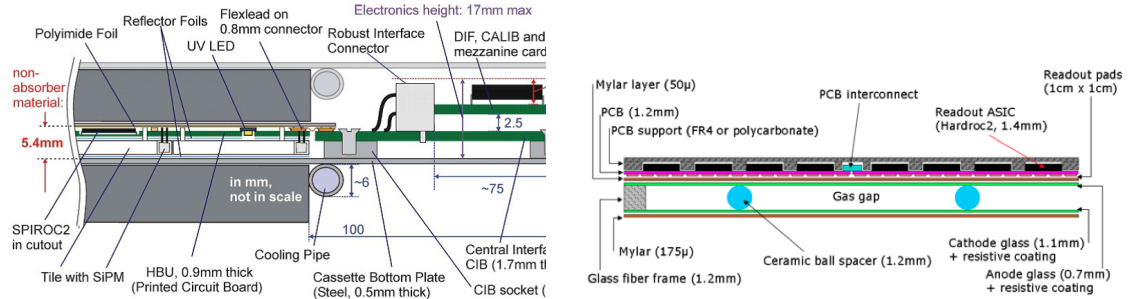


Figure 5.10. HCAL sensitive layer; left: scintillator option; right: RPC option.

The overall layout of the detectors is shown in Figure 5.11 left. Their longitudinal positioning has been adapted as shown in Figure 5.11 right to account for the new ILC optics (chapter 3).

The very forward detectors are based on similar technologies as the ILD electromagnetic calorimeter, taking into account the specific conditions of the forward region such as the harder radiation environment or the need for an improved compactness to identify electromagnetic showers in a high occupancy environment. For the detectors positioned closest to the beam pipe new sensors such as saphire are considered. The LumiCAL has the most advanced design and will be based on silicon sensors similar to the ECAL (Figure 5.12), with thinner instrumentation layers to minimize the lateral spread of the showers .

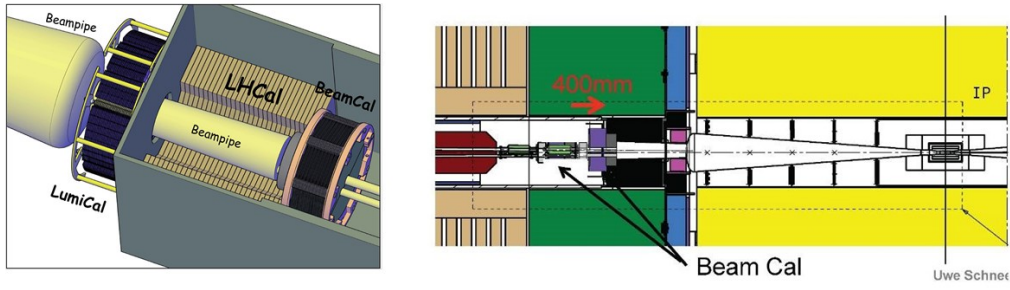


Figure 5.11. Overall layout of the Very Forward detectors (left) and adaptations performed for the new ILC optics (right).

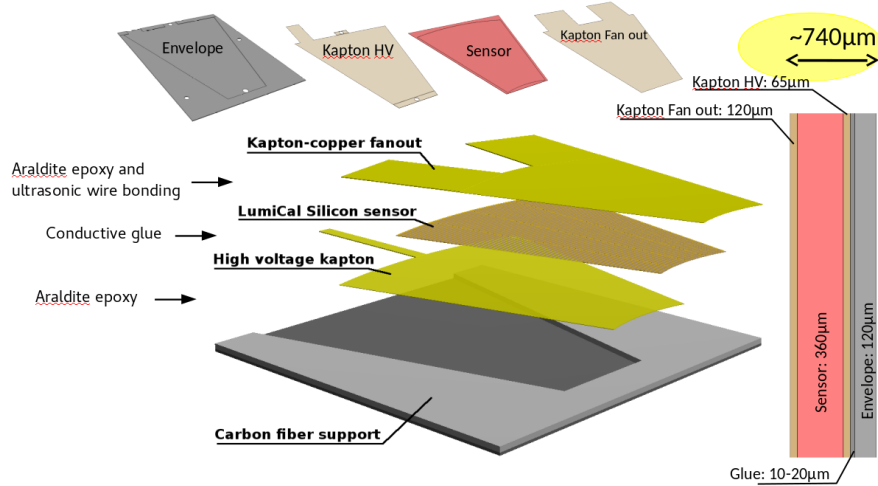


Figure 5.12. Structure of a sensitive layer of the LumiCAL calorimeter.

A large volume superconducting coil surrounds the calorimeters, creating an axial B -field of nominally 3.5 Tesla (large ILD) or 4 Tesla (small ILD). An iron yoke returns the magnetic flux of the solenoid, and, at the same time, serves as a muon filter, muon detector and tail catcher calorimeter. The baseline structure of the yoke is shown in Figure 5.13 left for a configuration accounting for the maximum stray fields allowed in the push-pull configuration (chapter 3). Optimisation of the yoke size is ongoing to minimize the overall cost driven by the amount of iron. A number of iron yoke gaps will be instrumented for muon tracking and measurement of the tails of the hadronic showers. The required muon tracking precision is of the order of 1 cm in azimuth and of a few cm longitudinally. The instrumentation is expected to consist in scintillator bars but RPCs are also considered. In the scintillator option the light will be collected by Wave Length Shifting (WLS) fibers readout with SiPMs at both extremities (Figure 5.13 right top). The WLS fibers will be positioned either in an extruded groove at the center of the large side of the bar, or along the small side of the bar (Figure 5.13 right bottom).

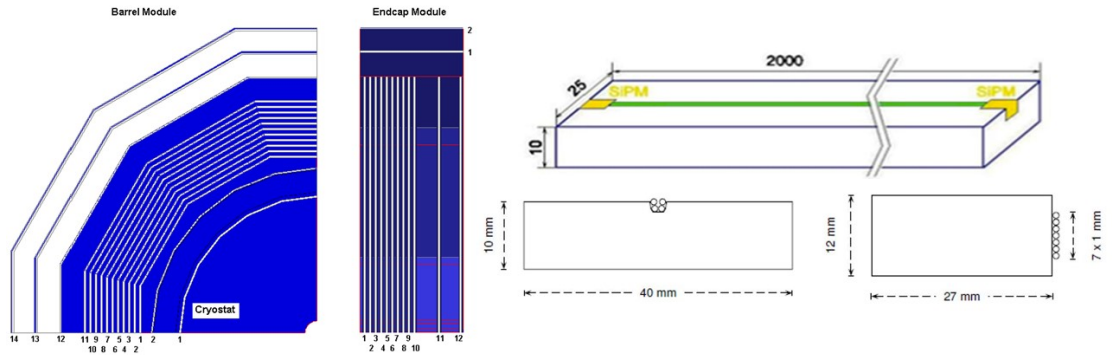


Figure 5.13. Iron yoke baseline structure (left) and scintillator/SiPM instrumentation options (right).

5.2 Subdetector technology status

All ILD detector technologies under consideration have benefited from substantial developments since the DBD publication. Many activities are coordinated within worldwide R&D Collaborations such as LCTPC [ref], CALICE [ref] or FCAL [ref]. Compared to the DBD studies, which were still focused on intrinsic physics response and performance, many technologies have now developed operational implementations with technological prototypes which are mature for extrapolation to a full detector. Applications have indeed already started with many spin-offs to existing experiments such as the high-luminosity LHC detector upgrades. The experience gained with these projects will be a strong asset to the final design and construction of ILD.

Auguste Besson, Akimasa Ishikawa, Marcel Vos
3 pages

5.2.1 Vertex detector

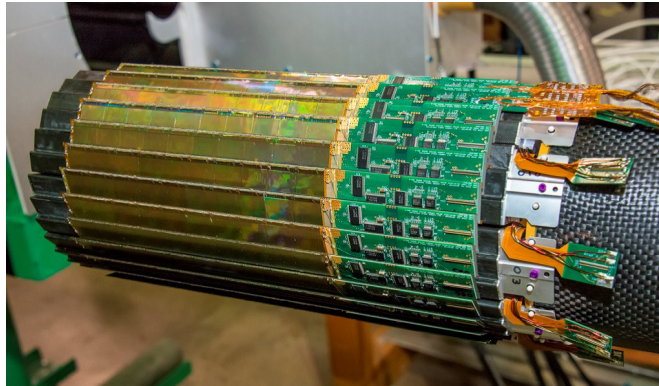
The vertex detector is a high-precision small device which is expected to be one of the latest subdetectors to be built and inserted within ILD. The development of optimal technologies can therefore proceed until a few years before the start of ILC. There has been much progress in this direction in the past 5 years for the three main options under consideration: CMOS, DEPFET and FPCCD sensors.

CMOS sensors: The use of CMOS sensors for particle physics has benefited a lot from the development in the past two decades of the MIMOSA chip series by the IPHC Institute [ref]. A first full scale particle physics detector application has been realized with the STAR vertex detector (Figure 5.14) on the RHIC hadron collider. Since then the technology has further developed as a widespread standard for pixel detectors, including many applications to e.g. LHC upgrades or new experiments.

The general trend of performance improvements towards ILD specifications is summarized in table 5.3. Compared to STAR the new applications for the ALICE upgrade and CBM at FAIR have moved to a technology with a smaller pattern, have implemented a new data driven readout scheme,

Table 5.3. Development path of CMOS pixel sensors towards ILD.

DETECTOR:	STAR-PXL (ULTIMATE) 2014-16	ALICE-ITS (ALPIDE) 2021-22	CBM-MVD (MIMOSIS) 2021-22	ILD-VXD (PSIRA) 2030
Technology (AMS):	0.35 μm	0.18 μm	0.18 μm	< 0.18 μm ?
Readout mode:	rolling shutter	data driven	data driven	data driven
Time resolution (μs):	135	5-10	5	1-4
Power (mW/cm^2):	150	35	200	50-100
Material (X_0/layer):	0.39%	0.3%		0.15%

**Figure 5.14.** The vertex detector of the STAR experiment based on the "ULTIMATE" CMOS pixel sensor.

and have improved the time resolution and power consumption to values close to ILD needs. The ALICE detector also concerns a very large area of more than 10 m^2 , which qualifies the technology for the inner layers of a central tracker.

With these applications more attention is given to integration aspects of the technology. The chip intrinsic power consumption is now close to the ILD specification and could still be reduced by a factor $\simeq 10$ with power pulsing. To this respect a trade-off will have to be made between readout speed (related to time resolution) and power. With the expected heat production air cooling as done at STAR could be sufficient, but ILD has stronger constraints on the possible air flow due to a more forward instrumentation than STAR. This critical issue requires further studies. Low material ladder supports have been developed with the "PLUME" concept, consisting in a thin foam layer carrying pixel chips on both sides as a double layer [ref]. First PLUME ladders have been built and a second version has been successfully operated for the BELLE II beam commissioning (Figure 5.15 top).

DEPFET sensors: The development of DEPFET sensors in particle physics is reaching maturity. Following the demonstration of small prototypes [16, 17] and first operational ladders five years ago the technology was chosen as the baseline for the vertex detector [18] of the Belle II experiment [19]. As many requirements of Belle II are similar to those of the ILC, this can be seen as a 30% prototype of the ILC vertex detector. DEPFET ladders have been successfully used in the BELLE II beam commissioning detector (BEAST 2). The first layer of the pixel vertex detector was installed in 2018 and is now in operation in the experiment (Figure 5.15 bottom). Due to a low yield of the module assembly process, the second layer vertex detector is expected to be completed in 2020. While the experiment is taking data, studies towards future BELLE II upgrades based on advanced DEPFET technology are starting. The development of advanced DEPFET solutions for the ILD vertex detector is synergetic with this effort.

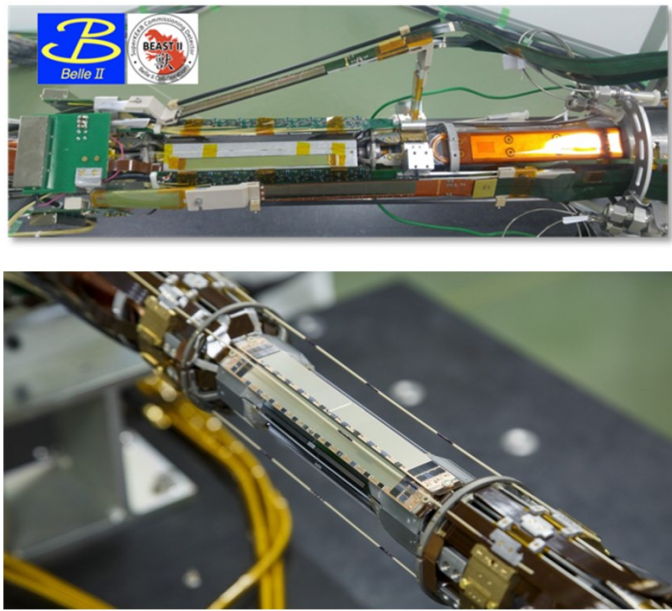


Figure 5.15. Pixel detectors of the BELLE II experiment. Top: beam commissioning with "PLUME" CMOS (inclined sensors) and DEPFET (barrel) ladders. Bottom: the BELLE II DEPFET vertex detector.

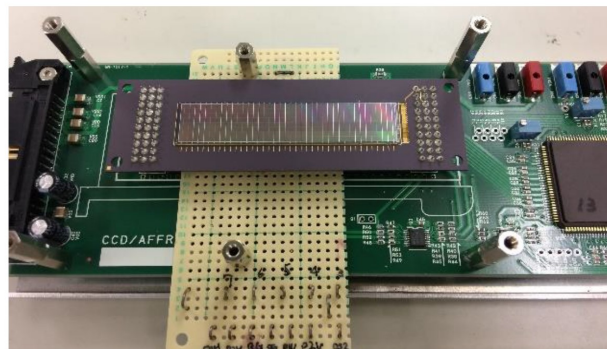


Figure 5.16. First full size FPCCD ladder on its test bed.

FPCCD sensors: The FPCCD technology is not yet used in full size detector applications but a first large prototype has been built [ref] with a sufficient size to cover the inner layer of the ILD vertex detector. The prototype is currently undergoing detailed characterization with e.g. radioactive source signals (Figure 5.16). Irradiation tests of FPCCDs are also being performed since radiation hardness is a critical aspect of this technology.

(Besson, Vos, Vila)
3 pages

5.2.2 Silicon trackers

The silicon sensors surrounding the vertex detector will directly benefit from the previous pixel detector R&D as regards their high-spatial resolution components. In the past years the specific silicon R&D has focused around two lines: a generic development of high-resolution timing sensors, and the prototyping of mechanical support structures of the Forward Tracking Detector.

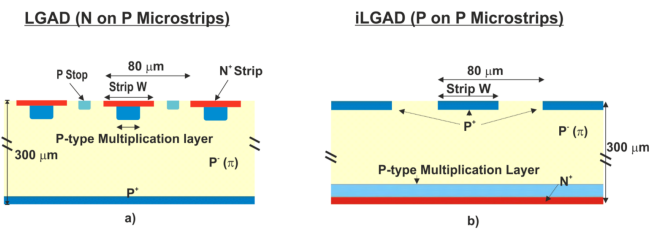


Figure 5.17. Cross-sections of the core layout of LGAD (left) and iLGAD (right) microstrip designs.

5.2.2.1 ILGADs for precise tracking and time stamping (4D-tracking)

The Low Gain Avalanche Detector (LGAD) is the baseline sensing technology of the recently proposed Minimum Ionizing Particle (MIP) end-cap timing detectors (MTD) at the Atlas and CMS experiments. LGADs are n-on-p silicon detectors with an internal gain. To obtain this gain, an extra, highly doped, layer is added just below the p-n junction of a PIN diode. This highly doped region creates a very high electric field region. This electric field induces an avalanche multiplication of the electrons and thus create additional electron-hole pairs [20].

The current MTD's sensor is designed as a multi-pad matrix detector delivering a poor position resolution, due to the relatively large pad area, around 1 mm^2 ; and a good timing resolution, around 20-30 ps. Besides, in his current technological incarnation, the timing resolution of the MTD's LGAD sensors is severely degraded once the MIP particle hits the inter-pad region since the signal amplification is missing for this region. This limitation is named as the LGAD fill-factor problem. For the ILD, a true 4D tracking must overcome the poor spatial resolution and fill factor limitations. A new p-in-p LGAD architecture named as inverse LGAD (iLGAD) tackles both issues [21]. Contrary to the conventional LGAD design, the iLGAD has a non-segmented multiplication layer, and it should ideally present a constant gain value over all the sensitive region of the device without gain drops between the signal collecting electrodes, see figure 5.17. This feature has been experimentally confirmed on a strip-like segmented iLGAD and compared against a conventional strip-like LGAD and PIN devices [22].

The tracking performances of one LGAD and one iLGAD strip detector manufactured at IMB-CNM were studied in a test beam at CERN-SPS and compared with a standard PIN strip detector. These three strip detectors were unirradiated and consisted of 45 strips with a $160\text{ }\mu\text{m}$ pitch. The big advantage of the iLGAD technology was confirmed during the test beam. It was proved that while in the LGAD strip detector the signal is severely degraded in the inter-pad region, the iLGAD presents a very constant gain value over all the sensitive region of the device. These results are shown on figure 5.18. The charge distribution of the LGAD measured during the test beam presents two peaks: one around 24 ke, corresponding to the MIP particles that cross the interstrip region where the generated signal is not amplified (same charge measure in the PIN strip); and one around 77 ke, corresponding to the particles that cross the region where the signal is amplified. On the other hand, the same plot produced for the iLGAD detector presents only one peak in the charge distribution around 75 ke. In this case, the signals produced for all MIP particles that cross the sensitive region of the device are amplified, resulting in a much better and uniform response along the sensitive region. The tracking and timing performances were also quantified during the test beam: they achieve values of tens of microns and picoseconds, respectively.

5.2.2.2 Thermo-mechanical studies of the FTD support structure

The combination of the requirements of minimal material and a mechanical stability to the level of several μm represents quite a challenge. A realistic, full-scale mechanical prototype of the disks has

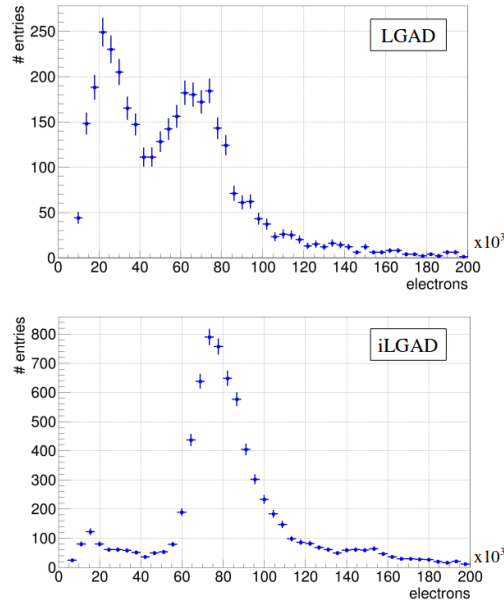


Figure 5.18. Charge distribution measured during the test beam for one LGAD strip detector (top) and one iLGAD strip detector (bottom). The fill-factor problem visible for the LGAD case is not present in the iLGAD structure.

Table 5.4. Contribution to the material budget of the Forward Tracking Disks. The contributions are determined for perpendicular incidence and average over the area of the disk.

Component	material (% X_0)
Silicon petals	
Carbon fibre (incl. cyano-ester resin)	0.038
Honeycomb core (Aramid)	0.0006
PEEK inserts	0.0019
PEEK screws	0.0014
glue	0.0006
total	

been developed to characterize its thermo-mechanical performance in conditions that resemble those of the experiment (Figure 5.19). This *mock-up* is based on a Carbon-fibre support disk and 50 μm thick silicon petals designed at IFIC Valencia.

The Carbon fibre disks were produced by INTA in Madrid. It consists of a 1 mm thick rohacell core covered on both sides by three-layer carbon fibre skins. The resulting structure adds less than XXX % of a radiation length (X_0) to the material budget. The mounting points for the Silicon sensors are formed by precisely machined PEEK inserts that are glued into the Carbon fibre structure. The gluing procedure controls the relative position of the mounting points to better than 50 μm with a custom jig.

The Silicon petals were produced at the HalbLeiterLabor of the Max Planck Society in Munich (MPG-HLL) using the Silicon-on-Oxide process that is at the heart of the all-silicon-ladder concept [15]. The 50 μm thick sensor area is supported by a 500 μm thick rim.

The contribution to the material budget of the sensors and support disks is summarized in Table 5.4. The Silicon sensors clearly dominate the total contribution.

The thermo-mechanical performance of the loaded disk has been tested extensively. The support disk is found to have a planarity of 200 μm (RMS). Despite the minimal material it is very stiff, with an eigenfrequency greater than 1 kHz. The silicon petals are mounted kinematically, such that are free to expand in response to a thermal load, while distortions of the sensors out of the nominal plane remain very tightly constrained. The torque applied to the screws must be carefully chosen: a torque of 3 mN · m is found to be optimal. With this choice, the first eigenfrequency of a free petal (167

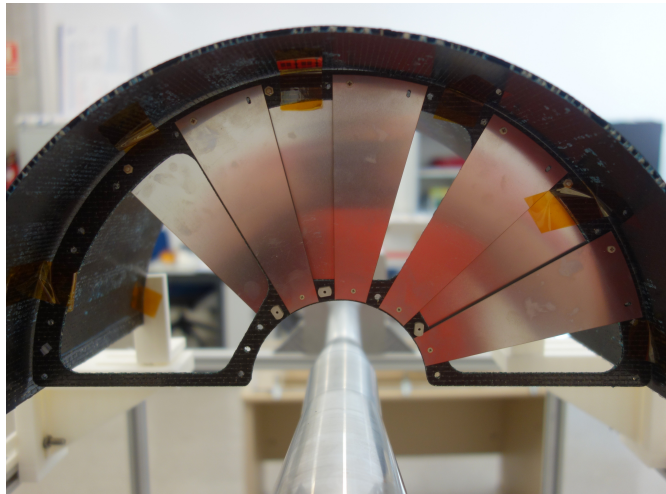


Figure 5.19. FTD thermo-mechanical mockup for the 2 inner disks.

Hz) is nearly doubled (to $\sim 270 \text{ Hz}$) when the sensor is clamped to the disk

The impact of air cooling on the mechanical stability is studied with a local, laminar air flow. The power consumption pattern mimics that of a DEPFET active pixel detector, assuming that the application of power pulsing reduces the average power consumption by a factor 20. In these conditions, a gentle, laminar flow of 1 m/s is found to be sufficient to keep the temperature gradient over the sensor to within 10 degrees C. Vibrations due to air flow have an amplitude of less than 1 μm for laminar air flow with a velocity up to 4 m/s.

These results indicate that an aggressive design based on a thin Carbon fibre support disk and ultra-thin self-supporting Silicon petals can meet the stringent requirements on mechanical stability of the ILD experiment.

Paul Colas, Akira Sugiyama
3 pages

5.2.3 Time projection chamber

The ILD TPC R&D is being conducted mainly within the LCTPC Collaboration [23].

The workhorse for validation of detector prototypes and operational conditions is the TPC test set-up installed permanently in the DESY test beam [24] (Figure 5.20). The TPC stands within a magnet providing a magnetic field of 1 Tesla, and the beam line is equipped with precise incident and outgoing particle beam telescopes allowing to quantify the TPC reconstruction precision as function of the particle parameters. The beam test set up is currently being upgraded with the high precision LYCORIS silicon telescope [25], and a new TPC field cage with reduced field distortion is being assembled.

Significant progress has been seen in the manufacturing process of detection modules for each of the readout options. A new micromegas layout with resistive anodes has been shown to exhibit reduced boundary distortions [26]. The flatness of the GEM modules has been improved significantly, increasing the gain uniformity by a factor 2 [ref]. Operational GridPix "QUAD" modules have been built based on the TimePix3 pixel chip [27]. Recent prototypes of the three types of detection modules are shown in Figure 5.21.

The performance of the three technologies has been measured in beam tests. Figure 5.22 shows the measured point resolution in 1 T magnetic field for drift distances from 0 to 0.6 m. This can

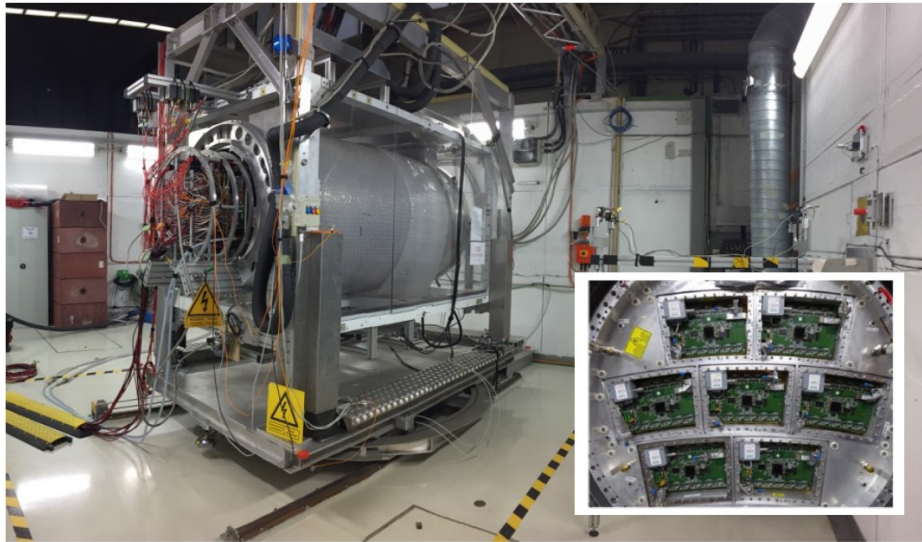


Figure 5.20. The TPC test setup at DESY. The insert shows the geometrical structure of the TPC end cap which can host prototypes of detection planes.

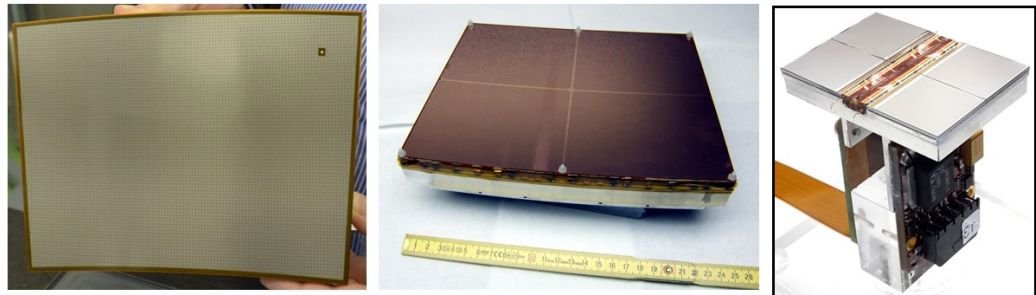


Figure 5.21. TPC prototype detection modules for the three baseline technologies under consideration: micromegas module (left), GEM module (middle) and GridPix QUAD module (right).

be safely extrapolated to $\sim 100 \mu\text{m}$ in a field of 3.5 T at a drift length of 2.3 m. The dE/dx resolution by the truncated mean method has been measured to be respectively 4.6%, 4.5% and 4.2% for Micromegas, GEM and GridPix technologies. It improves to 3.8% for GridPix using a cluster counting method. The conclusion is that the target goals of a spatial resolution of 100 microns and of a dE/dx resolution better than 5% have been reached in all cases.

Q: add performance plot of 2 track separation?

Two critical aspects of a TPC operation consist in the cooling of the readout endcaps, which must be realized with minimal dead material, and the mitigation of the drift field distortions which

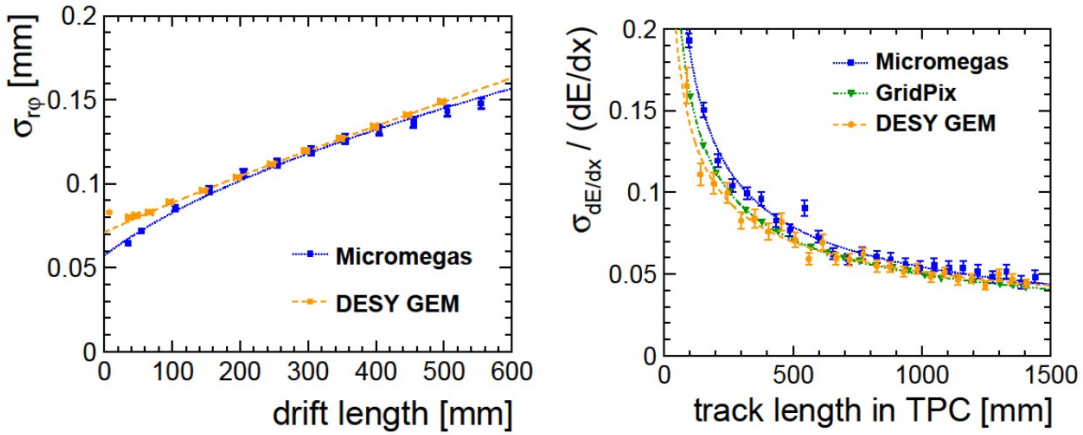


Figure 5.22. Resolution on the track position in $r\phi$ (left) as function of the drift length and resolution on the ionisation loss dE/dx (right) as function of the track length, for the three readout options under consideration.

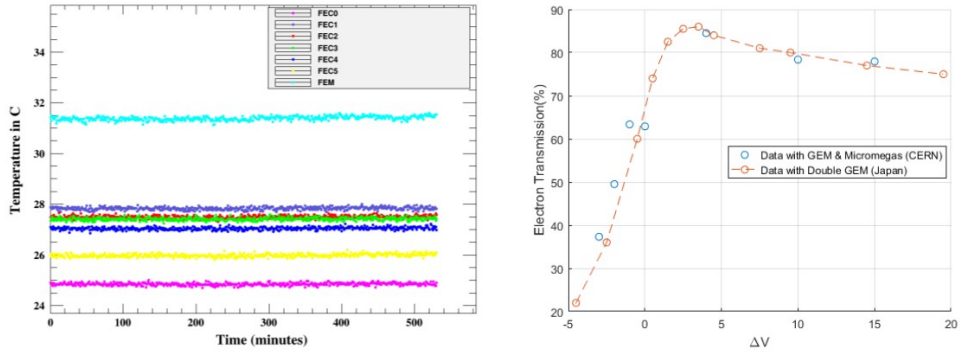


Figure 5.23. TPC operation achievements: temperature stability with double phase CO_2 cooling (left) and signal electron transparency with GEM gating (right).

may develop from the accumulation of ions in the drift volume. For the first point a double phase CO_2 cooling system with thin low-material fluid pipes has been developed and shown to perform adequately (Figure 5.23 left). For the second point an ion gating scheme based on GEM foils has been implemented and beam tested. Results show that a good transparency for drift electron signals can be maintained while preventing the accumulation of ions in the drift volume (Figure 5.23 right).

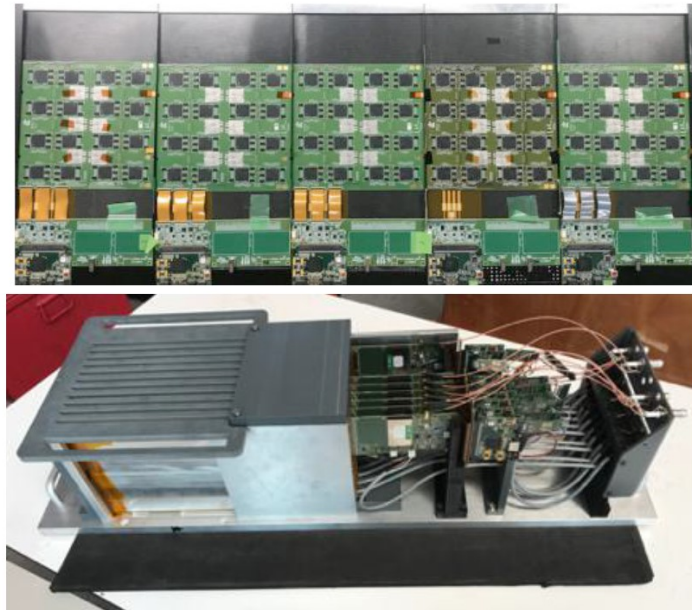


Figure 5.24. Technological prototype of the SiW ECAL. Top: set of integrated sensor&readout boards. Bottom: 10-layers calorimeter prototype used in beam tests at DESY and CERN.

Jean Claude Brient, Wataru Ootani
3 pages

5.2.4 Electromagnetic Calorimeter

5.2.4.1 Silicon option

In the past 5 years the Silicon option of the electromagnetic calorimeter has focused on the design and construction of technological prototypes of the detector including beam tests. The current technological developments have led to choosing 20cm wafers for making the diode matrices, with a standard thickness of up to 725 micrometers. When applied to ILD this would result in a slightly thicker EM calorimeter than foreseen in the baseline design, and is one of the motivations to reduce the numbers of layers from 30 to 26 (see section 5.1.2).

A fully integrated layout of the detection board has been designed with the required dimension of $16 \times 16 \text{ cm}^2$ corresponding to 1024 channels (Figure 5.24 top). The board hosts 16 SKIROC ASICs developed by OMEGA [ref] to process 64 channels each. A calorimeter prototype based on 10 such detection layers has been built (Figure 5.24 bottom) and beam-tested on several occasions at DESY and CERN, including a combined test with a SDHCAL prototype of the hadronic calorimeter (next section).

The response of this technological prototype to particles behaves as expected. A signal-to-noise ratio of 20 is measured for MIPs in single pads (Figure 5.25 left). Such a large signal/noise ratio of MIPs is important for isolated particle identification in particle flow energy reconstruction. First response to high energy electrons has recently been measured at CERN in a combined test with the SDHCAL (Figure 5.25 right). The beam tests have also been used to validate the power pulsing of the front-end electronics required to minimize heat production within the calorimeter. A new version of the detector slabs is currently in production from a joint development in LLR and Kyushu. A total number of 20 detection layers could be reached in the coming year. This will allow the construction of a full ECAL prototype to be used in test beams for measurements of the energy resolution.

More developments are ongoing to reach the requirements of the full-size ILD detector. The layout of the sensitive layer diode matrices has been revisited since the technological prototype construction. A large detector slab with dimensions similar to those of the calorimeter modules has been built and tested with MIPs (Figure 5.26 right). A 10% signal drop has been observed along the full length of the slab and could be attributed to power voltage drops and clock reflections. An

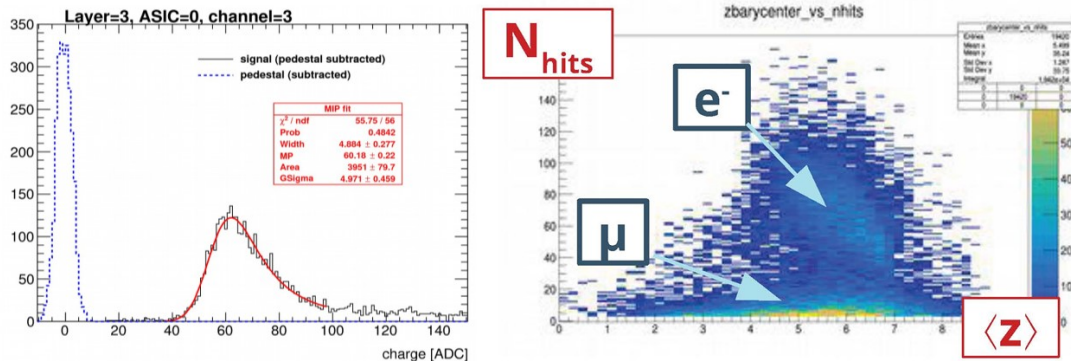


Figure 5.25. Particle response of the SiW ECAL prototype: MIP response of a single pad (left) and shower profile of muons and 80 GeV electrons (right).

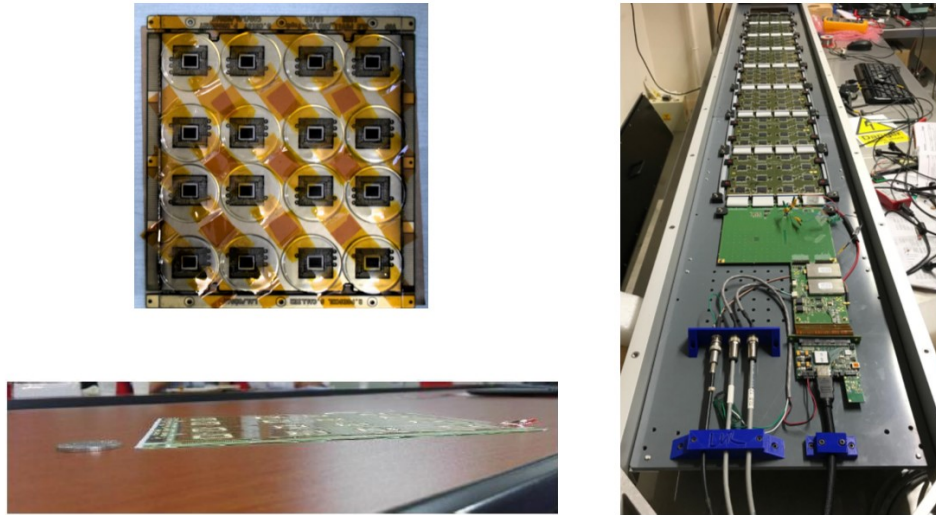


Figure 5.26. SiW-ECAL developments towards the final detector: thin chip-on-board sensors (left) and long slabs corresponding to ILD dimensions (right).

updated long slab is under construction to correct these effects and validate the solutions. In addition, an electronics readout concentrator and interface board with the detector slabs, located at the end of the slabs, is under development in LAL with a size and performance close to those needed for the ILD detector. Ultra thin detection boards with ASICs integrated within the PCB have also been developed and are under test with cosmics (Figure 5.26 left). Provided industrial aspects are under control, they may allow even more compact layouts of the electromagnetic calorimeter.

It is worth reminding that the Silicon technology developed for ILD has been retained as the baseline for the electromagnetic section of the CMS High Granularity Calorimeter (HGCAL) upgrade [ref]. The HGCAL layout is based on hexagonal readout modules with a technology similar to the ILD one. It incorporates a new version of the SKIROC ASIC with a sub-ns timing functionality which may

also be of interest for the ILD detector. A HGCAL prototype of 27 layers has been successfully tested by CMS in a combined beam test at CERN with the AHCAL ILD prototype (next section). The full HGCAL represents a 10% prototype of the ILD SiW ECAL as regards the number of channels. Its construction will be a strong asset to validate the large scale assembly and fabrication processes for ILD.

5.2.4.2 Scintillator option

Similarly to the silicon option, the scintillator option of the electromagnetic calorimeter (ScW-ECAL), after the validation of the concept using the physics prototype, has focused its R&D towards a technological prototype with fully integrated detection layers. The design of the detection layer is based on an integrated readout board, called ECAL base unit (EBU), of $18 \times 18 \text{ cm}^2$ with four SPIROC ASICs developed by OMEGA group [28] on which 144 scintillator strips ($5 \times 45 \times 2 \text{ mm}^3$ each) coupled to SiPMs are mounted.

Notable progresses have recently been made on the SiPMs for the ScW-ECAL. MPPCs with a smaller pixel pitch of 10 or $15 \mu\text{m}$ have been developed by Hamamatsu Photonics K.K, which can provide a larger dynamic range required for the ScW-ECAL [?]. Further improvements have been made for the most recent small-pixel MPPCs, including reduced optical cross-talk by a trench structure between pixels, lower dark noise and higher PDE, which have been confirmed by the prototype tests.

In the previous prototype studies, the SiPM was attached to the side edge of the strip. New designs of the SiPM readout at the bottom side of the strip are being developed for more uniform response and a better compatibility with future large-scale production. Especially a recently proposed design based on a strip with a dimple directly coupled to a surface-mounted SiPM on the PCB, which is similar to the SiPM-on-tile technology of AHCAL, shows a promising performance.

Low cost and high light yield plastic scintillator materials are also being developed for the ScW-ECAL. The development focuses on the polystyrene-based scintillator produced by the injection moulding method, which is suitable for large-scale production. A reasonably high light yield of 65–70% compared to that of the commercial PVT-based scintillator has been achieved by optimizing the production parameters.

Detection layer prototypes have been developed with the small pixel MPPCs ($15 \mu\text{m}$ pixel pitch) as shown in the left of Figure 5.27. A prototype layer was tested in positron beams of 50–800 MeV at ELPH of the Tohoku University. The right of Figure 5.27 shows the typical charge distribution obtained for the positron beam where the MIP peak is well separated from the pedestal.

A fully integrated technological prototype with 30 alternating layers of a tungsten absorber and the detection layer is planned to be constructed as a joint effort with the Sc-ECAL R&D for CEPC to demonstrate the performance of the ScW-ECAL technology and its scalability to the full-size detector.

Felix Sefkow, Imad Laktineh 4 pages
--

5.2.5 Hadronic Calorimeter

5.2.5.1 Scintillator option (AHCAL)

The particle flow [?] and energy resolution performance [29] of the scintillator SiPM ("SiPM-on-Tile") technology had been demonstrated using the CALICE AHCAL physics prototype, operated at 2006–2011, and reported in the ILC TDR. In subsequently published papers [30–36] the adequate modelling of instrumental effects and shower evolution has been further established, and the hadronic

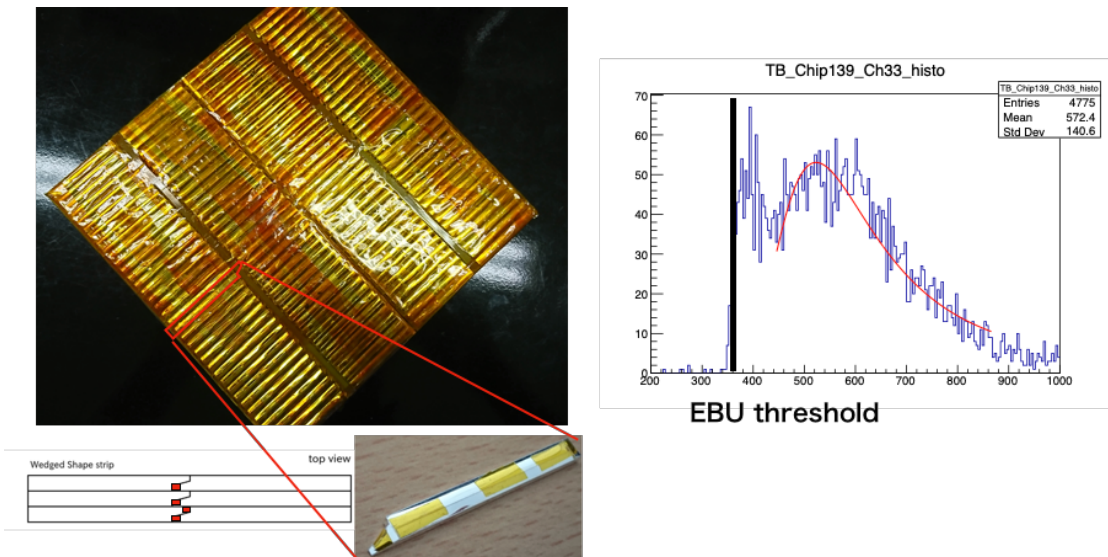


Figure 5.27. (Left) Prototype detection layer with small pixel MPPCs and (right) typical charge distribution obtained for positron beam where a MIP peak is nicely separated from the pedestal.

energy resolution and linearity of a combined system with a scintillator tungsten ECAL in front was shown [37] to be as good as that of the AHCAL alone. The same software that is used to model the detector effects such as photo-electron statistics in the SiPM and that has been validated by the test beam data is also used in ILD, after adjusting for a small difference in sampling fraction only [38].

With the establishment of the principal viability of the AHCAL technology, the focus has shifted from the study of the physical performance characteristics of such a detector to the demonstration of the feasibility of the concept while satisfying the spatial constraints and scalability requirements of collider experiments such as ILD. Such a concept must be based on a scintillator tile design well-suited for mass production and automatic assembly, originally proposed in [39] and subsequently varied and optimised in further studies [?, 40].

The new AHCAL technological prototype consists of a non-magnetic stainless steel absorber structure with 38 active layers and has 21888 channels. The structure has been produced from standard rolled plates, which had undergone a cost-effective roller-levelling procedure, ensuring a flatness of ± 1 mm, demonstrated over an area of 2×2 m². The plates were assembled using screws as foreseen for the full ILD structure. The basic unit of the active elements is the HCAL Base Unit HBU [?], with a size of 36×36 cm², holding 144 SiPMs controlled by four SPIROC2E ASICs [?]. A key element of the electronics is the capability for power-pulsed operation. In addition to dual-gain energy measurement, the electronics also provides a cell-by-cell auto trigger and time stamping on the few ns level in test beam operations. In operating conditions with shorter data-taking windows closer to the bunch train structure of linear colliders, sub-ns time resolution is achieved.

The prototype uses Hamamatsu MPPC S13360-1325PE photon sensors and injection-moulded polystyrene scintillator tiles with a central dimple [?] for optimal light collection, as shown in Figure ??.

Spot-samples of all SiPM lots, and each one of the ASICs, had undergone semi-automatic testing procedures before soldering the HBUs [?]. The gain of the SiPMs was found to be uniform within 2.4% when operated at a common over-voltage. Without any further surface treatment, the scintillator tiles are wrapped in laser-cut reflective foil by a robotic procedure and mounted on the HBUs using a pick-and-place machine, after glue dispensing with a screen printer.

The HBUs have been integrated into cassettes with interfaces for DAQ [?], LED pulsing and power distribution, which provide active compensation of temperature variations by automatic adjustments

of the common bias voltage of the photon sensors in each layer. This was routinely used in test beam operation and stabilises the gain within $\pm 1\%$.

The active layers were calibrated in the DESY test beam, assembled into the absorber stack and connected to data concentration, power distribution and cooling service systems which are also scalable to the full ILD detector. The full prototype has been commissioned with cosmic muons, exploiting its self-triggering capabilities and then installed in the test beam for data taking at the CERN SPS. During two periods in May and in June 2018, several 10^7 events with muon tracks, as well as electron and pion showers in the energy ranges 10 – 100 GeV and 10 – 200 GeV, respectively, have been recorded.

Figure ?? from the quasi-instantaneous data quality monitoring shows the distribution of the number of hits vs. the hit-energy weighted centre-of-gravity (cog) along the beam axis z for an electron run with a beam momentum of 100 GeV/c and admixtures of muons and hadrons. The different particle types populate different regions of the plot

While electron showers are characterised by a relatively narrow distribution of number of hits and a cog near the front face of the detector, hadrons exhibit a wider distribution of the cog, and a larger number of hits, decreasing as the cog moves towards the rear of the detector, and leakage increases. Muons appear as a narrow band with ~ 38 hits and a cog on z at about half the depth of the detector. The rich data sample collected in the two test beam periods in 2018 is being used for shower separation studies based on 5-dimensional reconstruction algorithms exploiting the high spatial, energy and time resolution of the prototype. While this is in progress, it can already be noted that in several aspects the performance exceeds that of the physics prototype: the noise is a factor 100 lower, the dynamic range of the SiPMs is 3 times larger, and 99.96% of the total 21888 channels are working.

The HBUs of the new prototype have also been used to build a large layer with two slabs of 6 HBUs each, corresponding to the full length of an ILD barrel sector. The signal quality was unaffected, and the rise time of the power pulsing was within specifications.

The AGCAL developments have also inspired the design of the scintillator section of the CMS end-cap calorimeter upgrade for the high luminosity phase of the LHC [?], and the new prototype has been used together with silicon-instrumented sections in front in a common beam test, further illustrating the maturity of the technology.

5.2.5.2 RPC option (SDHCAL)

The SDHCAL technological prototype built in 2011 has been regularly tested in beams in the past years with various configurations [ref], including a combined test with the SiW-ECAL prototype in 2018 (previous section). The SDHCAL prototype consists in 48 single-gap RPC layers of 1 m^2 (Figure 5.28). Each detection gap is instrumented with 6 Active Sensitive Units (ASU) made of a $50 \times 33\text{ cm}^2$ PCB with 24 "HARDROC" ASICs from OMEGA [ref]. The RPC pad size is 1 cm^2 and the pad signals can be readout either in digital (1 bit and 1 threshold) or semi-digital (2 bits and 3 thresholds) modes.

The numerous data sets collected at CERN with high-energy hadron beams have been used to validate the performance of the technology. Special reconstruction methods adapted to the high granularity semi-digital structure of the calorimeter have been developed [ref] to relate the energy estimation to the hit number and density. The current state of the performance is summarized in Figure 5.29. A good linearity is observed and the multi-threshold mode is found to mitigate saturation and improve the resolution at high energy. The description of the measured resolution by the simulation is however found to be sensitive to the description of the core of the hadronic showers, with a tendency for the Monte-Carlo to underestimate the performance due to harder cores in the

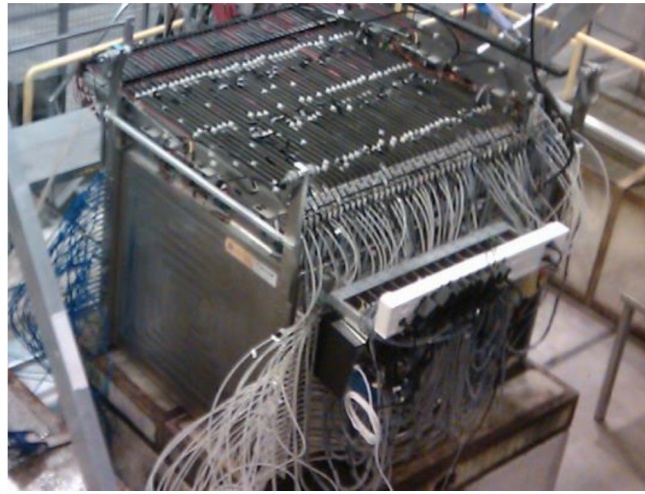


Figure 5.28. Technological prototype of the Semi-Digital Hadronic Calorimeter.

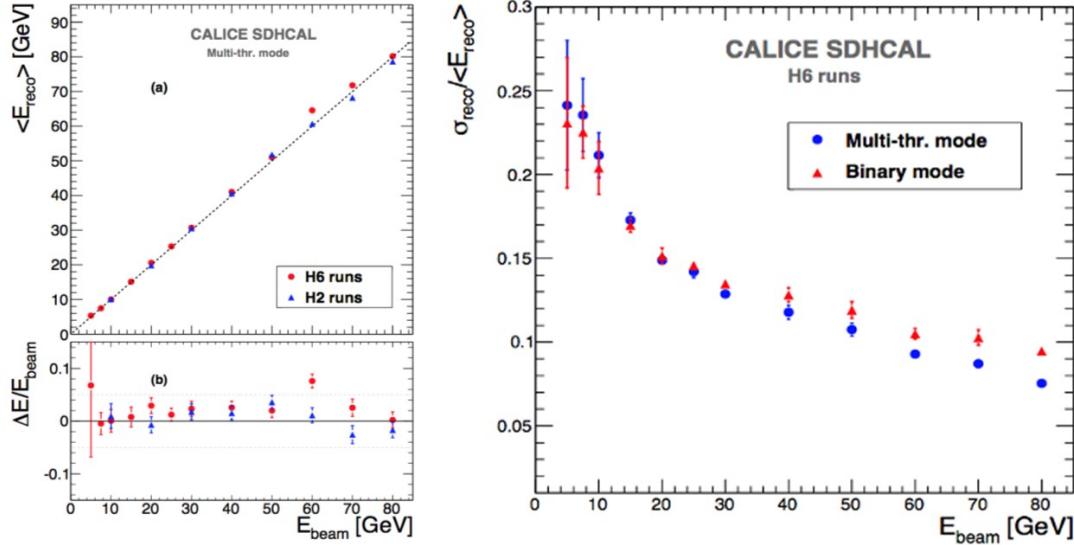


Figure 5.29. Performance of the SDHCAL technological prototype as measured in beam tests: linearity (left) and energy resolution for the digital and semi-digital readout options (right).

showers. This point will require further tuning of the simulation.

In the recent years the SDHCAL teams have focused on adapting the technology to the full-size ILD requirements, in order to cover detection surfaces of up to $1 \times 3 \text{ m}^2$ required by the ILD Hadronic Calorimeter in its "Videau" configuration (section 5.1.2). An improved RPC gas circulation system with better uniformity has been designed and validated with the construction of two large RPC's. Larger ASUs of $100 \times 33 \text{ cm}^2$ have been designed with a new version of the HARDROC ASIC including 0-suppression (Figure 5.30 left), and their interconnection improved to allow chaining of up to 9 ASUs. Efforts have also been invested in the manufacturing process of self-sustained hadron calorimeter structures with high precision mechanical tolerance as required by the RPC insertion. A method of "roller levelling" has been used to machine steel absorber plates with a high flatness. A high precision electro-welding has been used to built a first large size prototype of 4 calorimeter layers (Figure 5.30 right) which has proven that gap size variations well below 1 mm can be reached on such large structures.

For the longer term the option of multi-gap RPC's with a high timing resolution of $\approx 20 \text{ ps}$ is

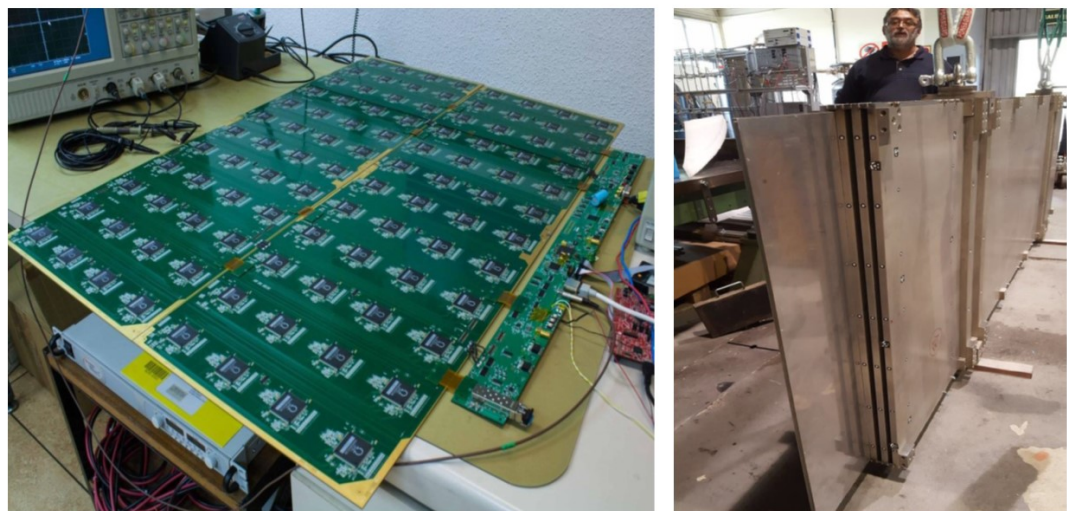


Figure 5.30. SDHCAL ongoing developments for the final ILD dimensions: two active sensor units of $100 \times 33 \text{ cm}^2$ chained to each other and connected to the outside with a new compact DAQ interface (left), and self-sustained welded structure of 4 calorimeter plates of $1 \times 3 \text{ m}^2$ with the required mechanical tolerances (right).

prototyped based on the "PETIROC" ASIC [ref].

Yan Benhammou, Sergej Schuwalow
2 pages

5.2.6 Very forward detectors

In the past years the development of the ILD forward detectors has mostly been pursued by the FCAL R&D Collaboration [ref]. Progress concerns mainly the LUMICAL calorimeter and, more recently, the BEAMCAL sensors.

Based on a specific ASIC [ref] developed after the DBD, calorimeter silicon sensitive layers have been built to assemble a first LUMICAL 4-layer tungsten calorimeter prototype and, two years later, a more compact 8-layer calorimeter prototype (Figure 5.31 left). The two prototypes were beam-tested in 2014 and 2016, respectively. The test data [ref] confirm the expected significant improvement of the transverse compactness of the electromagnetic showers in the compact prototype compared to the earlier one (Figure 5.31 right).

A new ASIC "FLAME" [ref] based on 130 nm CMOS technology is currently under final validation. FLAME features the low power, in-situ digitisation and fast readout required by the final detector. A new ≈ 20 - layers SiW calorimeter prototype based on FLAME, with specifications and configuration close to the final LUMICAL detector, is under construction and planned to be beam-tested in 2019.

The LHCAL and BEAMCAL calorimeters can be based on similar technologies as the LUMICAL, with radiation hardness requirements increasing as function of the sensor proximity to the beam. For the BEAMCAL, new sensors such as sapphire are being considered. Irradiation campaigns are under way to characterize them (Figure 5.31 right) and provide input for the final choice.

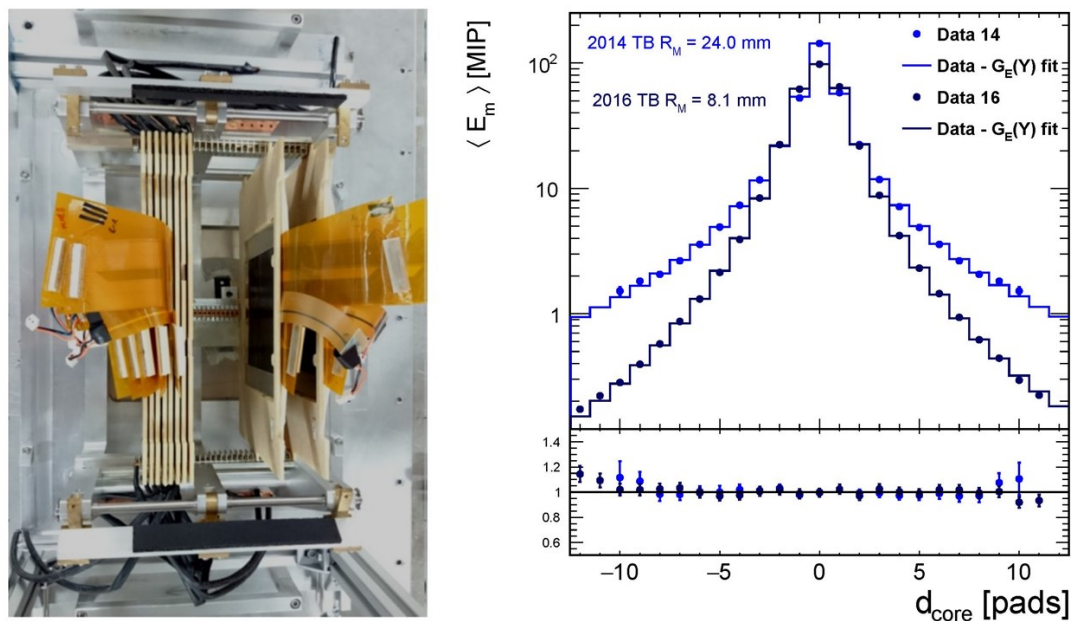


Figure 5.31. LUMICAL compact prototype tested in the DESY electron beam in 2016 (left) and corresponding improvement in shower compactness achieved versus the 2014 prototype (right).

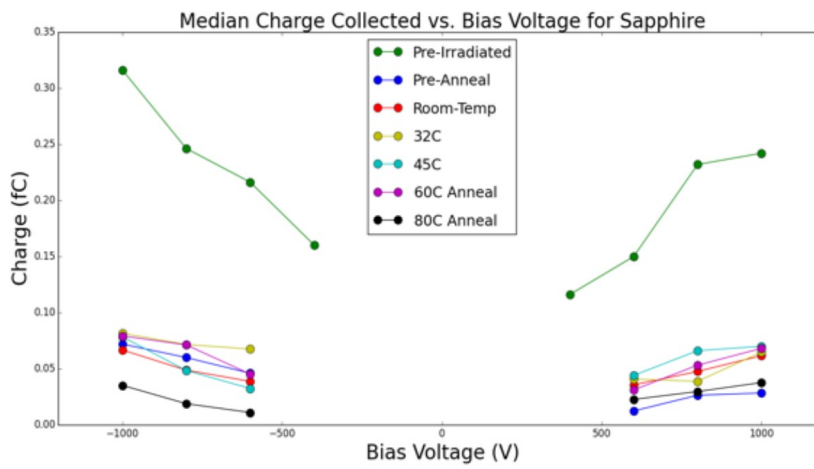


Figure 5.32. results of irradiation tests performed at SLAC for sapphire sensors considered

Valery Saveliev

1 pages

5.2.7 Iron instrumentation

Dedicated studies have been conducted at FNAL in the past years to optimize the layout of scintillator bars adapted to muon detection. Prototypes have been built and tested with muon beams [ref]. They are all based on long scintillator bars with signal collected by WLS fibers and readout by SiPMs at both extremities. The transverse resolution of $\approx 1\text{cm}$ required for the muon momentum measurement is defined by the bar widths of a few cm. The longitudinal position is measured from the time difference of the signals of both extremities and depends on the WLS configuration. The two options under consideration described in section 5.1.2 (Figure 5.13) have been tested: longitudinal resolutions of 5 to 10 cm are measured and found roughly independent of the longitudinal position of the muon within the bar (Figure 5.33).

More studies are ongoing to develop low cost SiPMs also adapted to the measurement of the tails of high energy jets (tail catcher function).

The RPC option for the iron yoke instrumentation was not specifically studied but would directly

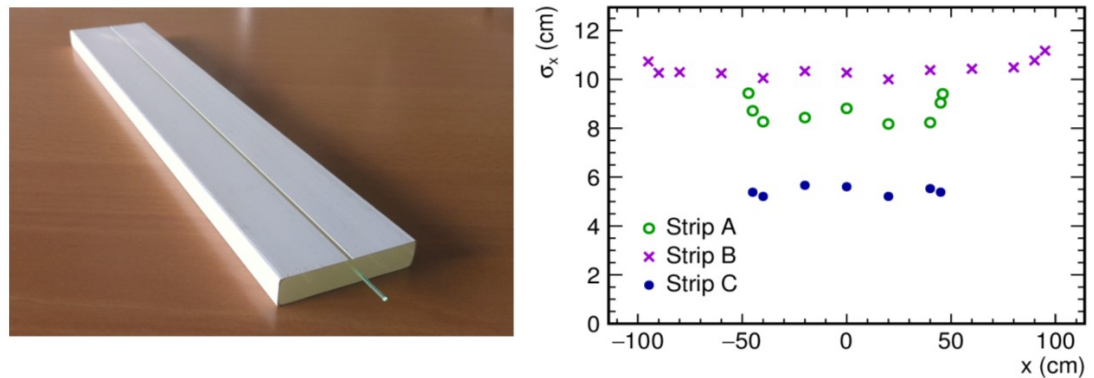


Figure 5.33. Left: example of prototype scintillator bar built for the muon detector; right: longitudinal resolution on reconstructed muon as function of longitudinal coordinate: strip A and B as on left figure with lengths of 1 and 2 m respectively, strip C of 1m length with WLS fibers positioned on the small edge of the strip.

benefit from the RPC developments of the SDHCAL hadronic calorimetry option (section 5.2.4).

6 ILD Global Integration

Karsten Buesser, Claude Vallee
1 pages

Yasuhiro Sugimoto
1 pages

6.1 External ILD integration

The proposed site for the ILC is located in the Kitakami mountains in the north of the Japanese main island Honshu. Dedicated studies are under way to adapt the generic ILC design, as described in the Technical Design Report, to the realities in this environment. For ILD, the arrangements of the surface and underground installations around the interaction point (IP) are of natural importance. The current conceptual design of the civil facilities and the plans for the detector related infrastructure and services have been coordinated between the relevant detector and ILC machine groups as well as with local experts.

6.1.1 Site-related Infrastructure

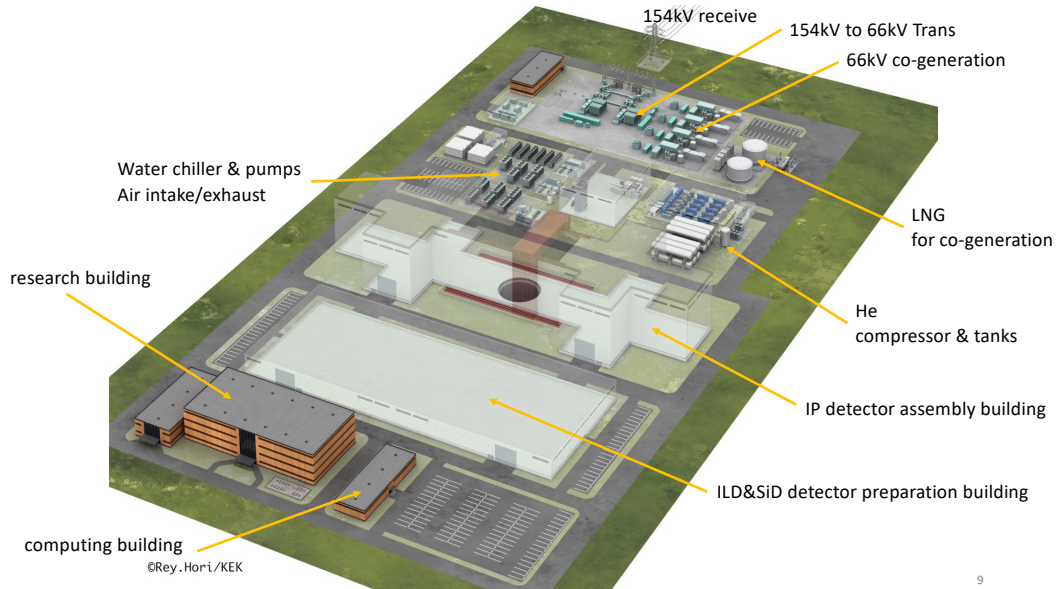
ILD will be assembled on the surface, similar to CMS at LHC. Figure 6.1 shows a rendering of the surface installations above the ILC interaction point. At the heart is the detector assembly building that is located directly over the central shaft that gives access to the underground collider hall. A large gantry crane above the shaft allows for the lowering of the pre-instrumented detector parts into the underground area. A preparation building is foreseen where sub-detector elements can be assembled and tested. A research building and a computing building provide the infrastructure for the operation of the detectors at the IP Campus.

The underground experimental hall is about 100 m below the surface and hosts two experiments, ILD and SiD, in a "push-pull" arrangement (c.f. figure 6.2). Both detectors share one interaction region and are installed on movable platforms and can be rolled into or out of the beam line within a few hours. The detectors can be opened and maintained in their parking positions. Access to the underground hall is provided by two vertical shafts and an access tunnel that allows for vehicles to drive directly into the underground area 6.3.

Yasuhiro Sugimoto
1 pages

6.1.2 Detector Utilities and Cavern Ancillary Services

In order to operate the ILD detector in the underground detector cavern, electricity, cooling water and other services have to be supplied from surface facilities. Though conceptual designs existed at the time of the TDR, more detailed knowledge about the requirements from the detector exists by now and should lead to an optimisation of the facilities layout and locations.



9

Figure 6.1. Conceptual design (artist's view) of the surface facilities ("IP Campus") above the ILC interaction point [41].

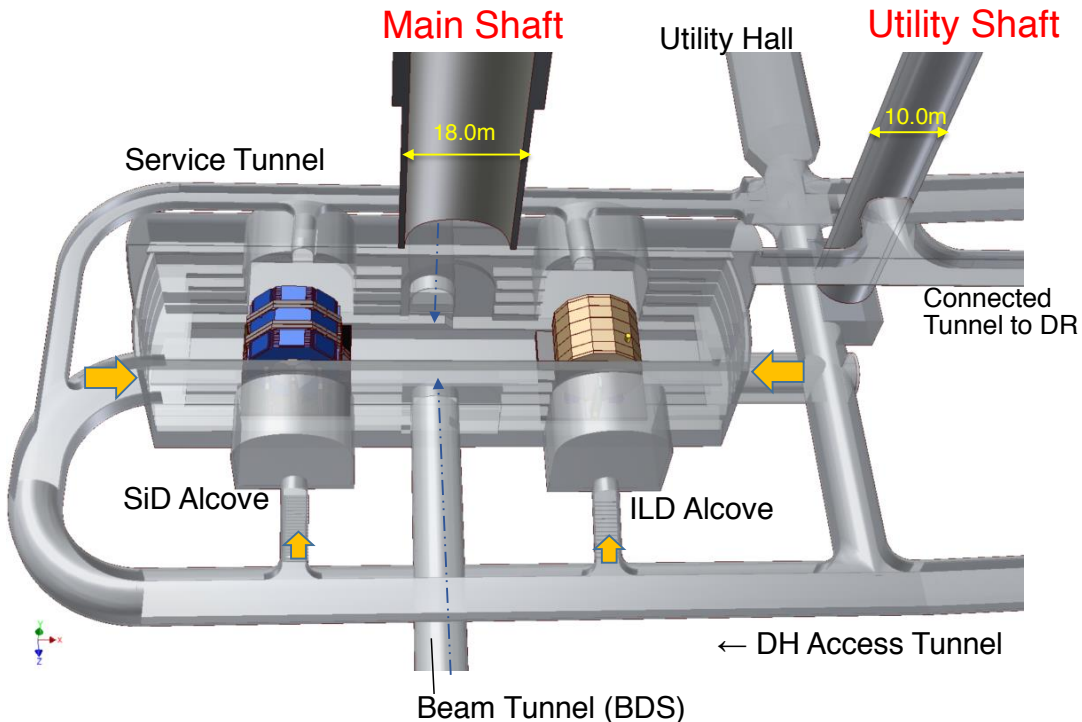


Figure 6.2. Underground facilities with the detector hall, ILD and SiD in push-pull configuration, access tunnels and shafts [42].

6.1.2.1 Service Locations

There are several possible locations for detector services: on the detector platform, on service galleries on the wall of the detector hall, in dedicated utility/service caverns, and on surface. A possible

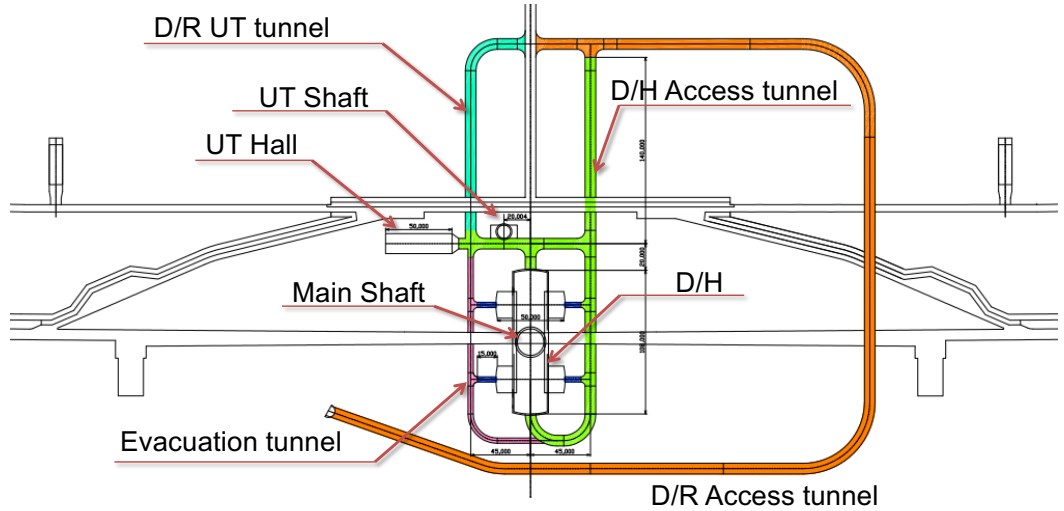


Figure 6.3. Access to the underground infrastructure is provided by two shafts, main shaft and utility (UT) shaft, and a system of access tunnels [43] that serve the detector hall (DH) as well as the damping rings (DR).

configuration is shown in Figure 6.4. We assume that large or noisy apparatus such as transformers (6.6 kV → 400/200/100 V), heat exchangers and pumps for cooling water, sub-detector cooling plants, etc. should be located in the utility/service cavern. Cryogenic plant for QF1 is also supposed to be located in the utility/service cavern.

The utility/service cavern should be relatively close to the detector, but well isolated from the detector hall regarding the noise, vibration, and radiation. Design of the facilities including caverns (CFS) for detector utilities/services has to be made based on requirements from the detector side. In order to clarify the requirements, a rough estimation on the ILD needs in electricity, cooling water, and space has been made (c.f. section 6.1.2.2).

The Design of the utility/service cavern is not fixed yet. In the baseline design (TDR-modified), the utility/service cavern has a dead-end as shown in Figure 6.3 (UT Hall in this figure). In addition, this cavern is supposed to be used for both detectors and accelerators, and does not have enough space for the estimated ILD needs. ILD proposes another design as shown in Figure 6.5. In this design, there are three utility/service caverns for accelerator, ILD, and SiD, respectively. The size of a detector utility/service cavern of $12\text{ m} \times 34\text{ m}$ with two floors would be large enough for one detector. Figure 6.4 is drawn assuming this utility/service cavern design.

6.1.2.2 Power Consumption and Cooling Requirements

The requirements for power and cooling at ILD have been studied in a bottom-up approach where the current information from all detector components has been assembled and cross-checked.

A tentative estimation of the power consumption in the detector hall and surface facilities for ILD is listed in Table 6.1. The total power consumption in the underground caverns is about 1 MW, dominated by the ILD solenoid and the machine components associated to the detector.

The cooling water which is necessary for extracting the power consumption is shown in Table 6.2. Distribution of the underground power is visualized in Figure 6.6. It can be seen that the fraction of the power consumption that is coming from the sub-detectors is small.

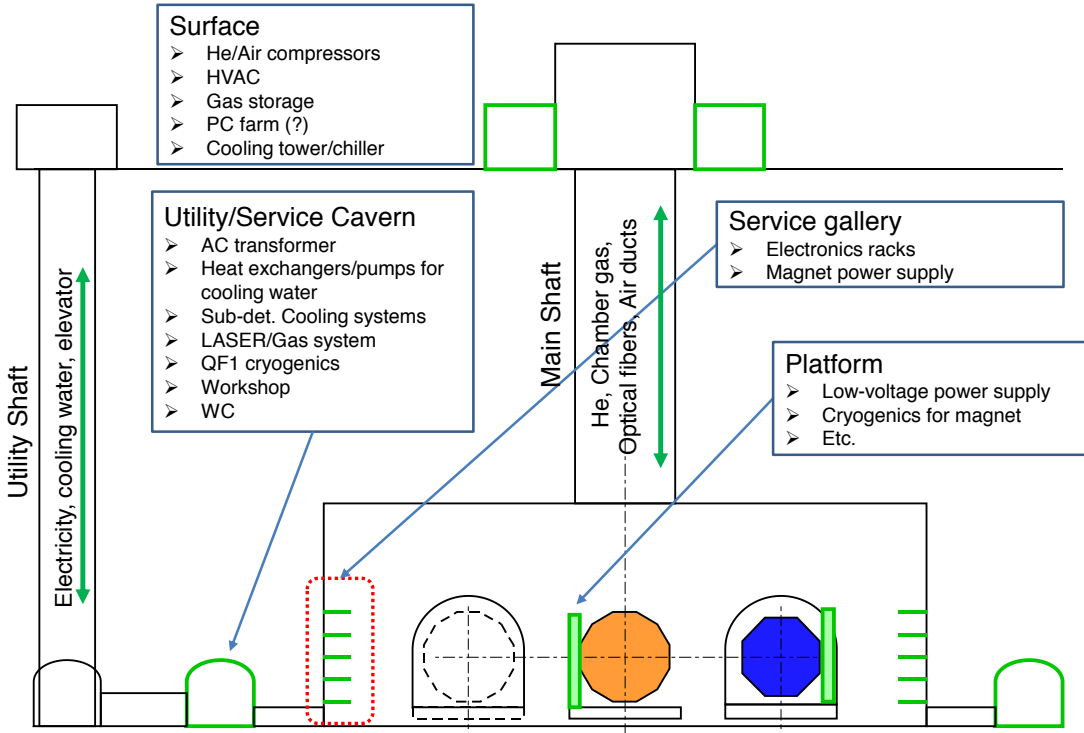


Figure 6.4. Schematic drawing of the possible locations for detector services. The Utility/Service cavern for the detector is proposed but not yet implemented into the ILC baseline design [44].

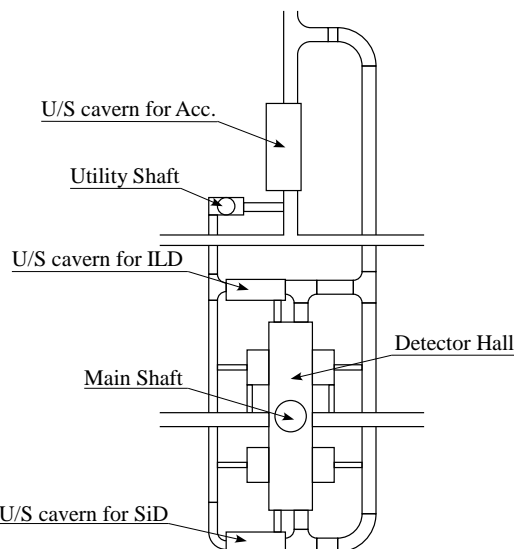


Figure 6.5. A possible design of Utility/Service caverns.

Table 6.1. Breakdown of the power consumption estimates for the ILD detector and appended ILC components (in kW) [44].

Item	Power			
QD0/QF1/Crab Cavity	Power Supply	150	on surface	
	Cold Box	150		
	He Compressor	300		
Detector Solenoid	Power Supply	250	on surface	
	Cold Box	50		
	He Compressor	500		
Subdetectors	Total	161	Front-end Electr.	Back-end Electr.
	Muon	12	5	5
	HCAL	45.5	27.5	8
	ECAL	40	20	12
	VFS	9	2	5
	SET	9	2	5
	TPC	16.2	15	-
	SIT	8	1	5
	FTD	8	1	5
	VTX	13.5	2	1.5
Computer Farm		1000	on surface	
Water Pump		25		
HVAC		600	on surface	
Lighting		25		
Air Compressor		50	on surface	
Platform Mover		100		
Cranes	3x5t	21		
	40t	50		
TOTAL		3432		
Underground		982		

Table 6.2. Breakdown of the cooling water requirement estimates for ILD and appended ILC components [44].

		Chilled Water			Low-conductive Water			Normal Water		
Item		Heat (kW)	ΔT (K)	Flow (l/min)	Heat (kW)	ΔT (K)	Flow (l/min)	Heat (kW)	ΔT (K)	Flow (l/min)
QD0/QF1/ Crab Cav.	Power Supply				150	10	214			
	Cold Box				150	10	214			
Detector Solenoid	Power Supply				250	10	357			
	Cold Box				50	10	71			
Subdetectors	Muon	12	5	34						
	HCAL	45.5	5	130						
	ECAL	40	5	114						
	VFS	9	5	26						
	SET	9	5	26						
	TPC	3	5	5				13	5	38
	SIT	8	5	23						
	FTD	8	5	23						
	VTX	13.5	5	39						
	Pump	11	5	31	11	10	16	3.7	5	11
AC Transformer		49	5	140						
Total		208		595	611		873	17		48
Total Chilled Water				595						
Total Normal Temp. Water										921

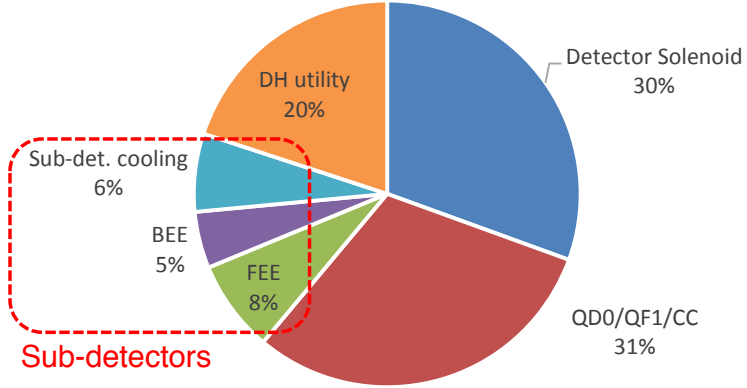


Figure 6.6. Distribution of the underground power consumption for ILD [44]. While the detector solenoid, the machine elements (magnets QD0/QF1 and the crab cavity system CC) use the major part of the power, the detector hall (DH) utilities and the sub-detectors cooling, back- and front-end electronics (BEE, FEE) contribute less. The total power consumption sums up to about 1 MW.

6.1.3 Access and Assembly

The Kitakami site of the ILC is located in a mountainous and rural area, only accessible by road (c.f. figure 3.2). The nearest port, Kesennuma, is about 40 km away on the Pacific coast. All ILD parts need to be shipped via the central access roads into the mountains. Typically, street transport in Japan is limited to trucks with up to 25 t of mass (including the weight of the truck itself). The total mass of ILD is of about 15,500 t, posing a specific challenge for the logistics infrastructure. Heavy-load transports of up to 70 t loads are possible in exceptional cases. For the transport of the ILD solenoid modules, this option is under study (c.f. figure 6.36).

The heaviest parts of ILD are the yoke rings. They need to be assembled on-site from pre-fabricated iron blocks. Figure 6.7 shows three options that are under study for the procedures. If a remote campus close to the interaction region could be made available, with a dedicated reinforced street in-between, then the pre-fabricated iron slabs from the factory could be assembled into blocks of up to 200 t there. The blocks could then be transported via the dedicated road to the interaction region for assembly of the yoke rings. Another option would be the construction of a pre-assembly hall at the interaction region. The construction of the iron block could then take place there, in vicinity of the detector assembly hall and therefore a reduced transportation problem. A remote area would still be useful as storage space.

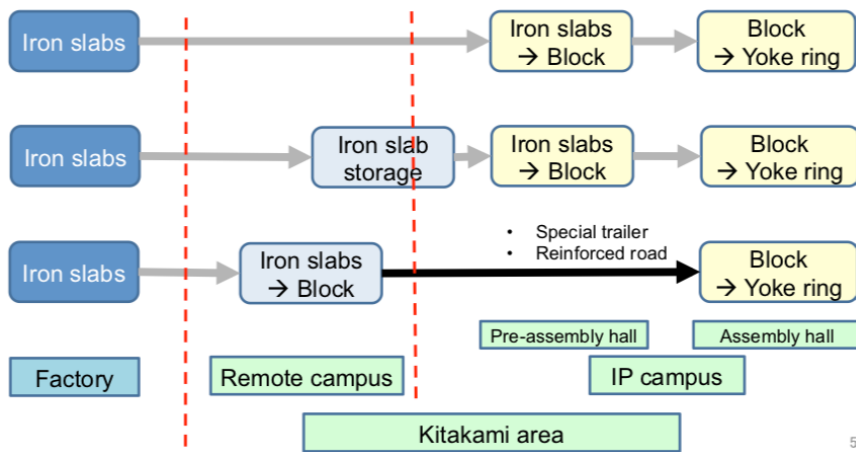


Figure 6.7. Options under study for the (pre)assembly of the ILD iron return yoke [45].

Figure 6.9 shows a conceptual layout of the surface installations above the interaction region. The central detector assembly hall serves both detectors, SiD and ILD, and is located above the central access shaft to the underground areas (compare figure 6.2). A pre-assembly building for SiD and ILD is located right next to it. Heavy and large parts, like the ILD yoke blocks, could be assembled in the pre-assembly area before they are moved to the central assembly hall for the installation of the yoke rings. A survey has been done within ILD to assemble the requirements of the sub-detectors on assembly, storage and on-site testing space. Figure 6.9 shows the results from SDHCAL, TPC and SiECAL (barrel and endcap). Though the information is at a very conceptual level, it serves as valuable input for the planners of the interaction region surface installations that need to be accommodated in the Kitakami mountains.

The final assembly of ILD and SiD should happen above ground in the central detector assembly hall. The major parts, the SiD barrel detector and the ILD yoke rings, have masses of up to 4500 t and will be lowered through the central access shaft into the underground areas with the help of a gantry crane. A similar procedure has been followed for the CMS detector at CERN and was proven to be very efficient. Figure 6.10 shows an artist's view of the SiD barrel detector hanging from a

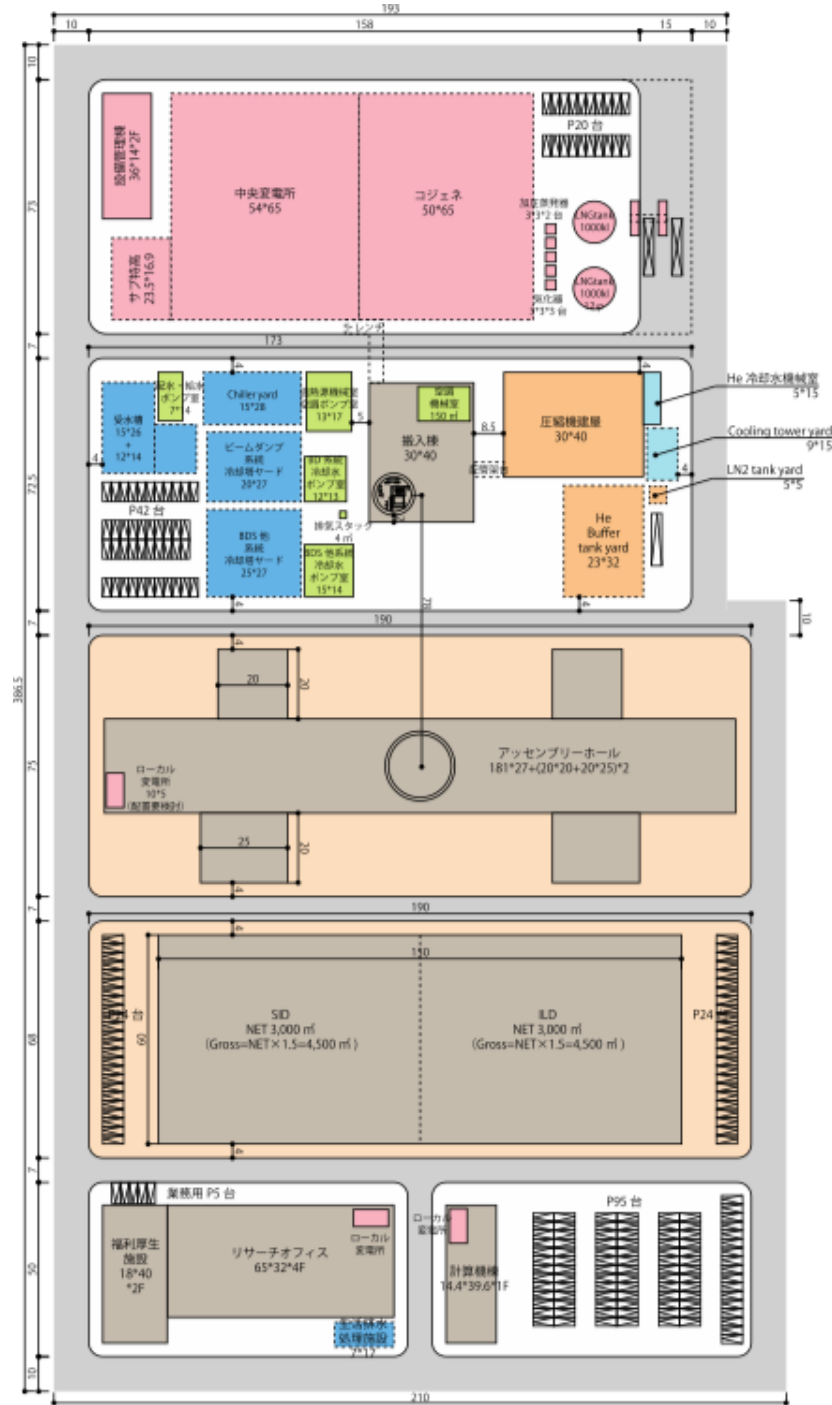


Figure 6.8. Conceptual design of the interaction area surface installations with the detector assembly hall over the large shaft in the middle and with a dedicated detector pre-assembly building next to it [45].

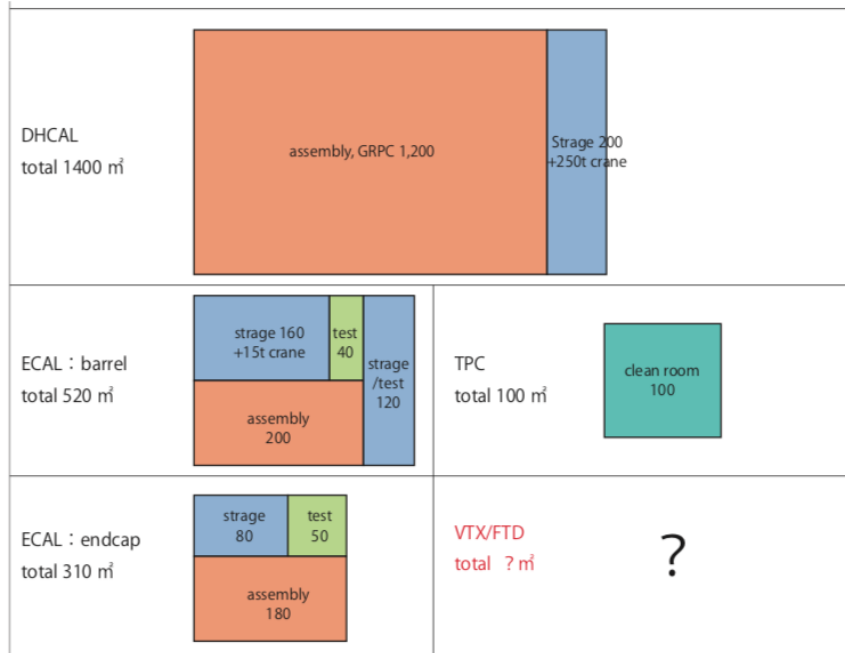


Figure 6.9. Result of a subdetector survey on assembly space requirements [45].

gantry crane.

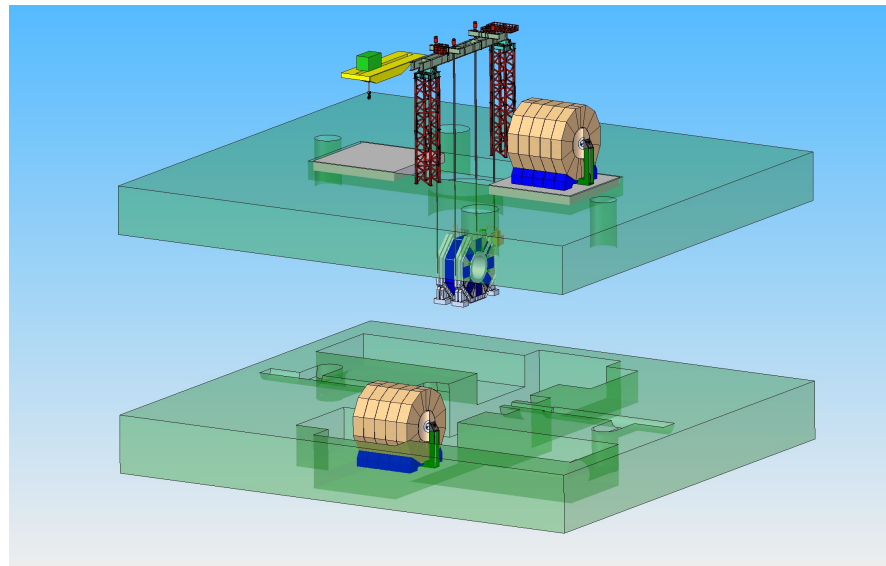


Figure 6.10. Lowering of SiD and ILD main parts via the central shaft into the underground detector hall with the help of a heavy load gantry crane [46].

The main advantage of the CMS-style surface assembly of the detectors lies in the decoupled time lines for the construction of the machine and the detectors. In this case, the on-site assembly can start as soon as the surface buildings are ready while the underground excavations and constructions can carry on. Figure 6.11 shows a rough schedule for the detector construction. On-site assembly can start 2.5 y after the ground breaking when the surface buildings are ready. The lowering of the large detector parts only takes place about one year before the commissioning of the machine would start. The total technical construction and assembly time is of about 9 years.

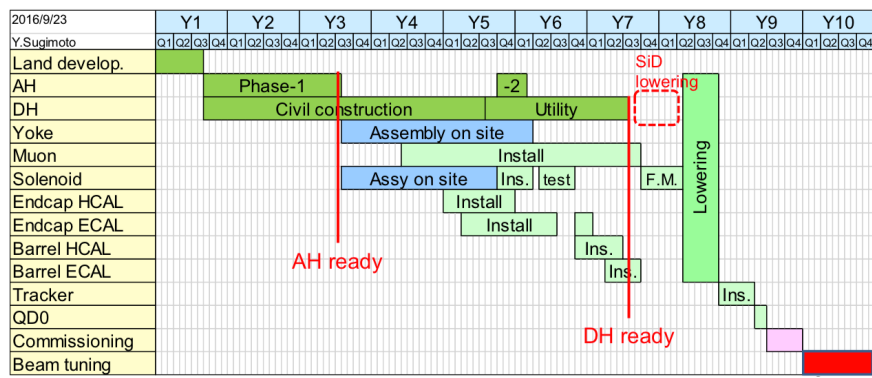


Figure 6.11. Tentative timeline for the detector construction and assembly [45].

Karsten Buesser, Roman
Poeschl, Toshiaki Tauchi
3 pages

6.2 Internal ILD integration

The ILD detector concept underwent a dedicated effort to come to an integrated design that from subdetector level up to the major structures gives a conceptual engineering view of the full system. This includes realistic mechanical designs with tolerances, deformations and dead material zones as well as an integrated design of all detector services: electrical, cooling, gases, etc.

6.2.1 ILD Mechanical Structure

The mechanical structure of ILD has not changed since the TDR. The main parts are the three barrel yoke rings and the two endcaps. The central barrel ring carries the solenoid coil in its cryostat; all barrel detectors are suspended from the cryostat. The two other central yoke rings can move over the cryostat. The endcaps can be opened as well. All rings can be moved using airpad systems. Figure 6.12 shows the mechanical model of the ILD yoke structure.

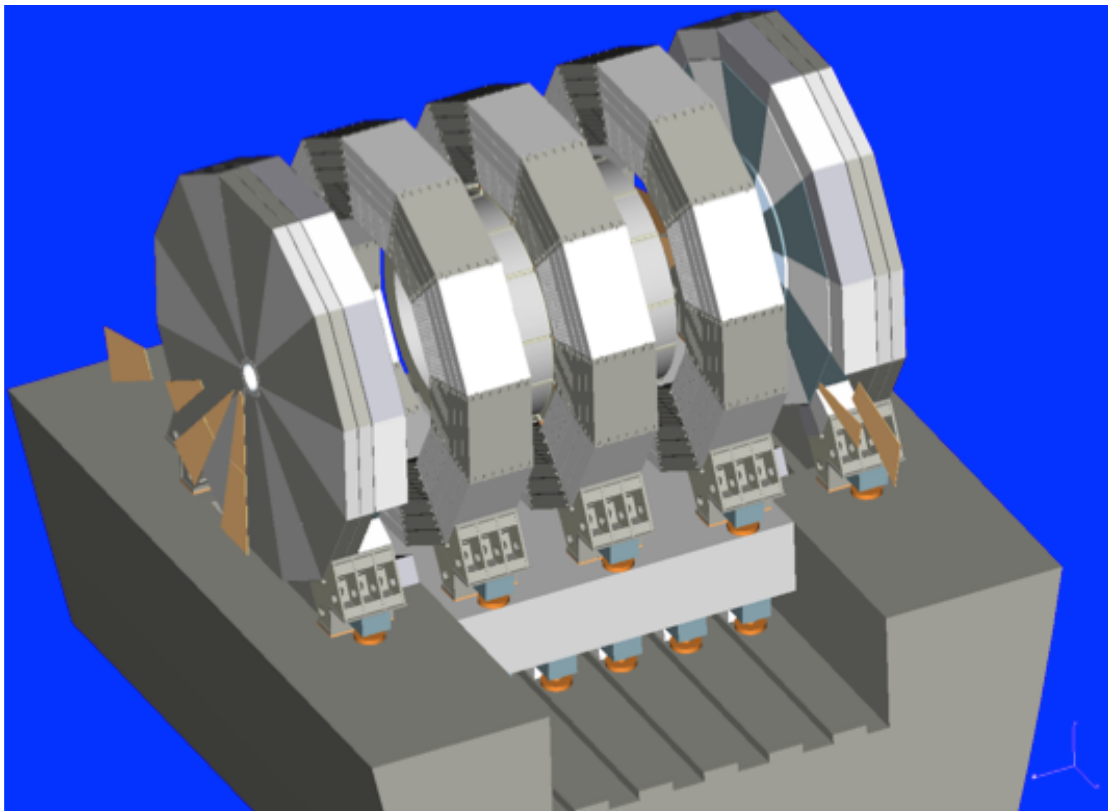


Figure 6.12. Mechanical structure of the ILD detector [2].

6.2.2 ILD Services and Utilities

Each component of ILD has requirements on services and utilities that are needed for operations and maintenance. This typically includes power and data lines, gas and cooling systems, guidances for laser beams, etc. All major support systems for those services, e.g. power supplies, cooling plants, lasers, DAQ computers, or gas systems are located outside of the detector, sometimes even far away (c.f. section 6.1.2.1). General paths have been defined in the global detector structure where space is allocated for those services. The routing of those paths has to be designed to minimise the amount of gaps and dead material in the active detector areas, while at the same time provide enough space for the foreseen utilities. Three main pathways have been defined for ILD:

1. The services of all barrel detectors are collected at the front-face of the barrel, go around the solenoid cryostat and leave the detector through the gap between the central yoke ring and the neighbouring rings.
2. The services of the endcap detectors (ECAL, HCAL, Muon) leave the detector along the endcap yoke ring.
3. The services for the forward calorimeter systems (FCAL, ECAL ring) pass parallel to the beamline, outside of the QD0 magnet.

This scheme allows for the opening of the yoke endcaps as well as for moving the barrel yoke rings independently from each other. The front-end electronic systems of the subdetectors can often drive only a limited cable length. Therefore, space for additional patch panels, drivers, data concentrators needs to be provided inside the ILD detector. While the exact requirements for those are not known in each case, conceptual locations have been defined. Figure 6.13 shows the general service paths and proposed locations for the patch panels in ILD.

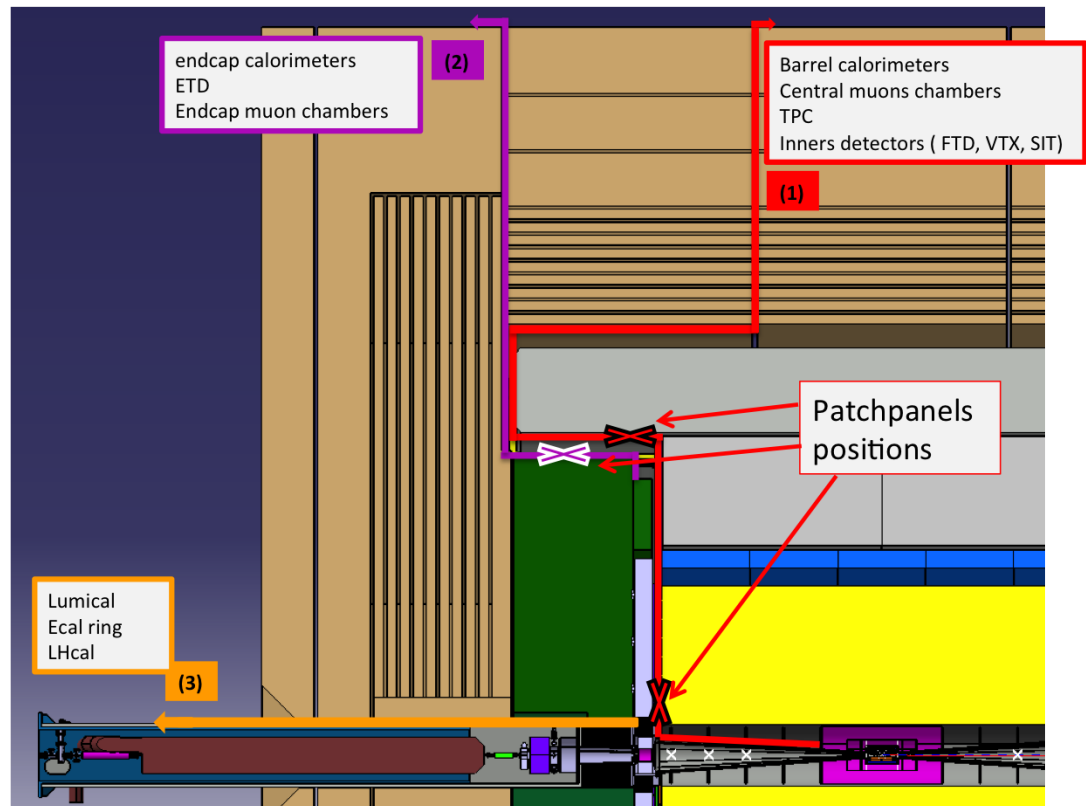


Figure 6.13. Service paths in the ILD detector and suggested positions for patch panels [2].

6.2.3 Inner Detector Integration

At the heart of ILD, directly at the interaction point, is the inner detector that comprises the beam pipe as well as the vertex detector and the intermediate silicon tracking devices, SIT and FTD (c.f. figure 6.14).

6.2.3.1 Mechanical Integration

The vertex detector is suspended from the beam pipe that itself is carried together with the Forward Tracking Disks and the Si Intermediate Tracker from the Inner Detector Support Structure (ISS). The ISS is a support tube made out of carbon-fibre reinforced plastic and is suspended from the end flanges of the TPC. A piezo-based active alignment system (see figure 6.15) allows for the positioning of the ISS with a precision better than 0.01 mm [47], independently of the main ILD detector structure. This is required to adjust the beam pipe and the inner tracking devices with respect to the beam axis, to better precision than what can be achieved with the complete ILD detector, e.g. after push-pull operations.

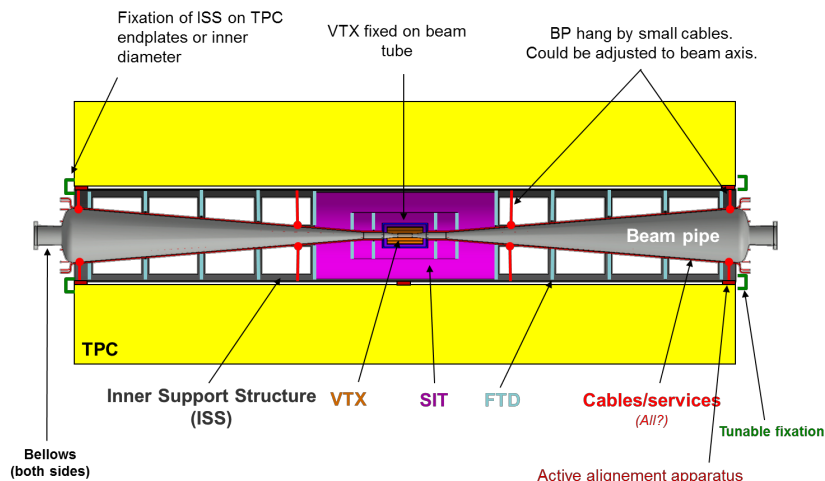


Figure 6.14. Schematic of the inner tracking detector system [47].

6.2.3.2 Electrical Services and Cooling

A rather detailed concept has been developed for the power scheme of the vertex detector (CMOS version), see figure 6.16. Copper based power and control cables as well as optical fibres for the data readout connect the vertex detector with patch panels at either ends of the ISS. From here, the cables are routed as described in section 6.2.2 to the outside of the detector. An engineering design for the details of the cabling and patch panels inside the ISS is still pending. Figure 6.17 shows the place holders for the cables in the current model. The vertex detector will be cooled using air flow cooling, where the cooling pipes also need to follow the general services paths.

6.2.4 TPC Integration

6.2.4.1 Mechanical integration

The mechanical integration of the TPC is still under study. Two possible concepts are being followed up. Either the TPC will be suspended directly from the solenoid cryostat with the help of carbon ribbons or support struts. Or it can be mounted to the absorber structure of the hadronic calorimeter.

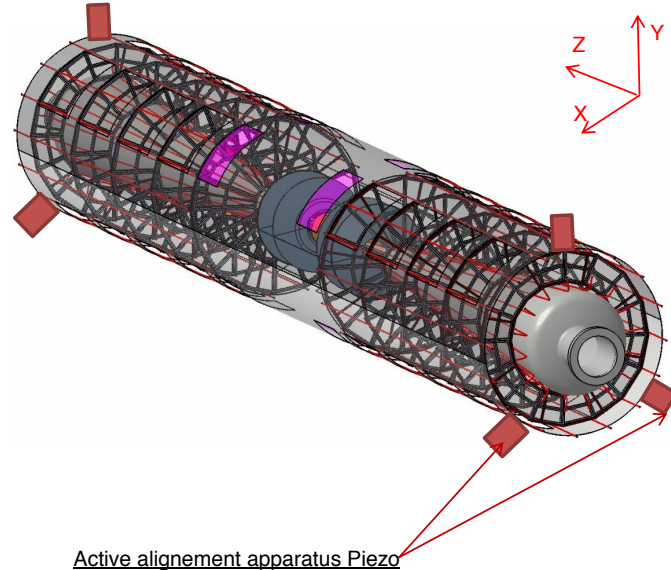


Figure 6.15. Engineering design of the inner detector [47].

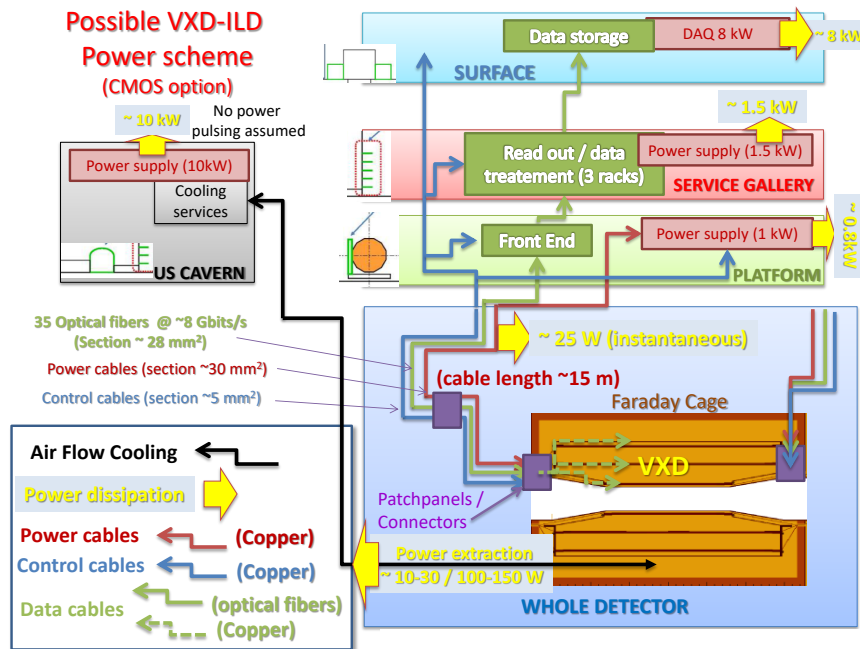


Figure 6.16. Diagram of a power scheme for the vertex detector (CMOS option) [48].

In the first case, the TPC would be decoupled from the mechanical properties of the calorimeters, at the price of having larger lever arms that might amplify vibrations. A longitudinal damping system would probably be required. In the second case, the lever arms would be much shorter, but the dynamic behaviour of the full system of the cryostat, hadronic and electromagnetic calorimeter as well as the TPC itself needs to be understood. Figure 6.18 shows the front face of the TPC, suspended from the hadronic calorimeter.

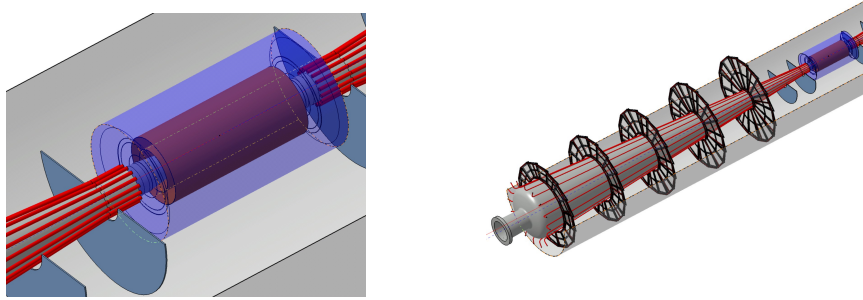


Figure 6.17. Cable placeholders for the inner Si detectors (VTX, SIT, FTD) [49].

6.2.4.2 Electrical Services and Cooling

The electrical services and the cooling pipes of the TPC start on both end plates and will be routed through gaps in the front-faces of the calorimeters, between the end-cap and barrel detectors (c.f. figure 6.18). A cooling system based on 2-phase CO₂ has been tested in 2014 and 2018 on a system of 7 Micromegas modules. Figure 6.19 shows a solution with a 6-loop geometry. The outer supplies of the TPC need to be accommodated in the detector environment. While a gas mixing and supply system will most probably be placed on the surface area, distribution sub-systems need to be closer to the detector, e.g. on the detector platform. The high-voltage power supplies will be placed in the detector hall at reasonable cable-length distances. Figure 6.20 shows a schematic drawing of the TPC connections to the outer world.

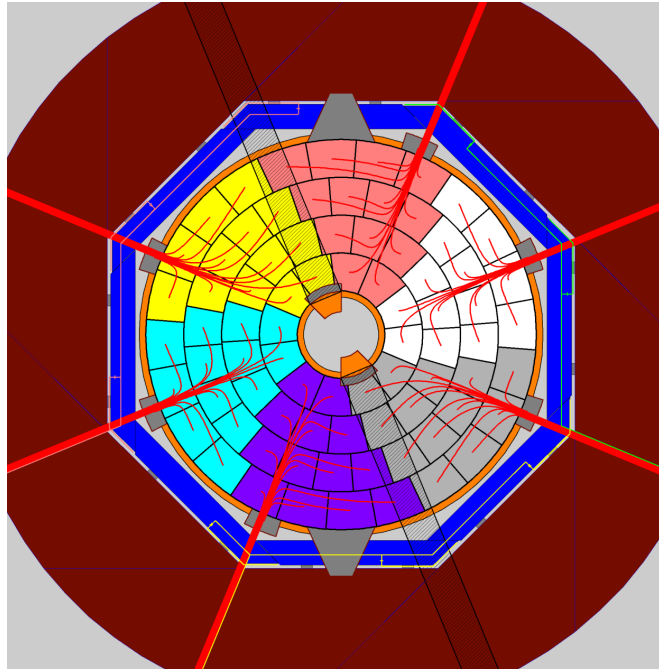


Figure 6.18. Conceptual design of the cable paths on the front-end of the TPC. The cables are routed to the outside in the marked gaps of the HCAL barrel electronics [50].

6.2.5 Electromagnetic Calorimeters Integration

6.2.5.1 Mechanical Integration

The two options under study for the ILD electromagnetic calorimeters, SiECAL and ScECAL, share the same mechanical design as shown in figure 5.7. The ECAL barrel consists of eight staves that

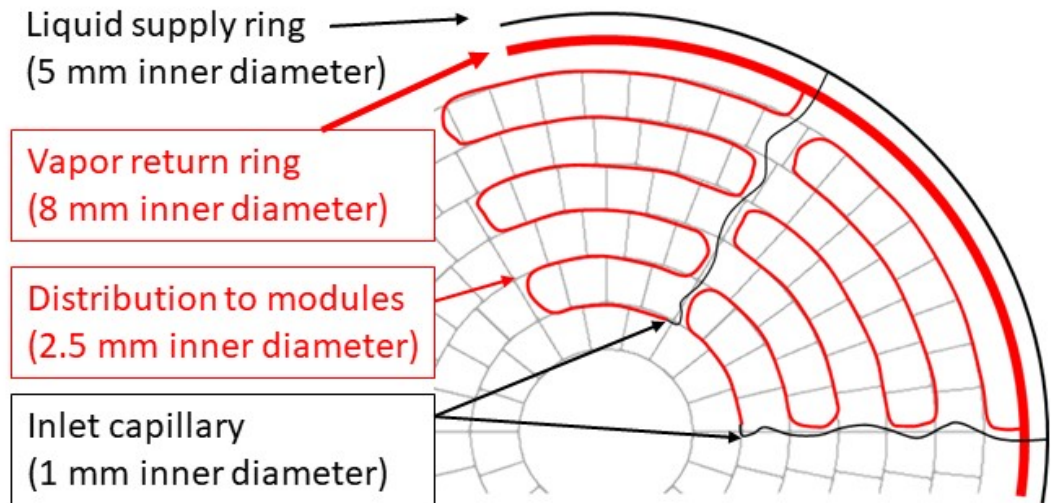


Figure 6.19. Conceptual design of a TPC cooling system with tube routing on the TPC end plate. Figure courtesy of Bart Verlaat, Nikhef.

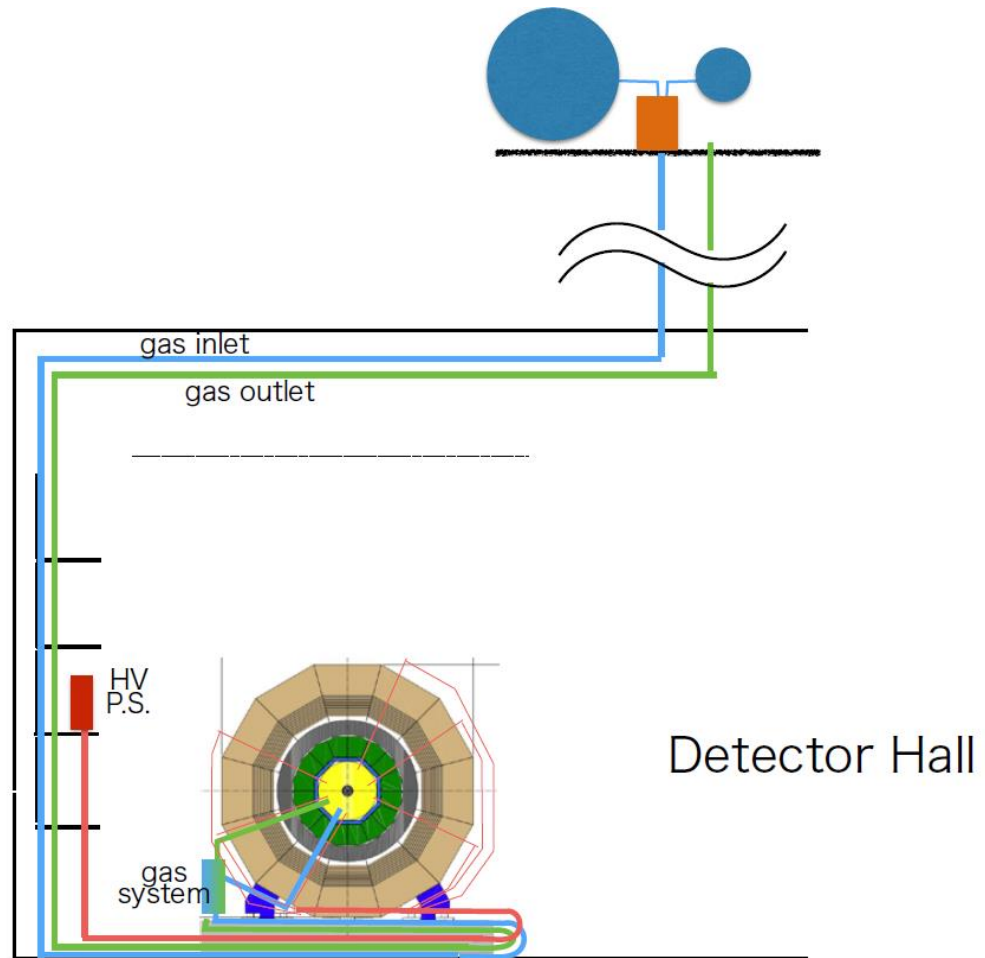


Figure 6.20. Gas and HC interfaces of the TPC [50].

are built from five modules each (c.f. figure 6.21). The staves are supported from the HCAL barrel sections. The ECAL endcaps are supported from the HCAL endcap detector.

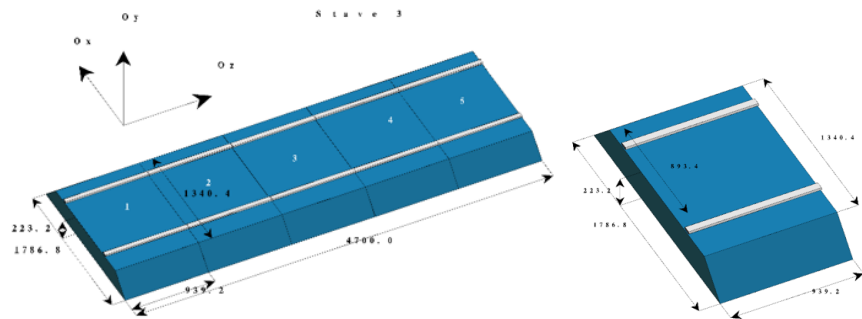


Figure 6.21. ECAL stave and module [51]

6.2.5.2 SiECAL Electrical Services and Cooling

A detailed integrated design of the SiECAL electrical services and of the cooling system has been developed. Figure 6.22 shows a close-up view of the upper side of an SiECAL module. The front-end electronics is located at the end of the readout slabs. The services are collected at dedicated hubs for a full column of slabs ("SiECAL Hub2" in the figure). The service from the column hubs are collected at one central hub for each full stave ("SiECAL Hub1"). Figure 6.23 shows a block diagram of the electrical services for the SiECAL and the connections from "Hub1" to the outside power supplies, to the common clock and the DAQ.

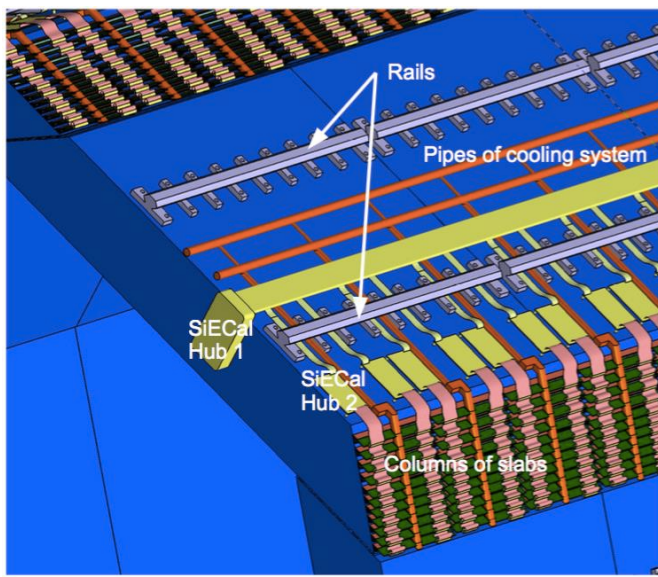


Figure 6.22. Services on an SiECAL module [51].

A conceptual design for the SiECAL cooling system is shown in figure 6.24. The system foresees leakless water cooling, where a cooling station would be located outside of the ILD detector in the underground area. The water will be distributed via an hierarchical system of cooling lines ("A" to "F") to the barrel and endcap detectors.

6.2.5.3 ScECAL Electrical Services

The distribution of the electrical services for the ScECAL is very similar to the SiECAL case. Figure 6.25 show a block diagram of the service distributions. Also in this case, two series of hubs are planned, one for each stave and one for each column of slabs, to distribute HV and signals accordingly.

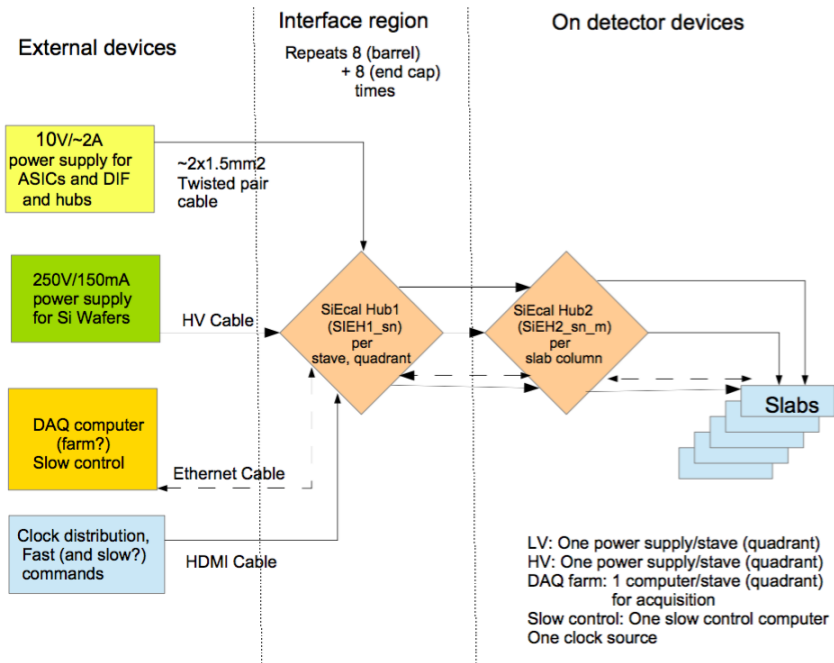


Figure 6.23. Block diagram of the electrical services for the SiECAL [51].

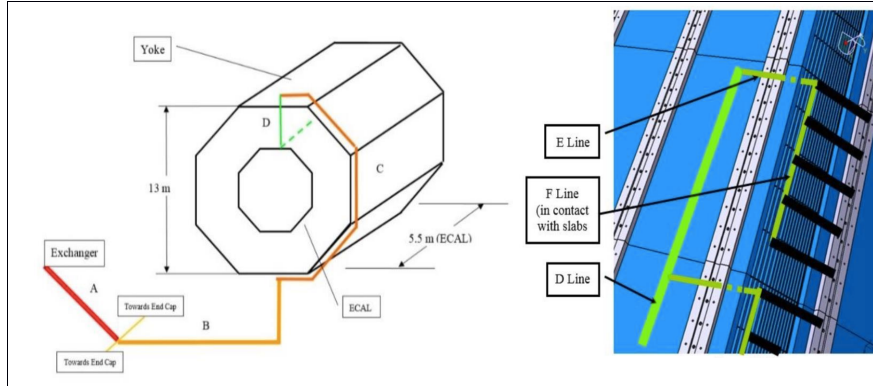


Figure 6.24. Conceptual design of the SiECAL cooling system [51].

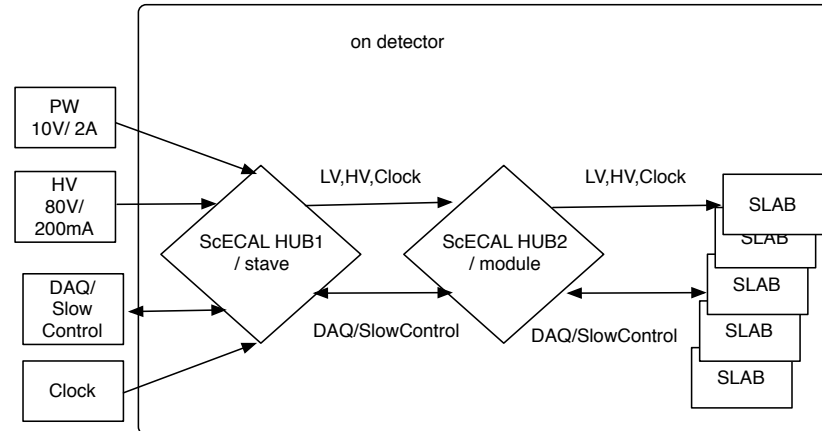


Figure 6.25. Block diagram of the electrical services for the ScECAL [52].

6.2.6 Hadronic Calorimeters Integration

6.2.6.1 Mechanical Integration

Two absorber structures are under study for ILD, the so-called "TESLA" and "Videau" structure (c.f. figure 5.9). The main differences from the viewpoint of the detector integration are the mechanical behaviour, further discussed in section 6.4, and the layout of the detector electrical and cooling services. Though both technological options for a hadronic calorimeter, the analogue AHCAL and the semi-digital SDHCAL can be adapted to both mechanical structures, the AHCAL has been designed with the "TESLA" structure in mind, while the SD-HCAL is optimised for the "Videau" case.

6.2.6.2 AHCAL Electrical Services and Cooling

An engineering model of the AHCAL barrel section in the "TESLA" structure has been designed and is shown in figure 6.26. Eight of these modules form a ring, two rings form the barrel detector. The active layers are read out via electronic boards that are located on the outside of the absorber structure. The front-end electronics are accessible when the endcaps of the ILD detector are open. A

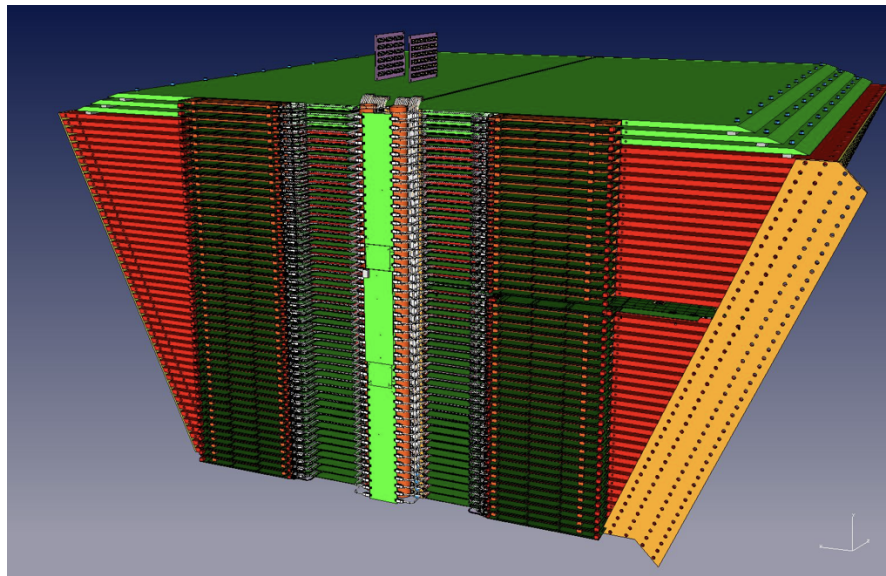


Figure 6.26. Engineering design of an AHCAL module with electrical and cooling services. Only one instrumented layer is shown for the wedge shape outer parts of the module.¹

close-up of the readout boards, the electrical services and the cooling system is shown in figure 6.27. The electrical and cooling lines of ECAL, AHCAL, the TPC and the inner detector are routed via the gaps in the AHCAL front between the barrel and the endcap detector, as shown in figure 6.28.

6.2.6.3 SDHCAL Electrical Services and Cooling

The SDHCAL barrel detector consists of three or five rings of eight wedge-shaped modules. As the active layers are installed tangential to the ring structure, access requires the removal of the respective barrel rings from the detector solenoid. The cables and cooling services run on the outside of each module to the barrel front face, as shown in figure 6.29. The SDHCAL services are routed around the detector solenoid to the outside. The service of the inner detector, the ECAL and the TPC can be routed on the front side of the SDHCAL barrel detector, as shown in figure 6.30.

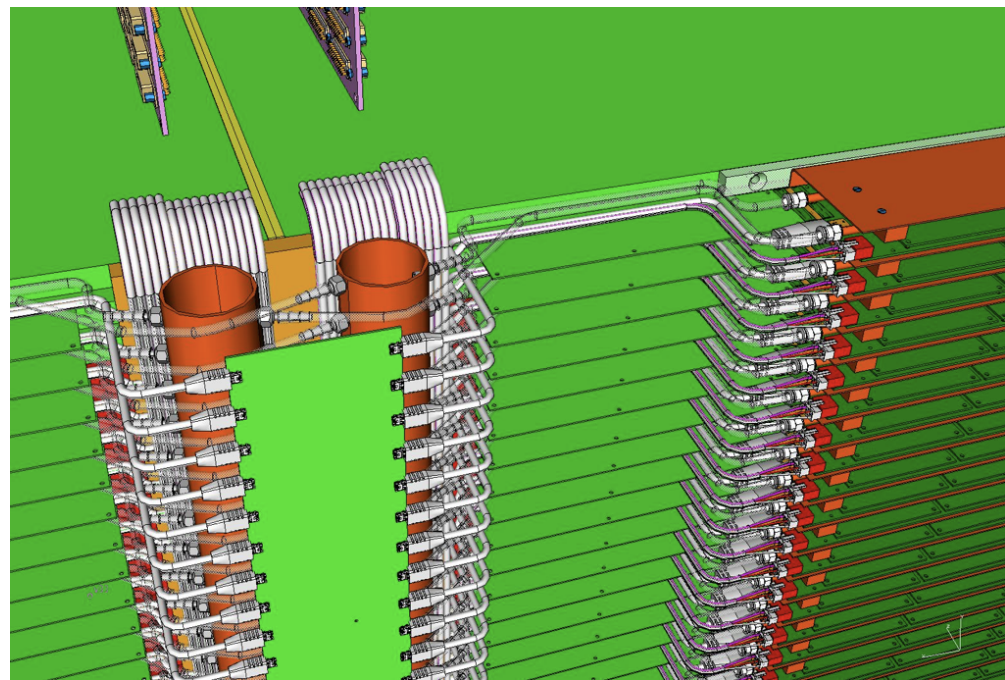


Figure 6.27. AHCAL module front face with readout boards, cables and cooling lines.

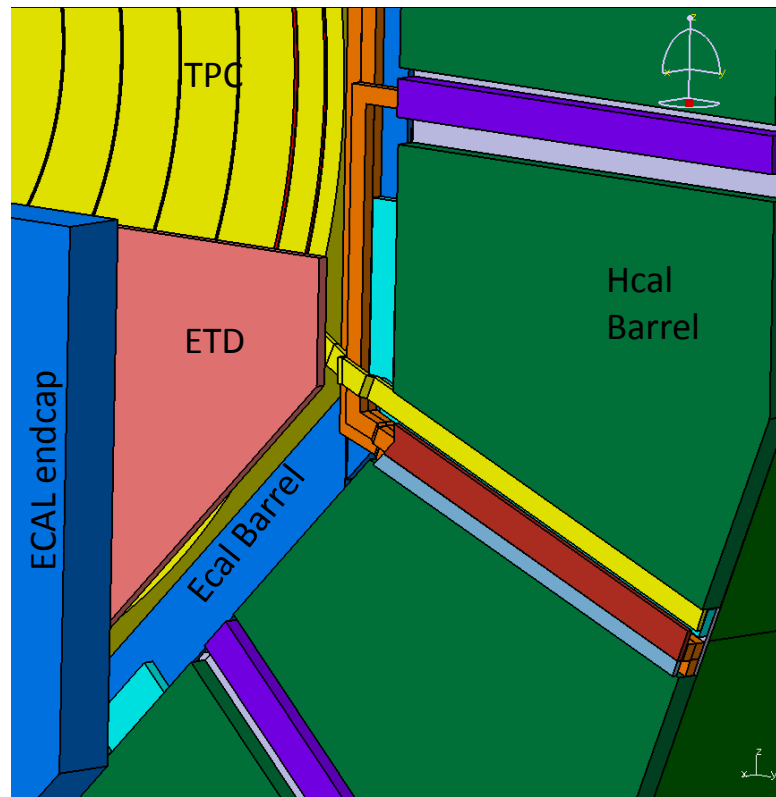


Figure 6.28. Service paths on the AHCAL barrel front.

6.2.7 Very Forward System Integration

The very forward systems, BeamCal, LumiCal and LHCAL, are carried by the support structure for the final focus quadrupole QD0. Figure 6.31 shows the mechanical layout and the conceptual service paths of the forward calorimeters.

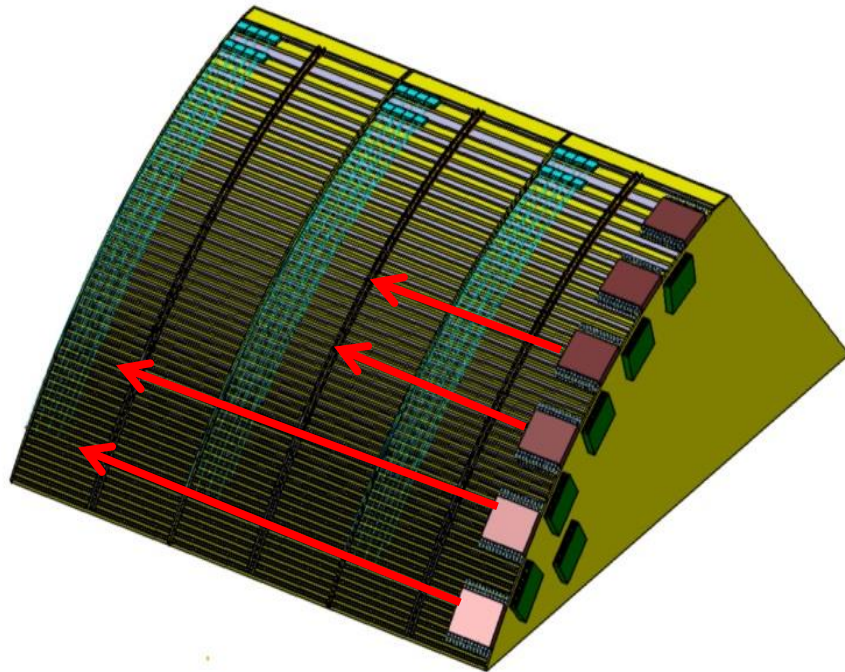


Figure 6.29. SDHCAL module with readout boards, cables and cooling lines.

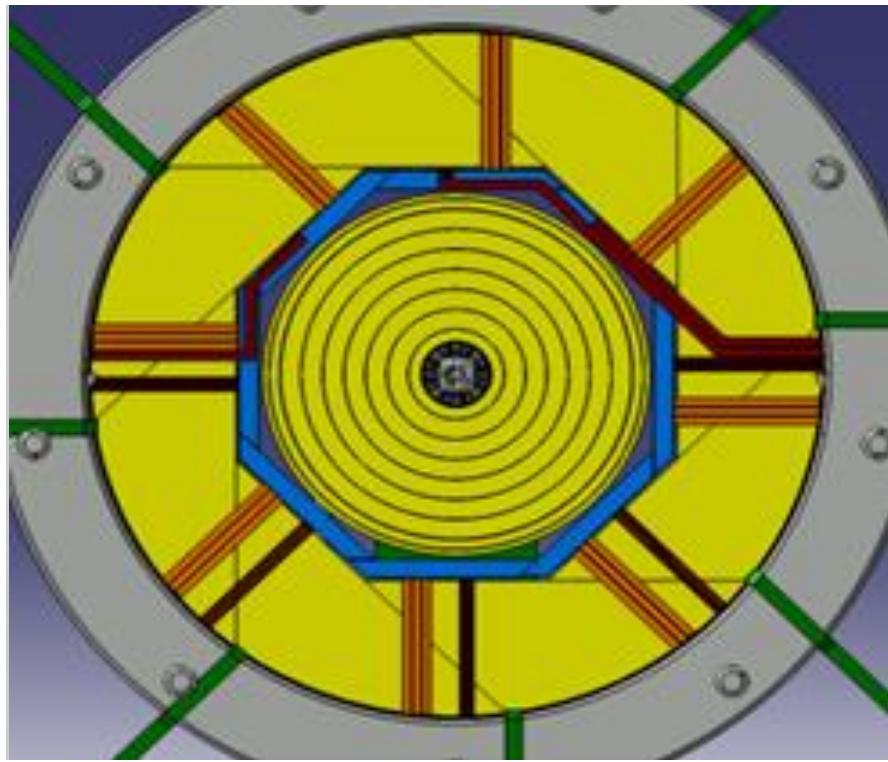


Figure 6.30. Service paths on the SDHCAL barrel front.

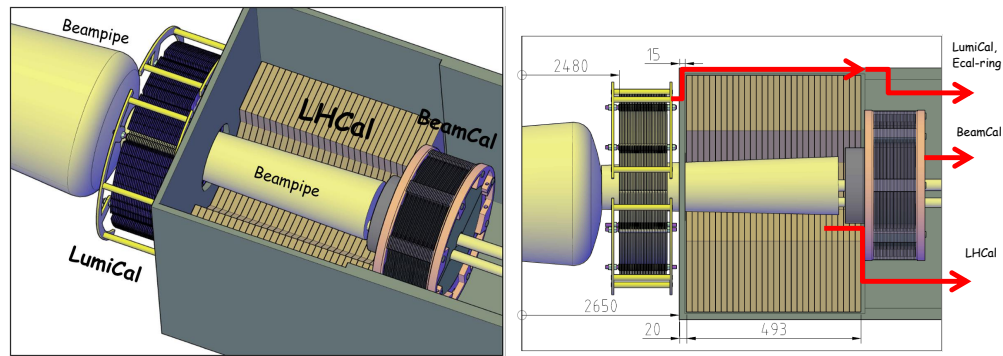


Figure 6.31. Design of the very forward systems with conceptual service and cable paths [53].

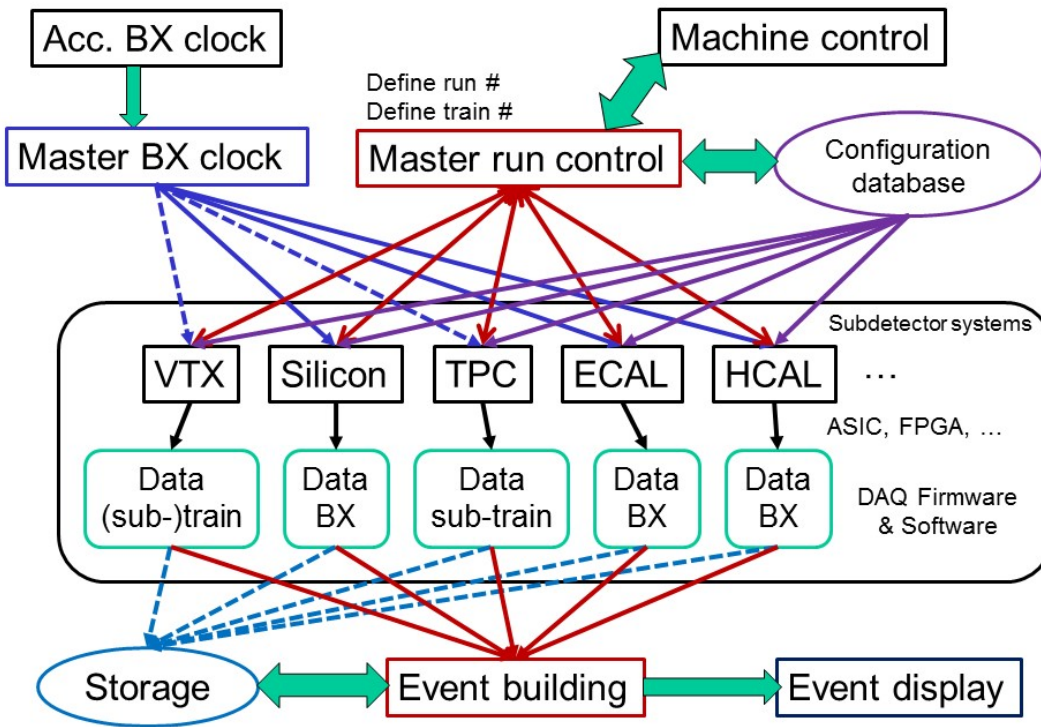


Figure 6.32. Global architecture of the ILD data acquisition system.

Matthew Wing, Taikan Sue-hara
2 pages

6.3 Data acquisition

The ILD data acquisition takes advantage of the relatively low rate of relevant physics e^+e^- interactions ($O(0.1)$ hadronic evt)/BC) and of the long idle periods between bunch trains (chapter 3) to provide a triggerless readout of the detector. The subdetector data of all BCs of a given bunch train are collected before the next bunch train and processed offline as a single data set for identification, bunch tagging and reconstruction of the individual interactions.

6.3.1 DAQ architecture

The overall organisation of the DAQ system is summarized in Figure 6.32.

The processing of subdetector data is first performed locally with a high parallelism within FPGA and ASIC boards which each typically treat $O(100)$ subdetector channels. The individual data are zero-suppressed, amplified, time stamped and digitized, depending on the subdetector, and stored in local pipelines dimensioned adequately for a full bunch train. The "event building" is performed between bunch trains by gathering all subdetector data of a given bunch train into a single bunch train data set. The bunch train data sets are stored locally on the IP Campus (section 6.2.1) and transferred to an offline computing farm which may be located on the main campus. In the farm each bunch train data set is processed individually by one processor in order to identify individual events, tag their bunch crossings and perform calibration and reconstruction. This scheme caters for the different time resolutions of the subdetectors, which range from individual bunch tagging as done e.g. in the calorimeters, to a full train integration time as in the TPC.

One critical component of the system is the clock distribution to the subdetector front-ends: this has to be done on the overall ILD detector with a precision better than 10 ps to enable time-of-flight measurements. On the other hand the overall data flow requirements are moderate. They have not



Figure 6.33. The AIDA-2020 newly developed Trigger Logic Unit. Top: table top enclosure. Bottom: 19-inch rack-mounted enclosure. The two enclosures have identical inner components and provide the same functionalities.

changed significantly compared to the estimates reported in [DBD], and correspond to a raw data rate of $O(100\text{MB})/\text{train}$ for a storage data size of $O(10\text{PB})/\text{year}$. The data flow is dominated by high granularity detectors exposed to high beam background close to the beampipe (Vertex and Beamcal). If needed it could be further reduced by local partial event processing ahead of the event building.

6.3.2 DAQ R&D

The front-end processing has benefited from the development of subdetector technological prototypes including final readout front-end components as reported in section 5.2. ASIC and FPGA boards with the required ILD specifications are now available for most subdetectors.

A number of common DAQ aspects relevant for the final ILD central DAQ have been developed [54] within the AIDA-2020 programme. They include both hardware and software components which have been used for different detectors or combinations of detectors in beam tests involving not only ILD prototypes but also detectors developed for the HL-LHC.

The core hardware component of the central DAQ system, the Trigger Logic Unit (TLU), provides a common interface for synchronisation and control of subdetectors. A new TLU has been developed to distribute signals to multiple detectors in beam tests. The AIDA-2020 TLU (Figure 6.33) has been extended over the previous version to be able to synchronise detectors with differing trigger and readout schemes, such as the CALICE calorimeters, pixel detectors and tracking devices, as well as being able to operate at a higher particle flux. Therefore, data from different detectors corresponding to the same particle in a test beam can be combined. The TLU is used extensively in test-beam facilities at CERN and DESY and will continue to do so thereby serving the needs of many detectors also beyond ILC R&D.

Within AIDA-2020 DAQ software packages have also been developed for both data collection and monitoring. The EUDAQ2 software is an extension of the EUDAQ software developed for the EUDET pixel beam telescope. It supports detectors with different trigger schemes and different readout speeds, enabling combined beam tests of very different detectors to be performed. The software has been tested and used in several beam tests so far, notably for the AHCal (also in conjunction with the CMS HGCAL), and for tracker modules of the ATLAS upgrade. The TLU is also fully integrated

into the EUDAQ2 framework. The monitoring software, DQM4HEP, originally developed for the SDHCAL, has been used for data quality monitoring and slow control monitoring. This software is a generic development which has extendibility built in and so can be used to monitor data from any detector in any format. It has already been successfully used by the AHCAL+beam telescope and SDHCAL+SiW-ECAL combined beam tests.

These DAQ developments have allowed multiple detectors to be more easily integrated, sparing time for understanding technical aspects of the detector technologies and the physics performances. Further detector developments will also benefit from this. The work also informs our understanding of integration and DAQ issues for the final ILD.

Felix Sefkow, Henri Videau,
Karsten Buesser, Roman
Poeschl, Toshiaki Tauchi
3 pages

6.4 Mechanical structure and studies

The mechanical behaviour of the ILD components is crucial in two respects. On the one hand, the high-precision and hermeticity of the detector requires a precise relative adjustment of subdetector components within each other, with tight tolerances at the interfaces and boundaries. These aspects were studied by simulating static deformations of the components under gravity and other constraints. On the other hand large devices in Japan must obey strict rules as regards their behaviour in case of seismic events (see section 6.9). This was investigated by modelling the dynamic behaviour of components, including the computation of their "eigen modes" and their reaction to reference earthquake parameters from the foreseen ILC Kitakami site. Most of the attention has up to now been given to the calorimeter mechanical structure which governs the global stiffness of the ILD detector inside the coil. Some evaluations have also started for other subdetectors such as the TPC.

6.4.1 Calorimeter structure

As mentioned in section 5.1.2 two options of the hadronic calorimeter, so-called "Videau" and "TESLA", are under consideration. In both cases, the electromagnetic modules are fixed to the inner plates of the hadronic wheels with two rails parallel to the z direction. Two critical aspects are of particular importance for the calorimeters: the respect of the tolerances of the thin azimuthal clearance (2.5mm) between the electromagnetic modules, to avoid mutual contact and possible damage of the modules, and the flatness of the hadronic absorber plates which define the gaps in which the sensitive layers are introduced. The latter is particularly important for the SDHCAL instrumentation option since RPC's require a high level of flatness. Both Videau and TESLA mechanical options have been simulated in detail and the results provide input for further optimization of the layouts.

Videau simulations: The static behaviour of a full Videau calorimeter wheel was simulated with a shell model with ??? nodes. In order to save computing time, the electromagnetic modules were approximated by a 3D solid model. This simplification was validated separately by a comparison to a single module shell model simulation. The results are shown in Figure 6.34: the hadronic structure turns out to be very stiff with largest deformations of a fraction of a mm. This is due to the vertical flanges of the Videau modules which strongly rigidify the overall structure. The electromagnetic modules are also only slightly distorted: the largest deformation stays below 1mm and the azimuthal clearance between modules is reduced to 2.3 mm in the worst case, well within the required tolerances.

One advantage of the Videau layout is to avoid a projective dead zone at a polar angle of 90^0 , but the number of dead zones in z is 4 for the baseline number of 5 wheels. One question is whether

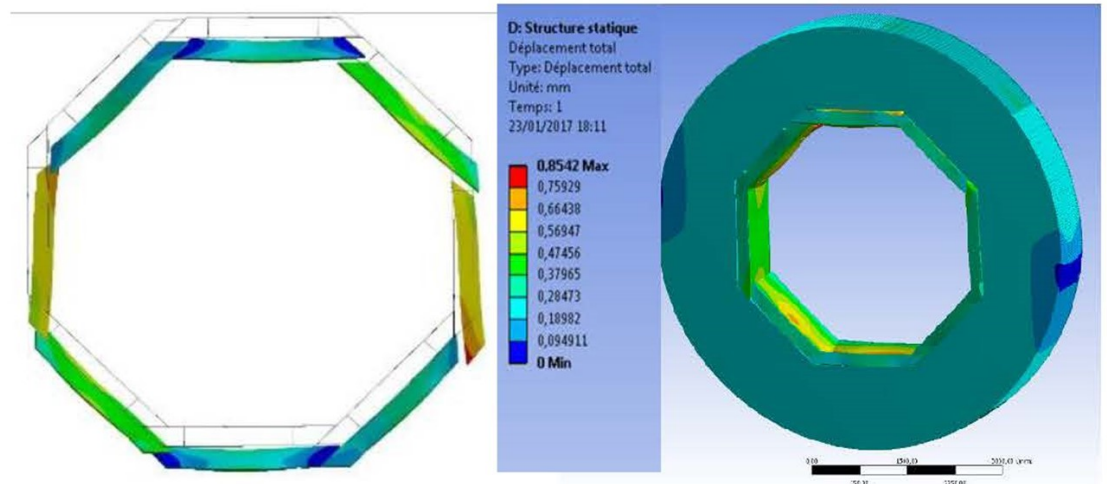


Figure 6.34. Static deformations of the calorimeter "Videau" structure (right) and zoom on the electromagnetic modules displacements with a magnification factor of ??? (left).

one could reduce this number of dead zones by reducing the number of wheels to 3. Mechanical simulations show that for 3 wheels it is possible to keep deformations at the boundary with the electromagnetic modules within specifications, provided the inner hadronic absorber plate thickness is slightly increased.

First dynamic simulations of the Videau structure were also performed with the computation of eigen modes. They show that the overall calorimeter barrel behaves as a rigid structure under oscillating accelerations, with little variation of the z distance between the wheels.

TESLA simulations: *Static and dynamic behaviour of TESLA structure
Comment on LLR-DESY crosscheck.*

6.4.2 Other subdetectors

If available, results on the mechanical behaviour of other subdetectors (e.g. TPC) are also welcome.

6.5 Coil and yoke studies

Karsten Buesser, Uwe Schneekloth
3 pages

A conceptual design of the ILD solenoid, the yoke and the cryostat has been developed for the ILD DBD, c.f. [55, 56]. Recently, studies have been done to optimise the engineering design of the magnet, to study the magnetic properties of the large and small ILD detector model, and to explore possible cost reductions.

6.5.1 Magnet Engineering Studies

A common study by KEK, Toshiba and Hitachi has been started to better understand the engineering challenges in the design and manufacturing of the ILD solenoid coil and the Anti-DID. Figure 6.35

shows a conceptual design of the manufacturing process. While the three solenoid modules and the Anti-DID coils would be fabricated in industry, transportation boundary conditions require the assembly of the complete magnet on or close to the final detector site. A case study by Toshiba

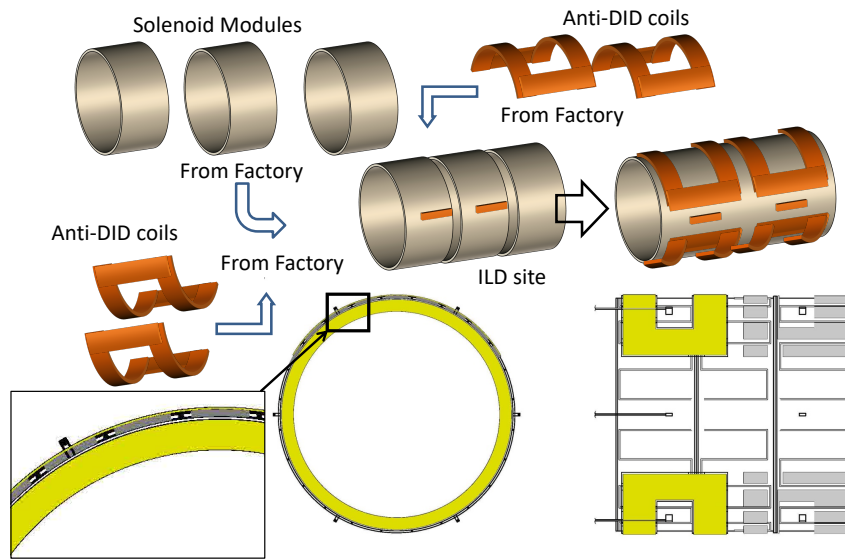


Figure 6.35. Conceptual manufacturing process of the ILD solenoid and the Anti-DID coils [?].

concluded that the main solenoid modules can be transported on street with the use of a specialised Jumbo Carrier while the modules of the Anti-DID would fit on a flatbed trailer (figure 6.36).

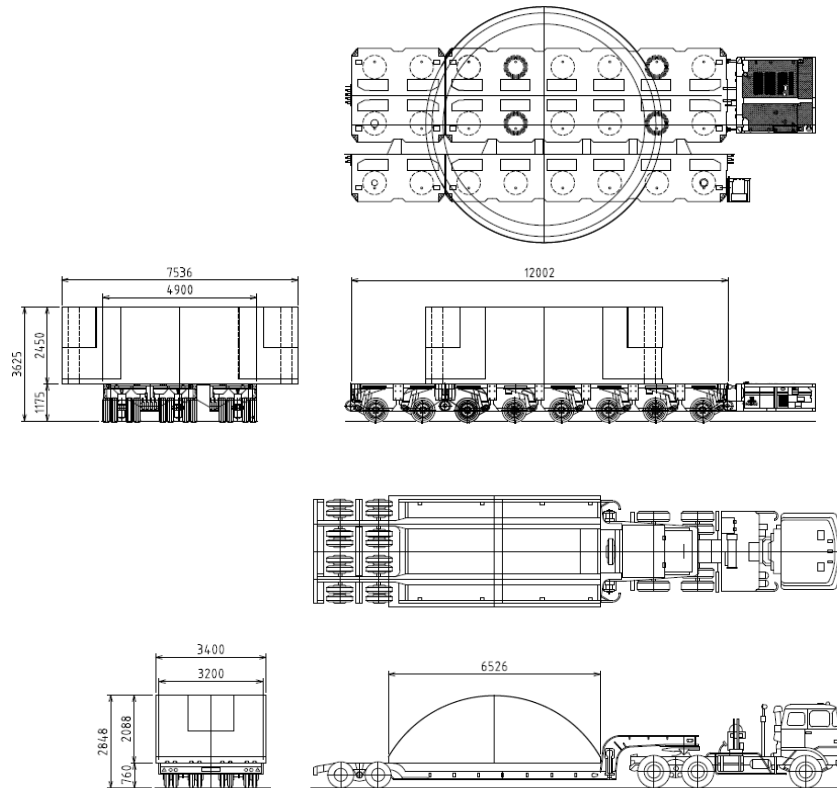


Figure 6.36. While a solenoid module requires transportation by a specialised Jumbo Carrier (top), the Anti-DID modules would fit on a low flatbed trailer (bottom) [?]

The so-called "Anti-DID" coil has been proposed to add a small additional dipole field to the solenoid for better suppression of backgrounds (c.f. section 6.6 and [57]). Figure 6.37 shows a

conceptual design of the Anti-DID coils and the resulting simulated dipole field with a maximum value of 0.036 T. Splitting the Anti-DID coils in four makes construction at the manufacturer and transport to the ILC site easier (c.f. figure 6.36). The Anti-DID coils could be fastened directly onto the outside of the solenoid shell, as also shown in figure 6.36.

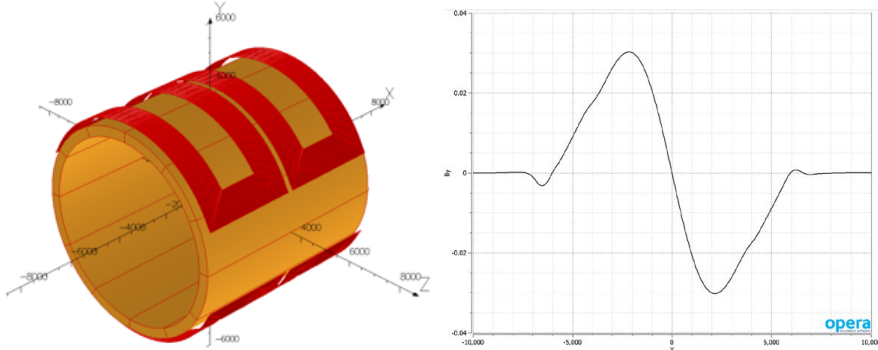


Figure 6.37. Conceptual design study of the Anti-DID coils (left) and simulated Anti-DID field (right) [58]

6.5.2 Field Optimisation Studies

The coil and yoke system should provide at the same time a high magnetic field in the central region and low stray field on the outside of the detector. The maximum nominal fields for the large (small) ILD detector model are 3.5T (4T). To allow for safety margins and possible extensions to higher field values, the coil design has been developed to reach 0.5T more in each case. Figure ?? therefore shows the field map and the field distribution for the large ILD detector model and a maximum field of 4T. The corresponding distributions for the small ILD detector model are shown in figure 6.39. The field maps are the result of 3D magnetic field simulations and are implemented in the physics simulations of the detector to allow for reconstruction conditions with maximum realism.

The ILD detector should share its experimental environment with another detector, e.g. SiD, in a push-pull scenario. This model of operations assumes that each detector could run its magnetic field but would still allow the other detector crew to work on their detector with the use of standard iron-based tools. Therefore a limit on the maximum magnetic stray fields has been agreed upon at a maximum of 5 mT at a distance of 15 m from the detector axis [9]. This requirement is the main driver for the thickness of the iron yoke of ILD. Figures 6.40 and 6.41 show the simulated stray fields for the large and the small detector model at 4 T and 4.5 T maximum central field. Simulations have been done with different codes and the results are very consistent with an average value for the large detector of 5.6 ± 0.6 mT for the maximum stray field at 15 m [59]. The stray fields for the small detector model are very similar.

The stringent limits on the stray fields are a cost driver for ILC as they drive the thickness of the iron return yoke. If the thickness would be reduced by 60 cm, the maximum stray fields at 15 m would increase to 9.3 ± 0.8 mT but at the same time reduce the cost for the yoke by about 15 MEUR for the large ILD detector model [59].

A further cost reduction of in total 44 MEUR can be reached if the iron yoke is reduced further to a thickness of 2.04 m (including gaps). The stray fields at 1 m distance from the outside of the yoke would be at the level of 100 mT which is acceptable for the operation of magnetically sensitive equipment and which is well below limits given by human safety regulations. The far stray fields in direction of the other detector need to be shielded in that case, e.g. by using a magnetic shielding wall. Figure 6.42 shows the simulation of the large ILD detector model magnetic fields with a reduced yoke and a shielding wall.

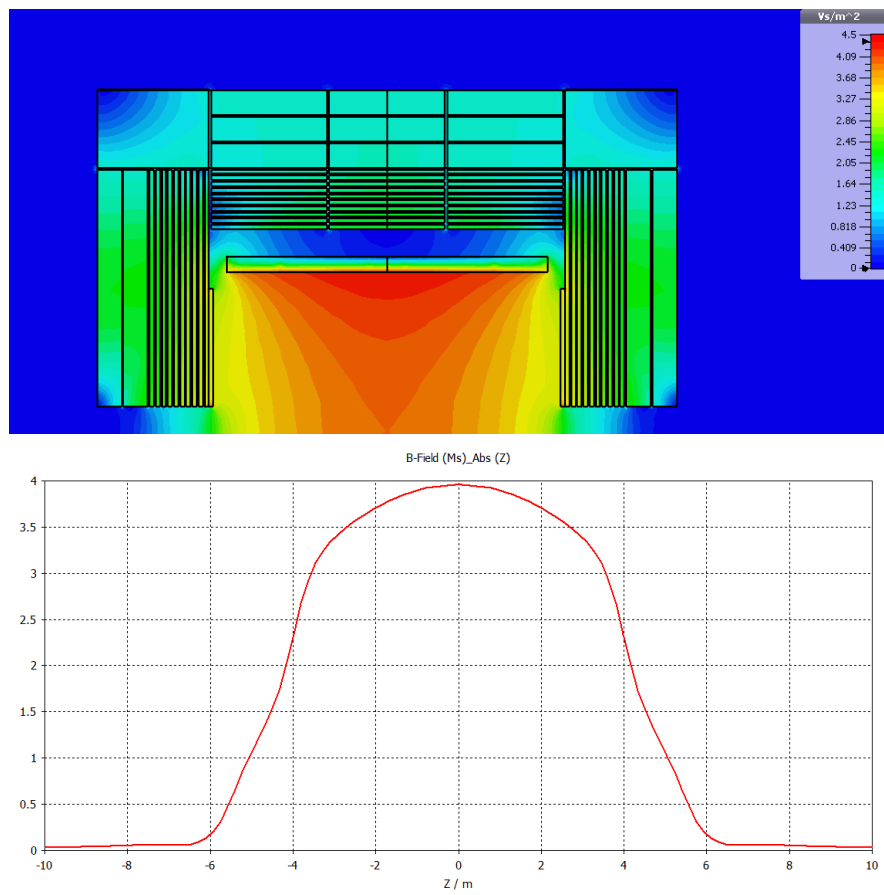


Figure 6.38. Field map of the ILD solenoid for the large ILD model with a maximum field of 4 T (top) and field distribution along the detector axis (bottom) [59]

Though this concept looks attractive, further studies are required. The shielding wall needs to be mobile and has to follow the push-pull movements. An engineering solution needs to be developed. Another problem is the radiation shielding. In the present design, the thick iron yoke serves as a radiation shield and allows for access to the outer side of the detector while the ILC delivers beams to the interaction region [60]. A reduced yoke might be too thin to serve for this purpose alone and additional radiation shielding, e.g. made from concrete, might need to be added.

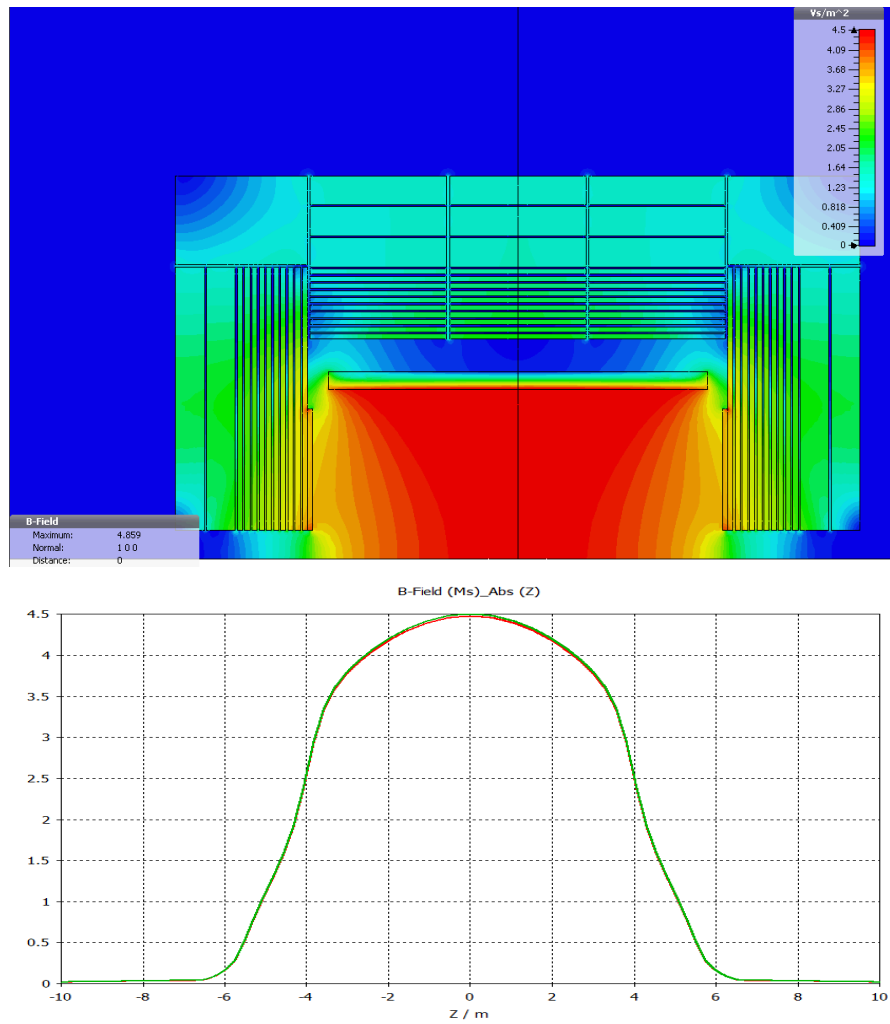


Figure 6.39. Field map of the ILD solenoid for the small ILD model with a maximum field of 4.5 T (top) and field distribution along the detector axis (bottom) [59]

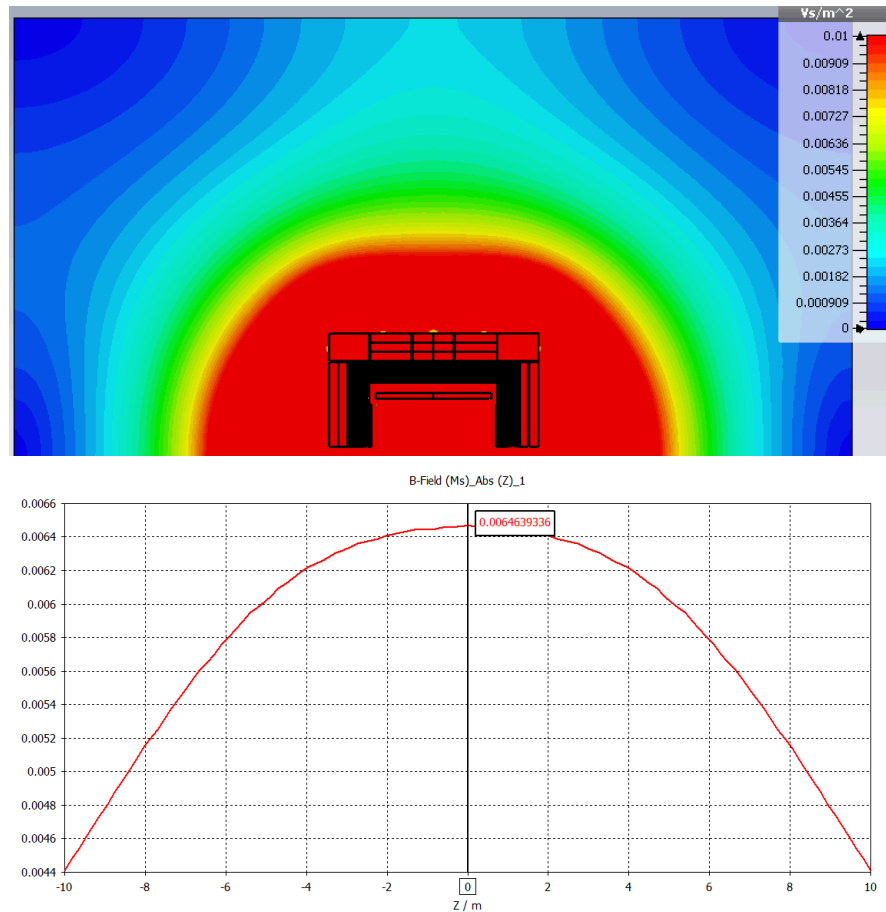


Figure 6.40. Map of the ILD solenoid strayfield for the large ILD model with a maximum central field of 4 T (top) and field distribution at a distance of 15 m parallel to the detector axis (bottom) [59].

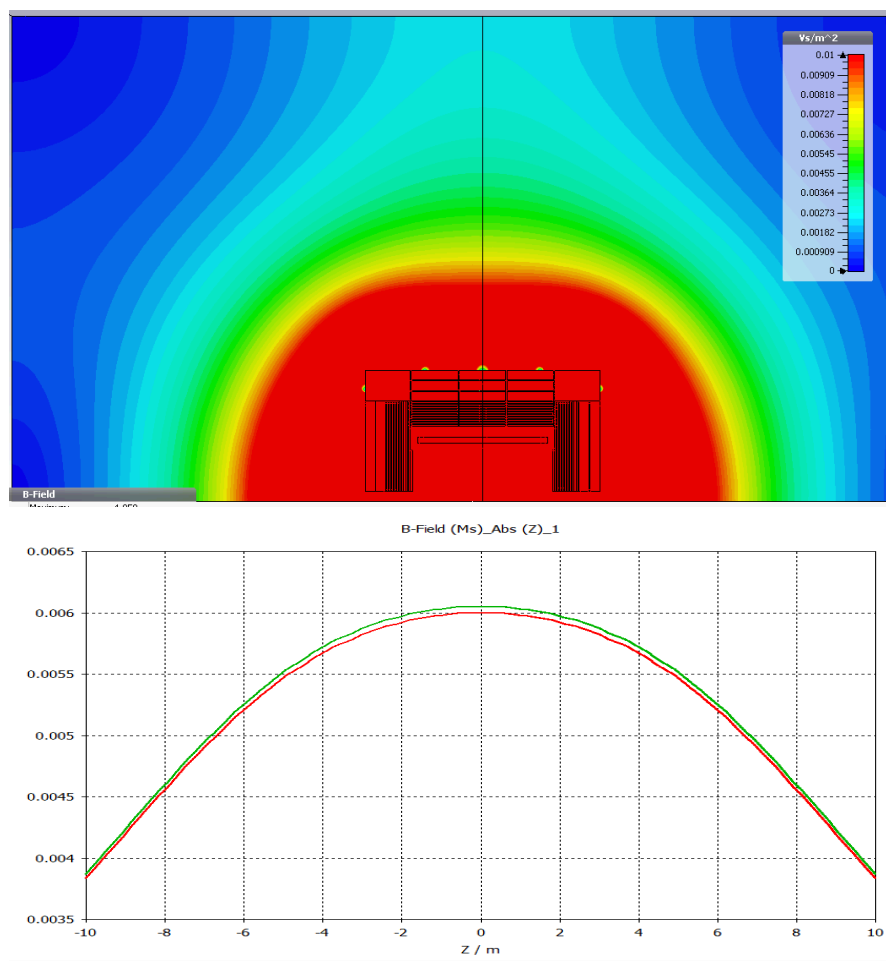


Figure 6.41. Field map of the ILD solenoid for the small ILD model with a maximum field of 4.5 T (top) and field distribution at a distance of 15 m parallel to the detector axis (bottom) [59].

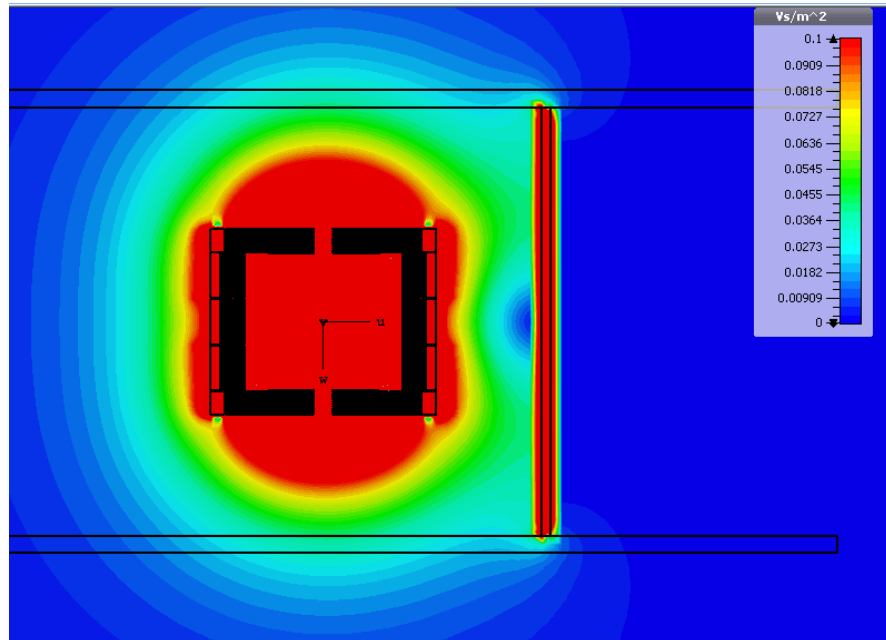


Figure 6.42. Field map of the ILD solenoid for the large ILD model with a iron shielding wall towards the direction of the other detector in the experimental hall [59].

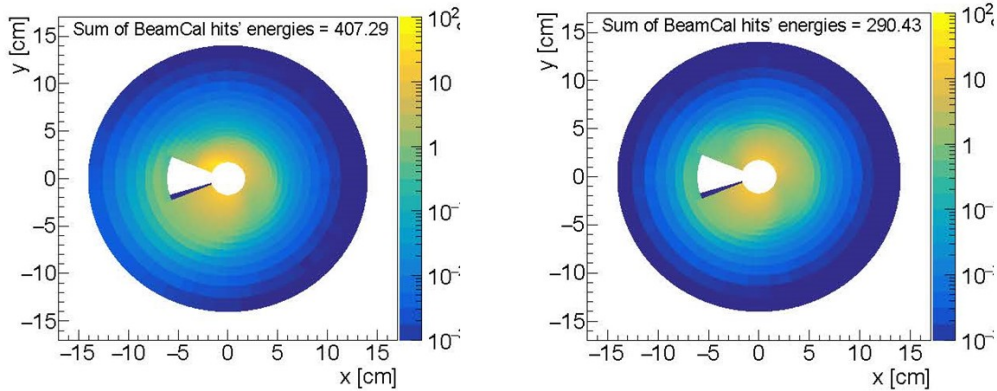


Figure 6.43. Beamstrahlung energy deposition in the BeamCal without (left) and with (right) anti-DID field for the large ILD version at ILC250.

Daniel Jeans, Yan Benhamou, Sergej Schuwalow,
 Claude Vallee
 2 pages

6.6 Beam background studies

The ILD detector response is affected by three main sources of beam-related background: beamstrahlung emitted at the crossing point of the electron and positron bunches, halo muons produced upstream of the detector along the beamline, and low energy neutrons back-scattered from the electron beam dumps. Their impact on the detector occupancies has been quantified and possible mitigation investigated. Results are similar for both options of the ILD detector and are shown here for the large version.

6.6.1 Beamstrahlung

Beamstrahlung consists in e^+e^- conversion pairs of the photons radiated in the crossing of the dense electron and positron bunches. Most of the low-energy pairs are confined close to the z axis by the large solenoid magnetic field but, due to the crossing angle between the colliding beams, a significant fraction hit the very forward detectors in the region between the incoming and outgoing beam pipes. The central detectors are also affected, both directly by the e^+e^- pairs, and indirectly through back-scattering of low-energy particles from the forward detectors. It was proposed to mitigate these effects by the addition of a small dipole field to the main solenoidal field. This so-called "anti-DID" field can be tuned to guide the e^+e^- pairs into the outgoing beampipe.

These effects have been quantified for the updated 250 GeV ILC conditions (ILC250, see chapter 3), using a full simulation of the beamstrahlung particle production and of their tracking within ILD. Special care has been taken to ensure stable results by adapting the GEANT tracking parameters to low energy particles within the beampipe. A realistic field map of both solenoid and anti-DID fields has been used. The response of the most affected detector, the BeamCal, is shown in Figure 6.43 with and without anti-DID. A positive effect of the anti-DID is clearly visible: when the anti-DID field is applied, the energy distribution is more symmetric around the central beampipe, and its overall amount is reduced by about 30%.

A similar improvement is seen for the central detectors in Figure 6.44. The most affected are the inner layers of the vertex detector, where the background is equally shared between direct hits rather

VXD 1	1402	\pm	778	914	\pm	364
VXD 2	971	\pm	558	545	\pm	207
VXD 3	151	\pm	77	129	\pm	60
VXD 4	111	\pm	59	107	\pm	53
VXD 5	44	\pm	30	40	\pm	26
VXD 6	39	\pm	27	34	\pm	24
FTD 1	42	\pm	30	38	\pm	26
FTD 2	27	\pm	19	24	\pm	15
FTD 3	62	\pm	45	40	\pm	27
FTD 4	42	\pm	33	25	\pm	17
FTD 5	29	\pm	23	18	\pm	13
FTD 6	16	\pm	13	9	\pm	7
FTD 7	10	\pm	8	6	\pm	5
SIT 1	51	\pm	37	24	\pm	16
SIT 2	49	\pm	36	21	\pm	12
SIT 3	77	\pm	56	34	\pm	24
SIT 4	71	\pm	54	31	\pm	21
SET 1	39	\pm	28	15	\pm	10
SET 2	46	\pm	36	18	\pm	12

Figure 6.44. Number of beamstrahlung hits per bunch crossing in the silicon trackers without (left) and with (right) anti-DID field for the large ILD version at ILC250. Give rates per cm^2 and transform figure into latex table.

uniformly distributed, and back-scattered particles showing hot spots in azimuth. Background hits further away from the beampipe are dominated by direct e^+e^- pairs. The anti-DID has a little effect on direct e^+e^- hits but efficiently suppresses back-scattered particles and associated hot spots in the central detectors. *Comment also on TPC hits.*

For the small ILD version, the overall beamstrahlung background hit rates are reduced by $\approx 10\%$ thanks to better confinement within the beampipe by the higher solenoid field of 4T.

Add info on beamstrahlung effects on beamcal reconstruction and on HCAL occupancy near beampipe

6.6.2 Halo muons

The electrons and positrons of the beam halo produce high-energy penetrating muons parallel to the beam by interacting with beamline components such as collimators. Five magnetized muon spoilers and one optional larger magnetized muon wall are foreseen to deviate these muons outside the ILC experimental hall. The resulting rate of muons in ILD has been simulated for ILC250 and ILC500 assuming a beam halo fraction of 10^{-3} (Chapter 3).

Figure 6.45 shows the energy spectra of the muons crossing the ILD detector for the two filtering options. The muon wall significantly reduces the flux of the lower energy muons below a few 10 GeV. At ILC500 the rate of halo muons crossing ILD is of the order of 4 (resp. 0.6) muons/BC without (resp. with) the optional muon wall. At ILC250 the corresponding numbers are of the order 1 and 0.03 muons/BC for the two filtering options, respectively.

These halo muons will affect the occupancy of the detector but should be easily identified and subtracted from the physics events using topological and timing information.

6.6.3 Backscattered neutrons from beam dumps

A potential additional source of beam-related background consists in particles back-scattered from the electron and positron beam dumps located 300m from the interaction point in both beam directions. This background is expected to be dominated by low energy neutrons which can propagate over a long distance. Their contribution has been fully simulated with FLUKA in the context of SiD, including a detailed description of the beamline up to the beam dump as well as of the dump system itself [ref]. The incoming neutron fluxes close to SiD are expected to be the same as for ILD and were

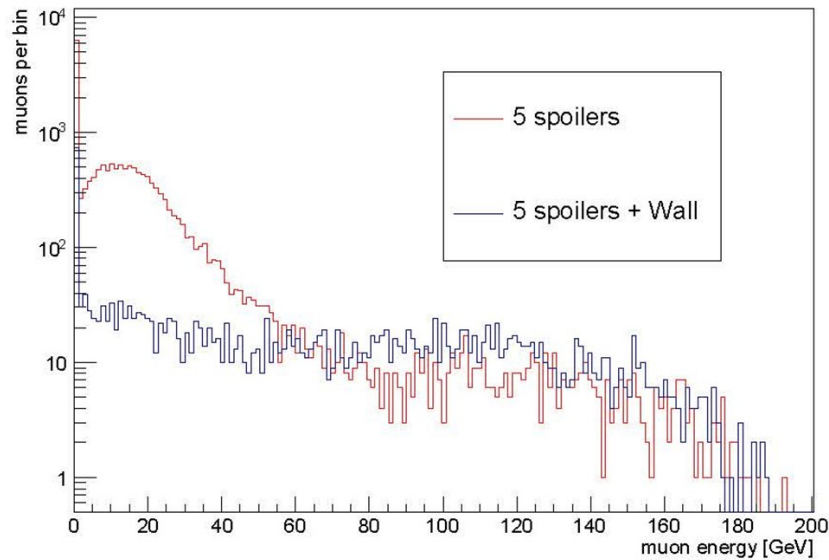


Figure 6.45. Energy spectrum of muons entering the ILC experimental hall for ILC500, normalized to a full single train of 2625 bunches assuming a beam halo fraction of 10^{-3} . Red curve: muon filtering with 5 spoilers only; Blue curve: muon filtering with an additional muon wall.

interfaced to the ILD detector simulation to estimate their impact in the detector. The simulation was normalized to the dump of one full electron bunch on the $+z$ side of the detector.

The total number of neutrons reaching the ILD detector region is found to be $O(10^6)$ per electron bunch dump. These neutrons have very low momenta of a few 10 MeV. Their propagation in ILD was simulated and the map of their stopping points in the detector is shown in Figure 6.46. The results are in line of what is found for SiD [ref]: most neutrons are absorbed in the external layers of the ILD iron yoke, with a very small fraction reaching the external layers of the very forward calorimeters. Their energy depositions concentrate close to their stopping points: they are very small (≈ 0.1 MIP in average) and asynchronous with respect to the bunch crossings. No visible signal is seen in the ILD vertex detector and central tracker. This indicates that the neutron background should not be a critical issue within its current state of understanding.

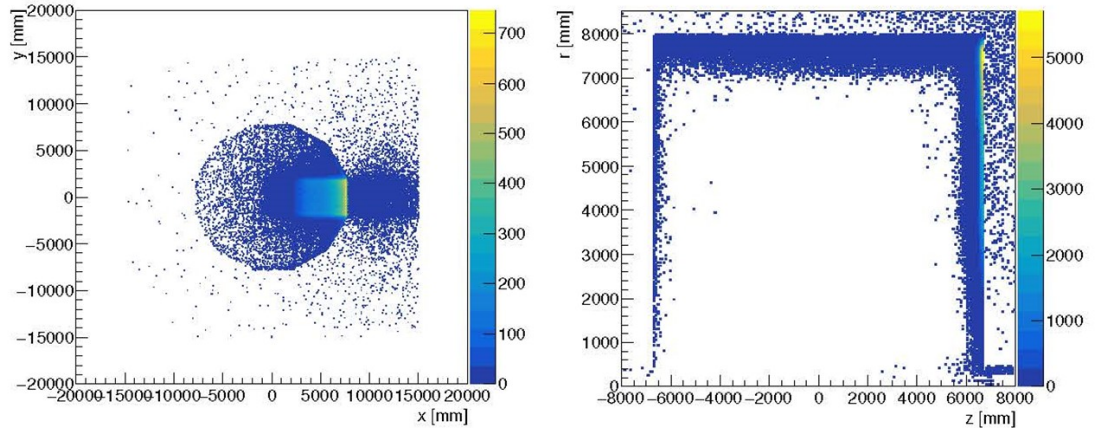


Figure 6.46. Map of the stopping points in ILD of neutrons back-scattered from the beamdump: transverse coordinates (left) and longitudinal coordinates (right). The map is normalized to the dump of one electron bunch on the $+z$ side of ILD.

Graham Wilson, Ties Behnke
1 pages

6.7 Alignment/ calibration procedures

There was little progress here since the LOI/DBD. Most of the corresponding text of these documents could be recovered and summarized for the IDR, taking into account the latest considerations about in-situ calibration with particles/collisions and subdetector requirements.

6.8 Earthquake Safety

Japan is one of most seismically active regions in the world. The proposed site for the ILC in the Kitakami mountains of northern Honshu has been especially selected putting emphasis on benign seismic conditions. Earthquake history has been taken into account as well as recent surveys on active tectonic faults. Nevertheless, earthquakes can occur and need to be taken into account. Figure 6.47 shows all earthquakes that were detected during 30 days in winter 2019/2019 in northern Honshu. The ILD interaction region is in the region around (39N, 141,2E).

6.8.1 Structural Design

Emphasis has been put on the design of the ILD detector with respect to earthquake safety in view of operability of the detector as well as disaster prevention. General rules are provided by the ISO3010 standard: "Bases for design of structures – seismic actions on structures". The ISO standard states two basic principles:

- The structure should not collapse nor experience other similar forms of structural failure due to severe earthquake ground motions that could occur at the site (ultimate limit state: ULS).
- The structure should withstand moderate earthquake ground motions which may be expected to occur at the site during the service life of the structure with damage within accepted

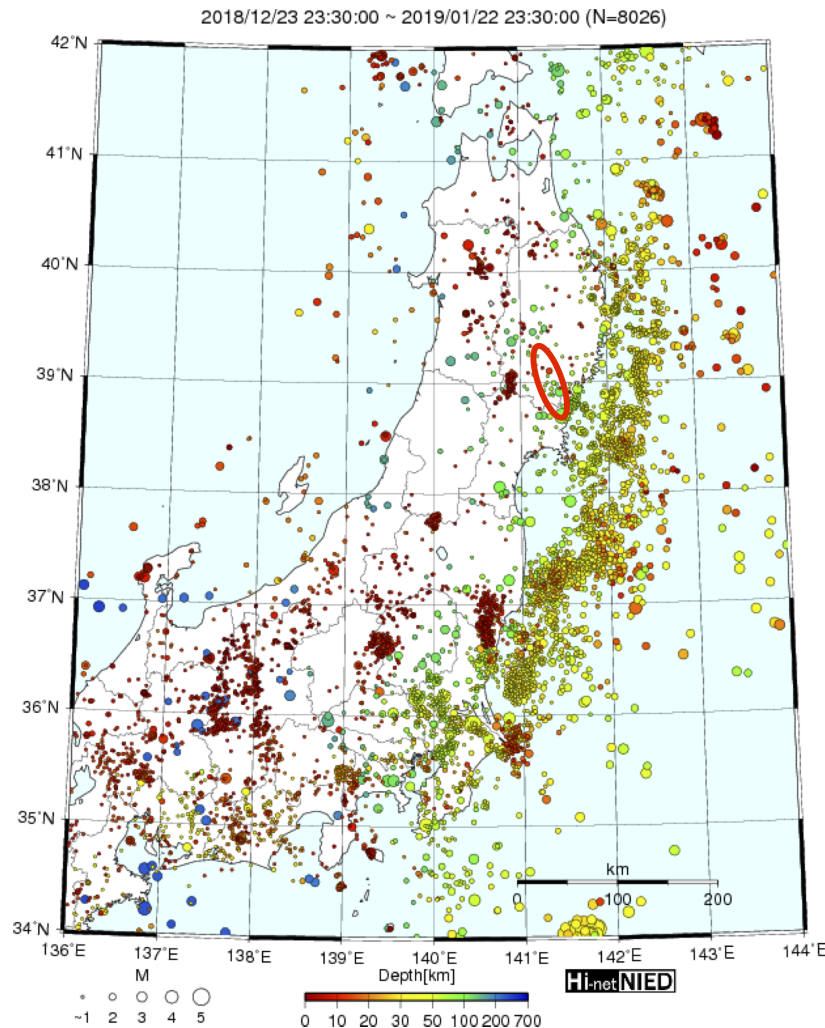


Figure 6.47. Map of northern Honshu with all detected earthquakes between 23rd December 2018 and 23rd January 2019 (30 days) [61]. The ILC interaction region is close to coordinates (39N, 141.2E)

limits(serviceability limit state: SLS).

The design seismic forces on mechanical structures can be determined by taking into account normalised design response spectra, weighted with load factors that take into account the respective state, ULS or SLS, local conditions and structural factors. In addition, required degrees of reliability of the structures can be taken into account.

An acceleration response spectrum for the SLS state at the Kitakami site is shown in figure 6.48 for structures with different damping behaviours. In the ULS state, the accelerations are assumed to be larger by about a factor of two. These type of standard spectra serve as input for the structural studies described in section 6.4.

6.8.2 Seismic Isolation

Seismic isolation could be an attractive solution to mitigate the risk of earthquake induced accidents. Base isolation systems are in use in many cases in seismic active countries like Japan, under buildings, bridges and other critical infrastructure. A recent study has explored the possibility to install seismic damping systems underneath the ILD detector, e.g. under the detector platform [63]. Standard isolation systems consist of rubber bearings in combination with oil dampers. Figure 6.49 shows that accelerations acting on the ILD detector could be damped by a factor of ≈ 35 in case of a

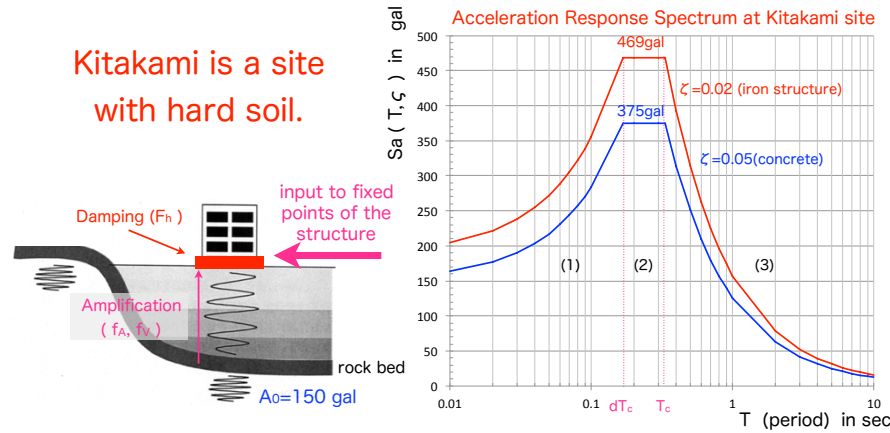


Figure 6.48. Standard response spectra for earthquakes in Kitakami (hard soil) for structures with different damping behaviour [62]. A maximum acceleration of 150 gal for an earthquake with a recurrence frequency of 100 years has been assumed.

catastrophic earthquake. At the same time, such a system unfortunately increases the displacements of the detector in case of seismic microtremors that occur frequently in Japan, also at the Kitakami site (c.f. figure 6.50). An extended system that adds a rigid sliding bearing could mitigate the problem. Here, friction keeps the detector coupled to the ground at lower acceleration forces. Figure 6.50 shows that no amplification of microtremors happens in that case. At the same time, the damping behaviour in case of major earthquakes is still in the order of a factor of ≈ 22 better than without base isolation figure 6.49. A seismic base isolation system underneath the detector platform could

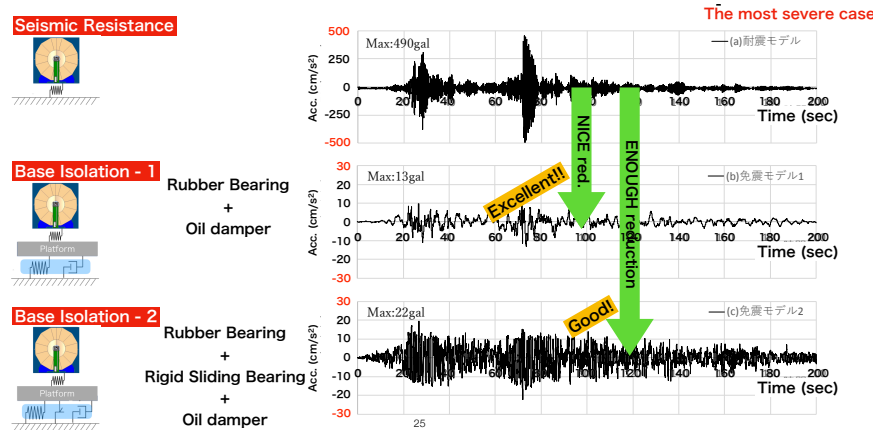


Figure 6.49. Simulated accelerations on the ILD detector in case of a catastrophic earthquake without base isolation (top) with an rubber bearing/oil damper system (middle) and with an additional rigid sliding bearing (bottom). Acceleration spectra from the 2011 Tohoku earthquake have been used as a case study for a most severe case [63].

mitigate seismic risks for the ILD detector. However, earthquakes could occur when the detector is still under construction or has been opened and moved partially away from the platform. Systematic risk evaluations and the development of mitigation strategies for the full lifetime of ILD still need to be done.

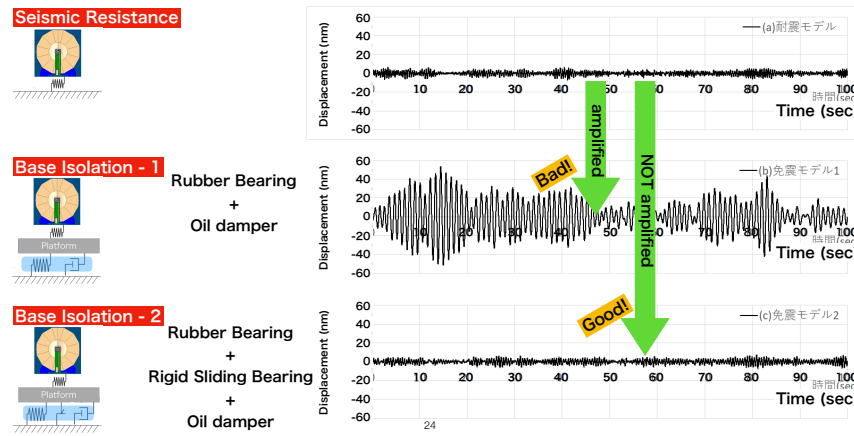


Figure 6.50. Simulated displacements of the ILD detector in case of microtremors without base isolation (top) with an rubber bearing/oil damper system (middle) and with an additional rigid sliding bearing (bottom) [63].

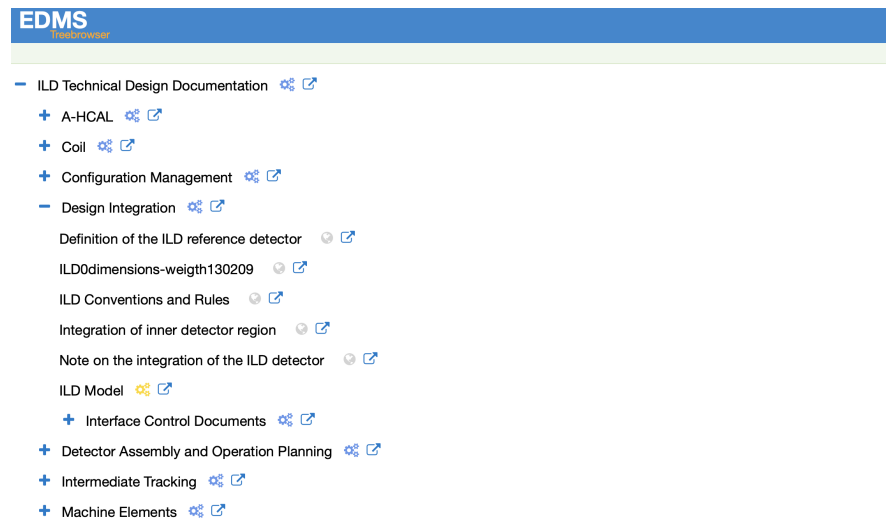


Figure 6.51. Part of the treebrowser of the ILD technical documentation Work Breakdown Structure in the ILC Engineering Data Management System. The top level node "Design Integration" is shown expanded.

6.9 Technical Documentation

The technical description of the ILD detector concept comprises specification and design documents as well as 3d engineering models, interface descriptions and drawings. All these documents that form the backbone of the ILD technical documentation are stored in the ILC Engineering Data Management System ILC-EDMS [64]. As this powerful system is made for experts and requires appropriate attention, an easy accessible frontend ("EDMSdirect") has been made available. The ILD technical documentation is organised in a Work Breakdown Structure (WBS) that is mapped on a tree browser that can be accessed on the web [65]. Figure 6.51 shows the tree browser for the ILD technical documentation. All WBS top nodes can be expanded by clicking on them. In the figure, this has been done for the node "Design Integration".

Figure 6.52 shows the document browser that opens for the documents stored in the EDMSdirect system. Shown here is the "Conventions and Rules" document that belongs to the previous mentioned WBS node "Design Integration". A preview of the document is shown in the document browser. The document browser allows for preview of the respective documents as well as downloads of pdf or source files, depending on the authorisation of the users. Documents can be made worldwide visible as well as protected for selected users.

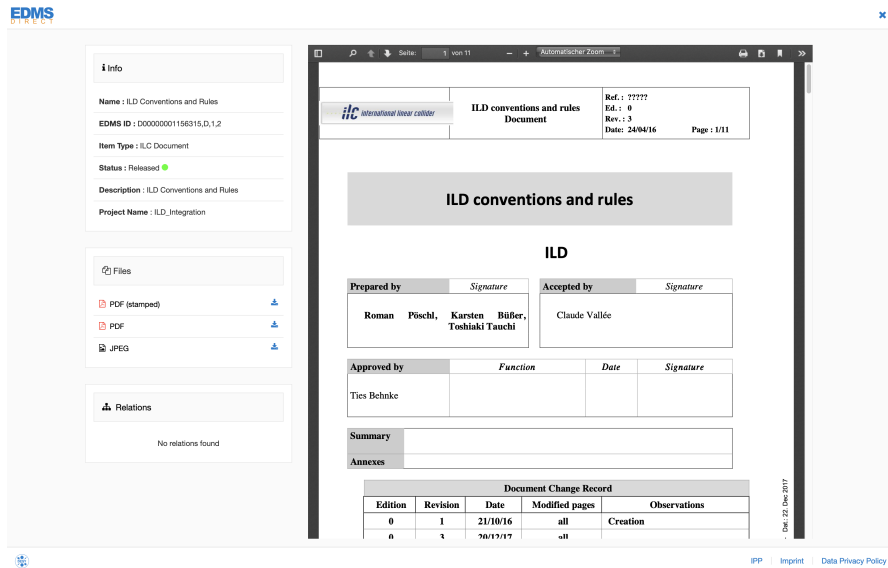


Figure 6.52. Example document (here: "ILD Conventions and Rules") in the document browser of EDMSdirect.

6.9.1 Interface Control Documents

The technical integration of the ILD detector is based on a set of Interface Control Documents which describe the interfaces of each subdetector to its environment:

- Mechanical Interface
 - Local coordinate system
 - Mechanical concept
 - Critical dimensions
 - Weights
 - Positioning and alignment constraints
- Electrical Interface
 - Block and connection diagrams
 - List of connectors
 - Cabling and connection sheets
 - Grounding circuits
 - Power consumption
- Gas and Liquid Interfaces
- Thermal Interfaces
- Test Interfaces

The Interface Control Documents are living documents that are updated as the design and understanding of the subdetector technologies advance. All documents are stored in EDMS [64] and are accessible via the treebrowser of the ILD technical documentation [65].

A dedicated document describes the ILD Conventions and Rules (c.f. figure 6.52). It contains a definition of the global ILD coordinate system, unit conventions, naming and numbering conventions as well as mechanical, electrical and cooling constraints and rules. This document is also available on [65].

The interface descriptions together with the conventions and rules contain the information that has been used in creating the integrated model of the ILD detector.

7 Physics and Detector M

F.Gaede, A.Miyamoto
4 pages

Accurate and detailed modelling of the physics interactions as well as the detector response are crucial for making realistic predictions about the expected physics and detector performance. The ILD software for detector simulation, reconstruction and analysis is entirely based on the common linear collider software ecosystem called *iLCSoft* [66]. It will be described in more detail in the next sections.

7.1 Modelling of ILC Conditions and Physics Processes

Large, realistic Monte Carlo samples with the full Standard Model physics ($E_{cms} = 500$ GeV) as well as various BSM scenarios have been created for the purpose of detector optimization and performance evaluation as presented in chapter 8. The input samples for the full detector simulation are created with the Whizard [67] event generator. Whizard uses tree-level matrix elements and loop corrections to generate events with the final state partons and leptons based on a realistic beam energy spectrum, the so called *hard sub-process*. The hadronization into the visible final state is performed with Pythia [68] tuned to describe the LEP data. The beam energy input spectrum is created with Guinea-Pig [69], a dedicated simulation program for computing beam-beam interactions at linear colliders. The two main effects of the strong beam-beam interactions are the energy loss due to beamstrahlung leading to the available luminosity spectrum (see Fig 7.1) and the creation of incoherent e^+e^- -pairs that are the source of the dominating background at the ILC. These electrons and positrons are predominantly created in a forward cone as shown in Fig 7.1. It is this cone that restricts the minimal allowed radius of the innermost layer of the vertex detector. Another source of background at the ILC are $\gamma\gamma \rightarrow \text{hadrons}$ events, due to beamstrahlung photons. These type of events are generated for $\gamma\gamma$

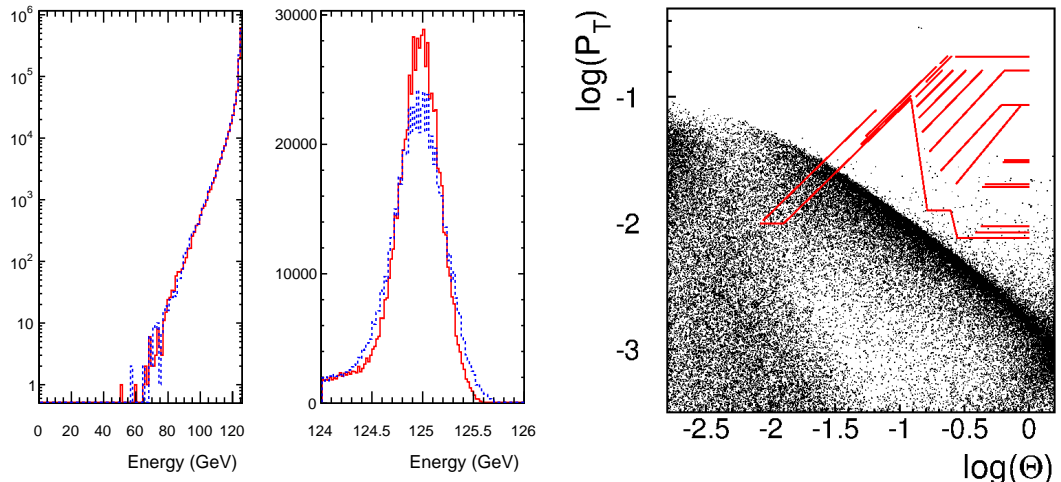


Figure 7.1. Left: Beam energy spectra for $\sqrt{s} = 250$ GeV Set-A, created with GuineaPig (blue-dashed: e^- , red-solid e^+). Right: Cone of incoherent e^+e^- -pairs in the ILD detector. Shown is $\log(p_t)$, corresponding to the largest radial extend of the helical trajectory as a function of $\log\theta$. Also shown are the inner detector elements of the ILD detector (horizontal lines represent barrel elements and diagonal lines represent end-cap elements).

cms-energies from 300 MeV 2 GeV with a dedicated generator based on [70], whereas for higher energies Pythia is used. For the large Monte Carlo data sets both backgrounds are overlaid to the actual physics event that is simulated. For the incoherent pairs, only *reconstructable tracks*, i.e. those that leave at least three hits in the tracking detectors, are selected. $\gamma\gamma \rightarrow \text{hadrons}$ events are overlaid according to a Poisson-distribution with a total expectation value of $\lambda = 1.1$, resulting from the four different combinations of the photon virtuality (see table 7.1).

Table 7.1. Key parameters used in the overlay of $\gamma\gamma \rightarrow \text{hadron}$ background at $\sqrt{s} = 500$ GeV for the four different combinations of photon virtualities. W denotes a virtual photon and B a real photon.

process type	Vertex z offset (μm)	Vertex z sigma (μm)	expected events per BX
WW	0	196.8	0.211
WB	-42.22	186.0	0.246
BW	+42.22	186.0	0.244
BB	0	169.8	0.351

7.2 Detector Simulation

The main core software tools in iLCSoft used by ILD are the common event data model and persistency tool LCIO [71] and the C++ application framework Marlin [72] and the recently added generic detector description toolkit DD4hep [73, 74]. DD4hep provides a single source of information for describing the detector geometry, its materials and the readout properties of individual sub detectors. Various components of DD4hep provide different functionality. Here we use DDG4, the interface to full simulations with Geant4 [75] and DDRec the specialized view into the geometry needed for reconstruction.

7.2.1 ILD Simulation Models

For detector optimization studies two ILD simulation models: *ILD_I5_v02* (large) and *ILD_s5_v02* (small) with the dimensions described in tables 5.1 and 5.2, have been implemented using DD4hep and released in a dedicated software package: Icgeo [76]. A quadrant view of the large simulation model is shown in Fig. 7.2 together with a plot of simulated hits in the large and small detector

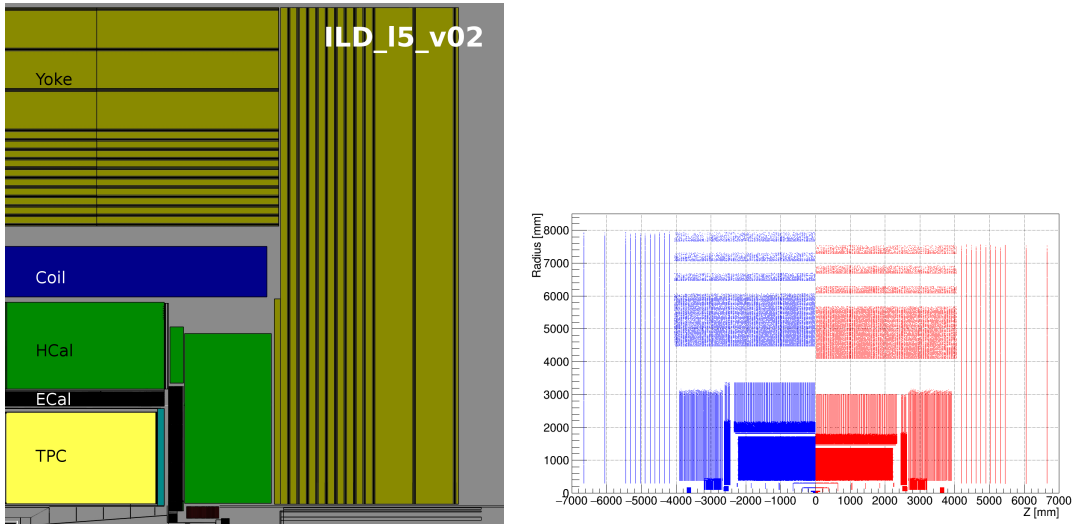


Figure 7.2. Left: Quadrant view of the (large) ILD simulation model. Not labeled in the figure are the inner silicon tracking detectors: VXD, SIT and FTD, the outer silicon tracker SET as well as the forward calorimeters LCal, LHCal and BeamCal. Right: Simulated hits in the large and small ILD simulation models in the rz -view.

model for comparison. The main difference between the two models are the reduced radii of the TPC, the barrels of Ecal, Hcal, Yoke and the Coil. All other detector dimensions including all material thicknesses have not been modified. Considerable effort has been invested into making the ILD simulation models as realistic as possible, in particular by

- following the exact dimensions and layout of detector elements from engineering models
- implementing correct material properties
- implementing precise descriptions of the actual detector technology
- adding realistic amounts of dead material from supports and services, such as cables and cooling pipes
- introducing realistic gaps and imperfections into the subdetectors

Care has been taken to include realistic material estimates in particular in the tracking region where the material budget has a direct impact on the detector performance. Fig. 7.3-left shows the material budget in the ILD tracking volume resulting from the individual tracking subdetectors including dead material and services. The spike at the edge of the tracking fiducial volume at $\theta \approx 5^\circ$ is due to the shallow crossing of cables routed along the conical part of the beam pipe. Fig. 7.3-right shows the material distribution in the inner tracking region close to the IP.

7.2.2 Hybrid Simulation

In order to be able to study and compare the different calorimeter technologies proposed for ILD (see chapter 5.2.5) *hybrid simulation* models have been implemented for the ILD simulation models, where two different readout technologies are implemented in the gaps of the sandwich absorber structure as shown in Fig. 7.4 (right). As the calorimeter shower development is almost entirely dominated by the absorber structure, this approach provides results that are equivalent to the stand alone simulation of each individual technology to better than 1%, as shown in Fig. 7.4 (left) for the longitudinal shower profile. Equivalent results have been obtained for other parameters, such as the total number of hits and the transverse shower profile. With this approach one can simulate a large set of Monte Carlo events for several calorimeter technologies using only little more CPU time than would be needed for simulating just one technology choice and at the same time one can compare different technologies with identical physics events.

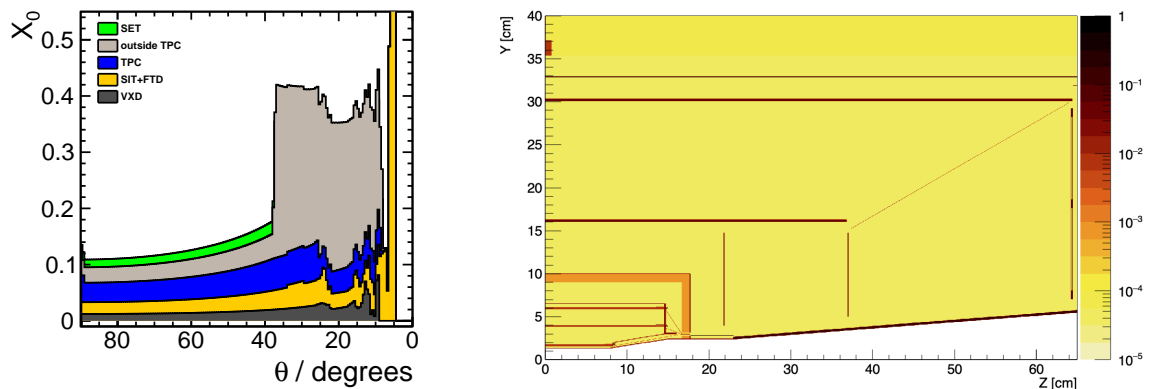
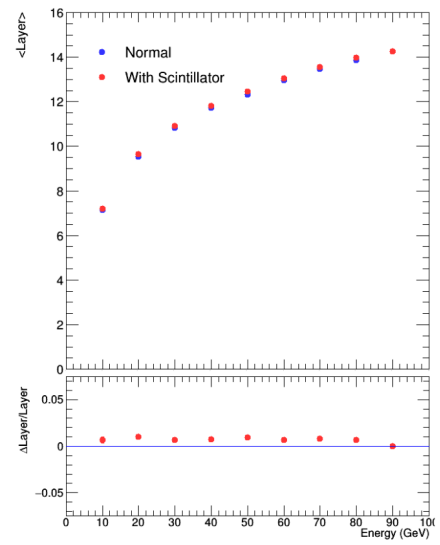
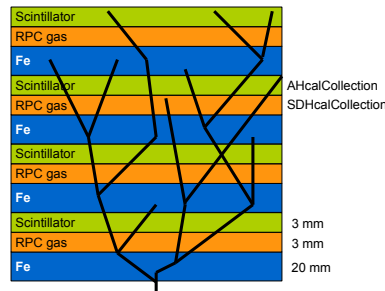


Figure 7.3. Left: Integrated radiation lengths of the tracking detectors in the ILD simulation models. Right: Material scan in inner tracking region of the simulation model (inverse X_0 in arbitrary units) showing detector components of the VXD, SIT and FTD as well as dead material from the beam pipe, support structures, cables and services.

Figure 7.4

Left: Schematic view of the *hybrid simulation* model for two different calorimeter technologies using scintillator and RPCs respectively. Right: Longitudinal shower profile for the individual simulation of the RPCs (*normal*) compared to the hybrid simulation (*with scintillator*).



7.3 Event Reconstruction

The detailed simulation with Geant4 provides hit objects with the exact amount and position of energy depositions in individual sensitive detector elements, such as silicon pixels or calorimeter cells. In the *Digitization* step all relevant effects from the detector technology and the readout electronics are applied to the simulated hits.

7.3.1 Digitization

For silicon strip-and pixel detectors as well as the ILD-TPC, the hit positions are smeared according to resolutions that have been established from test beam campaigns for the different sensor technologies, thereby including effects from charge sharing, clustering and position reconstruction. Table 7.2 shows the point resolution parameters used in the current ILD simulation models. In the TPC hit digitization,

Table 7.2. Effective point resolutions as used in the digitization of the ILD tracking detectors. The parameterization for the TPC takes into account geometric effects due to the direction of the track with respect to the pad row and has been established from test beam data.

Subdetector	Point Resolution	
VTX	$\sigma_{r\phi,z}$	= 3.0 μm (layers 1-6)
SIT	$\sigma_{r\phi,z}$	= 7.0 μm (layers 1-4)
SET	σ_{α_z}	= 7.0 μm (layers 1-2)
	α_z	= $\pm 7^\circ$ (angle with z-axis)
FTD	σ_r	= 3.0 μm (layers 1-2)
Pixel	$\sigma_{r\perp}$	= 3.0 μm
FTD	σ_{α_r}	= 7.0 μm (layers 3-7)
Strip	α_r	= $\pm 5^\circ$ (angle with radial direction)
TPC	$\sigma_{r\phi}^2$	= $(50^2 + 900^2 \sin^2 \phi + ((25^2/22) \times (4 \text{ T/B})^2 \sin \theta)(z/\text{cm})) \mu\text{m}^2$
	σ_z^2	= $(400^2 + 80^2 \times (z/\text{cm})) \mu\text{m}^2$
	where ϕ and θ are the azimuthal and polar angle of the track direction	

simulated hits that are closer than the established double-hit resolution of 2 mm in $r\phi$ and 5 mm in z are merged into one. For the silicon detectors this treatment is not necessary, due to the expected low occupancies. During the calorimeter digitization a two step calibration is applied for every calorimeter type and sampling structure. In a first step the hits are calibrated to a MIP signal and in a second step, the total energy is calibrated to an absolute value of the cell energy in GeV. This calibration is an iterative procedure, based on the application of the full *particle flow algorithm* to single particle events with γ and K^0 and thereby repeatedly adjusting the calibration constants. For scintillating calorimeters Birk's Law, resulting in different light yields for different particles, is already applied during the simulation. Dedicated digitizers take into account effects of non-uniformity of the light yield for scintillators as well as cross-talk between neighboring channels.

7.3.2 Track reconstruction

The ILD track reconstruction is described in more detail in [77]. The *pattern recognition* step is carried out independently in three regions:

- inner Si-trackers VXD and SIT (and partly FTD)
brute-force triplet seeding followed by a road search using extrapolations to the next layer
- forward Si-tracker: FTD
a Cellular-Automaton finding many track candidates; reduced to a unique and consistent set

through the use of a Hopfield Network.

- the TPC
topological clustering in the outer TPC pad row layers for seeding, followed by a Kalman-Filter based road search inwards

In a final step the track candidates and segments are combined into a unique set and then, after assignment of left-over hits, a final refit is performed with a Kalman filter. The correct reconstruction of the kinematics of charged particles requires a sufficiently detailed description of the material the particles have traversed, in order to correctly account for effects of energy-loss and multiple-scattering in the fit. The DD4hep component DDRec provides dedicated surface classes for track reconstruction and fitting. These surface classes provide the geometric information of the corresponding measurement surfaces as well as material properties, averaged automatically from the detailed model. Surfaces are also used to account for effects from dead material layers, such as support structures or cables and services. Fig. 7.5 shows the tracking surfaces used for the inner tracking detectors of ILD.

7.3.3 Particle Flow

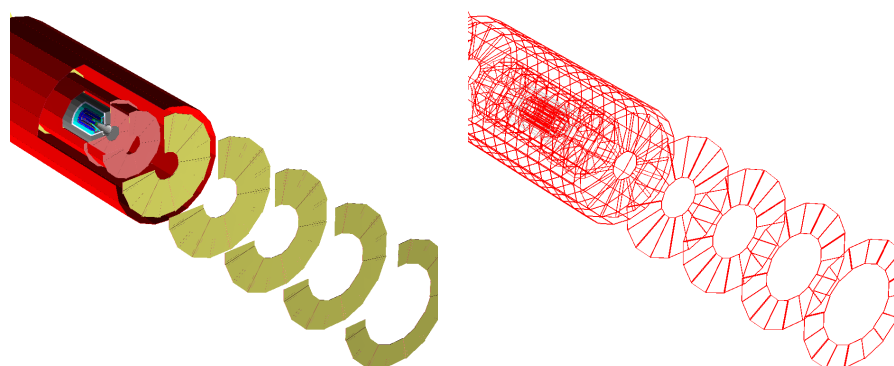
After the reconstruction of charged particle tracks the *particle flow algorithm* (PFA) is applied to reconstruct particle showers in the calorimeters. PFA aims at reconstructing every individual particle created in the event in order to take the best available measurement for the given type, i.e.:

- charged particles
using the momentum measured in the tracking detectors with the excellent resolution described in sec. 8.1
- photons
measured in the Ecal with an energy resolution of $\sigma(E)/E \sim 17\%/\sqrt{(E/\text{GeV})}$
- neutral hadrons
measured predominantly in the Hcal¹ with an energy resolution of $\sigma(E)/E \sim 50\%/\sqrt{(E/\text{GeV})}$

The best jet energy measurement in hadronic events would be achieved if the above algorithm would work perfectly. However in reality there is always confusion in the assignment of individual *CalorimeterHits* to Clusters and showers as well as in the assignment of tracks to clusters. The best PFA implementation to date is PandoraPFA [78], which is available in iLCSoft and used by ILD. The input to PandoraPFA are the reconstructed tracks, candidates for kinks and V0s as well as all digitized calorimeter hits. A number of sophisticated clustering algorithms are applied in an iterative way, thereby optimizing the track-cluster matching based on the momentum-energy consistency.

¹hadronic showers often start in the Ecal and might extend into the Muon system - this is taken into account in PandorPFA

Figure 7.5
Left: Inner tracking detectors in the ILD simulation model.
Right: Surfaces used for track reconstruction, attached to the volumes of the simulation model.



7.3.4 High Level Reconstruction

After having reconstructed all the individual particles in the event, the next step in the processing is the reconstruction of primary and secondary vertices. This is carried out in iLCSoft with the LCFIPlus [79] package. The primary vertex of the event is found in a tear-down procedure taking into account constraints from the expected beam spot ($\sigma_x = 516 \text{ nm}$, $\sigma_y = 7.7 \text{ nm}$, $\sigma_z \sim 200 \mu\text{m}$ at $E_{\text{cms}} = 250 \text{ GeV}$). In a second step LCFIPlus tries to identify secondary vertices, applying suitable requirements for invariant masses, momentum directions and χ^2 's. Secondary vertices and optionally isolated Leptons can be used by LCFIPlus for jet clustering, aiming at high efficiency for correctly identifying heavy flavor jets. The actual jet clustering is then performed by using a cone-based clustering with a Durham-like algorithm. Alternatively users can use k_T jet clustering algorithms from the Fastjet [80] that is interfaced to Marlin in a dedicated package MarlinFastJet. LCFIPlus also provides algorithms for jet flavor tagging using boosted decision trees (BDTs) based on suitable variables from tracks and vertices. A palette of additional high level reconstruction algorithms is used for physics analyses:

- particle identification using dE/dx , shower shapes and multi-variate methods
- $\gamma\gamma$ -finders for the identification of π^0 's and η 's
- reconstructed particle to Monte-Carlo truth linker for cross checking analysis and reconstruction efficiencies
- tools for jet clustering using Monte-Carlo truth information
- processors for the computation of various event shapes

7.4 Monte Carlo Production on the Grid

The linear collider community uses the ILCDirac [81] toolkit for large scale Monte Carlo production on the Grid. ILCDirac is highly configurable and ILD uses a dedicated production chain [82], a schematic view of which is shown in Fig. 7.6. The Monte Carlo production is split into four main steps:

- GenSplit
Split generator file to many files with small number of event files so that simulation and reconstruction jobs complete in adequate CPU time and produce a manageable size of output files. This has the advantage that the same input files can also be used for fast simulation programs such as SGV [83].
- Simulation
Simulation of the detector response to the generated particles in the events using ddsim, a python application using the Geant4 gateway DDG4 with the detailed detector simulation model.
- Reconstruction
Full event reconstruction with the algorithms described in sec. 7.3, writing out detailed *REC*-files with all available information, including digitized hits and a much reduced *DST*-file format.
- Merging of DST files
The rather small DST-files are merged into larger files for easier handling.

In order to investigate the effect reducing the detector dimensions on the physics performance, two large Monte Carlo data sets for the large and small ILD simulation models have been produced. The produced data sets correspond roughly to 500 fb^{-1} at $E_{\text{cms}} = 500 \text{ GeV}$ with the exact numbers of events processed for the different classes shown in table ??.

Table 7.3. Number of Monte Carlo events produced for the different event classes. About same number of events were produced for the large and the small ILD simulation model. Sum of two models are shown in the table.

event class	description	events processed
2f	two fermion final states	60.0×10^6
4f	four fermion final states	22.6×10^6
5f	five fermion final states	4.01×10^6
6f	six fermion final states	13.8×10^6
aa_4f	two fermion by $\gamma\gamma$ interaction	1.63×10^6
higgs	higgs process	3.97×10^6
np	new physics process	3.25×10^6
aa_lowpt	$\gamma\gamma \rightarrow \text{hadrons}$ background	2.50×10^6
seeablepairs	$e^+ e^-$ -pair background	1.00×10^5 BXs
calibration	single particle, $q\bar{q}$ events	27.71×10^6
6f(WW)	dedicated 6f sample at $E_{cms} = 1$ TeV	1.75×10^6

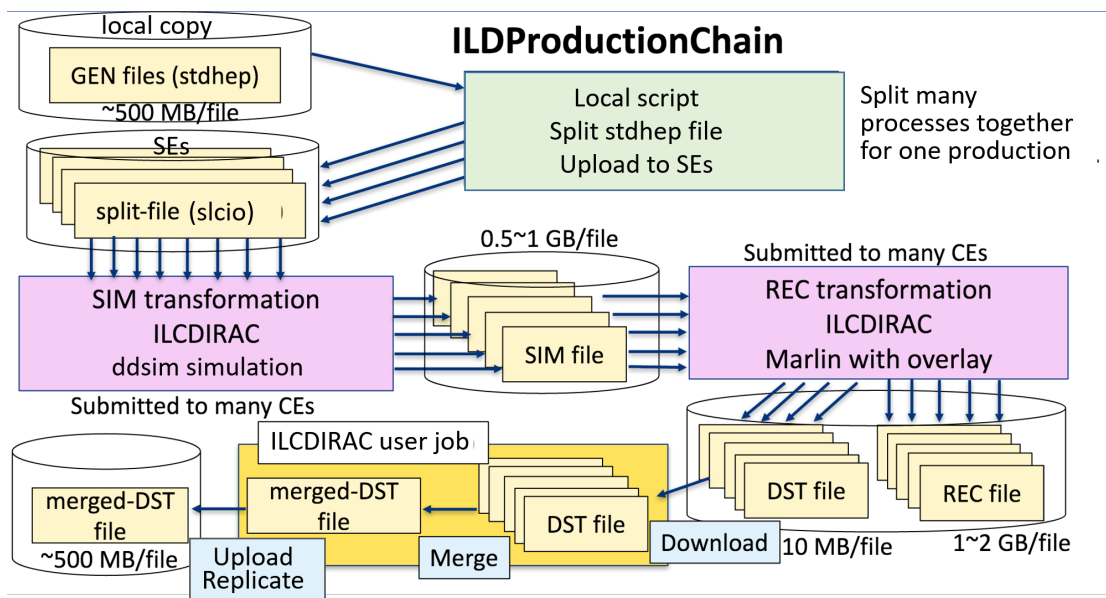


Figure 7.6. Schematic view of the Monte Carlo production system used for ILD.

8 Detector and Physics Performance

The overall performance of the ILD detector is a combination of the excellent resolutions and efficiencies of the individual sub-detectors and the sophisticated reconstruction and analysis algorithms described in the previous chapter. Here we review this performance, beginning with the pure system performance that is achieved from reconstructing individual long lived particles, followed by the high-level reconstruction of jets and physics objects, ending with selected detector physics benchmarks. Where applicable this performance is presented for the large (ILD-L) and the small (ILD-S) detector model.

Frank Gaede

5 pages

8.1 System performance

8.1.1 Tracking

The efficient identification and precise reconstruction of charged particle tracks is crucial for the overall physics performance of the ILD detector. The goal for the asymptotic momentum resolution [84] is

$$\sigma_{1/p_T} \approx 2 \times 10^{-5} \text{ GeV}^{-1}.$$

ensuring that the Higgs mass measurement from $e^+e^- \rightarrow H, Z \rightarrow \mu^-\mu^+$ events is dominated by the beam energy spread rather than the detector resolution.

To evaluate the tracking resolution of the ILD detector models, samples of single μ -events at fixed momenta ($p=1,3,5,10,15,30,100 \text{ GeV}$) and polar angles ($\theta = 10, 20, 40, 85^\circ$) have been run through the full simulation and reconstruction as described in sections 7.2 and 7.3 with the single point resolutions given in table 7.2. Fig. 8.1 shows the results for the inverse transverse momentum resolution σ_{1/p_T} and the impact parameter resolutions σ_{d0} and σ_{Z0} in the $r\phi$ -plane and along the z -axis respectively for the large and small detector models ILD-L and ILD-S. The performance goal for the asymptotic momentum resolution is met by both detector modes as can be seen in Fig. 8.1a. Fig. 8.1b shows the ratio of the resolution for the small and large detector. In the barrel region the larger detector is slightly better, due to the larger number of hits and the corresponding larger lever arm, despite the lower B-field. In the forward region this behaviour is reversed as here the same number of hits are available due to the identical detector geometry in this region and it is the higher B-field that causes a better measurement of the curvature and thus the momentum. The impact parameter resolutions for the large and small detector models are equal to within a few percent, as can be seen from Fig. 8.1d and 8.1f, except at low momenta in the forward region, where the large detector is better. In the barrel region, one observes very similar resolutions for the impact parameter in the $r\phi$ -plane and that along the z -axis, whereas in the forward region, where less VTX-hits contribute, σ_{Z0} is significantly worse than σ_{d0} (see Fig. 8.1c and 8.1e)

The track finding efficiency of the algorithms described in section 7.3 is evaluated with $t\bar{t}$ -events at $E_{cms} = 500 \text{ GeV}$ fully simulated and reconstructed for both detector models. The tracking efficiency is defined as the ratio of the number of correctly reconstructed tracks with a hit purity of

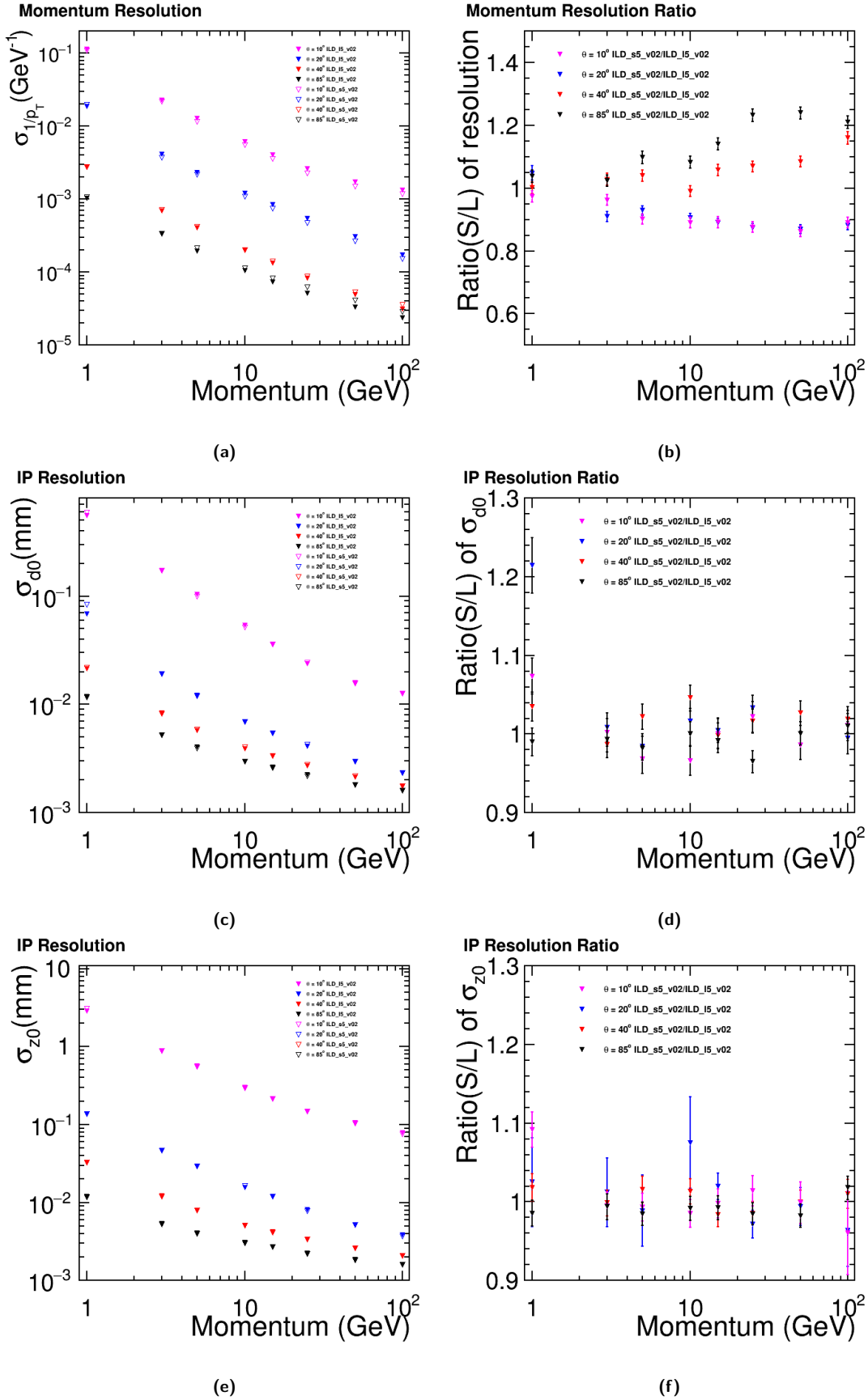


Figure 8.1. Tracking resolutions for single muons for the large and small ILD detector models. (a) Inverse transverse momentum resolution σ_{1/p_T} as a function of momentum and the ratio small/large in (b). (c) Impact parameter in the $r\phi$ -plane σ_{d0} as a function of momentum and the ratio small/large in (d). (e) Impact parameter along the z -axis σ_{z0} as a function of momentum and the ratio small/large in (f).

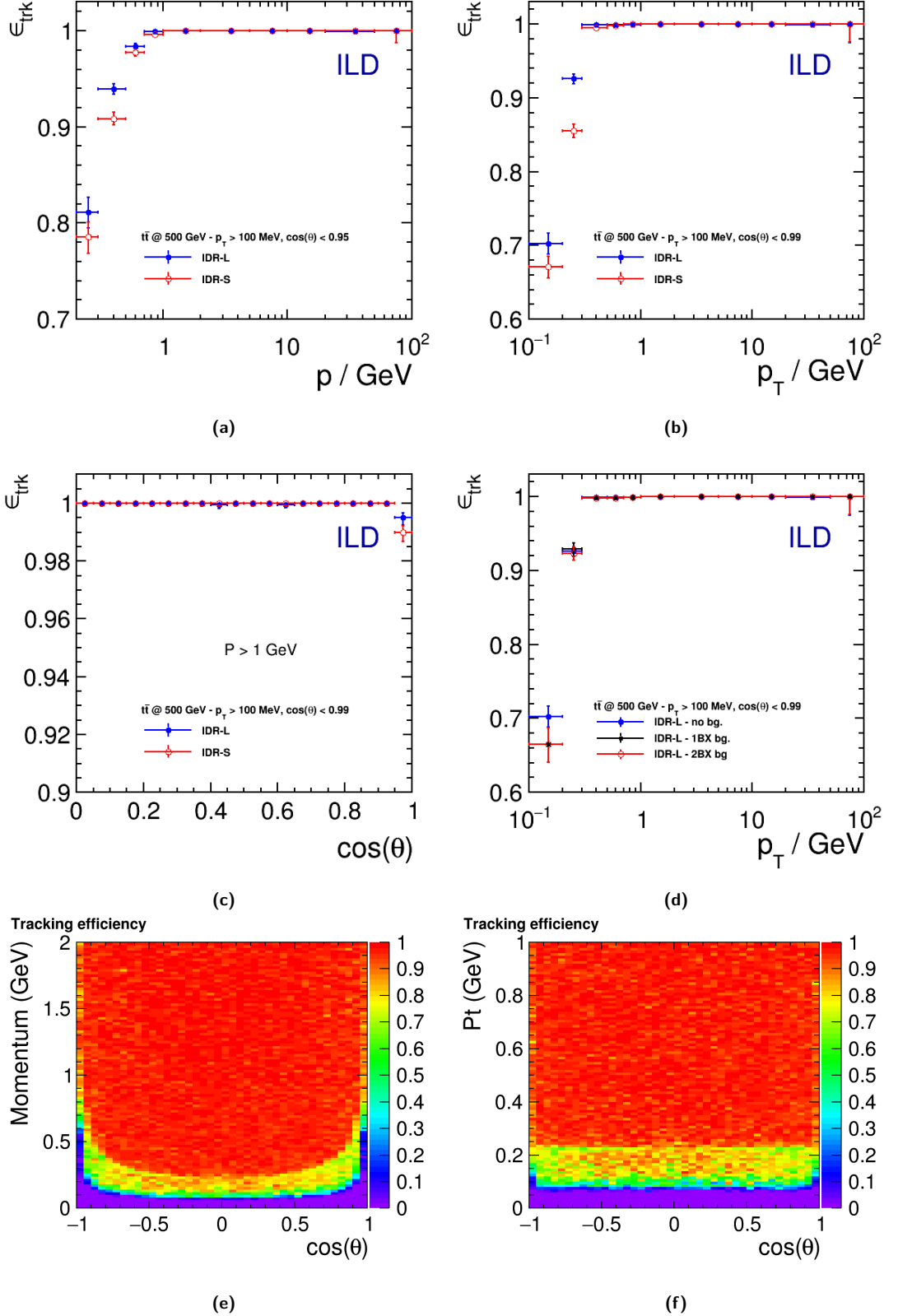


Figure 8.2. Track finding efficiency for prompt ($r_{\text{vertex}} < 10 \text{ cm}$) tracks in $t\bar{t}$ -events at 500 GeV as a function of kinematic variables for the large and small detector: (a) as a function of momentum p (b) as a function of transverse momentum p_T (c) as a function of $\cos(\theta)$). The effect on the efficiency of overlaying hits from 1BX and 2BX of pair background is shown in (d). The tracking efficiency as a function of $\cos(\theta)$ and either momentum or transverse momentum is shown for the large model in (e) and (f) respectively.

75 % to the number of Monte Carlo tracks that are created within 10 cm of the *IP*, left at least 4 hits in the detector and did not decay in flight. The resulting efficiency is shown in Fig. 8.2 as a function of momentum p in (a), transverse momentum p_T in (b) and $\cos(\theta)$ in (c). As can be seen in (c), the tracking is almost perfect for particles with $p > 1$ GeV and $p_T > 100$ MeV down to $\cos(\theta) \approx 0.95$ and better than 99 % in the very forward direction. At low momenta and in the forward direction, the small detector performs slightly worse than the larger variant. The qualitative dependency of the efficiency on momentum and polar angle together is shown in the 2D plots (e) and (f) for the large detector model. The efficiency is basically flat as a function of transverse momentum in all but the very forward ($\cos(\theta) > 0.95$) part and almost perfect above $p_T > 250$ MeV in that region. A small inefficiency persists in the very forward region also for higher momenta.

8.1.2 Particle Flow performance and JER

The performance of the Particle Flow Algorithm (PFA) is evaluated with dedicated $Z \rightarrow q\bar{q}$ -events, where the Z decays at rest in order to distinguish the measurement of the actual jet energy resolution (JER) from other effects like ISR-photons or confusion in jet clustering that occur in more complex, realistic events. The jet energy resolution is then evaluated as

$$\frac{\sigma_{E_{jet}}}{E_{jet}} := \frac{\text{rms}_{90}(E_{jet})}{\text{mean}_{90}(E_{jet})} \quad (8.1)$$

for $Z \rightarrow q\bar{q}$ -events with $|\cos(\theta_{q\bar{q}})| < 0.7$ and $q \in [u, d, s]$. This measure is robust against large tails and should be multiplied by a factor of ~ 1.1 to obtain an equivalent Gaussian analyzing power [85]. Fig. 8.3a shows the JER as a function of the jet energy for selected energies $E_{jet} = (20, 45, 100, 175, 250)$ GeV for the large and small detector model. For $E_{jet} \geq 45$ GeV the resolution is better than 4% and approaches 3% (3.2%) for the large (small) model at higher energies. The linearity of the jet energy measurement is shown in Fig. 8.3b to be better than 5% in the barrel region. The JER as a function of the polar angle of the jets (the *thrust-axis* of the di-quark events) is shown in Fig. 8.3d for the large detector model. The observed dependency is rather flat throughout the barrel region, increasing somewhat after the barrel-end-cap transition with a visible rise in the very forward region, similar for all energies. The effect of heavy flavor quarks on the jet energy resolution is shown in Fig. 8.3c, where the resolutions is plotted for u, d, s di-quark events together with $c\bar{c}$ and $b\bar{b}$ events for the large model. The observed degradation in the JER for the heavy quark jets can be fully recovered by correcting the ν -energies using Monte Carlo truth information, as can be seen from the dashed lines.

8.1.3 Vertexing

The correct identification of heavy flavour decays in jets requires a precise measurement of the coordinates of secondary vertices. The vertex resolution is studied using dedicated $e^+e^- \rightarrow 6 c$ events, along the longitudinal direction \vec{e}_L and two transverse directions \vec{e}_{T1} and \vec{e}_{T2} , defined as:

$$\vec{e}_L = \frac{\vec{p}_c}{|\vec{p}_c|}; \quad \vec{e}_{T1} = \vec{e}_L \times \vec{z}; \quad \vec{e}_{T2} = \vec{e}_L \times \vec{e}_{T1} \quad (8.2)$$

whith the 3-momentum of the c -quark \vec{p}_c . The result is shown for the transverse (a) and longitudinal (b) components of the secondary vertices as a function of the distance from the *IP* in Fig. 8.4. Fig. 8.4c shows the resolution of the primary vertex' z-position as a function of the number of associated tracks. The resolution is better than 3 μm for low multiplicity events and approaches 1 μm for high multiplicity events. The radial component of the primary vertex is already known extremely

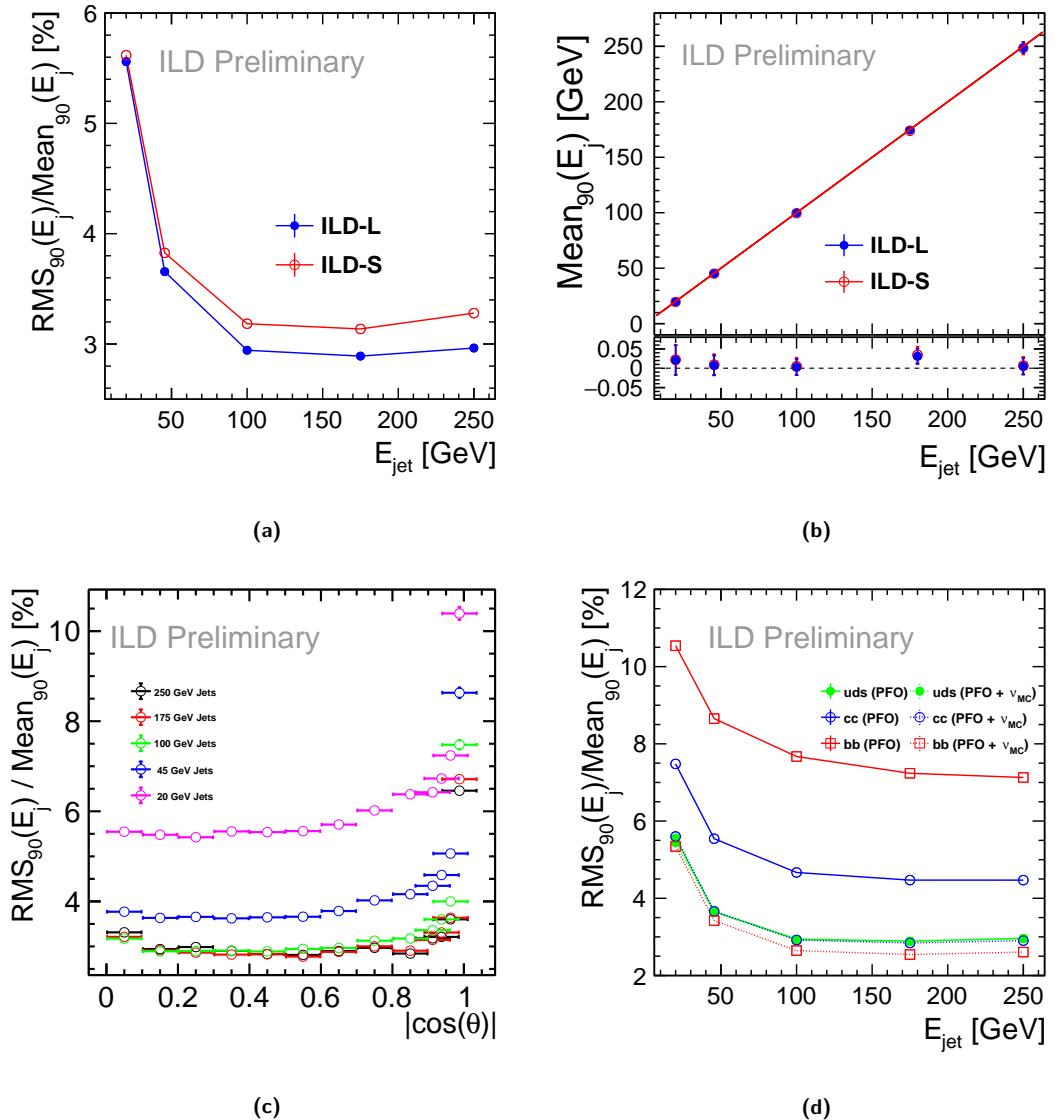


Figure 8.3. Jet energy resolution (JER), evaluated as defined in eq. 8.1 for $Z \rightarrow q\bar{q}$ -events with $|\cos(\theta_{q\bar{q}})| < 0.7$ and $q \in [u, d, s]$. (a) comparison of the JER for the large and small ILD detector. (b) jet energy scale for the two models. (c) JER as function of the polar angle (*thrust-axis*) of the event. (d) JER for u, d, s di-jet events together with $c\bar{c}$ and $b\bar{b}$ events, with (dashed lines) and without (solid lines) correcting the ν energies using Monte Carlo truth information.

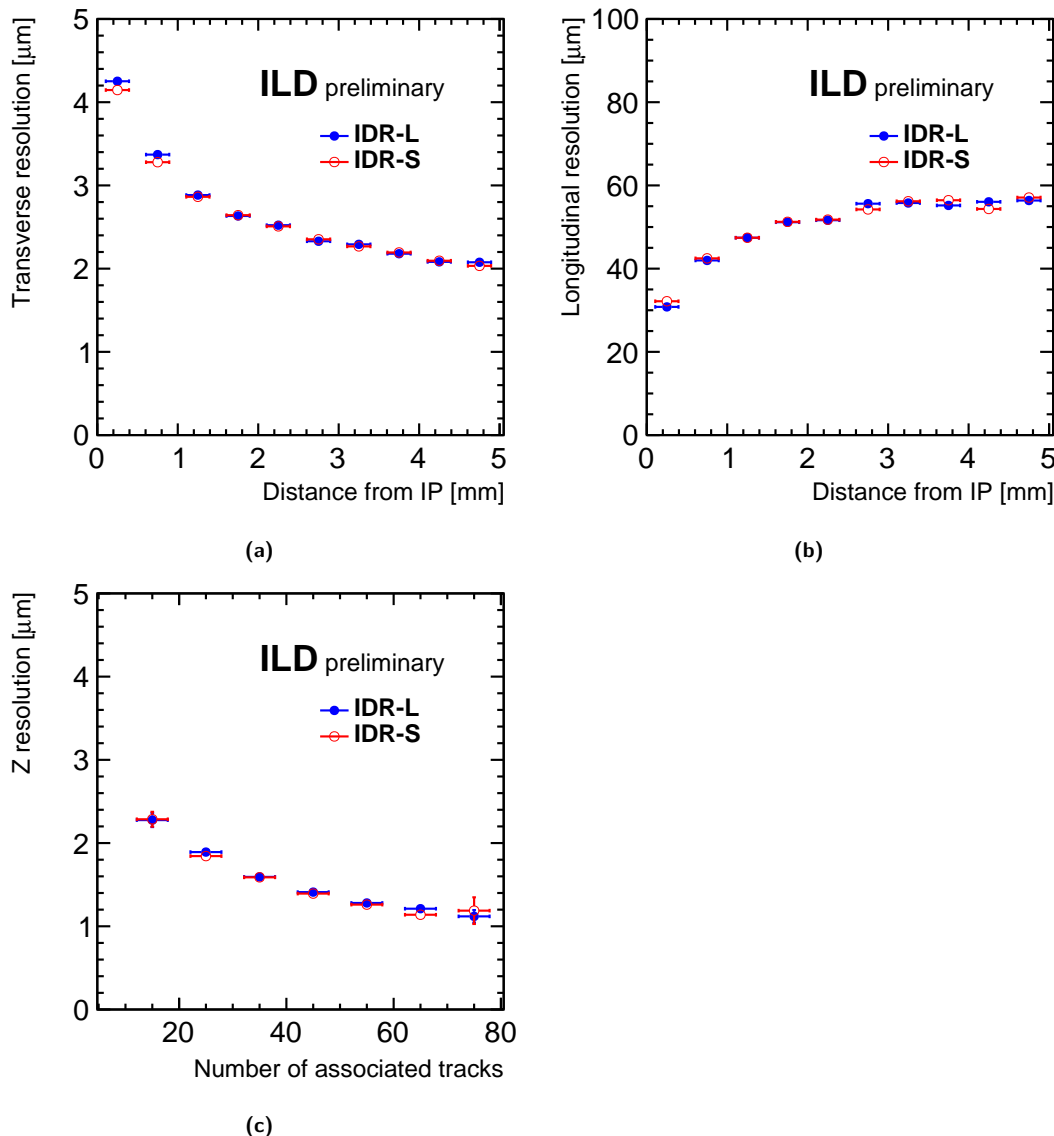


Figure 8.4. Vertex resolutions for the large and small ILD detector models. (a) Resolution of the z-coordinate of secondary vertices as a function of the distance from the *IP* and the same for the radial component in (b). (c) Resolution of the z-coordinate of the primary vertex as a function of the number of tracks used in the fit. Note that the radial component of the primary vertex is known extremely well to $O(10)$ nm from the beam-spot position.

well from the beam-spot position to O(10) nm. The overall vertexing performance for the large and small detector models is very similar, as expected already from the single track impact parameter resolutions shown in Fig. 8.1 (c)-(f).

8.1.4 Photon Reconstruction

no publishable results for photon ID available ...

8.1.5 Lepton ID

muons, electrons - no publishable results for lepton ID available ...

8.1.6 Charged Particle identification

Measuring the energy loss of charged particles in the ILD-TPC provides powerful tool for identifying the type of the particle. Fig. 8.5 shows the dE/dx reconstructed from a truncated mean for charged particle tracks in the TPC as a function of the particle momentum, clearly revealing the bands of the most abundant particle types $e^\pm, \mu^\pm, \pi^\pm, K^\pm$ and p . By fitting Gaussian distributions, with mean $\mu(p)$ and standard deviation $\sigma(p)$, to individual bands in momentum bins one can define a separation power $\eta_{A,B}$ for distinguishing the two particle types A and B:

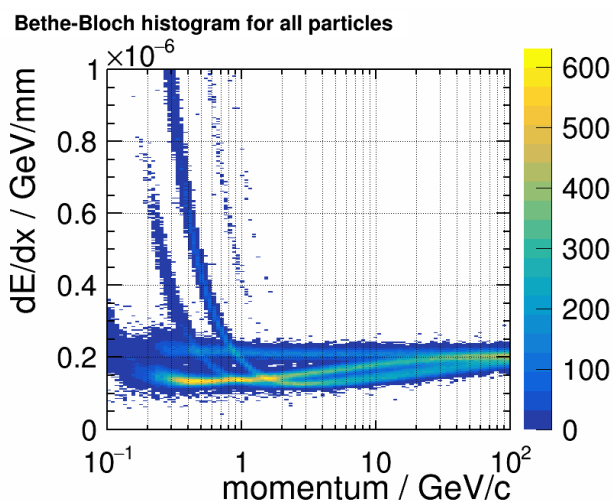
$$\eta_{A,B}(p) = \frac{|\mu_A(p) - \mu_B(p)|}{\sqrt{\frac{1}{2}(\sigma_A^2(p) + \sigma_B^2(p))}} \quad (8.3)$$

Figure 8.6 shows the separation power for π, K and K, p based on the dE/dx measurement in the TPC of the large and small detector model (a) and the possible improvement that could be achieved by combining it with a *time-of-flight (TOF)* measurement in the large detector (b). The TOF estimator used here is computed, using the first ten calorimeter hits in the Ecal that are closest to the straight line, resulting from extrapolation of the particle's momentum into the calorimeter, assuming an individual time resolution of 100 ps per hit¹, motivating further studies on timing measurements in the ILD calorimeters.

An example in the context of physics analyses can be seen in Fig. 8.7. It compares the performance of the charged Kaon identification based on dE/dx for the large and small detector models, as obtained

¹While this time resolution seems realistically possible, it has to be noted, that so far it has not yet been demonstrated in a test beam prototype.

Figure 8.5
 dE/dx as a function of particle momentum as reconstructed from a full simulation of particles in the TPC of the large detector model.



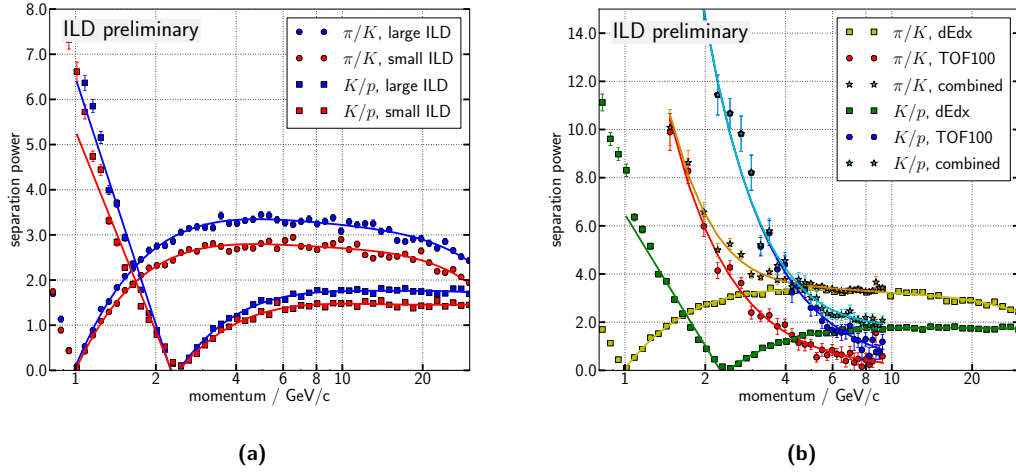
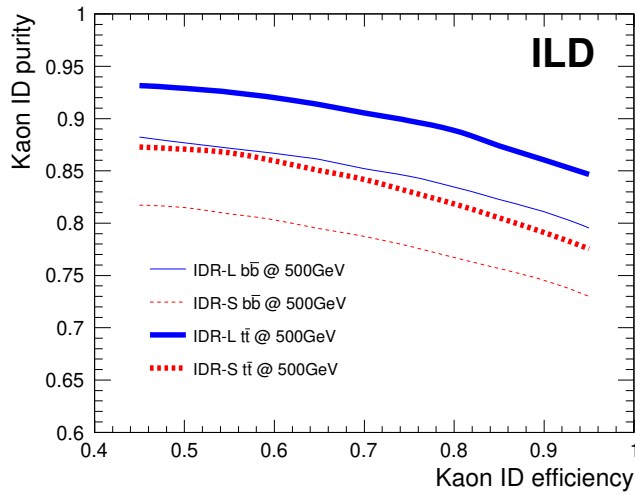


Figure 8.6. (a) particle separation power (eq. 8.3) for π , K and K , p based on the dE/dx measurement in the TPC. (b) improvement of the same separation power if combined with a *time-of-flight* (TOF) estimator from the first ten Ecal layers, where $\eta_{dE/dx, \text{TOF}} = \eta_{dE/dx} \oplus \eta_{\text{TOF}}$

from the $b\bar{b}$ and $t\bar{t}$ benchmarks described in Sec. 8.3.8 and 8.3.9, respectively. For the same efficiency, the large detector reaches a 5% higher purity due to its larger TPC radius, which results in a better dE/dx resolution. Additional methods for charged particle identification using calorimeter shower shapes have been developed and used in specific physics analyses [need references...]

Figure 8.7
Efficiency-purity curves for charged Kaon identification in the context of the $t\bar{t}$ and $b\bar{b}$ analyses. For the same efficiency, the large detector reaches a 5% higher purity due to its larger TPC radius, which results in a better dE/dx resolution. Details on the analyses can be found in Sec. 8.3.8 and 8.3.9.



8.2 High-level Reconstruction Performance

8.2.1 Flavour-Tag Performance

The efficient identification of heavy flavour jets in hadronic events is an indispensable ingredient to many important physics analyses, such as the $H \rightarrow c\bar{c}$ and $H \rightarrow b\bar{b}$ branching ratio measurements. The flavour tagging performance is studied using simulated and fully reconstructed samples of dedicated $e^+e^- \rightarrow 6q$ events at $\sqrt{s} = 500$ GeV, where all quarks are chosen to have the same flavour. The samples are divided into two sub-samples, where one is used for training the BDT and the other is used as a test sample. The resulting performance is shown in Fig. 8.8 for the large and small ILD detector model. In (a) the background rate as a function of the c-tagging efficiency for b-quark and light flavour quark jets is plotted and (b) shows the background rate for c-quark and light flavour quark jets as a function of the b-tagging efficiency. As expected from the impact parameter

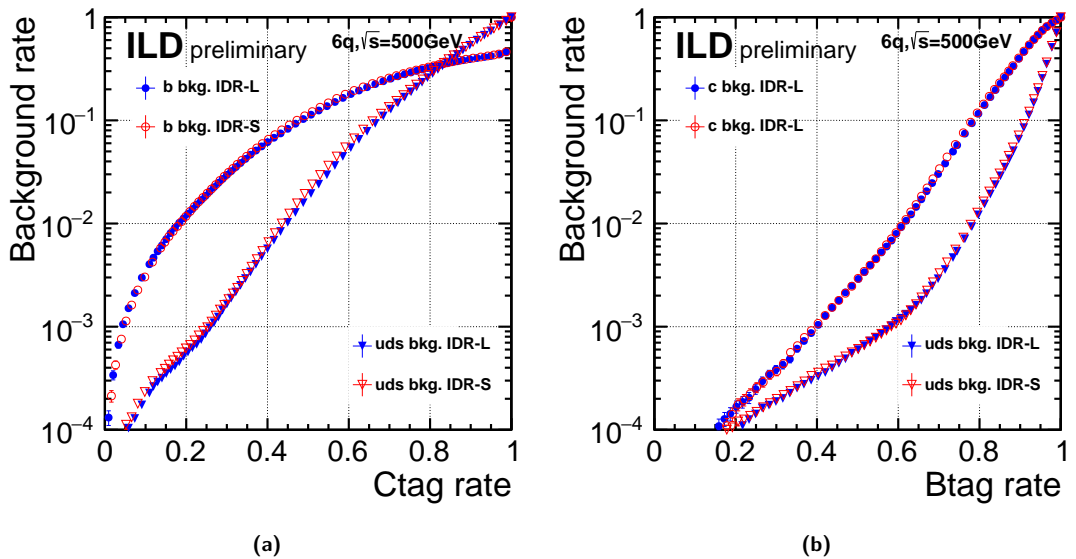


Figure 8.8. Flavour tag performance for the large and small ILD detector models. (a) background rate as a function of the c-tagging efficiency for b-quark and light flavour quark jets. (b) background rate as a function of the b-tagging efficiency for c-quark and light flavour quark jets.

and vertex resolutions there are no significant differences observed between the large and small ILD variants for the flavour tagging performance. The flavour tagging performance has been seen to vary with the jet energy and jet multiplicity [79]. The ideal performance in a physics study can be achieved by retraining the BDTs for the corresponding signal event topology. In practice, several sets of training weights are centrally produced, which are compared and chosen for the best performance.

8.2.2 Hadronically decaying τ ID

The correct identification of τ lepton decay modes is of particular importance in the extraction of observables sensitive to the τ lepton spin direction: examples are measurements of the τ polarisation and Higgs CP based on spin correlations in $H \rightarrow \tau\tau$ decays. Hadronic τ decays are typically offer the most sensitivity to the spin, due the presence of a single neutrino. The identification of these hadronic decay modes can be factorised into the charged and neutral components. The charged part is typically rather straight-forward in the TPC of ILD, so we concentrate efforts on understanding the identification of the neutral part, which consists largely of photons from neutral pion (and to a lesser extent other neutral meson) decays. In the decays of highly boosted taus, these photons are typically rather close to both a charged particle and one or more additional photons produced in the same τ decay. The separation between these photons in the calorimeter depends on its inner radius, while the

distance to charged particles additionally depends on the magnetic field strength. We can therefore expect some differences in performance for the large and small ILD detector models.

The performance of τ decay mode identification was studied in τ -pair production events at a centre-of-mass energy of 500 GeV. These very highly boosted τ decays are the most challenging to reconstruct due to the small distance between particles in the highly collimated τ decay jets. The standard ILD reconstruction algorithms were applied to these events.

In each event, two high momentum, back-to-back, charged PFOs were identified as τ jet "seeds". Figure 8.9 shows the number of photon PFOs identified in a cone around these τ seed tracks, in the case when the τ lepton decayed to $\pi^\pm \pi^0 \nu$. In these events, exactly two photons are expected in the vast majority of cases. The distribution shows that it is challenging to reconstruct both photons: in around half of the cases only a single photon cluster was reconstructed, which is due to the merging of the two photons into a single reconstructed particle. A difference is seen between the two detector models, with the large version somewhat more often correctly resolving the two photons, which can be understood as being due to the larger ECAL radius increasing the distance between the photons' electromagnetic showers.

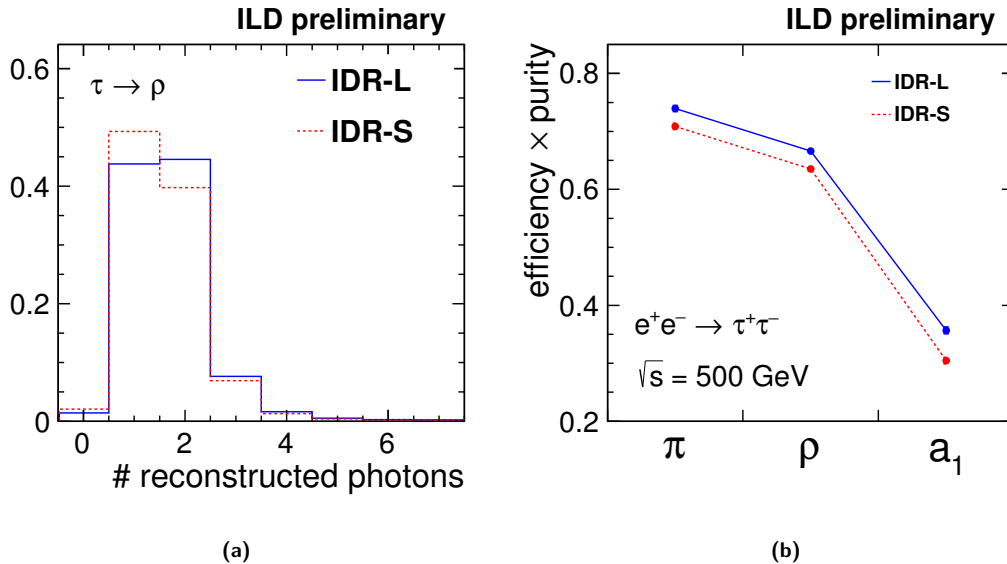


Figure 8.9. Hadronic decay mode identification for isolated τ -leptons with momenta near 250 GeV. (a) The number of reconstructed photon PFOs in $\tau \rightarrow \rho \nu \rightarrow \pi^\pm \pi^0 \nu$. (b) The performance of a simple τ decay mode identification algorithm.

A simple cut-based approach to the identification of single-prong hadronic τ decays was developed, based on the number of reconstructed photon PFOs, and the invariant mass of this set of photon PFOs both alone and together with the charged PFO around which the τ candidate jet was built. The ability of this algorithm to distinguish $\tau \rightarrow \pi^\pm \nu$ (" π "), $\tau \rightarrow \pi^\pm \pi^0 \nu$ (" ρ "), and $\tau \rightarrow \pi^\pm \pi^0 \pi^0 \nu$ (" a_1 ") decays is shown in Fig. 8.9. The product of selection efficiency and purity varies between around 30% and 75% among these three decay modes. The large detector model performs slightly better, as expected thanks to the larger inner ECAL radius.

8.2.3 J/ψ reconstruction

With the excellent particle flow, particle identification and vertexing capabilities of ILD discussed in the previous sections, there is a great potential to reconstruct various exclusive decay chains of short-lived baryons and mesons. This is of special interest in case the ILC will be operated at the Z pole, but also at higher energies we expect further improvements to flavour tagging and jet energy resolution once this potential is fully exploited in reconstruction and analyses. This is an area where

new algorithmic developments could still lead to a significant improvement of the ILD performance.

At the current stage, we only provide a very simple example, namely the reconstruction of $J/\psi \rightarrow \mu^+ \mu^-$ decays. Due to its extremely well-known mass (known to 3.6 ppm [86]), the J/ψ is an important standard candle, e.g. for calibration of the tracker momentum scale.

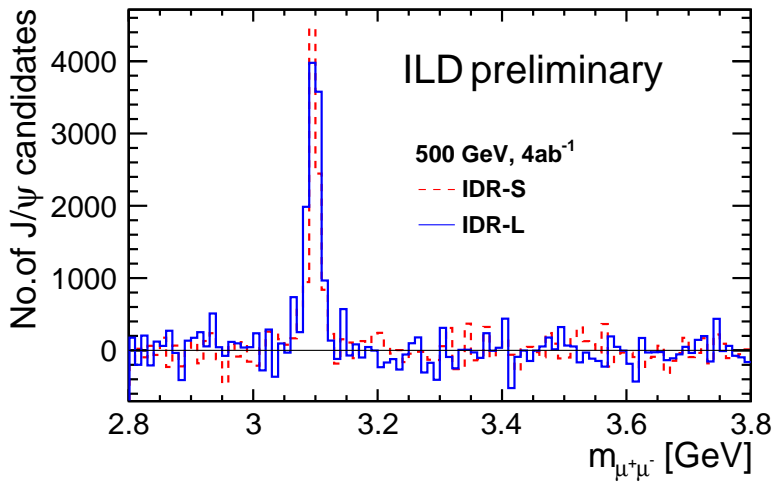


Figure 8.10. $J/\psi \rightarrow \mu^+ \mu^-$ candidates as reconstructed with IDR-L and IDR-S.

Figure 8.10 shows the invariant mass spectrum of reconstructed muon pairs in the J/ψ region, comparing the large and small detector. All available SM MC events from the optimisation production at $\sqrt{s} = 500$ GeV have been used and weighted to the full luminosity of 4 ab^{-1} with the canonical sharing between the polarisation configurations. The combinatorial background has been determined from like-sign muon pairs and has been subtracted from the opposite-sign pairs, leading to the fluctuations around zero in the off-peak regions. At 500 GeV, most J/ψ candidates are produced in the forward direction, with $|\cos \theta| > 0.8$ and at rather low transverse momenta, typically below 30 GeV. Therefore, the small detector has a smaller acceptance than the large detector, with about 10k vs 12k reconstructed J/ψ 's compared to about 20k available at generator level. On the other hand, the better momentum resolution of the small detector in the forward region leads to a more narrow peak.

Jenny List
20 pages

8.3 Physics Benchmarks

Each benchmark has its own confluence page, where a lot more material, including the draft of the ILD note and the names of the main analysis reponsibles can be found:
<https://confluence.desy.de/display/ILD/Benchmarks+for+physics-driven+detector+optimisation>
Note that several benchmark are still work in progress. A short comment at the beginning of each section gives a rough summary of the status.

The performance of the two ILD detector models IDR-L and IDR-S has been evaluated on a number physics benchmarks, which will be discussed in this section. Despite the fact that a 250-GeV version of the ILC is currently under political consideration in Japan, the detector benchmarking has been performed at higher center-of-mass energies, mostly at 500 GeV, and in one case even at 1 TeV. This choice has been made in order to make sure that both detector models perform adequately also under the more challenging experimental conditions of the higher energy stages, and in order to cover e.g. a wider range of jet, lepton and photon energies.

Unless stated otherwise, all results have been scaled to the integrated luminosity and beam

polarisation of the full H20 running scenario originally defined in [3], which is — for the higher center-of-mass energies — unchanged since [5]. In particular, the H20 scenario comprises 4 ab^{-1} at 500 GeV, with beam polarisation absolute values of 80% for the electron and 30% for the positron beam. The total luminosity is shared between the different polarisation sign combinations according to $f(-+, +-, ++, --) = (40\%, 40\%, 10\%, 10\%)$. Analogously, 8 ab^{-1} are considered at 1 TeV, with absolute polarisation values of 80% for the electron and 30% for the positron beam, with the same $f(-+, +-, ++, --) = (40\%, 40\%, 10\%, 10\%)$ sharing.

The benchmarks presented in this section have been chosen to illustrate many performance aspects with a minimum number of benchmarks, and are not meant to cover the *complete* physics case. The main focus of the analysis work was not always the pure optimisation for utmost physics performance, but rather to better understand and highlight the role of individual performance aspects and their interplay.

Unless stated otherwise, the analyses performed for and since the time of the ILC TDR remain valid in their physics message. For an up-to-date review of the ILC physics case, based on ILD detector simulations, see e.g. [5].

8.3.1 Hadronic Branching Ratios of the Higgs Boson

few open questions between Masakazu, Frank Simon and JL, see email June 25.

The measurement of the hadronic branching ratios of the Higgs boson, including in particular $H \rightarrow c\bar{c}$, is one of the unique items on the menu of future e^+e^- colliders. This crucially depends on an excellent flavour tag, c.f. Sec. 8.2.1, enabled by vertex detectors with micrometer point resolution with a first layer placed as close as 1.4 cm to the beam line.

As a benchmark, the $\nu\bar{\nu}H \rightarrow \nu\bar{\nu}jj$ final state was chosen in order to minimize the impact of other performance aspects like e.g. jet clustering. Thus the target physics observable here is $\sigma(\nu\bar{\nu}H) \times BR(H \rightarrow b\bar{b}/c\bar{c}/gg)$. With the full 500 GeV data set, about 200000 $H \rightarrow b\bar{b}$ events would be produced in this final state alone, while about 30000 and 10000 $H \rightarrow gg$ and $H \rightarrow c\bar{c}$ would be available, respectively. In the limit of 100% signal efficiency and zero background, this would correspond to statistical precisions of 0.2%, 0.6% and 1% for $H \rightarrow b\bar{b}$, $H \rightarrow gg$ and $H \rightarrow c\bar{c}$, respectively.

The benchmark analysis is documented in detail in [87], and follows earlier analyses [88–90]. The full performance of the ILC on Higgs branching ratio measurements, combining all final states, can be found in [5]. After a cut-based preselection, the kinematic selection of $\nu\bar{\nu}H \rightarrow \nu\bar{\nu}jj$ events is refined by a multi-variate approach. Up to this point, no flavour-tag information is used. Figure 8.11 shows the distributions of the reconstructed Higgs mass at this stage of the analysis for the signal on top of the remaining SM backgrounds, comparing both detector models.

Figure 8.12 shows the 2D distributions of c - vs b -likeliness (c.f. Sec. 8.2.1) for the different Higgs decay modes. The “data” distribution is then fitted in 3D template approach in order to determine the contained fractions of the various hadronic Higgs decay modes, where the 3rd dimension is the bc -likeliness. Due to the limited available statistics of background MC, a much smaller number of bins than displayed in Fig. 8.12 was used [87]. The resulting precisions from this template fit are displayed in Fig. 8.13. Thereby, Fig. 8.13a compares the actual results for IDR-L and IDR-S with the $P(e^-, e^+) = (-80\%, +30\%)$ data only with the result obtained for a perfect flavour tag. It shows that for $H \rightarrow b\bar{b}$ and $H \rightarrow gg$ the current flavour tag performance yields a close to perfect identification of these final states. For $H \rightarrow c\bar{c}$, however, the real flavour tag performs worse by a factor of two. On the other hand, for a worse flavour separation, especially the expected precision for $H \rightarrow c\bar{c}$ degrades rapidly [87], thus the performance of the ILD detector and reconstruction is crucial for the ability to measure $H \rightarrow c\bar{c}$.

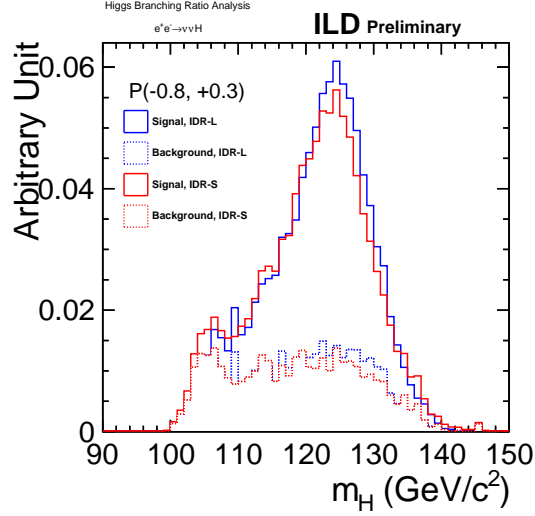


Figure 8.11. Reconstructed Higgs mass distribution after the kinematic selection. The signal is shown on top of the remaining SM background for both detector models.

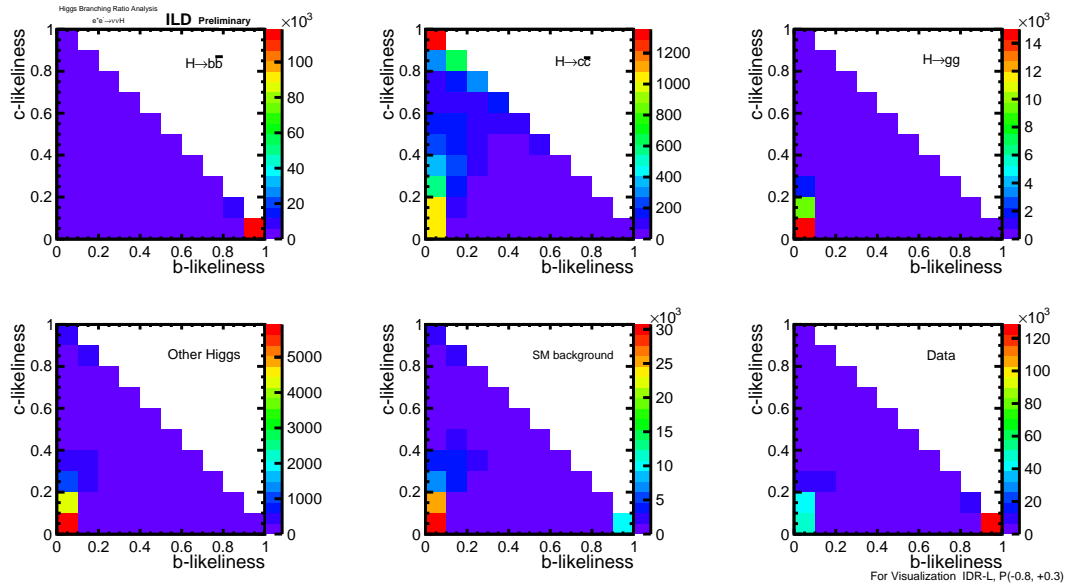


Figure 8.12. Visualisation of the flavour tag performance in $\nu\bar{\nu}H$. The panels show the 2D distributions of c - vs b -likeliness separately for $H \rightarrow b\bar{b}$, $H \rightarrow c\bar{c}$, $H \rightarrow gg$, $H \rightarrow$ other, the SM background and their mix expected in data.

Figure 8.13b finally compares the precisions from all data sets combined for IDR-L and IDR-S. It shows a rather equivalent performance of both detector models. In the case of $H \rightarrow c\bar{c}$, which is most sensitive to the detector performance, the smaller detector model actually performs a little better due to its stronger magnetic field and the resulting better momentum resolution in the forward region, c.f. Fig. 8.1.

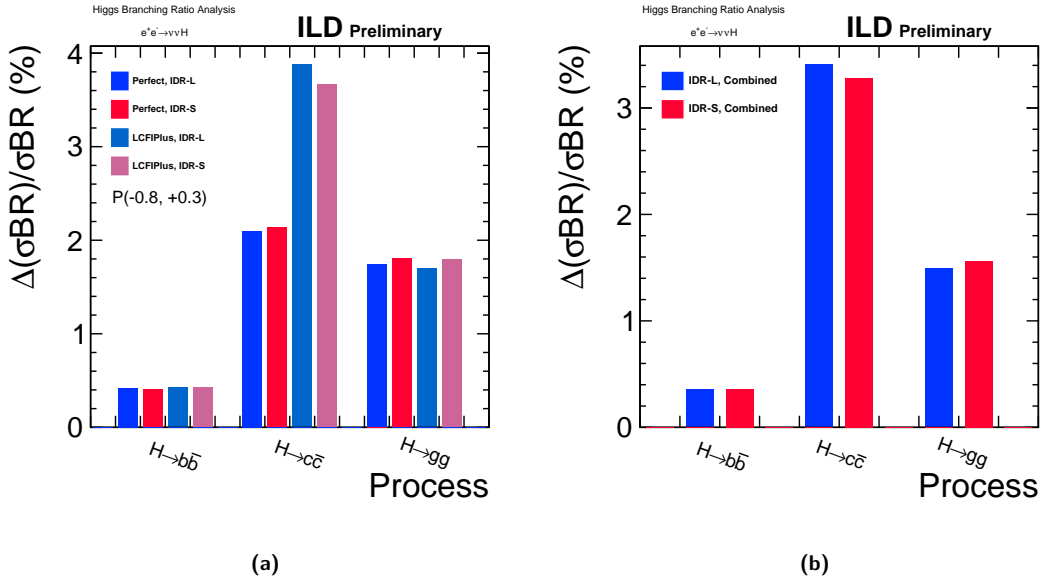


Figure 8.13. (a) Comparison of current and ideal flavour tag performance. The precision on $H \rightarrow c\bar{c}$ is most sensitive to the actual flavour tag performance. (b) Comparison of IDR-L and IDR-S for all polarisation configurations combined.

8.3.2 Higgs Mass from $ZH \rightarrow llb\bar{b}$

IDR text and plots okayed by Frank Simon(referee). Main missing item: complete note.

The single most precise method to measure the Higgs mass is the recoil analysis at $\sqrt{s} = 250$ GeV [91]. At \sqrt{s} much higher than the ZH production threshold, the recoil technique suffers substantially from the increasing amount of ISR and beamstrahlung. In addition, the momenta of the muons from $Z \rightarrow \mu\mu$ increase in magnitude and thus are measured less precisely. Still, the data collected at higher centre-of-mass energies can be exploited effectively when using the fully-reconstructable decay modes of the Higgs boson in combination with kinematic constraints from the known initial state. E.g. the constraints $\sum_i p_{iy} = 0$ and $\sum_i p_{ix} = 3.5$ GeV² can replace the measured energies of the Higgs decay products, so that only on the angles of the Higgs decay products and the momenta of the muons from $Z \rightarrow \mu^+ \mu^-$ enter in the mass reconstruction. Thus the technique is independent of systematic uncertainties as e.g. associated with the b -jet energy scale. The detailed description of the technique can be found in [92].

The resolutions on the kinematic quantities which enter the Higgs mass reconstruction, namely azimuthal and polar angles of the jets and the muon energy, are compared in Figs. 8.14a and 8.15 for IDR-L and IDR-S. For this, the jet angles obtained from clustering the MC particles after hadronisation serve as truth reference, so that the detector performance is singled out from other influences. Figure 8.14b illustrates the effect of hadronisation by comparing to the quark-level direction taking IDR-L as example. It shows that the detector resolution (blue histogram, same as in Fig. 8.14a) is comparable, but subdominant to the hadronisation effect (red histogram). While the angular

²In x direction the initial momentum is not zero due to the crossing angle of the beams, but given by $\sqrt{s} \cdot \sin 14$ mrad.

resolutions are very similar for both detector models, the muon energy resolution is worse for the small detector, reflecting the somewhat worse p_t resolution for high-momentum tracks in the central region of the detector, c.f. Fig. 8.1.

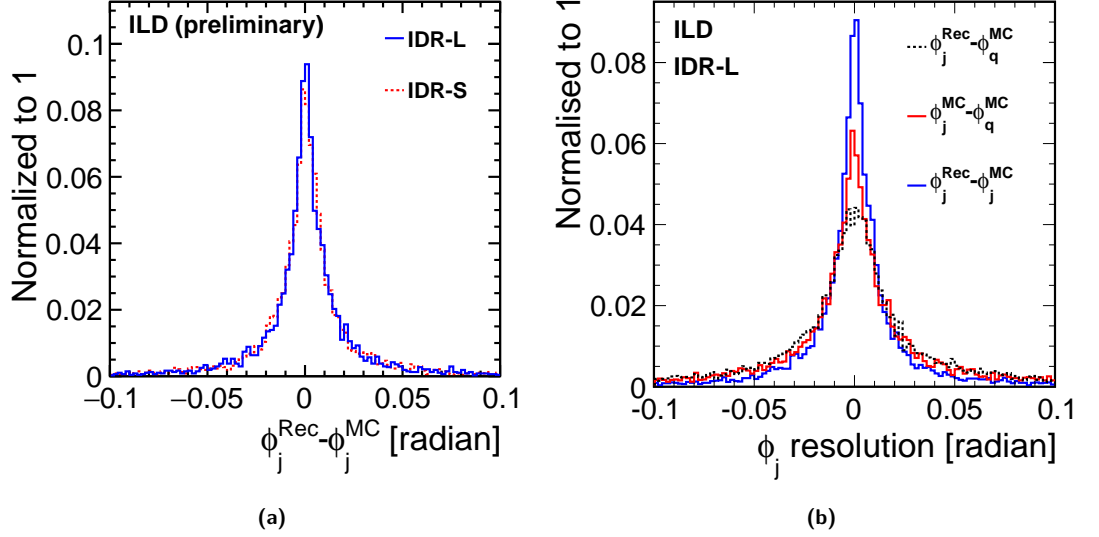


Figure 8.14. (a) Resolution obtained with IDR-L and IDR-S for the jet azimuthal angle (b) Influence of hadronisation on the jet azimuthal angle

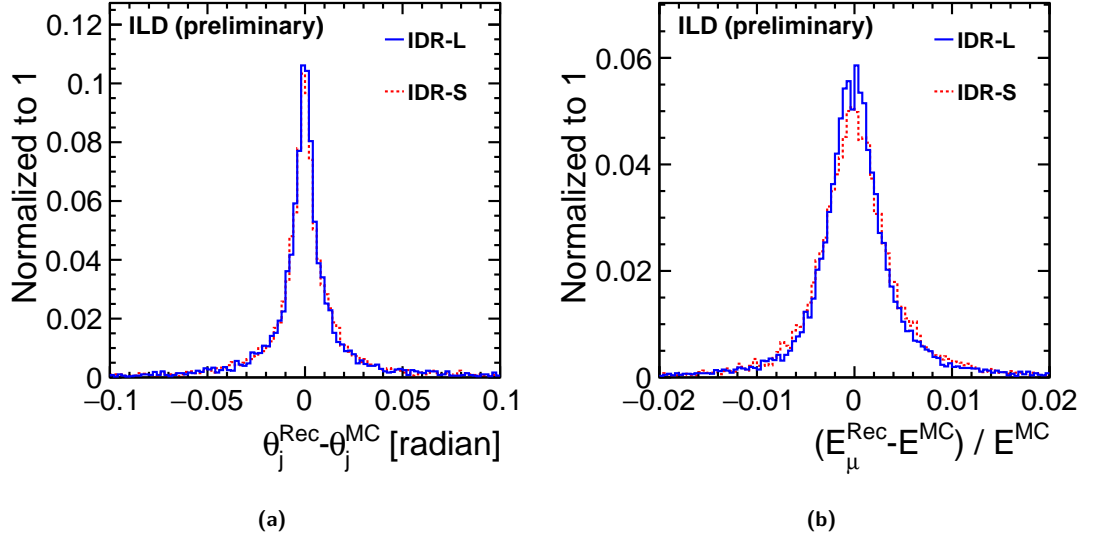


Figure 8.15. Resolutions obtained with IDR-L and IDR-S for (a) the jet polar angle (b) the muon energy, after recovery of FSR photons.

Figure 8.16 shows the propagation of this effect to the actual physics observable, i.e. the reconstructed mass of the Higgs candidates. IDR-L and IDR-S are compared for the muon channel in Fig. 8.16a and for the electron channel in Fig. 8.16b. In both cases signal and all backgrounds from the SM and other ZH modes are combined, with clear peaks visible around the nominal Higgs and Z boson masses. In particular in the muon channel, the worse momentum resolution of the small detector leads to the peaks being visibly wider. The uncertainty on the Higgs mass is extracted by fitting these distributions following the approach used for the recoil analysis [91]. This results in an uncertainty on the measured Higgs mass of 66 MeV in the case of IDR-L and 81 MeV for IDR-S, to an increase of about 22%.

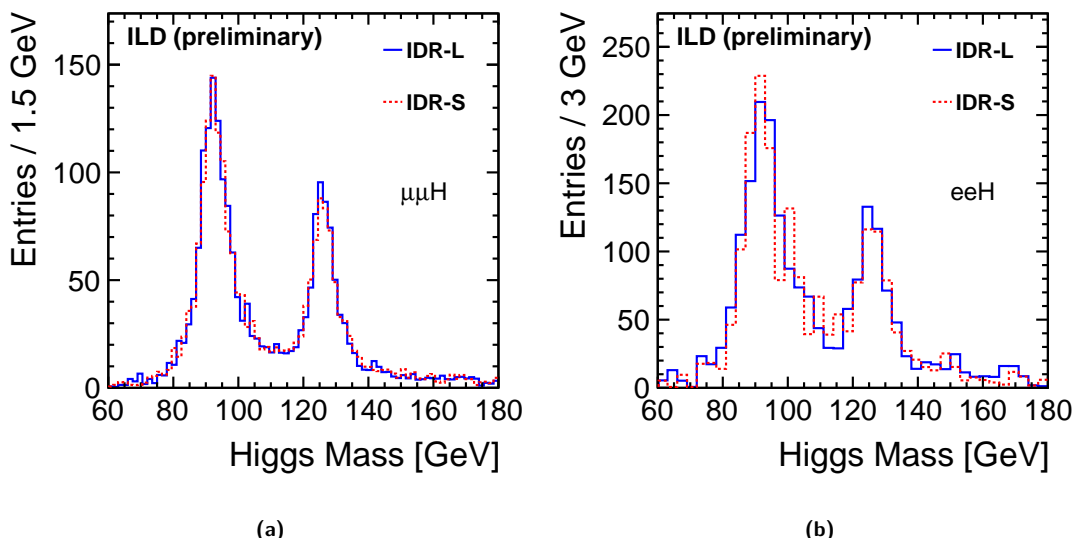


Figure 8.16. reconstructed Higgs mass distribution for signal and background for IDR-L and IDR-S (a) muon channel (b) electron channel (here with limited MC statistics, thus a reduced number of bins)

8.3.3 Branching Ratio of $H \rightarrow \mu^+ \mu^-$

IDR text and plots signed off by Ivanka and Filip (referees), note send for circulation
in ILD! :-(:-(:-(

In the SM, the decay of the Higgs boson into a pair of muons is a very rare decay, with a branching ratio of 2.2×10^{-4} . In order to identify this small signal, the achievable mass resolution, thus the precision to which the momenta of the two muons are measured, plays a crucial role. For the purpose of detector benchmarking, we consider only $\sigma(\nu\bar{\nu}H) \times BR(H \rightarrow \mu^+ \mu^-)$ as observable, which isolates best the effect of the muon momentum resolution.

The selection [93] targets events with substantial missing four-momentum plus two well-reconstructed, oppositely charged muons. Kinematic and angular variables are exploited in an MVA analysis. Figure 8.17a shows the di-muon invariant mass distribution for all selected signal events. In case of the small detector model, the mass peak is about 10% wider than for the large detector. This originates from the combination of the muons from the Higgs decay being high-energetic and rather central, plus the better momentum resolution of the large detector for high-momentum tracks in the barrel. This effect is seen more clearly in Fig. 8.17b, which compares the event-by-event resolution of the di-muon invariant mass for the selected signal events with both muons in the barrel region of the detector ($|\cos \theta| < 0.7$).

For the 500 GeV data set of the H20 scenario, the asymptotic precision on cross section times branching ratio for the case of 100% efficiency and no backgrounds would be 13%.

After the event selection, about 33 signal events, corresponding to a selection efficiency of 58%, remain over a evenly distributed background of about 1100 events (counted in a mass window between 120 and 130 GeV). Finally, the expectation values for the number of signal events observable above the backgrounds as well as for its uncertainty are obtained from many toy MC fits to the di-muon invariant mass spectrum [93]. The obtained precisions on $\sigma(\nu\bar{\nu}H) \times BR(H \rightarrow \mu^+\mu^-)$ are 40.2% for IDR-L and 41.3% for IDR-S. The relative difference of 2.8 is consistent with the expectation of a $\sim 10\%$ difference in the signal peak width over a flat background. Either number, however, is about a factor 3 worse than the asymptotic precision for the case of 100% efficiency and no backgrounds, which would be 13%. The difference is vastly dominated by the remaining “irreducible” backgrounds with two muons and two neutrinos from W pairs decaying either directly to muons or via tau-leptons.

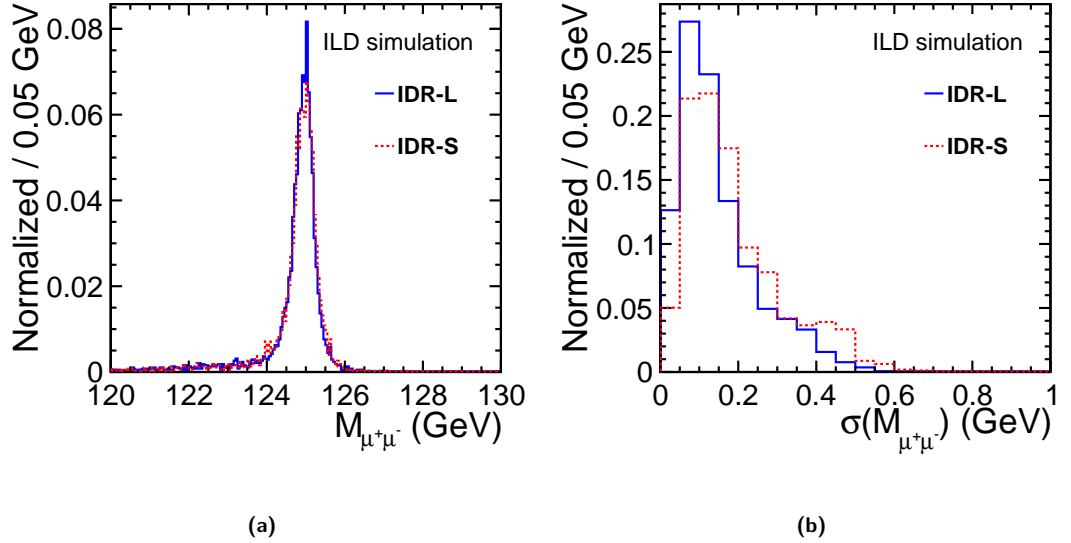


Figure 8.17. $H \rightarrow \mu^+ \mu^-$ benchmark: (a) di-muon invariant mass for all selected signal events (b) mass resolution for the case that both muons are in the barrel region of the detector ($|\cos \theta| < 0.7$)

While there is certainly room for improvement in rejecting these backgrounds, this will factorize from the impact of the signal peak width, as long as the background remains flat in the discriminating variable.

8.3.4 Sensitivity to $H \rightarrow$ invisible

Yu and Marcel (referee) okayed IDR draft, note incomplete

The decay of the Higgs boson into invisible particles is of particular interest because it could give important clues about the nature of Dark Matter. As a detector benchmark for testing the impact of the jet energy resolution, in particular the hadronic decay mode of the Z boson is considered here. Thus the physics observable will be the upper limit on $\sigma(q\bar{q}H) \times BR(H \rightarrow \text{inv.})$.

The event selection [94] targets events which are consistent with a di-jet plus missing four-momentum topology, where the di-jet invariant mass should be compatible with the Z boson mass. The jet finding step also serves to reject PFOs from overlay of $\gamma\gamma \rightarrow$ low- p_t hadron events. The final discriminating variable is the invariant mass of the “invisible” four-momentum recoiling against the Z boson.

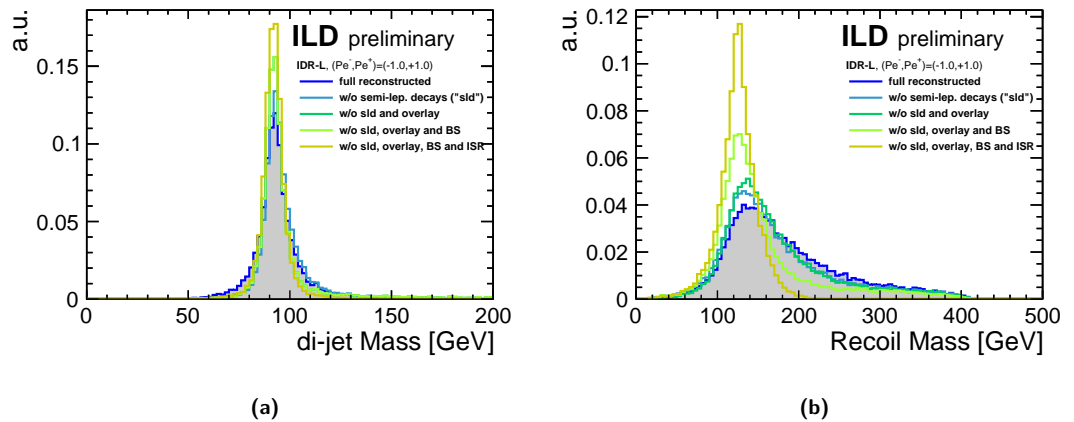


Figure 8.18. Impact of various effects on (a) the invariant di-jet mass and (b) the recoil mass, shown for the example of the large detector model.

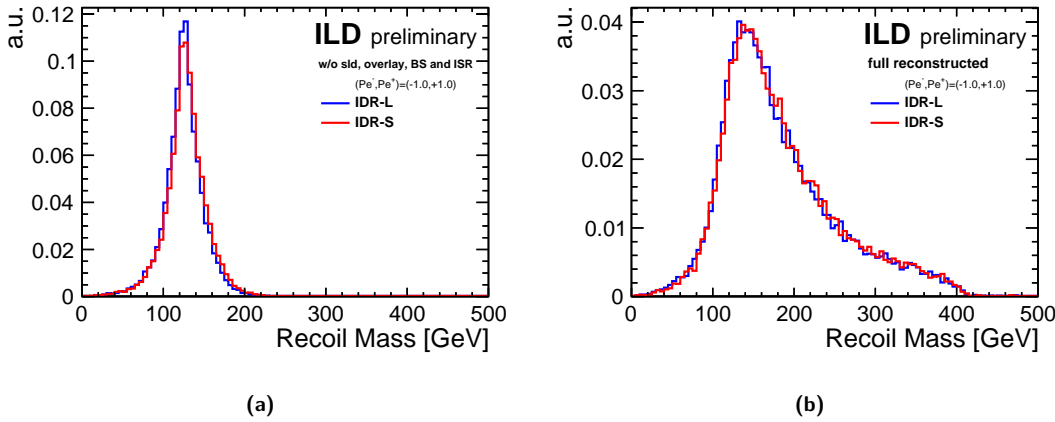


Figure 8.19. Comparison of the recoil mass distributions for IDR-L and IDR-S (a) when cheating semi-leptonic decays, overlay removal, beam spectrum and ISR (b) at full reconstruction level.

Figure 8.18a shows the di-jet invariant mass for the selected signal events at various levels of realism from the full reconstruction to cheating everything but the detector and particle flow performance. The first step of partial cheating removes jets with semileptonic heavy flavour decays. In a detector like ILD shower shapes in the highly-granular calorimeter and specific energy loss information from the TPC should allow an excellent identification of leptons in jets, which, combined with secondary vertex information should allow to significantly improve scale and resolution for heavy flavour jets with semileptonic decays. However, the corresponding reconstruction algorithms are still under development and thus could not be applied here. Similarly, work is ongoing to improve the removal of overlay backgrounds, see e.g. Sec. 8.3.11 and Ref. [95]. Thus, we expect that with future reconstruction improvements, a performance similar to the case “w/o sld and overlay” could be reached. The beam spectrum (BS) by construction does not affect the invariant di-jet mass. ISR, on the contrary, can lead to photons in the detector. In this analysis, no attempt has been made to identify the corresponding particle flow objects. Therefore, also a large part of the effect of ISR on the di-jet mass should be recoverable with a more sophisticated analysis.

The corresponding situation for the recoil mass is shown in Fig. 8.18b. Here, ISR and BS have a large impact since they lead to a deviation of the actual initial state of the hard interaction from the naive assumption. Since this effect is dominated by photons from ISR and BS which escape undetected along the beam pipe, no attempt has been made to correct the kinematics of those events in which a photon is detected. See e.g. Sec. 8.3.10 for an analysis where such a correction is applied.

The recoil mass distributions obtained with the large and small detector model are compared in Fig. 8.19. Thereby, Fig. 8.19b shows the situation at the current full reconstruction level, while Fig. 8.19a cheats the effect of semi-leptonic decays, overlay removal, beam spectrum and ISR. In both cases, the recoil mass is slightly shifted to higher values in case of the small detector, due to differences in the calibration of the particle flow for the two models. In addition, the cheated recoil mass distribution is a bit wider for the small detector, as expected from its slightly worse JER, c.f. Fig. 8.3a.

The results in terms of the physics observable, namely the 95% C.L. upper limit on $\sigma(q\bar{q}H) \times BR(H \rightarrow \text{inv.})$, are summarized in Fig. 8.20 for both detector models at the various cheating levels. In the case of full reconstruction, the upper limit is at 0.78% for IDR-L and at 0.79% for IDR-S, corresponding to a relative change of about 1%. At when isolating the effect of the particle flow performance by cheating all other aspects, the limit would be 0.50% (0.51%) for IDR-L (IDR-S), i.e. a relative change of about 2%. Also displayed is an estimate of how the cheated results would change when scaling the JER up and down. This clearly shows that larger variations of the JER, by 20% or

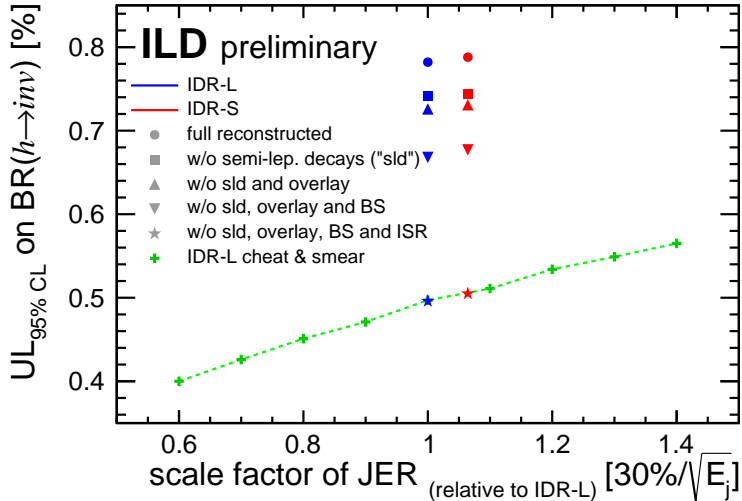


Figure 8.20. Upper limit on $BR(\rightarrow \text{invisible})$ at 95% C.L. as a function of the jet energy resolution. The blue and red symbols show the results obtained from simulation of the IDR-L and IDR-S detector models, respectively, in full reconstruction and at various levels of cheating. The green crosses are obtained by varying the JER up and down w.r.t. IDR-L. [JL: fix axis titles!]

so, have a clear impact on this physics analysis. In the case of $\sqrt{s} = 250$ GeV, the impact of ISR and BS is much smaller, increasing the relative contribution from the JER.

8.3.5 τ polarisation, in $e^+e^- \rightarrow \tau^+\tau^-$

a few open points between Daniel, Mikael (referee) and JL, note in very advanced state

As shown in Sec. 8.2.2, the smaller ECAL inner radius of the small detector model slightly reduces the ability to identify the correct number of photons in highly-boosted τ decays. Using the product of efficiency times purity as a figure of merit, this leads to a 5% worse identification of $\tau \rightarrow \pi\nu$ and $\tau \rightarrow \rho\nu$ decays, while the identification of $\tau \rightarrow a_1\nu$ decays deteriorates by about 15% relative, c.f. Fig. 8.9.

In order to evaluate the impact of this difference in a physics example, the measurement of the τ polarisation in $e^+e^- \rightarrow \tau^+\tau^-$ has been studied, looking specifically at events with no significant ISR, so those *not* returning to the Z pole. For the $\tau \rightarrow \pi\nu$ channels, the magnitude of the π^\pm momentum can directly be used to extract the polarisation. In case of the $\tau \rightarrow \rho\nu$ decay, a polarimeter vector is constructed from the momenta of the π^\pm and the π^0 . A detailed description of the analysis and the polarisation extraction can be found in [96].

Figure 8.21 illustrates the precision on the τ polarisation achieved with IDR-L and IDR-S based on the π and ρ channels in the $P(e^-, e^+) = (-80\%, +30\%)$ data set, which dominates the combined precision. Thereby, various levels of cheating are shown, starting from the optimal result when using all MC information, including the neutrino momentum. The next entry shows by how much the performance in the ρ channel degrades by the approximate definition of the polarimeters used here³. The most significant effect occurs when reducing the number of signal events according to the selection efficiency of about 55% observed in the full analysis [JL: under clarification with Daniel]. The last three steps use the fully simulated and reconstructed events, apart from the entry “cheat ECAL”, which uses MC information for the π^0 in the ρ channel. In the last step, the full SM

³In principle, improved methods can be used, which however need further investigation [96].

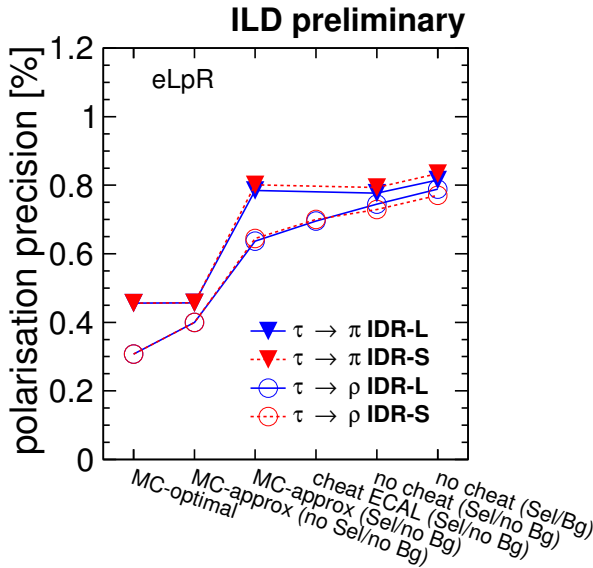


Figure 8.21. Precision on the τ polarisation achieved with IDR-L and IDR-S at various levels of cheating (see text) based on the π and ρ channels in the $P(e^-, e^+) = (-80\%, +30\%)$ data set.

background is added. Overall, the differences between IDR-L and IDR-S are very small, and probably due to limited MC statistics. The largest deterioration of the precision occurs when applying the selection efficiency. Thus, future improvements of the di- τ selection have the largest potential for improving this measurement.

8.3.6 Hadronic WW and ZZ separation in Vector Boson Scattering

IDR draft okayed by Taikan (referee). Note awaiting addition of plots from new high- Q^2 samples and comments from Taikan, otherwise ready for circulation.

Vector boson scattering is an important process for testing the unitarisation of WW scattering by the Higgs boson, as well as for measuring quartic gauge couplings, and thereby probing for anomalous contributions. Among all relevant final states, the reaction $e^+e^- \rightarrow \nu\nu VV \rightarrow \nu\nu qqqq$, where VV can be WW or ZZ , poses a particular challenge to the detectors and reconstruction algorithms, since it requires the separation of the hadronic W and Z decays without the ability to exploit kinematic constraints e.g. on the total event energy due to the two invisible neutrinos.

This benchmark, at a center-of-mass energy of 1 TeV, has already been studied in full detector simulation for the ILD LoI [1]. Now, we include for the first time all relevant aspects, in particular the full overlay from $\gamma\gamma \rightarrow$ low- p_t hadrons and from e^+e^- pair background, and we consider all quark flavours in the final state [97]. The W and Z mass distributions obtained with the current full reconstruction are shown in Fig. 8.22. Therein Fig. 8.22a shows the average di-jet mass per event, comparing ILD-L and ILD-S, while Fig. 8.22b shows the 2-dimensional distribution in the mass plane of the two invariant di-jet masses for ILD-L. At this level, no significant difference between the detector models can be observed.

Figure 8.23 shows the analogous distributions obtained when cheating the jet clustering (incl. the overlay removal), the jet pairing and when excluding events with semi-leptonic decays of heavy quarks, so that only the effects of the natural widths of the bosons, of fragmentation and hadronisation as well as the JER itself remain. Also here, no striking difference between the models can be seen, which leads to the conclusion that on this event sample, which is dominated by events with rather low invariant masses of the di-boson system, the effect of the slightly worse JER of ILD-S is hidden beneath the width and fragmentation/hadronisation corrections.

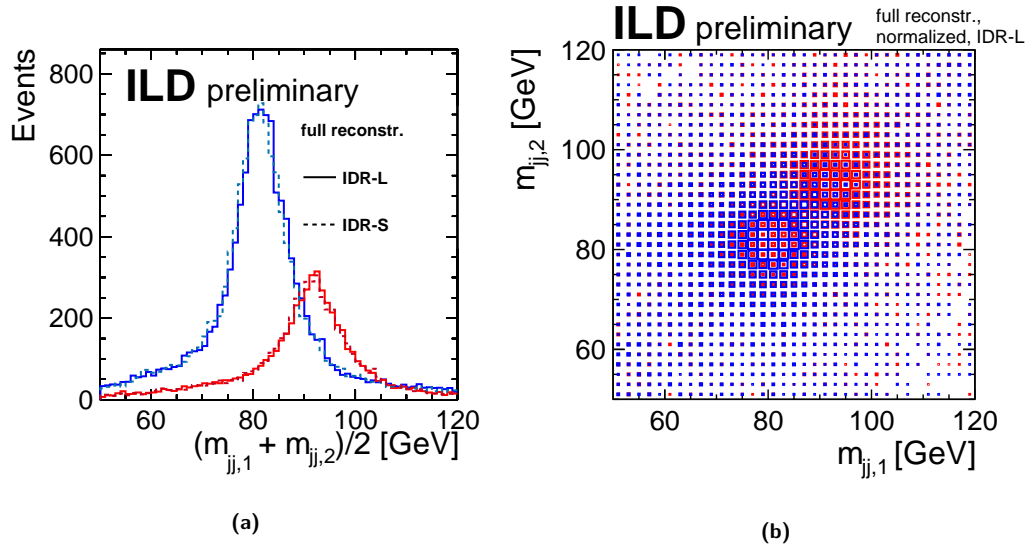


Figure 8.22. Dijet masses in $e^+e^- \rightarrow \nu\nu WW$ (blue) and $e^+e^- \rightarrow \nu\nu ZZ$ (red) events as obtained from the current full reconstruction.
(a) Average of the two di-jet masses per event. (b) 2D illustration of the two di-jet masses per event.

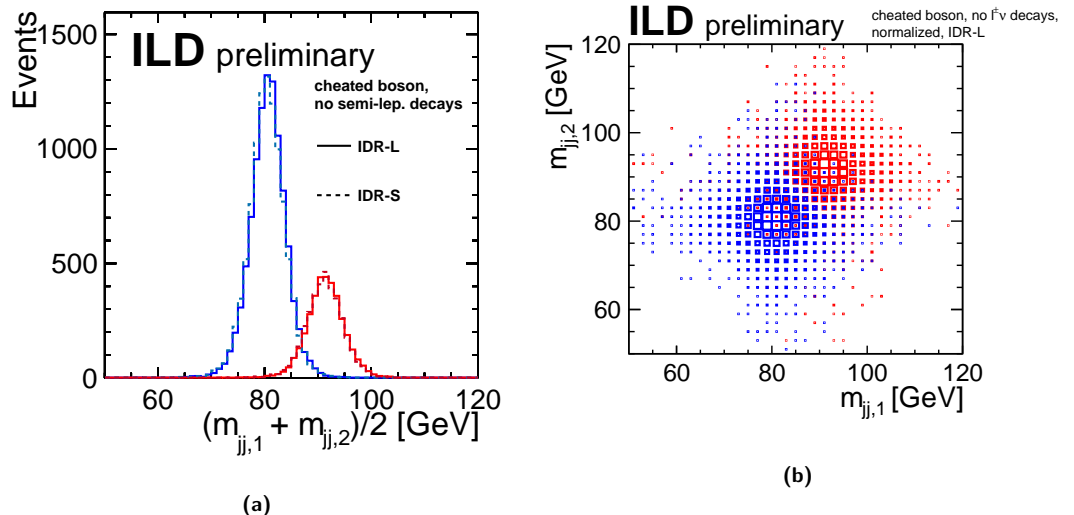


Figure 8.23. Dijet masses in $e^+e^- \rightarrow \nu\nu WW$ (blue) and $e^+e^- \rightarrow \nu\nu ZZ$ (red) events as obtained when cheating the jet clustering and excluding events where one (or more) jets contain semi-leptonic charm or beauty decays.
(a) Average of the two di-jet masses per event. (b) 2D illustration of the two di-jet masses per event.

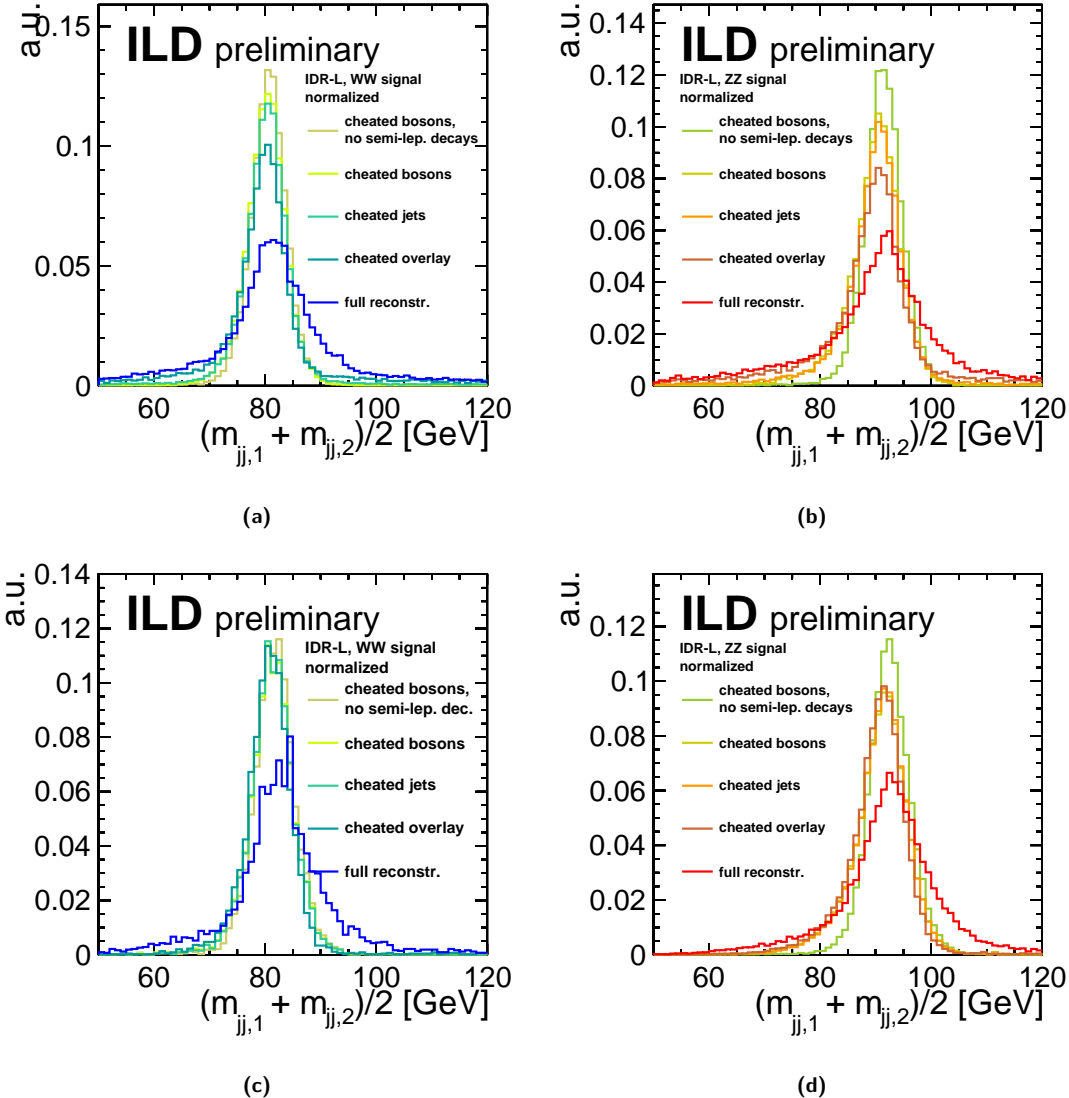


Figure 8.24. Average di-jet masses as obtained in full reconstruction at various levels of cheating.
 (a) inclusive $e^+e^- \rightarrow \nu\nu WW$ events. (b) inclusive $e^+e^- \rightarrow \nu\nu ZZ$ events. (c) $e^+e^- \rightarrow \nu\nu WW$ events with $M(WW) > 500$ GeV. (d) $e^+e^- \rightarrow \nu\nu ZZ$ events with $M(ZZ) > 500$ GeV.

Nevertheless, the differences between Fig. 8.22 and Fig. 8.23 are striking. Therefore, we investigated the impact of the size of various contributions individually as shown in Fig. 8.24, for ILD-L only. For the inclusive WW and ZZ samples, shown in Figs. 8.24a and 8.24b, the dominant effect is the residual of the non-perfect overlay removal, followed by the jet clustering itself and the semi-leptonic decays. Non-perfect jet pairing only plays a minor role. This can be compared to the situation found when only considering events with high WW/ZZ invariant masses, shown in Figs. 8.24c and 8.24d. In this case, the impact of non-perfect jet clustering is reduced to a negligible level. Instead, the effect of the residual overlay from low- $p_t \gamma\gamma \rightarrow \text{hadron}$ events dominates. For the ZZ events, also the missing neutrinos from semi-leptonic heavy quark decays play a visible role. These results demonstrate the need for development of more sophisticated high-level reconstruction algorithms, in particular for the overlay removal, the jet clustering and the identification and correction of semi-leptonic heavy flavour decays. For all these cases promising tools are under development, see e.g. Sec. 8.3.11 and Ref. [95].

8.3.7 Photon Energy Scale Calibration from $e^+e^- \rightarrow \gamma Z \rightarrow \gamma\mu^+\mu^-$

IDR draft signed off by Matthew (referee) and Takahiro. Note in a very incomplete state.

Di-fermion production, with or without radiative return to the Z pole, is an integral part of the ILC physics case. In addition, the radiative return events offer an important opportunity to cross calibrate the energy scales of various subdetectors. As a detector benchmark, we chose here the example of calibrating the photon energy scale against the momentum scale of the tracker. Thereby, the momenta and angles of the muons as well as the polar and azimuthal angle of the photon serve as input, from which the energy of the photon and the amount of energy lost in beamstrahlung and collinear ISR are determined by requiring conservation of energy and p_y between initial and final state. It should be stressed that it is not necessary to apply a Z mass constraint, which would introduce an additional uncertainty due to the large natural width of the Z resonance. A full description of this and alternative methods can be found in [98].

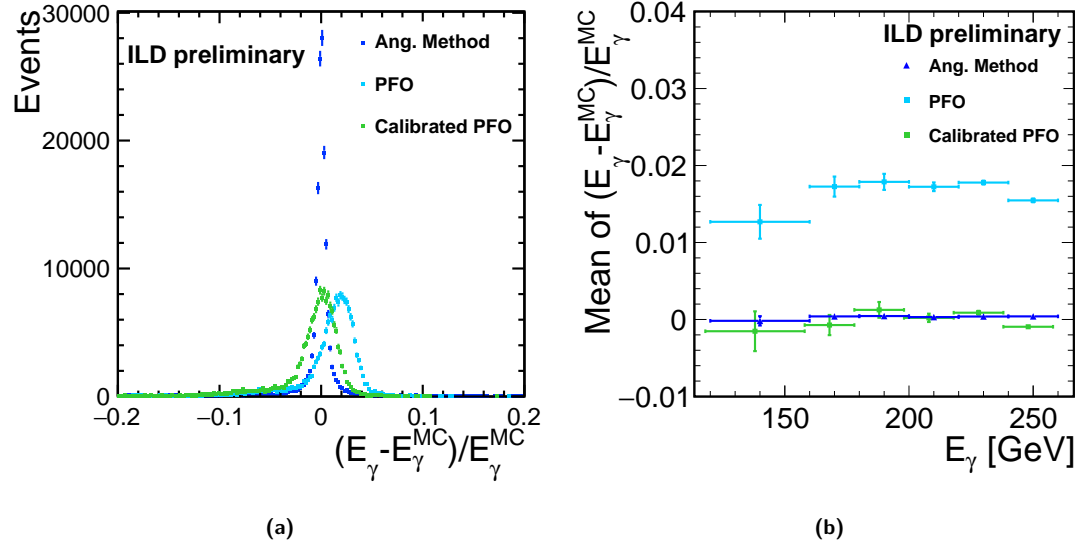


Figure 8.25. Deviation of the photon energy from its true value when using non-perfectly calibrated PFO-level energies (cyan), when calculating the photon energy from the μ momenta and kinematic constraints (blue, “angular method”) and after calibrating the mean PFO-level w.r.t. the mean obtained from the μ momenta (green). (a) Distribution of deviation for all photons in the sample. (b) Mean deviation in bins of the photon energy.

Figure 8.25 illustrates the power of this method by application to a non-perfectly calibrated

photon reconstruction in the large detector model, both inclusively for all photons (Fig. 8.25a) and in bins of the photon energy (Fig. 8.25b). Since the $e^+e^- \rightarrow \mu^+\mu^-\gamma$ sample is dominated by radiative returns to the Z pole, the majority of photons has high energies close to 241 GeV.

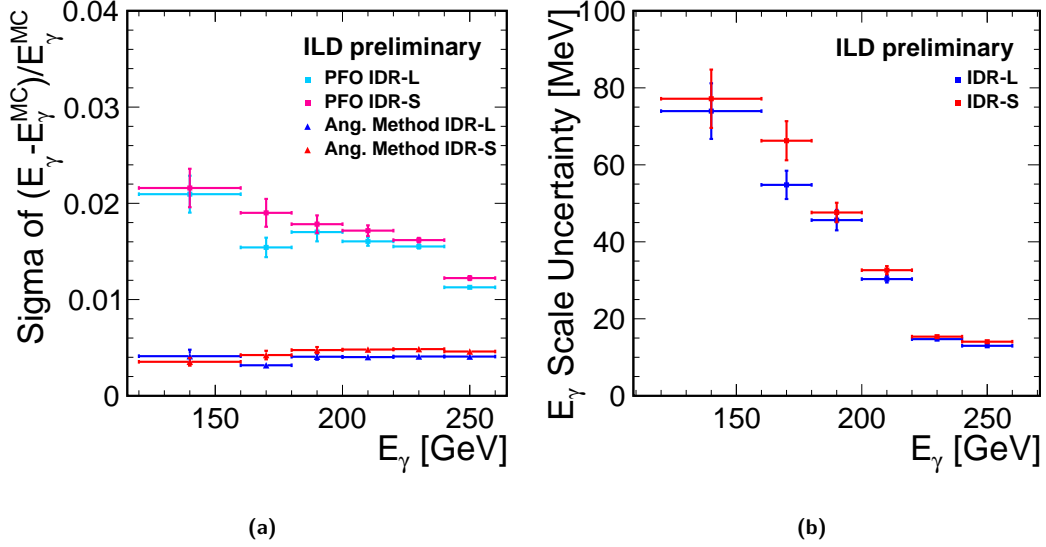


Figure 8.26. Uncertainty on the photon energy scale calibration as a function of the photon energy for IDR-L and IDR-S. (a) Relative uncertainty when using non-perfectly calibrated PFO-level energies (cyan/magenta) and when calculating the photon energy from the μ momenta and kinematic constraints (blue/red, “angular method”). (b) Absolute uncertainty from the angular method in MeV.

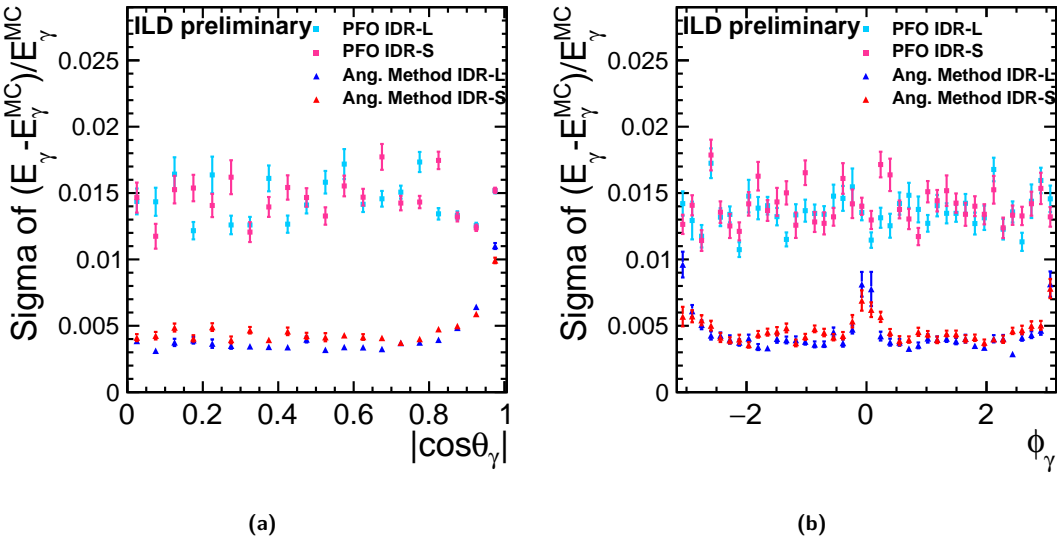


Figure 8.27. Resolution of the photon energy when using non-perfectly calibrated PFO-level energies (cyan/magenta) and when calculating the photon energy from the μ momenta and kinematic constraints (blue/red, “angular method”). (a) as a function of the polar angle (b) as a function of the azimuthal angle

The resolution of angular method, i.e. the width of the blue distribution in Fig. 8.25a is shown for IDR-L and IDR-R in Fig. 8.26a as a function of the photon energy. This translates into an absolute uncertainty on the photon energy scale calibration of about 10 MeV for high-energy photons, as shown in Fig. 8.26b. The angular dependencies of the resolution of this method are shown in Fig. 8.27. As a function of the polar angle, Fig. 8.27a clearly shows the effect of the better momentum resolution of IDR-L for central high-momentum tracks, while in the two most forward bins, the small detector performs better due to its higher magnetic field. As a function of the azimuthal angle, there is

no particular region where the performance of the two detector models differs, as can be seen in Fig. 8.27b. The modulation of the resolution with ϕ is an effect of using the p_y constraint only, which is the easiest method as the p_y conservation is not influenced by the beam crossing angle. The modulation will be reduced when also p_x balance is exploited e.g. in a kinematic fit.

8.3.8 A_{FB} and A_{LR} from $e^+e^- \rightarrow b\bar{b}$

awaiting potentially new plots (?) and /or confirmation after final checks from Adrian

The measurement of the left-right- and forward-backward asymmetries of b -quarks requires to distinguish the jet from the b -quark from the \bar{b} -jet. The two most important techniques for this are to reconstruct the charge of the secondary vertex, and to identify charged Kaons in the b -decay chain and exploit their charge. While the first method requires a complete reconstruction of all tracks from the secondary vertices as possible, the Kaon ID hinges upon a special feature of ILD, namely the measurement of the specific energy loss dE/dx in the TPC. In order to arrive at a reliable b -charge measurement, a consistent double-tag is required for each event, allowing for all four possible combinations of the two techniques. All details of the event reconstruction and selection can be found in [99].

Figure 8.28a compares the acceptance of the b -jet reconstruction for the large and the small version of ILD. For $|\cos \theta_b| < 0.5$, corresponding to a large part of the endcap region, the acceptance of IDR-L is about 1% larger than for IDR-S. [JL: do we understand why? Loss of soft tracks due to higher B-field?] The purity of the four combinations of charge-ID (two methods times two jets) is shown in Fig. 8.28b. While the charge-ID via vertex charge performs identically for both detectors, the Kaon-charge ID yields a higher purity for IDR-L due to the larger radius of the TPC, which improves the dE/dx resolution.

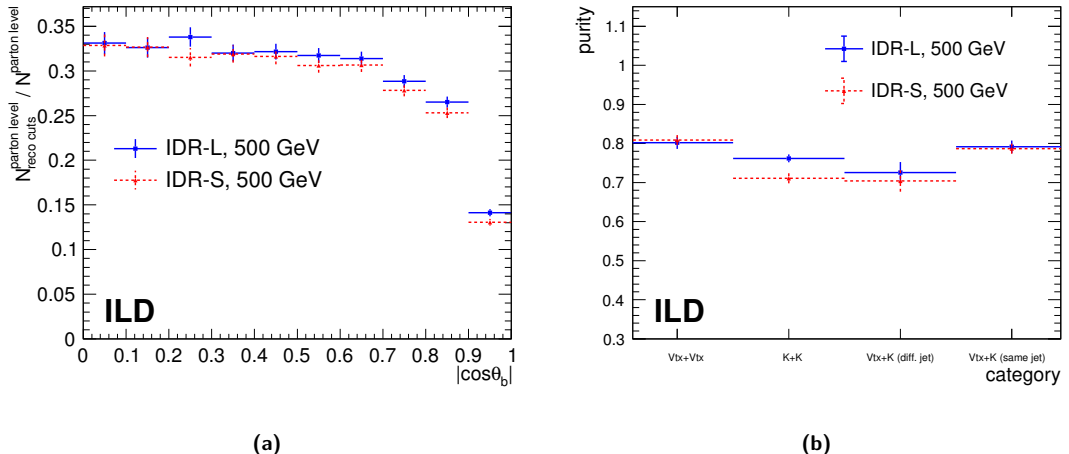


Figure 8.28. (a) Acceptance of the $e^+e^- \rightarrow b\bar{b}$ analysis as a function of $\cos \theta_b$ of the b -quark for IDR-L and IDR-S. (b) Purity of the four different categories for charge tagging for IDR-L and IDR-S.

The final physics observable, namely the reconstructed $|\cos \theta_b|$ distribution, is shown for the example of 46 fb^{-1} of purely left-handed electron and purely right-handed positron data in Fig. 8.29. The result for both detector models is compared to the parton-level distribution. [Precisions on A_{FB} and/or A_{LR} to come after first circulation.]

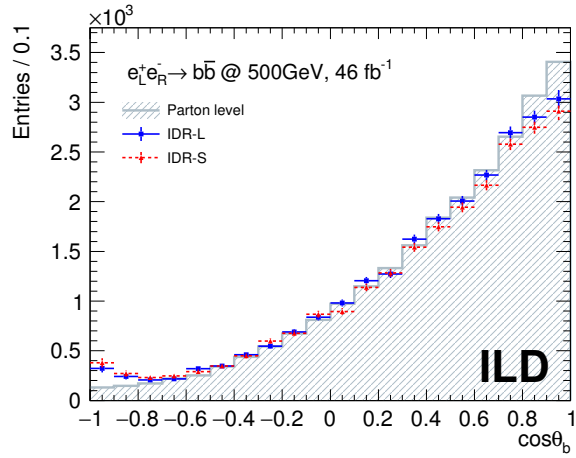


Figure 8.29. Generator-level distribution of $\cos\theta_b$ and the corresponding reconstructed distributions for IDR-L and IDR-S. The distribution is shown for 46 fb^{-1} of pure $e_L^- e_R^+$ data.

8.3.9 A_{FB} and A_{LR} from $t\bar{t} \rightarrow bbqql\nu$

awaiting new version of Fig 8.30 and a matching purity plot, precisions on asymmetries and full draft of note.

Building on the $e^+e^- \rightarrow b\bar{b}$ benchmark described in the previous section, the analogous study has also been performed for the case of $e^+e^- \rightarrow t\bar{t}$ [99]. So far, only the semi-leptonic channel has been analyzed, while the clean environment of a lepton collider in principle also allows to include the large statistics available in fully hadronic $t\bar{t}$ events. In order to prepare for the fully hadronic case, the vertexing and Kaon-ID based methods for charge identification have already been included in the analysis. The acceptances of the lepton-tag as well as of several double-tag combinations are compared for the large and small detector models in Fig. 8.30. The single-tag based on the lepton charge (“ L_{cut} ”) is 100% efficient since the presence of a lepton is already required in the event selection. In fully hadronic $t\bar{t}$ events, only the double-tags without lepton information as shown in the first four bins, could be used, in analogy to the case of the $b\bar{b}$ analysis, c.f. Fig. 8.28a. While the size of the detector has no direct influence on the semi-leptonic analysis, both the vertex and Kaon-ID based methods are more efficient in case of the large detector.

The final physics observable, namely the reconstructed $|\cos\theta_t|$ distribution, is shown for the example of 46 fb^{-1} of purely left-handed electron and purely right-handed positron data in Fig. 8.31b, along with the corresponding distribution for the b -quark in Fig. 8.31a. The results for both detector models are compared to the parton-level distribution. No difference is found here between the two detector models since the analysis is only based on the lepton-tag.

[Precisions on A_{FB} and/or A_{LR} will be added after first circulation.]

8.3.10 Discovery Reach for extra Higgs Bosons in $e^+e^- \rightarrow Zh$

[Limit plot will be added after circulation. Note will be updated soon.]

Searches for additional Higgs bosons or other new scalar particles are theoretically well-motivated and highly complementary to the sensitivity of hadron colliders. Due to the SM-likeness of the 125-GeV Higgs boson, additional Higgs bosons are expected to have a suppressed coupling to the Z boson. Nevertheless, they can be searched for using the same recoil technique which is the basis of the decay-mode independent measurement of the total Higgsstrahlung cross section. While in principle all visible decay modes of the Z boson can be exploited in this search, $Z \rightarrow \mu^+\mu^-$ as the cleanest mode has been chosen as a benchmark here [100]. The two most important detector performance

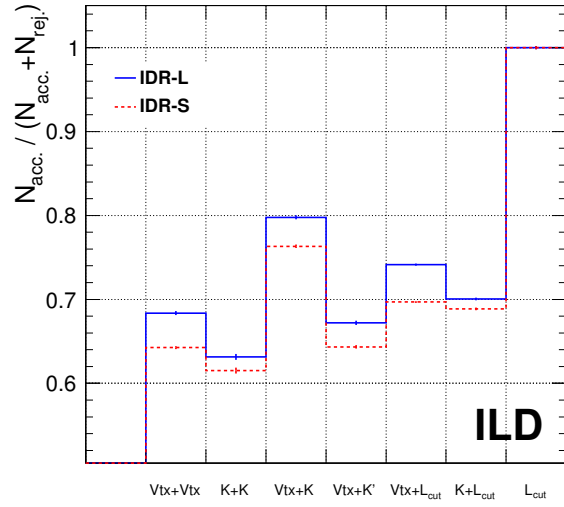


Figure 8.30. Acceptance of various methods to identify the charge of the t/\bar{t} quarks. In the actual analysis, only the single-tag based on the lepton charge (“ L_{cut} ”) is used. The double-tag categories without lepton-tag are shown here as proxy for the fully hadronic channel. [matching purity plot, like in Fig. 8.28b, will be added after first circulation]

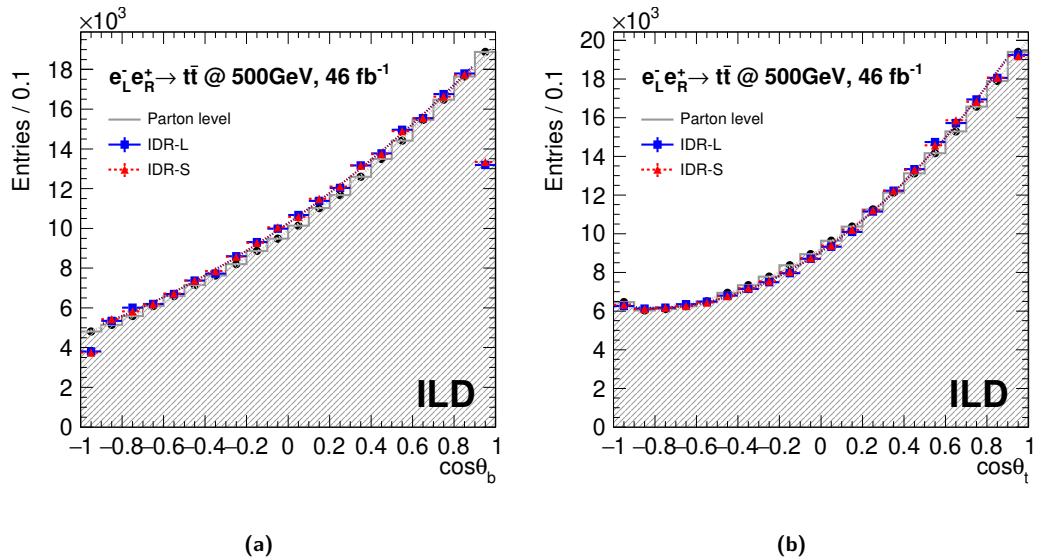


Figure 8.31. Generator-level polar angle distributions and the corresponding reconstructed distributions for IDR-L and IDR-S. The distributions are shown for 46fb^{-1} of pure $e_L^- e_R^+$ data. (a) Polar angle of the b -quark $\cos \theta_b$. (b) Polar angle of the t -quark $\cos \theta_t$.

aspects for this analysis are the momentum resolution for the two muons and the ability to detect and identify ISR photons in the detector. The latter applies in particular for the lower Higgs masses, where $M_h + M_Z \ll \sqrt{s}$ and thus significant photon radiation occurs frequently. If the photon is detected, then the event kinematics can be corrected accordingly, improving the separation of signal and background significantly.

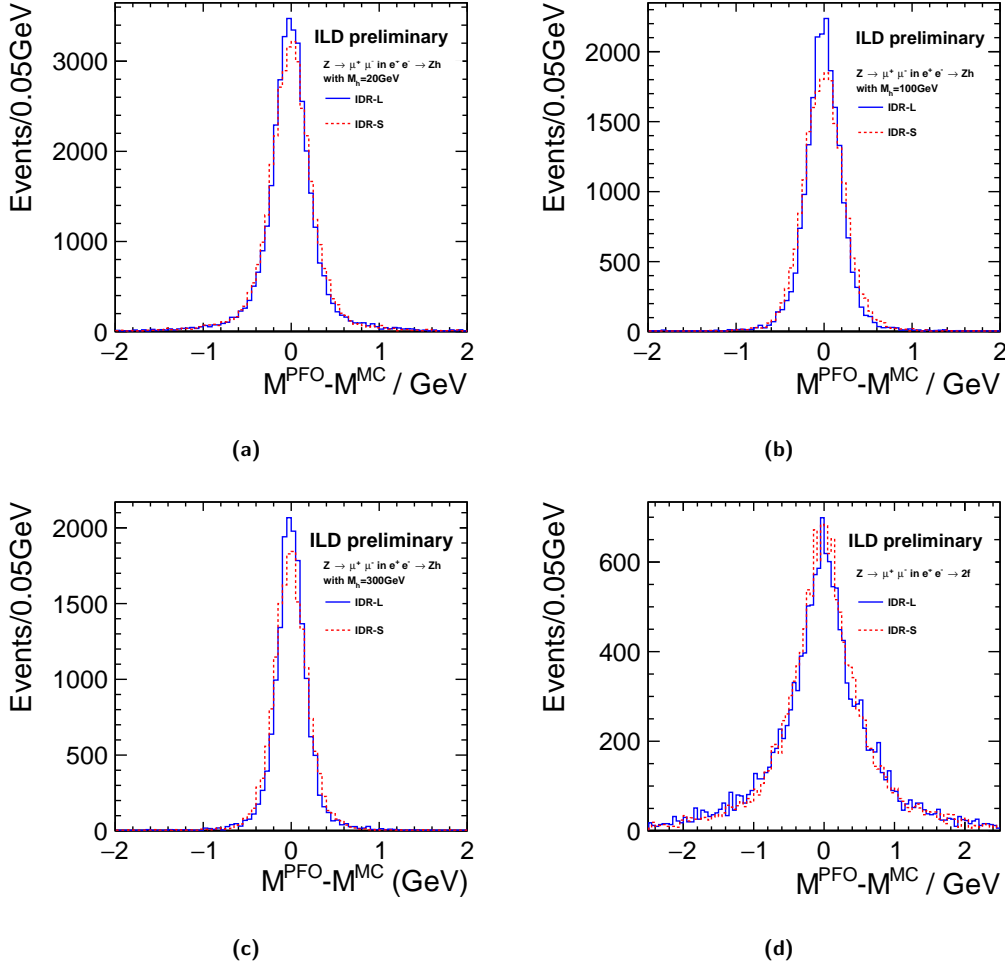


Figure 8.32. Event-by-event difference between reconstructed and generated di-muon mass for different types of events sampling different ranges in polar angle and momentum of the muons in IDR-L and IDR-S: (a) $Z h$ signal with $M_h = 20\text{ GeV}$ (b) $Z h$ signal with $M_h = 100\text{ GeV}$ (c) $Z h$ signal with $M_h = 300\text{ GeV}$ (d) $2f$ background.

Figure 8.32 shows the event-by-event difference between the reconstructed and generated di-muon mass for signal events with different Higgs masses as well as for the 2-fermion background. Since the underlying distributions in momentum and polar angle differ significantly, also the difference between IDR-L and IDR-S varies between the different samples. With higher Higgs masses, the Z is less and less boosted, thus the muons are more and more central and back-to-back, resulting in an overall better mass reconstruction and a better performance of the large detector. In case of the 2-fermion background, about half of the events returns to the Z pole, resulting in forward boosted Z 's with a small opening angle between the also forward-going muons. In those events which do not return to the Z , the muons have higher momenta than in the signal samples. In combination, the mass reconstruction in the 2-fermion events is worse, but when comparing the two detector models, the better momentum resolution of ILD-S in the forward region and its worse resolution in the barrel roughly cancel.

This can be seen much more clearly from the event-by-event mass resolution as calculated from

the errors on the track parameters, shown in Fig 8.33 for the same four event samples. In case of the Higgs signal, the large detector always gives a significantly better resolution. In case of the 2-fermion background, there is a population at the best resolutions which behaves like the signal, while at the worse resolutions the small detector performs better than the large.

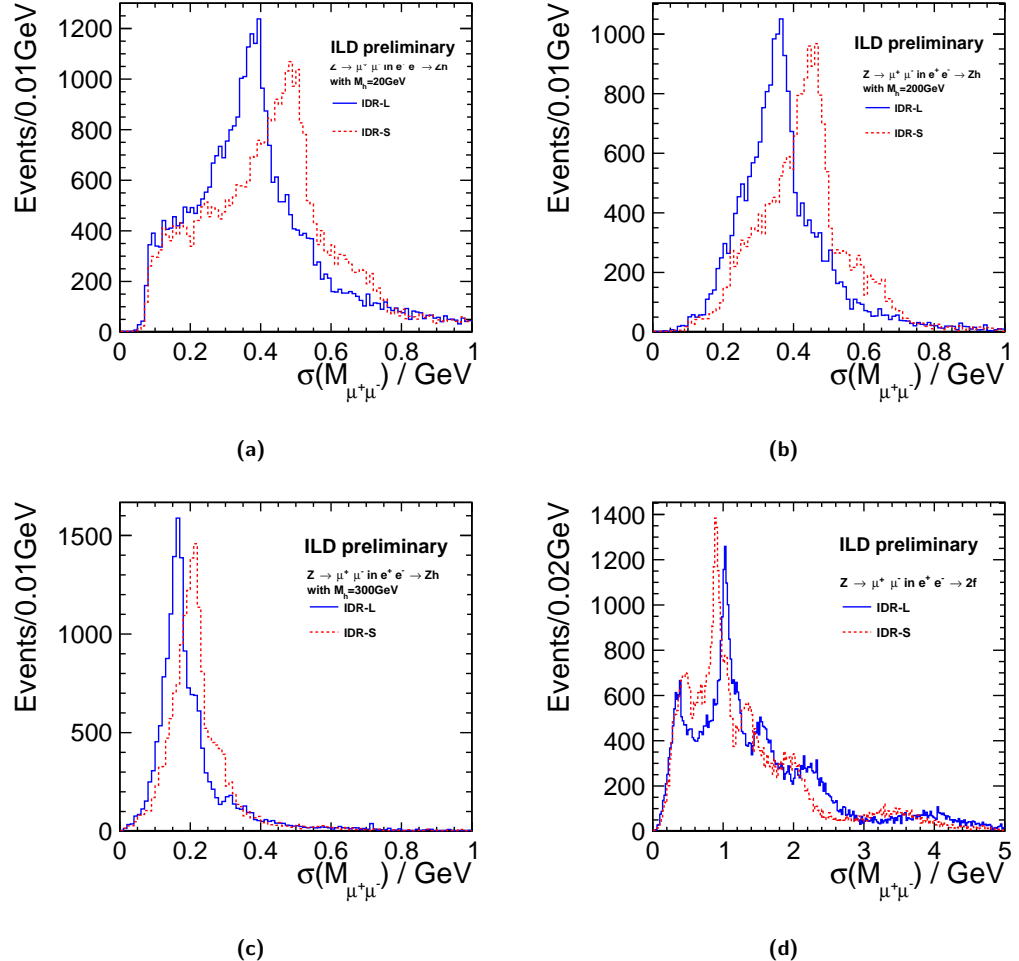


Figure 8.33. Event-by-event mass resolution calculated by error propagation from the track fit for different types of events sampling different ranges in polar angle and momentum of the muons in IDR-L and IDR-S: (a) Zh signal with $M_h = 20 \text{ GeV}$ (b) Zh signal with $M_h = 100 \text{ GeV}$ (c) Zh signal with $M_h = 300 \text{ GeV}$ (d) $2f$ background.

Figure 8.34 compares the performance of IDR-L and IDR-S in terms of the identification of ISR photons. [JL: at which level of the analysis is this plot made, and with which algorithm? Need documentation in note...]

Limit plot to come.

8.3.11 Discovery Reach for and Characterisation of low ΔM Higgsinos

[physics performance still w.i.p., will be added after first circulation] New particles with maximally electroweak interactions and small mass differences in the decay chain are among the prime examples of discovery opportunities at future $e^+ e^-$ colliders. A famous example of such kind of new physics are higgsinos, which are expected to be light in natural SUSY models and tend to have small mass splittings, in particular when the gaugino masses are much heavier. One of the model points studied previously in fast detector simulation [101], with a mass splitting of only 770 MeV between the chargino and the LSP, is used as a detector performance benchmark here [102]. The mass of the chargino is about 167 GeV.

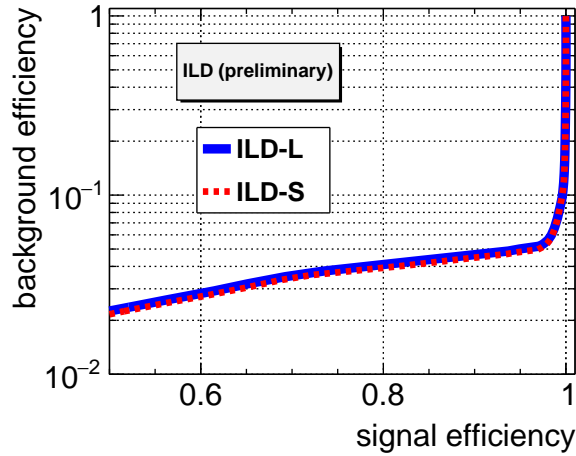


Figure 8.34. Performance of the ISR photon identification in IDR-L and IDR-S. True ISR photons are considered as signal, while the background comprises all PFOs identified as ISR photon, but having another true origin. [JL: improve plot layout]

Figure 8.35 shows the tracking efficiency as a function of transverse momentum as obtained in these events at a center-of-mass energy of 500 GeV. For transverse momenta below $p_t = 300$ MeV, a clear difference can be seen between the two detector models due to the higher magnetic field of IDR-S. For this specific model point, which lies – with $2M(\tilde{\chi}_1^\pm) \approx 330$ GeV – significantly below the kinematic limit, the efficiency to detect all charged decay products is around 60% and differs only by 2% between IDR-L and IDR-S, thanks to the sufficient boost of the charginos. For chargino masses closer to the kinematic limit, however, the typical p_t will be even lower, and the difference visible in Fig 8.35 will lead to a larger effect. The low p_t tracking efficiency could be recovered at least partially by reducing the radii of the vertex detector layers for IDR-S, which is possible since the higher magnetic field also confines the pair background at smaller radii.

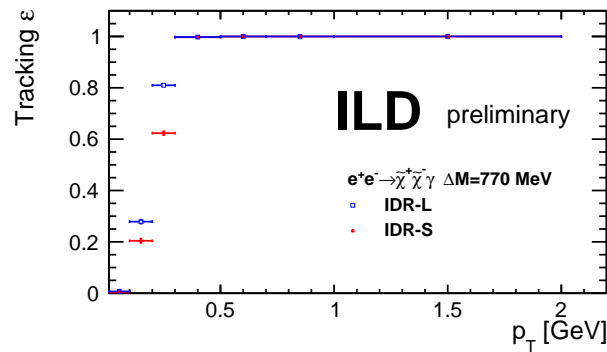


Figure 8.35. Tracking efficiency obtained in IDR-L and IDR-S for pair production of charginos which are only 770 MeV more heavy than the LSP and thus have only very few and soft visible decay products.

Main analysis plots to come.

8.3.12 WIMP Discovery Reach and Characterisation in the Mono-Photon Channel

[preliminary material suffering from BCAL issue available on confluence, awaiting final plots after fix] The search for WIMP production via the mono-photon signature is another example of a search highly complementary to the HL-LHC, which predominantly probes couplings of WIMPs to quarks. This channel has been chosen as a benchmark specifically in order to test the

photon reconstruction and the performance of the BeamCal, which plays an essential role in vetoing background from Bhabha scattering. The benchmark analysis is described in more detail in [103] and closely follows [104].

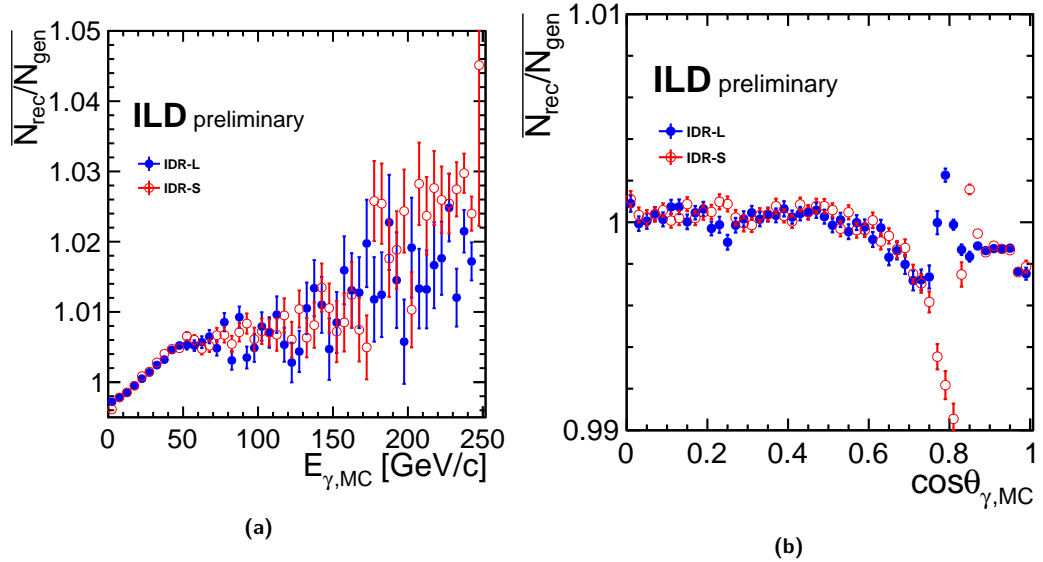


Figure 8.36. PLOTS ARE PLACEHOLDERS Ratio of reconstructed and generated photons per event as a function of (a) the photon energy (b) the photon polar angle.

Figure 8.36 shows the ratio of reconstructed and generated photons per event as a function of the photon's energy and polar angle. While it has been shown in [104] that the actual energy resolution is not very critical in this analysis, it is important that the number of photons is correct, since the signature of a single photon and no other significant detector activity forms the basis of the selection. As can be seen in Fig. 8.36a, the average number of reconstructed photons per generated photon tends to be a few permille below 1 at low photon energies. With increasing photon energy, the tendency of the particle flow reconstruction to split a photon into two increases, but stays below the level of 3%. Figure 8.36b shows that these splits predominantly occur in the corner region between the barrel and the endcap, which sits at different values of $\cos \theta$ for IDR-L and IDR-S due to the different aspect ratios of the two detector models. The apparent inefficiency of about 1% in case the small detector has been tracked to a correction in the reconstruction which has not been appropriately adjusted for the different aspect ratio of the small detector, which leads to the artefact that the PFOs exist, but are not recognized as photons by the particle flow. All the features in these two plots are expected to be reducible with further development of the particle flow reconstruction.

Figure 8.37 compares the number of reconstructed clusters in the BeamCal of the two detector models. Ideally, the $\nu\bar{\nu}\gamma$ events, which serve as proxy for the WIMP signal, should have no BeamCal cluster, while in case of the $e^+e^-\gamma$ events at least one BeamCal cluster should be found. Events with at least one cluster in the BeamCal will be rejected in the analysis. As expected, the probability to falsely reject a $\nu\bar{\nu}\gamma$ event is somewhat lower in case of the small detector, since the stronger magnetic field confines the pair background to smaller radii.

The final result of the analysis is compared in Fig. 8.38 for the two detector models.

add description once finl plot is available.

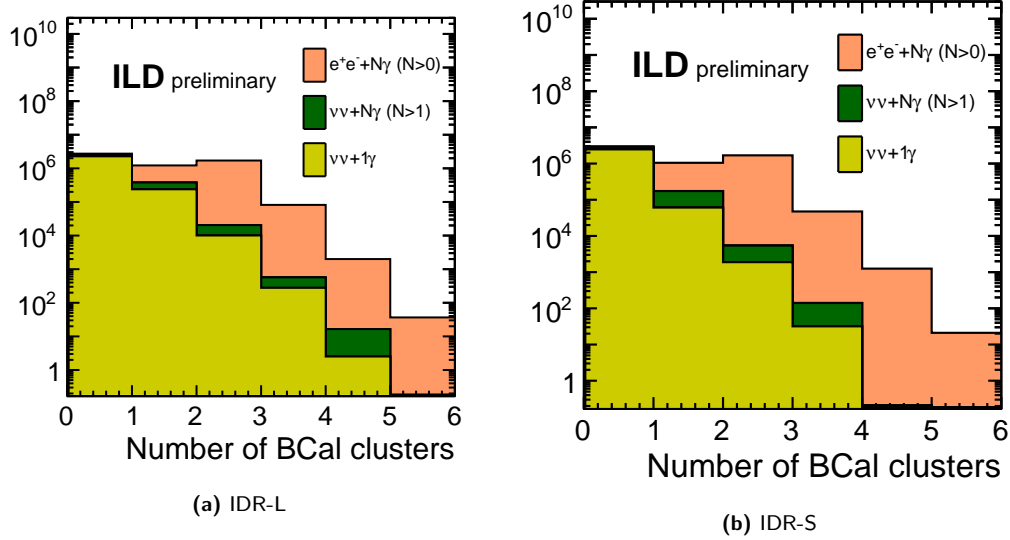


Figure 8.37. PLOTS ARE PLACEHOLDERS [JL: put detector labels on plots] Number of BeamCal clusters reconstructed in radiative neutrino and radiative Bhabha events.

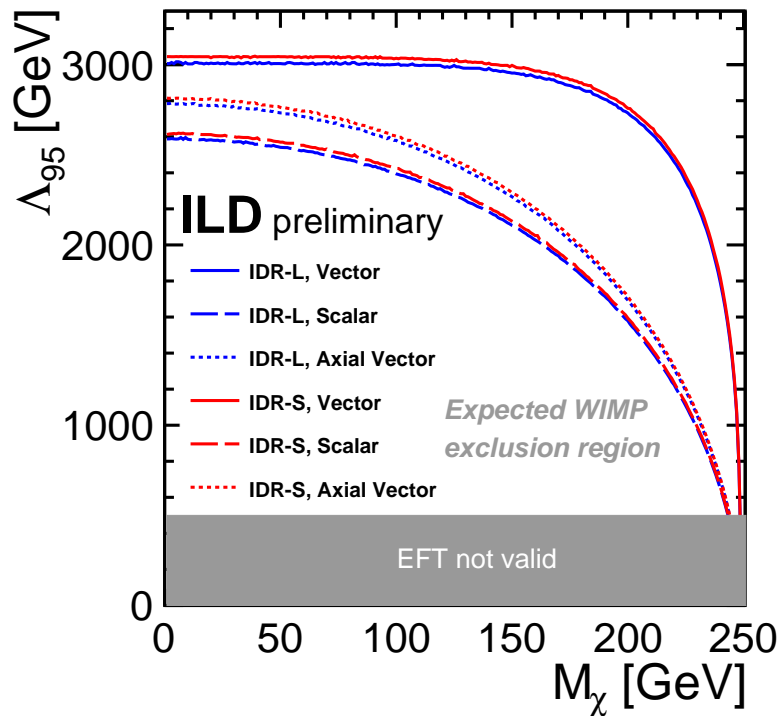


Figure 8.38. PLOT IS PLACEHOLDER Expected sensitivity at 95% CL in the plane of the new physics scale Λ vs the WIMP mass M_χ for the cases of a vector, axial-vector or scalar operator describing the WIMP-SM interaction.

9 Costing

Henri Videau
6 pages

9.1 Introduction

In this chapter the current state of the ILD costing is presented. There is a strong similarity with the costing exercise for the DBD but also quite some differences. The most obvious is that the dimensions have evolved and that we try now to cost two models of ILD: the "large model" very similar to the DBD baseline and the "small model" where the outer radius of the TPC has been reduced grossly by 30cm. One important issue is to relate the cost difference between the two models with the difference observed in their relative performances. It provides an evaluation of the impact of the size much better defined than was done with just some scaling laws. For the ECal, a version with a slightly coarser sampling is also estimated.

9.2 The method

At the time of the DBD the effort had been put on trying to have a costing coherent with the SiD estimate and the method of the accelerator had been used, i.e estimating in an "ILC currency", the ILCU. This implied making translations from different currencies using the exchange rates but mostly "Purchase Power Parities" and the difference between these two estimates may generate huge differences. At that time an ILCU was 0.97 Euros using PPP's. For todays exercise ILD decided to use Euros as counting units. When originating from Japan, like for silicon diode matrices, the prices in euros were provided by the vendors.

Except for this question the method used to establish the costing is totally similar to the DBD. It rests on the knowledge of the fabrication processes and the prices provided by the numerous prototypes built these last years. The idea is to identify the cost drivers, often very sensitive to strong price evolution, and have a precise Work Breakdown System identifying the procurements, the tooling, the fabrication operations to estimate also the manpower, which is now most often included in the cost. The manpower may be twofold, in house manpower linked mostly to the follow-up of the operations but also to some work when the quality required requests it and the rather limited amount permits it, but we consider also industrial manpower when we do not have already industrial offers and we try to figure out a possible price by estimating the cost of a fabrication.

9.3 The costing of the different sub-detectors

The cost of each sub-detector making ILD is reviewed. This is done for both ILD models, the large and the small. As anything inside the TPC in radius is untouched, there is only one price quoted for the vertex detector, the inner tracker, the forward tracker and the forward calorimetry, this last item being composed of the Lumical, the ECal ring, the LHCAL and the BeamCal. On the contrary the costs for the TPC, the SET, the electromagnetic and hadronic calorimeters, the magnet system and the muon system are to be provided for both versions.

Table 9.1. Elements of cost of the vertex detector in kEuros.

Vertex detector						
Cost	Sensors	Mechanics	Electronics	Services	Installation	Total
Material	1152	452	486	770	100	2960
Manpower	100	500	400	250	200	1450
Total	1252	952	886	1020	300	4410

Table 9.2. Elements of cost of the SIT in kEuros.

Silicon Inner Tracking						
Cost	Sensors	Mechanics	Electronics	Services	Installation	Total
Material	3820	760	1275	1580	110	7545
Manpower	200	500	800	300	200	2000
Total	4020	1260	2075	1880	310	9545

9.3.1 The vertex detector

This cost estimate has been provided by the note "ILD VXD and SIT Costing Estimates" by Auguste Besson and Marc Winter (January 2019) which updates the DBD. See table 9.1

9.3.2 The SIT

This is a version for a SIT using pixels in contrary to the DBD version which used strips. The costing of this version is provided by the note by A. Besson and M. Winter referenced above for the vertex. Therefore no direct comparison between the DBD cost and this one, in particular since in the DBD SIT and forward tracker were put together. See table 9.2.

9.3.3 The forward tracking

No update since the DBD where all the elements using silicon strips (strip forward disks, SIT, SET and even ETD) were summed together. There are 4 disks using pixel technology, the 12 other disks use strip technology. We guess a global estimate of 2MEuros expecting a real update from Marcel Vos.

9.3.4 The forward calorimeters

In the DBD This has been updated except for the ECal ring which remains more or less an orphan. Since the DBD the L* has been changed and the calorimeters adjusted. The three forward calorimeters, namely the BeamCal, the LumiCal and the LHCAL have been reexamined in detail considering for each of them the mechanical elements, sensors, ASICs, front-end electronics, power supplies, data acquisition, tooling and manpower. On top of these common items LumiCal and LHCAL need some specific fan-outs and the LumiCal needs a laser positioning system. This is summarised in the table 9.3 for a total of 8.44 MEuros and 6 man-years equivalent to 0.48MEuros.

9.3.5 The Time Projection Chamber (TPC)

Should exist in two versions large and small. In the DBD the TPC price quoted was 35.9 MILCU which translates to 36.6 MEuros of today. This is for the large model, for the small one it may be scaled down to 27.0 MEuros. Should come sometimes dixit Paul Colas.

Table 9.3. Elements of cost of the forward calorimeters in kEuros and manpower in MY.

	BeamCal	LumiCal	LHCAL
Mechanics	650.	635	990
Connectivity		90	140
Sensors	900.	1600	1200
Laser system		70	
Front-end ASICs	175.	280	215
Front-end electronics	94.5	152.5	54.5
Power supplies	80.	170	80
Data acquisition	217.	337	217
Tooling	30.	30	30
Total	2150.	3365	2927
Manpower	2	2	2

9.3.6 The outer silicon tracker (SET)

No real design exists. The end cap part, coined ETD, has disappeared since the DBD. The cost from the DBD is quoted 21 MILCU for both SET and ETD. A cost for the SET alone can be guessed from the areas but the number of layers is different; the SET area over the total is about 0.73 and its cost is then claimed to be 15.3 MILCU or 14.84 MEuros 2008, or about 15.5 MEuros 2018 after running the Euro. No cost was established for the small model. It could be scaled from the large with the ratio of the radii: 0.807, providing a cost of 12.6 MEuros.

An estimate can more accurately be derived from the cost of the CMS tracker. It is about 275kCHF per square meter of detector, silicon and mechanics. The SET area in the large model is about 52.9 square m with two layers like in the CMS tracker. That makes 14.5 MCHF to which miscellaneous things like cooling power supply and back-end electronics should be added for about 3 MCHF, say 20%: $14.5 * 1.20 * 0.89 = 15.5$ MEuros. In the small model the area is 42.7 square m for a cost of 12.5 MEuros.

9.3.7 The electromagnetic calorimeter (ECal)

9.3.7.1 The silicon version

A costing had been done at the time of the DBD, amounting to 157 MILCU or 152MEuros, about half of it in the cost of the diode matrices. The manpower was left aside. The new costing of the silicon electromagnetic calorimeter has been derived from a more detailed WBS in the form of about 400 lines of Excel. This WBS follows a detailed and chronological fabrication description which estimates the procurements for the different operations, the tooling needed and the operations with the amount of manpower and the duration of the operations caring about the fact that none should have a duration longer than two years. Almost all the difference, except for a slight tungsten price rise, between the DBD estimate and the actual large version comes from the change in the diode matrices cost estimate. For the new version we use the offer to CMS for making the HGCAL matrices. The total price, manpower excluded, reaches then 117 MEuros. In this case the manpower has also been estimated at 158 MY equivalent to 13 MEuros, bringing the total amount to 130 MEuros.

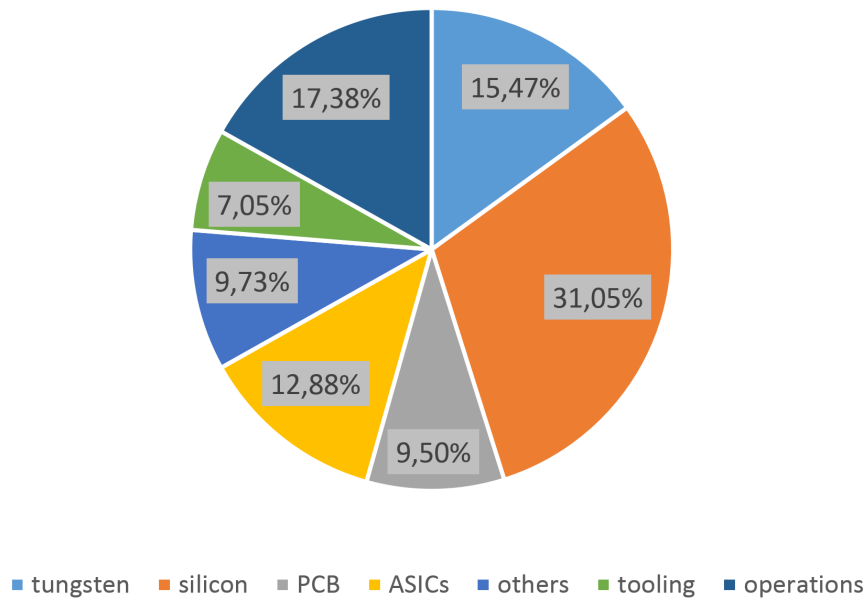
Aside the large version the small one has been also fully costed to 90MEuros + 11MEuros for the manpower making 101 MEuros. For this version a model with the small size but also with a slightly reduced number of active layers (26 instead of 30) is also costed. The impact on the resolution of the sampling is compensated by an increase of the silicon thickness to 725 micrometers. This provides a further reduction of the cost to 80 + 10 MEuros. It has to be noted that the reason for this change in sampling is more dictated by technical reasons than cost. It has also to be noted that these estimates

Table 9.4. Estimates for the three versions of silicon ECal, in MEuros.

Version	Material	Manpower	Total
Large model	117	13	130
Small model	90	11	101
Small model with reduced sampling	80.	10	90

are slightly at the advantage of the large model since most of the tooling has been estimated at the same cost for the different options. These numbers are summarised in table 9.4

As a result, the sharing between the main items is presented. If the silicon matrices cost still dominates the procurements, others are important like tungsten, printed boards, ASIcs. This sharing is presented for the small model with reduced sampling in the Figure 9.1. The cost without manpower

**Figure 9.1.** Contributions of the different items to the cost in the case of the "small model" with a reduced sampling.

reaches 80 MEuros for 119 man-years.

9.3.7.2 The scintillator version

The cost is said to be unchanged from the DBD. It was 74 MILCU which translates to 75 MEuros after applying the price evolution. The assembly remains to be estimated as well as the manpower. No quote given for the small model but a scaling could be attempted.

9.3.8 The hadron calorimeter

9.3.8.1 The analogue version

No update for the large model, the DBD estimate appears as still valid today for essentially all the items. For the DBD the cost was 44.9 MILCU translating into 45.7 MEuros 2018 with no manpower quoted. No detailed quote for the small model, a simple scaling corresponds to a factor 0.84 from the large to the small which cost is then 38.4, 7.3 MEuros less.

Table 9.5. Elements of cost of the magnet system in MEuros.

Magnet system	88
Coil	29.4
Conductor and winding	18.5
Internal cryogenics and suspension	3.7
Suspension system	0.3
Internal instrumentation	0.9
Tooling, assembling	5.4
Qualification and partial testing	0.6
Ancillaries for coil	10.6
Cryogenics and vacuum	6.5
Electrical power circuits	0.9
Control and safety systems	0.6
Engineering (transport to cavern)	2.1
Integration in cavern	0.3
Field mapping	0.3
Yoke and vacuum tank	48.4
Yoke steel including works and vacuum tank	39.6
Support	1.2
Moving system	2.6
Assembly	4.8
Photogrammetry and survey	0.3

9.3.8.2 The semi-digital version

No update really available for the large model but the cost is estimated to remain similar. For the DBD the cost was 44.8 MILCU translating into 45.6 MEuros 2018 with no manpower quoted. No real quote for the small one, a simple scaling corresponds to a factor 0.84 from the large to the small which cost is then 38.3, 7.3 MEuros less.

9.3.9 The magnet

The magnet (coil and yoke) has been revisited fully. The source for the evaluation is still the CMS documents. But the way to derive the numbers has been strongly reconsidered. The CHF costs from CMS have been converted to Euros at the exchange parity of the time, then the prices in Euros have been evolved to 2018. Therefore a comparison between the DBD and actual costs may not be totally relevant. One thing to notice though is the strong reduction in the yoke cost. This is due to a change in the reference cost of the iron. At the time of the DBD a price of 6ILCU/kg had been agreed upon with SiD and CLIC, in the current costing, the price payed for CMS has been used, translated in Euros and scaled today providing a price of 3.5 Euros/kg. It is not perfectly clear that this reflects fully a market price. The anti-DID is not taken here into consideration since it is not clearly defined. All this is described in detail in a note by Ch. Berriaud.

No detailed approach for costing the small version has been taken. A priori we expect the cost for the small version to be reduced but instead of 3.5T the nominal field is 4T. The impact on the coil winding and on the flux return is not trivial and it is not even clear that the cost of the magnet system does not grow. A good approximation may be to keep the cost constant. Anyway the cost reduction linked to relaxing the stray field constraint would certainly dominate.

Some studies are going on with Japanese companies and at some point their offers shall be compared.

9.3.9.1 The muon system

In the DBD it is evaluated at 6.5 MILCU equivalent to 6.6 MEuros today. But no assembly, no tooling, no manpower are evaluated. This may add 25% to the cost growing to 8.3.

The small model can be inferred by a simple scaling where the end cap chambers are scaled by the square of the radii and the barrel ones by the radius. This provides an estimate of 6 + 1.55 Meuros for the small model.

9.4 The global cost of each of the models.

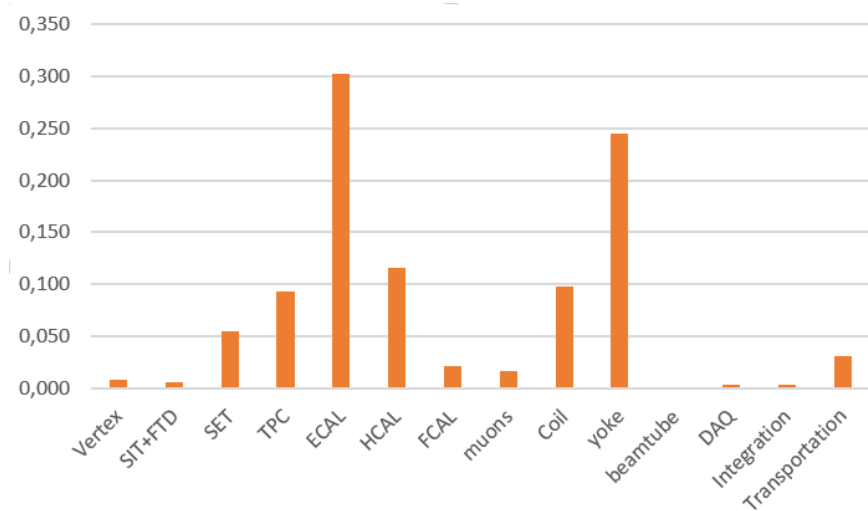
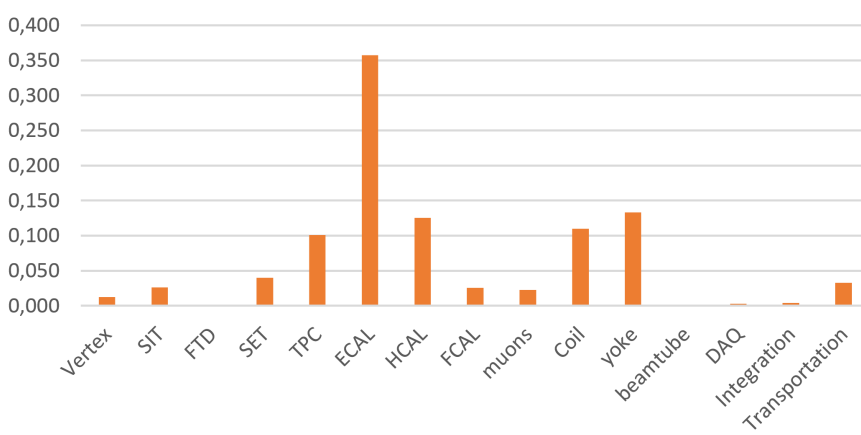
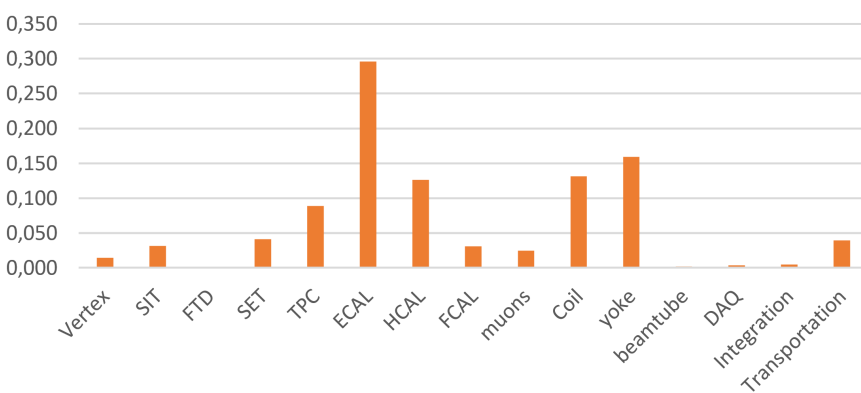
The information developed in the preceding subsections can be summed up in a table presenting the two models side by side.

Table 9.6. Elements of cost of ILD in MEuros. The numbers in italic are from the DBD. The manpower has been translated from man-years to euros.

Item	Large model	manpower	Small model	manpower
Vertex detector	2.96	1.45	idem	idem
Silicon Internal Tracker	7.55	2.0	idem	idem
Forward tracker	1.5	0.5	idem	idem
LumiCal	3.37	0.16	idem	idem
Ecal ring	0	0	idem	idem
LHCAL	2.93	0.16	idem	idem
BeamCal	2.15	0.16	idem	idem
Time Projection Chamber	36.6	0	27.0	0
Silicon External Tracker	12.6	1.9	10.8	1.7
Si Electromagnetic Calorimeter	117	13.0	90.	11.
Sc Electromagnetic Calorimeter	75	?	?	?
A. Hadron Calorimeter	45.7	?	38.4	?
sD. Hadron Calorimeter	45.6	?	38.3	?
Coil and ancillaries	40	0	idem	0
Yoke and vacuum tank	48.4	0	idem	0
Muon system	6.6	1.7	6	1.55
Total	327	21	281	18.7
Total with MP	348		299.7	0

9.5 Comparison with the DBD cost estimate.

When comparing the prices above to the DBD's 392MILCU it should be recalled that the new prices are in Euros, that for the DBD ECal it was a mix between the scintillator and the silicon versions and that globally the manpower cost was left out. The sharing between the sub-detectors is shown for the different versions in the figures 9.2, 9.3, 9.4. Using a reduced sampling in the ECal reduces the cost by 10MEuros, last figure. The increase in the fraction of the ECal comes from the fact that purely the silicon version is quoted here and with manpower.

**Figure 9.2.** ILD cost sharing as it is in the DBD**Figure 9.3.** ILD cost sharing in the large model**Figure 9.4.** ILD cost sharing in the small (26) model

10 Future of ILD

In this chapter we describe some directions ILD might take over the next few years. We discuss both technological developments or changes, as well as organisational steps.

11 Summary

Summary of the paper. Just a placeholder. Mastertest.

At this place, I try to annoy Thomas, for testing purposes — he is editing the same file at the same time in Overleaf, and we try to find out how well the merging / conflict handling tools really are.

Bibliography

- [1] **ILD Concept Group**, T. Abe *et al.*, “The International Large Detector: Letter of Intent” arXiv:1006.3396 [hep-ex]. FERMILAB-LOI-2010-03, FERMILAB-PUB-09-682-E, DESY-2009-87, KEK-REPORT-2009-6.
- [2] H. Abramowicz *et al.*, “The International Linear Collider Technical Design Report - Volume 4: Detectors” arXiv:1306.6329 [physics.ins-det].
- [3] T. Barklow, J. Brau, K. Fujii, J. Gao, J. List, N. Walker, and K. Yokoya, “ILC Operating Scenarios” arXiv:1506.07830 [hep-ex].
- [4] T. Behnke, J. E. Brau, B. Foster, J. Fuster, M. Harrison, J. M. Paterson, M. Peskin, M. Stanitzki, N. Walker, and H. Yamamoto, “The International Linear Collider Technical Design Report - Volume 1: Executive Summary” arXiv:1306.6327 [physics.acc-ph].
- [5] P. Bambade *et al.*, “The International Linear Collider: A Global Project” arXiv:1903.01629 [hep-ex].
- [6] M. Harrison, M. Ross, and N. Walker, “Luminosity Upgrades for ILC” in *Proceedings, 2013 Community Summer Study on the Future of U.S. Particle Physics: Snowmass on the Mississippi (CSS2013): Minneapolis, MN, USA, July 29-August 6, 2013*. 2013. arXiv:1308.3726 [physics.acc-ph].
- [7] JAHEP, “A Proposal for a Phased Execution of the International Linear Collider Project ”. http://www.jahep.org/office/doc/201210_ILC_staging_e.pdf.
- [8] B. Warmbein, “The Road to Kitakami ”. <http://newsline.linearcollider.org/2014/02/20/the-road-to-kitakami/>. ILC Newsline, 20. February 2014.
- [9] B. Parker, A. Mikhailichenko, K. Buesser, J. Hauptman, T. Tauchi, P. Burrows, T. Markiewicz, M. Oriunno, and A. Seryi, “Functional Requirements on the Design of the Detectors and the Interaction Region of an Electron-Positron Linear Collider with a Push-Pull Arrangement of Detectors” in *Particle accelerator. Proceedings, 23rd Conference, PAC'09, Vancouver, Canada, May 4-8, 2009*, pp. WE6PFP078, ILC-Note-2009-050. 2010. <http://www-public.slac.stanford.edu/sciDoc/docMeta.aspx?slacPubNumber=slac-pub-13657>.
- [10] **FCAL**, A. Levy, “The design of the ILD forward region” in *Proceedings, International Workshop on Future Linear Colliders 2016 (LCWS2016): Morioka, Iwate, Japan, December 05-09, 2016*. 2017. arXiv:1701.01923 [physics.ins-det].
- [11] G. White, “BASELINE OPTICS TO PROVIDE FOR A SINGLE FFS L* (QD0 EXIT, IP DISTANCE) OPTICS CONFIGURATION”. <https://edmsdirect.desy.de/item/D00000001082495,A,1,1>. ILC-CR-0002.

- [12] R. Karl and J. List, "Impact of Beam-Gas Interactions in the IP Region of ILD ".
[https://confluence.desy.de/download/attachments/42357928/
ILD-TECH-PUB-2017-001.pdf?version=1&modificationDate=1497399362316&api=v2](https://confluence.desy.de/download/attachments/42357928/ILD-TECH-PUB-2017-001.pdf?version=1&modificationDate=1497399362316&api=v2).
 ILD-TECH-PUB-2017-001.
- [13] **DEPFET**, O. Alonso *et al.*, "DEPFET active pixel detectors for a future linear e^+e^- collider"
IEEE Trans. Nucl. Sci. **60** (2013) 1457, arXiv:1212.2160 [physics.ins-det].
- [14] R. H. Richter *et al.*, "Design and technology of DEPFET pixel sensors for linear collider applications"
Nucl. Instrum. Meth. **A511** (2003) 250–256.
- [15] L. Andricek, G. Lutz, R. H. Richter, and M. Reiche, "Processing of ultra-thin silicon sensors for future e+ e- linear collider experiments" *IEEE Trans. Nucl. Sci.* **51** (2004) 1117–1120.
 [,667(2004)].
- [16] L. Andricek *et al.*, "Intrinsic resolutions of DEPFET detector prototypes measured at beam tests"
Nucl. Instrum. Meth. **A638** (2011) 24–32.
- [17] J. J. Velthuis *et al.*, "A DEPFET based beam telescope with submicron precision capability"
IEEE Trans. Nucl. Sci. **55** (2008) 662–666.
- [18] C. Marinas and M. Vos, "The Belle-II DEPFET pixel detector: A step forward in vertexing in the superKEKB flavour factory"
Nucl. Instrum. Meth. **A650** (2011) 59–63.
- [19] **Belle-II**, T. Abe *et al.*, "Belle II Technical Design Report" arXiv:1011.0352
 [physics.ins-det].
- [20] G. Pellegrini *et al.*, "Technology developments and first measurements of low gain avalanche detectors (lgad) for high energy physics applications" *Nuclear Instruments and Methods A* **765** (2014) 12 – 16.
<http://www.sciencedirect.com/science/article/pii/S0168900214007128>.
- [21] M. Carulla *et al.*, "Technology developments and first measurements on inverse low gain avalanche detector (iLGAD) for high energy physics applications" *Journal of Instrumentation* **11** (dec, 2016) C12039–C12039.
<https://doi.org/10.1088%2F1748-0221%2F11%2Fc12039>.
- [22] E. Currás, A. García, M. Centis Vignali, J. González, S. Hidalgo, M. Carulla, A. Merlos, D. Flores, J. Duarte-Campos, G. Pellegrini, *et al.*, "arxiv: Inverse low gain avalanche detectors (ilgads) for precise tracking and timing applications" tech. rep., 2019.
- [23] **LCTPC**. <https://www.lctpc.org>.
- [24] R. Diener *et al.*, "The desy ii test beam facility" *Nucl. Instrum. Meth.* **A922** (2019) 265–286.
- [25] M. Wu *et al.*, "Development of a large active area beam telescope based on the sid micro-strip sensor". <http://cds.cern.ch/record/2666439>. Poster presented at Vienna Conference of Instrumentation 2019.
- [26] **LCTPC**, "talks".
- [27] C. Ligtenberg *et al.*, "Performance of a gridpix detector based on the timepix3 chip" *Nucl. Instrum. Meth.* **A908** (2018) 18–23.

- [28] L. Raux *et al.*, “SPIROC (SiPM Integrated Read-Out Chip): Dedicated very front-end electronics for an ILC prototype hadronic calorimeter with SiPM read-out” *JINST* **6** (2011) C01098.
- [29] **CALICE Collaboration**, C. Adloff *et al.*, “Hadronic energy resolution of a highly granular scintillator-steel hadron calorimeter using software compensation techniques” *JINST* **7** (2012) P09017, arXiv:1207.4210 [physics.ins-det]. MPP-2012-116.
- [30] **CALICE**, C. Adloff *et al.*, “Track segments in hadronic showers in a highly granular scintillator-steel hadron calorimeter” *JINST* **8** (2013) P09001, arXiv:1305.7027 [physics.ins-det].
- [31] **CALICE**, C. Adloff *et al.*, “Validation of GEANT4 Monte Carlo Models with a Highly Granular Scintillator-Steel Hadron Calorimeter” *JINST* **8** (2013) 07005, arXiv:1306.3037 [physics.ins-det].
- [32] **CALICE**, C. Adloff *et al.*, “Shower development of particles with momenta from 1 to 10 GeV in the CALICE Scintillator-Tungsten HCAL” *JINST* **9** (2014) no. 01, P01004, arXiv:1311.3505 [physics.ins-det].
- [33] **CALICE**, C. Adloff *et al.*, “The Time Structure of Hadronic Showers in highly granular Calorimeters with Tungsten and Steel Absorbers” *JINST* **9** (2014) P07022, arXiv:1404.6454 [physics.ins-det].
- [34] **CALICE**, B. Bilki *et al.*, “Pion and proton showers in the CALICE scintillator-steel analogue hadron calorimeter” *JINST* **10** (2015) no. 04, P04014, arXiv:1412.2653 [physics.ins-det].
- [35] **CALICE**, M. Chefdeville *et al.*, “Shower development of particles with momenta from 15 GeV to 150 GeV in the CALICE scintillator-tungsten hadronic calorimeter” *JINST* **10** (2015) no. 12, P12006, arXiv:1509.00617 [physics.ins-det].
- [36] **CALICE**, G. Eigen *et al.*, “Hadron shower decomposition in the highly granular CALICE analogue hadron calorimeter” *JINST* **11** (2016) no. 06, P06013, arXiv:1602.08578 [physics.ins-det].
- [37] **CALICE**, J. Repond *et al.*, “Hadronic Energy Resolution of a Combined High Granularity Scintillator Calorimeter System” *JINST* **13** (2018) no. 12, P12022, arXiv:1809.03909 [physics.ins-det].
- [38] O. Hartbrich, *Scintillator Calorimeters for a Future Linear Collider Experiment*. PhD thesis, Hasylab, DESY, Hamburg, 2016. <http://bib-pubdb1.desy.de/search?cc=Publication+Database&of=hd&p=reportnumber:DESY-THESIS-2016-020>.
- [39] G. Blazey, D. Chakraborty, A. Dyshkant, K. Francis, D. Hedin, *et al.*, “Directly coupled tiles as elements of a scintillator calorimeter with MPPC readout” *Nucl.Instrum.Meth.* **A605** (2009) 277–281. FERMILAB-PUB-09-585-E.
- [40] F. Simon and C. Soldner, “Uniformity Studies of Scintillator Tiles directly coupled to SiPMs for Imaging Calorimetry” *Nucl.Instrum.Meth.* **A620** (2010) 196–201, arXiv:1001.4665 [physics.ins-det]. MPP-2010-10.
- [41] H. Hayano, “Kitakami Site-specific CFS Study Update”. <https://agenda.linearcollider.org/event/7645/>. International Workshop on Future Linear Colliders LCWS2017, Strasbourg, October 2017.

- [42] M. Miyahara, "Update on Detector Hall and Assembly Hall Layout".
<http://https://agenda.linearcollider.org/event/6910/>. Mini-Workshop on Infrastructure and CFS for Physics and Detectors, KEK, March 2016.
- [43] M. Miyahara, "Update on Detector Hall and Assembly Hall Design".
<https://agenda.linearcollider.org/event/6851/>. Mini-Workshop on Infrastructure and CFS for Physics and Detectors, KEK, September 2015.
- [44] Y. Sugimoto, "Detector Utility". <https://agenda.linearcollider.org/event/8123/>. Mini-Workshop on Infrastructure and CFS for Physics and Detectors, KEK, February 2019.
- [45] K. Buesser and T. Schoerner-Sadenius, "MDIPlan, E-JADE Deliverable Report 22".
https://www.e-jade.eu/sites/sites_custom/site_e-jade/content/e49893/e65922/e84403/D.22.WP3.MDI.v3.pdf. E-Jade.Deliverable.WP3.D22.MDIPlan.v3.
- [46] M. Oriunno, "SiD Underground Assembly".
<https://agenda.linearcollider.org/event/6404/>. MDI-CFS Meeting on ILC Interaction Region Issues, Ichinoseki, September 2014.
- [47] A. Gonnin and C. Bourgeois, "Integration of the inner detector region".
<https://edmsdirect.desy.de/item/D00000001003815,A,1,1>. EDMS ID: D00000001003815,A,1,1.
- [48] A. Besson, "VTX and Intermediate Tracking Status".
<https://agenda.linearcollider.org/event/8126/>. ILD Integration Meeting, DESY, February 2019.
- [49] A. Gonnin and R. Poeschl, "ILD Cabling - what we know today".
<https://agenda.linearcollider.org/event/8126/>. ILD Integration Meeting, DESY, February 2019.
- [50] P. Colas *et al.*, "TPC Interface Control Document".
<https://edmsdirect.desy.de/item/D00000001162555,A,1,1>. EDMS ID: D00000001162555,A,1,1.
- [51] R. Poeschl and H. Videau, "VFS Interface Control Document".
<https://edmsdirect.desy.de/item/D00000001162465,A,1,1>. EDMS-ID: D00000001162465,A,1,1.
- [52] T. Takeshita, "ScECAL Interface Control Document".
<https://edmsdirect.desy.de/item/D00000001162515,A,1,1>. EDMS-ID: D00000001162515,A,1,1.
- [53] S. Schuwalow and Y. Benhammou, "VFS Interface Control Document".
<https://edmsdirect.desy.de/item/D00000001163265,A,1,1>. EDMS-ID: D00000001163265,A,1,1.
- [54] M. Wing *et al.*, "Common DAQ system ready for combined tests, AIDA-2020 report, AIDA-2020-MS80 (2018)". <http://cds.cern.ch/record/2314260>.
- [55] F. Kircher *et al.*, "Conceptual Design of the ILD Detector Magnet System".
http://flc.desy.de/lcnotes/notes/localfsExplorer_read?currentPath=/afs/desy.de/group/flc/lcnotes/LC-DET-2012-081.pdf. LC-DET-2012-081.

- [56] R. Stromhagen, "Note on the integration of Cryostat into the Central Barrel - ILD Detector ".
<https://edmsdirect.desy.de/item/D00000001010065,A,1,1>. EDMS-ID:
D0000001162515,A,1,1.
- [57] A. Seryi, T. Maruyama, and B. Parker, "IR Optimization, DID and anti-DID".
SLAC-PUB-11662.
- [58] Y. Makida *et al.*, "Interim Report from Toshiba/Hitachi Studies on Solenoid and Anti-DID ".
<https://agenda.linearcollider.org/event/7520>. ILD Software and Technical Meeting, Lyon, April 2017.
- [59] U. Schneekloth, "ILD Magnet Activities ".
<https://agenda.linearcollider.org/event/7760/>. ILD Meeting, Ichinoseki, February 2018.
- [60] T. Sanami *et al.*, "IR Hall Dose Rate Estimates with Detector Concepts ". SLAC Radiation Physics Note, RP-09-08.
- [61] "High Sensitivity Seismograph Network Japan". <http://www.hinet.bosai.go.jp>.
- [62] T. Tauchi, "Standard Reference Earthquake Parameters".
<https://edmsdirect.desy.de/item/D0000001164345,A,1,1>. ILC-EDMS D*1164345.
- [63] T. Sanuki *et al.*, "Seismic Isolation ".
<https://agenda.linearcollider.org/event/7976/>. Mini-Workshop on ILC Infrastructure and CFS for Physics and Detectors, KEK, Tsukuba, November 2018.
- [64] "ILC Engineering Data Management System". <https://ilc-edms.desy.de>.
- [65] "ILD Technical Documentation". <https://edmsdirect.desy.de/treebrowser/ildtdr/>.
- [66] iLCSoft authors, "iLCSoft Project Page". <https://github.com/iLCSoft>, 2016.
- [67] W. Kilian, T. Ohl, and J. Reuter, "WHIZARD: Simulating Multi-Particle Processes at LHC and ILC" *Eur. Phys. J.* **C71** (2011) 1742, arXiv:0708.4233 [hep-ph].
- [68] T. Sjostrand, S. Mrenna, and P. Z. Skands, "PYTHIA 6.4 Physics and Manual" *JHEP* **05** (2006) 026, arXiv:hep-ph/0603175 [hep-ph].
- [69] D. Schulte, "Beam-beam simulations with Guinea-Pig" *eConf* **C980914** (1998) 127–131. [,127(1998)].
- [70] P. Chen, T. L. Barklow, and M. E. Peskin, "Hadron production in gamma gamma collisions as a background for e+ e- linear colliders" *Phys. Rev.* **D49** (1994) 3209–3227, arXiv:hep-ph/9305247 [hep-ph].
- [71] F. Gaede, T. Behnke, N. Graf, and T. Johnson, "LCIO: A Persistency framework for linear collider simulation studies" *eConf* **C0303241** (2003) TUKT001, arXiv:physics/0306114 [physics].
- [72] F. Gaede, "Marlin and LCCD: Software tools for the ILC" *Nucl. Instrum. Meth.* **A559** (2006) 177–180.
- [73] M. Frank, F. Gaede, C. Grefe, and P. Mato, "DD4hep: A Detector Description Toolkit for High Energy Physics Experiments" *J. Phys. Conf. Ser.* **513** (2014) 022010.

- [74] M. Frank, F. Gaede, N. Nikiforou, M. Petric, and A. Sailer, “DDG4 A Simulation Framework based on the DD4hep Detector Description Toolkit” *J. Phys. Conf. Ser.* **664** (2015) no. 7, 072017.
- [75] **GEANT4**, S. Agostinelli *et al.*, “GEANT4: A Simulation toolkit” *Nucl. Instrum. Meth.* **A506** (2003) 250–303.
- [76] Icgeo authors, “Icgeo Project Page”. <https://github.com/iLCSoft/icgeo>, 2016.
- [77] F. Gaede, S. Aplin, R. Glattauer, C. Rosemann, and G. Voutsinas, “Track reconstruction at the ILC: the ILD tracking software” *J. Phys. Conf. Ser.* **513** (2014) 022011.
- [78] J. S. Marshall and M. A. Thomson, “The Pandora Software Development Kit for Pattern Recognition” *Eur. Phys. J.* **C75** (2015) no. 9, 439, arXiv:1506.05348 [physics.data-an].
- [79] T. Suehara and T. Tanabe, “LCFIPlus: A Framework for Jet Analysis in Linear Collider Studies” *Nucl. Instrum. Meth.* **A808** (2016) 109–116, arXiv:1506.08371 [physics.ins-det].
- [80] M. Cacciari, “FastJet: A Code for fast k_t clustering, and more” in *Deep inelastic scattering. Proceedings, 14th International Workshop, DIS 2006, Tsukuba, Japan, April 20-24, 2006*, pp. 487–490. 2006. arXiv:hep-ph/0607071 [hep-ph]. [,125(2006)].
- [81] **CLIC detector, physics study**, C. Grefe, S. Poss, A. Sailer, and A. Tsaregorodtsev, “ILCDIRAC, a DIRAC extension for the Linear Collider community” *J. Phys. Conf. Ser.* **513** (2014) 032077.
- [82] A. Miyamoto and H. Ono, “ILD MC production for detector optimization” in *International Workshop on Future Linear Colliders (LCWS 2018) Arlington, Texas, USA, October 22-26, 2018*. 2019. arXiv:1902.02516 [physics.ins-det].
- [83] M. Berggren, “SGV 3.0 - a fast detector simulation” in *International Workshop on Future Linear Colliders (LCWS11) Granada, Spain, September 26-30, 2011*. 2012. arXiv:1203.0217 [physics.ins-det].
- [84] T. Barklow, “Physics Impact of Detector Performance”.
<http://www-conf.slac.stanford.edu/lcws05/program/talks/18mar2005.ppt>. Presentation for LCWS05.
- [85] M. Thomson, “Particle Flow Calorimetry and the PandoraPFA Algorithm” *Nucl.Instrum.Meth.* **A611** (2009) 25–40, arXiv:0907.3577 [physics.ins-det]. CU-HEP-09-11.
- [86] **Particle Data Group**, M. Tanabashi *et al.*, “Review of Particle Physics” *Phys. Rev.* **D98** (2018) no. 3, 030001.
- [87] M. Kurata and R. Yonamine, “Higgs branching ratio study for new detector models as benchmark process in ILD”. <https://confluence.desy.de/display/ILD/ILD+notes>, 2019.
- [88] F. J. Mueller, *Development of a Triple GEM Readout Module for a Time Projection Chamber & Measurement Accuracies of Hadronic Higgs Branching Fractions in $\nu\nu H$ at a 350 GeV ILC*. PhD thesis, DESY, Hamburg, 2016. <http://bib-pubdb1.desy.de/search?cc=Publication+Database&of=hd&p=reportnumber:DESY-THESIS-2016-018>.

- [89] H. Ono, “Higgs branching ratio study for DBD detector benchmarking in ILD” in *Helmholtz Alliance Linear Collider Forum: Proceedings of the Workshops Hamburg, Munich, Hamburg 2010-2012, Germany*, pp. 203–223, DESY. DESY, Hamburg, 2013.
- [90] H. Ono and A. Miyamoto, “A study of measurement precision of the Higgs boson branching ratios at the International Linear Collider” *Eur. Phys. J.* **C73** (2013) no. 3, 2343, arXiv:1207.0300 [hep-ex].
- [91] J. Yan, S. Watanuki, K. Fujii, A. Ishikawa, D. Jeans, J. Strube, J. Tian, and H. Yamamoto, “Measurement of the Higgs boson mass and $e^+e^- \rightarrow ZH$ cross section using $Z \rightarrow \mu^+\mu^-$ and $Z \rightarrow e^+e^-$ at the ILC” *Phys. Rev.* **D94** (2016) no. 11, 113002, arXiv:1604.07524 [hep-ex].
- [92] J. Tian, “Higgs Mass Measurement at $\sqrt{s} = 500$ GeV as benchmark process in ILD”. <https://confluence.desy.de/display/ILD/ILD+notes>, 2019.
- [93] S. Kawada, “Branching ratio $H \rightarrow \mu^+\mu^-$ at $\sqrt{s} = 500$ GeV as benchmark process in ILD”. <https://confluence.desy.de/display/ILD/ILD+notes>, 2019.
- [94] Y. Kato, “ $H \rightarrow$ invisible at $\sqrt{s} = 500$ GeV as benchmark process in ILD”. <https://confluence.desy.de/display/ILD/ILD+notes>, 2019.
- [95] M. Boronat, J. Fuster, I. Garcia, E. Ros, and M. Vos, “A robust jet reconstruction algorithm for high-energy lepton colliders” *Phys. Lett.* **B750** (2015) 95–99, arXiv:1404.4294 [hep-ex].
- [96] D. Jeans and K. Yumino, “ τ polarisation in $e^+e^- \rightarrow \tau^+\tau^-$ at $\sqrt{s} = 500$ GeV as benchmark process in ILD”. <https://confluence.desy.de/display/ILD/ILD+notes>, 2019.
- [97] J. Beyer, “Vector Boson Scattering at $\sqrt{s} = 1$ TeV as benchmark process in ILD”. <https://confluence.desy.de/display/ILD/ILD+notes>, 2019.
- [98] T. Mizuno, “Calibration of the photon energy scale from $e^+e^- \rightarrow \gamma\mu^+\mu^-$ as benchmark process in ILD”. <https://confluence.desy.de/display/ILD/ILD+notes>, 2019.
- [99] A. Irles and Y. Okugawa, “ $e^+e^- \rightarrow b\bar{b}$ and $e^+e^- \rightarrow t\bar{t}$ as benchmark processes in ILD”. <https://confluence.desy.de/display/ILD/ILD+notes>, 2019.
- [100] Y. Wang, “Search for additional Higgs bosons as benchmark processes in ILD”. <https://confluence.desy.de/display/ILD/ILD+notes>, 2019.
- [101] M. Berggren, F. Bruemmer, J. List, G. Moortgat-Pick, T. Robens, K. Rolbiecki, and H. Sert, “Tackling light higgsinos at the ILC” *Eur. Phys. J.* **C73** (2013) no. 12, 2660, arXiv:1307.3566 [hep-ph].
- [102] S. Sasikumar, “Light higgsinos as benchmark processes in ILD”. <https://confluence.desy.de/display/ILD/ILD+notes>, 2019.
- [103] R. Yonamine, “WIMP searches in the mono-photon channel as benchmark processes in ILD”. <https://confluence.desy.de/display/ILD/ILD+notes>, 2019.
- [104] M. Habermehl, *Dark Matter at the International Linear Collider*. PhD thesis, DESY, Hamburg, 2018.